UNIVERSITY OF LIVERPOOL

Experimental and Numerical Modelling of Blood Flow in Stenosed Arteries

Thesis submitted in accordance with the requirements of the University of Liverpool for the degree of Doctor in Philosophy

by

Luke Robert Aldred, MEng

August 2007

Abstract

Heart disease is the single biggest cause of death in the Western world. Poor circulation of the blood can lead to blockages in arteries and veins and the weakening of the heart caused by the increased strain to which it is subjected. It is therefore necessary to determine the causes of these problems which lead to millions of people dying prematurely each year. The study of blood flow is called Haemodynamics.

Experimental and numerical studies were conducted using two simplified representations of arterial stenoses, each defined by the reduction in cross-sectional area at the throat.

To assist the experimental acquisition of data, large-scale *in vitro* models were employed in which a non-Newtonian aqueous solution of Xanthan Gum was used as the test fluid. Steady and pulsatile experiments were conducted according to flow rate conditions considered representative of those found *in vivo*. Measurements of velocity were made in a two-dimensional plane through the centre of the test section using Particle Imaging Velocimetry (PIV), from which estimates were made of the local wall shear stress (WSS) environment. A numerical analysis, using Computational Fluid Dynamics (CFD), was conducted using three-dimensional reconstructions of the *in vitro* test sections used in the experiments. The measured fluid properties of the Xanthan Gum solution were used to define the fluid model, while the flow rate conditions were defined according to those used in the experimental analysis. It is shown that, despite the inability of CFD to model the observed unsteadiness distal to the stenosis in the experiments, CFD is able to accurately model both the flow in the vicinity of the stenosis and the mean WSS environment throughout the length of the domain.

The three-dimensional numerical geometries were then scaled to life-size and the flow rate conditions set according to those found *in vivo*. Two different fluid models were used to represent blood; a Newtonian approximation based on the high-shear plateau characteristic of blood, and a modified version of the Power-Law, limited at the extremities of the shear range, which is considered the more accurate representation of the viscous behaviour of blood. It is shown that the overall structure of the flow, and in particular the conditions at the wall, can be modelled sufficiently well by using a Newtonian approximation for blood. A discussion regarding the physiological implications of these results is also presented, with particular attention paid to the likely effect on further localized deterioration of arterial health.

Acknowledgements

I would like to acknowledge the support of my supervisor, Prof. Ieuan Owen who provided guidance and inspiration (always with enthusiasm!) throughout the course of this project. Also, the expertise and wisdom of Steve Bode, Derek Neary, Prof. Marcel Escudier and Dr. Robert Poole, whose help was always appreciated and whose doors were always open. Most importantly however, I would like to thank Ruth and my family and friends (particularly Ed – you'll be finished soon), whose support was invaluable; I couldn't have done this without you!

Table of Contents

Nomenclature

	Description	*Units*
a	occlusion offset distance	m
A_0	cross-sectional area of un-stenosed tube	m^2
A_N	cross-sectional area of stenosed tube at stenosis neck	m^2
d	tube diameter	m
e	strain/displacement	-
f	frequency of oscillation	Hz
G^*	complex modulus of rigidity	Pa
G'	storage modulus in viscoelastic fluid	Pa
G''	loss modulus in viscoelastic fluid	Pa
H	haematocrit	%
L_e	Entrance length for fully-developed laminar flow (Newtonian)	m
n	power-law index	-
P.I.	Pulsatility index $\left(=\frac{u_{max}-u_{min}}{\overline{U}_c}\right)$	-
q	volumetric flow rate	m^3/s
r	radial position	m
r_s	height of stenosis	m
r_w	waisted radius at stenosis throat	m
R	tube radius	m
Re	Reynolds number	-
Re_0	Newtonian Reynolds number, based on Newtonian viscosity in low shear $\left(=\frac{\rho d\overline{U}_c}{\eta_0}\right)$	-
Re_∞	Newtonian Reynolds number, based on Newtonian viscosity in high shear $\left(=\frac{\rho d\overline{U}_c}{\eta_\infty}\right)$	-
Re_N	Newtonian Reynolds number $\left(=\frac{\rho d\overline{U}_c}{\mu}\right)$	-

Re_{PL}	Power-law Reynolds number $\left(=\frac{\rho d^n \overline{U}_c^{(2-n)}}{\kappa}\right)$	-
S	stenosis severity	%
St	Strouhal number $\left(=\frac{\omega d}{\overline{U}_c}\right)$	-
T	time period	s
u_w	local velocity parallel to the wall	m/s
$\hat{u}$	peak to peak amplitude of waveform	m/s
$\overline{u}_{(x,r)}$	mean local velocity	m/s
u(r)	local axial velocity as a function of radial position	m/s
u_{max}	velocity at waveform peak	m/s
u_{min}	velocity at waveform trough	m/s
$\overline{U}$	mean/bulk velocity in steady flow	m/s
$\overline{U}_C$	cycle mean velocity in pulsatile flow	m/s
x	axial position	m
$\dot{\gamma}$	shear rate	s^{-1}
$\dot{\gamma}_{C0}$	critical shear rate at which viscosity changes from being Newtonian to being defined by the Power-Law (low shear)	s^{-1}
$\dot{\gamma}_{C\infty}$	critical shear rate at which viscosity changes from being defined by the Power-Law to being Newtonian (high shear)	s^{-1}
Γ	non-dimensional wall shear stress $\left(=\frac{\tau_w}{1/2 \rho \overline{U}_c^2}\right)$	-
δ	perpendicular distance from the wall to the velocity vector	m
η	Power-Law viscosity	Pa.s
η^*	complex coefficient of viscosity	Pa.s
η'	viscous component of complex viscosity	Pa.s
η''	elastic component of complex viscosity	Pa.s
η_0	Newtonian viscosity of blood at low shear	Pa.s
η_∞	Newtonian viscosity of blood at high shear	Pa.s
θ	azimuth position in the y-z plane	rad
κ	Power-Law consistency	$Pa.s^n$

λ_f	characteristic time of the flow (= d/$\overline{U}_C$)	s
λ_r	relaxation time	s
μ	Newtonian viscosity	Pa.s
ρ	fluid density	kg/m^3
σ	standard deviation	-
τ	shear stress	Pa
τ_w	wall shear stress	Pa
ω	angular frequency of oscillation	rad/s

Glossary of Medical Terminology

abdominal aorta ~ the part of the aorta below the diaphragm.

ABG ~ (abbreviation) artery bypass graft.

activation ~ the shape change of a platelet, resulting in the extrusion from its surface of pseudopods which increases significantly its hydrodynamic volume.

acute ~ (of a disease) coming sharply to a crisis; severe, not chronic.

aggregation ~ (of platelets or red blood cells) the formation of chains

albumin ~ a transport protein in blood plasma; responsible for the maintenance of plasma volume.

anastomosis ~ the connection of separate parts of a branching system to form a network. In particular, the surgical connection of blood vessels to form a continuous channel between a host artery and a bypass vessel.

aneurysm ~ an excessive, localised and balloon-like enlargement in the wall of an artery.

angina ~ suffocating pain in the chest brought on by exertion, owing to an inadequate blood supply to the heart.

aorta ~ the main artery of the body, from which all others derive.

anticoagulant ~ an agent which prevents the blood from clotting.

atherogenesis ~ initiation and early development of atherosclerosis; the formation of atheroma.

atheroma ~ the fatty plaques and scar tissue, characteristic of atherosclerosis.

atherosclerosis ~ a disease of the medium to large arteries characterised by the degenerative build-up of fatty deposits on the internal wall of an artery. Severe cases experience the eventual obstruction of blood flow.

bifurcation ~ the point at which division into two branches occurs.

bpm	~ beats per minute (of the cardiac cycle)
bypass graft	~ a vessel used to bypass a damaged part of artery. Typically used as treatment for a dangerously stenosed artery.
carotid arteries	~ the two main arteries in the neck, supplying blood to the head and neck.
cerebral	~ referring to the brain
cholesterol	~ pearly, fat-like sterol present in the blood and most tissues, usually in the form of low density lipoproteins (LDL).
chronic	~ (of a disease) persisting for a long duration.
collagen	~ principal constituent protein of white fibrous connective tissue. Relatively inelastic but has high tensile strength.
coronary arteries	~ arteries supplying blood to the heart.
diastole	~ time between contractions of the ventricles, during which time the ventricles fill with blood.
distal	~ situated away from the centre of the body; "downstream" in the case of arterial blood flow.
elastin	~ major constituent protein of elastic tissue fibres. Highly distensible.
endothelial cells	~ cells which make up the endothelium.
endothelium	~ a single layer of epithelial cells lining the internal walls of arteries and lymphatic vessels and cavities in the heart.
erythrocyte	~ red blood cell
external elastic lamina	~ the membrane separating the tunica media and tunica adventitia.
extracellular	~ situated or occurring outside the cell
femoral artery	~ artery carrying blood down through the upper leg.
femorodistal bypass	~ a bypass vessel running from one point on the femoral artery to another point downstream.
fibrin	~ insoluble blood coagulant formed by enzyme action on fibrinogen. Forms a mesh completing the clotting

	process.
fibrinogen	~ a protein in blood plasma; important in the final clotting process of blood.
foam cells	~ lipid-laden macrophages.
formed elements	~ the collective name for red blood cells, white blood cells and platelets.
globulin	~ a protein group in blood plasma; important functions include that as an antibody and in trace element transportation.
glycocalyx	~ the negatively charged biopolymer surface on the endothelium. Its charge repels similarly charged plasma proteins such as albumin and LDL away from the endothelium.
granulocyte	~ a class of leucocyte that destroys bacteria and parasites
haem-	~ (prefix) denoting blood.
haematocrit	~ concentration of red cells in blood; defined as the percentage volume red blood cells occupy after centrifugation of a blood sample.
haemodynamics	~ the study of forces involved with the circulation of blood.
haemoglobin	~ a protein found in red blood cells responsible for transporting oxygen around the body.
hyperplasia	~ the increased production of normal cells in a tissue or organ resulting in the affected area becoming enlarged.
iliac arteries	~ arteries carrying blood through the lower abdomen, supplying the femoral arteries.
in vitro	~ Latin: describing biological phenomena occurring outside the body; "in a glass".
in vivo	~ Latin: describing biological phenomena occurring inside the body; "in a living thing".
infarction	~ localised death of tissue due to inadequate blood supply; responsible artery is usually obstructed.
intercellular clefts	~ clefts between endothelial cells which hold them

	together.
internal elastic lamina	~ the membrane separating the tunica intima and tunica media.
internal thoracic artery	~ artery responsible for delivering blood to the chest.
intima	~ the innermost (and thinnest) layer of an artery (or vein) wall; composed of endothelial cells.
intimal	~ of the intima
ischaemia	~ an inadequate supply of blood to a part of the body; caused by the constriction or blockage of the blood vessels supplying it.
LDL	~ (abbreviation) Low Density Lipoprotein. Principal form in which cholesterol is transported around body.
leucocyte	~ white blood cells
lipid	~ a group of naturally occurring compounds, important in the diet because of their high energy value and because of certain vitamins and essential fatty acids associated with them.
lipoproteins	~ one of a group of compounds consisting of a protein combined with a lipid (which may be cholesterol, a triglyceride or a phospholipids)
lumen	~ the cavity or channel within a tubular or sac-like structure, such as a blood vessel. In the case of an artery, the cavity through which blood flows.
lymphocyte	~ a class of white blood cell. Main player in the immune response mechanism
macromolecules	~ complex molecules carried in blood.
macrophage	~ large scavenger cell present in connective tissue and many organs. Are in fact migrated plasma monocytes.
monocyte	~ a class of white blood cell whose function it is to ingest foreign particles such as bacteria and tissue debris.
myocardium	~ muscle tissue of the heart.
occlusion	~ the closing or obstruction of a hollow pipe.
patency rate	~ percentage of procedures which remain unobstructed

	after a given time.
plasma	~ clear straw-coloured fluid in which the formed elements are suspended.
plasma proteins	~ proteins transported in the blood.
platelets	~ cell fragments; important in the clotting process of blood.
proximal	~ situated close to the centre of the body; "upstream" in the case of arterial blood flow.
pseudopods	~ projections from the surface of platelets, caused by activation.
RBC	~ (abbreviation) red blood cells.
restenose	~ to re-form a stenosis.
rouleau	~ cylindrical structure formed by stacks of RBCs joined face to face (pl. rouleaux).
saphenous vein	~ vein draining blood from the foot up the length of the leg.
smooth muscle	~ muscle tissue which produces slow, long-term contractions without conscious control; occurs in hollow organs such as blood vessels and intestine.
stenosis	~ abnormal narrowing or stricture of a duct or canal; percentage refers to the percentage of the cross-sectional area which is restricted.
systole	~ time at which ventricular contraction occurs.
thrombocyte	~ platelets
thrombosis	~ formation of a blood clot in the vascular system which impedes blood flow.
tunica adventitia	~ the outer layer of the wall of an artery or vein, composed of loose (collagenous) connective tissue and vaso vasorum.
tunica intima	~ the inner layer of the wall of an artery or vein, lined with endothelial cells.
tunica media	~ the middle layer of the wall of an artery or vein, composed of smooth muscle cells and fibres of elastin.

vaso vasorum	~ the tiny arteries and veins that supply the walls of blood vessels.
vasoactive	~ affecting the diameter of blood vessels, especially arteries.
WBC	~ (abbreviation) white blood cells.

1: INTRODUCTION

1.1: Background

Atherosclerosis is a disease of the medium to large (≥3mm) arteries, complications from which are the main causes of death in the western world (in the UK, 43% of all deaths in 2003 were attributed to cardiovascular disease[1]). Atherosclerosis is characterised by the formation and deposition of fatty streaks on the internal surface of an arterial wall. Over time, these fatty deposits develop into raised plaques, causing progressive narrowing of the lumen (flow area), forming what is known as a stenosis. This causes both disturbances in the local flow field and a reduction in the supply of blood to distal tissues, a condition known as ischaemia. Ischemia is classed as either chronic or acute. (The reader is referred to the glossary for definitions of medical terms.)

Chronic ischaemia is a relatively stable condition, which deteriorates gradually over the course of many years. A reduction in lumen diameter causes an imbalance in the supply and demand for oxygen, particularly during times of exercise or high emotion, and is manifested as a crushing pain in the affected area. At rest, a 75% reduction in lumen diameter (~94% area reduction) is required to seriously affect blood flow while during exercise, just 30% diameter (~50% area) reduction is necessary[2]. A 50% reduction in lumen diameter (75% area reduction) is judged to be significant in clinical practice[2,3]. Chronic ischaemia can occur in any artery although it is given the specific name angina when referring to the coronary artery.

Acute ischaemia is the result of a sudden and dramatic occlusion of an already stenosed artery. The most common mechanism through which this condition is realised is called thrombosis. A small rupture of an atherosclerotic plaque triggers the natural reaction of the blood to clot, quickly resulting in total closure of the lumen[2]. This leads to infarction (localized tissue death caused by inadequate oxygen supply) of any distal tissue and can result in ischemic stroke or cardiac arrest in the respective cases of cerebral (that of the brain) or myocardial (heart muscle) infarction. Acute ischaemia in peripheral arteries (for example in the femoral or iliac

arteries) is not as immediately serious, although amputation of the respective limb must be considered to remove the threat of gangrene.

Atherosclerosis can also cause aneurysms. These are localised balloon-like enlargements of the arterial wall that are filled with blood. The normally elastic properties of arterial walls are degraded in the presence of atherosclerotic plaques[4]. Very high stresses are therefore generated at the boundaries between healthy wall tissue and plaque deposits, eventually causing the intima to tear along this boundary. Blood seeps through the tear and into the artery wall, forming the aneurysm. These often develop and grow over a number of years and are most common in the aorta (which originates from the left ventricle and delivers blood to all parts of the body other than the lungs), where their presence is also most dangerous. This is a potentially fatal condition since, if not treated, the aneurysm will eventually rupture causing massive internal bleeding and death.

1.2: Risk Factors, Prevention and Available Treatment

There are many risk factors associated with the development of atherosclerosis. These range from lifestyle factors (such as the level of cholesterol intake, smoking, obesity and exercise) to wholly unavoidable factors (such as race, gender, family history and personality)[2]. It is universally accepted that a healthy lifestyle, reflected in a low calorific and cholesterol diet, taking regular exercise and avoiding smoking, is the best preventative action one can take against atherogenesis. Although this advice is relevant, there is much discussion in the literature regarding the physiology behind the development of atherosclerosis. It is generally accepted that the occurrence of atherosclerotic plaques is not random and that its severity and location within the vascular system can, to some extent, be predicted. Qualitative judgements can be made with regard to the severity of the condition on the basis of a patient's age, diet and lifestyle. For example, a 20-year-old non-smoker, who exercises regularly and consumes an all-round healthy diet, can be expected to show little evidence of atherosclerosis when compared to a 65-year-old, obese smoker of 40 years. Locations within the vascular system which show a predilection to the development of atherosclerotic lesions has been the subject of much research. Vessels most commonly affected are the abdominal aorta, carotid arteries, coronary

arteries and major peripheral arteries such as the femoral and iliac arteries[5]. Many authors have found that preferred sites for the disease include regions of sharp curvature and arterial branching/bifurcation[e.g. 5-8]. These regions are certainly prone to sudden changes in the flow pattern, which indicates that local haemodynamics may play a pivotal role in the development of the disease.

There are two methods of treating the mid-term symptoms of atherosclerosis. Developed in the 1960s, arterial bypass grafts (ABG) use the patient's own saphenous vein (which drains blood from the lower leg) to bypass the diseased portion of artery. Recent years have seen a rise in the internal thoracic artery (which delivers blood to the chest) being the graft vessel of choice due to the superior patency rate (percentage of cases in which the treatment is judged successful); vein grafts re-stenose at a rate of 2-5% per annum, whereas artery grafts exhibit >95% original lumen size after 10 years[2]. Whichever graft vessel is used however, 75-90% of patients are free from angina following successful surgery on coronary arteries.

An alternative treatment using stent implantation was developed in the 1980s. This technique involves inserting a plastic or expandable metal mesh tube into the diseased artery. Once fixed into position, the tube helps maintain the desired lumen size, although re-stenosis is still a problem which can affect as much as 15-20% of patients[2]. This treatment is increasingly being used as an alternative to ABG because of its relative simplicity and the less invasive nature of the required surgery.

The reason why both types of treatment eventually fail is due to re-stenosis, the cause of which is thought to be a process called intimal hyperplasia. This is a biological reaction of the artery wall to changes in the local flow environment, which causes the proliferation of cells in the affected region. Eventually the lumen is occluded again, rendering the once successful treatment ineffective. An example of the seriousness of this condition is reflected in a patency rate of 30% for a femorodistal anastomosis[9]. The reasons why intimal hyperplasia occurs are not properly understood, although obviously a greater understanding will help increase the patency rate of these surgical techniques.

1.3: The Cardiovascular Environment

The cardiovascular system provides the body with a constant supply of blood. It consists of the heart connected to a network of blood vessels, whose lumen diameters vary in size between 6μm - 25mm[4]. In order to provide the reader with a sound understanding of the cardiovascular environment, there follows a brief description of the main structural elements from which arteries are made. The constituent parts of blood are also discussed, as are the processes believed to be responsible for the formation of atherosclerotic plaques and intimal hyperplasia.

All blood vessels (except capillaries) are constructed in a similar fashion, their walls comprising three distinct layers (see Fig.1). The outermost layer (tunica adventitia) is composed mainly of connective tissue, which tethers the vessel loosely to the surrounding tissue. The intermediate layer (tunica media) is separated from the adventitia by the external elastic lamina. It supplies the mechanical strength to the wall and is made up of smooth muscle cells arranged helically in a matrix of the proteins elastin and collagen[4]. Elastin is an extracellular protein and is six times more extensible than rubber[4]. It is found in high concentrations in large arteries such as the iliacs and femorals[4] (which supply the lower body), where the walls are required to be highly distensible. The presence of this protein in high concentrations enables arteries to expand radially by ~10% during each cardiac cycle[4]. Collagen, another extracellular protein, is 100 times stiffer than elastin and forms a strong network of fibres in the media which prevents over-distension of the artery[4]. The internal elastic membrane separates the media from the tunica intima, the inner-most layer. This is made up of a monolayer of flattened endothelial cells (collectively called the endothelium), 0.2-0.3μm thick[4], which rests on a thin layer of connective tissue. It forms the main barrier to the transport of particulates in the blood, from the lumen through the vessel wall.

The luminal surface of the endothelium is coated with a thin layer of negatively charged (anionic) polymers, which are given the collective name glycocalyx. Its thickness is between 60-570nm[4] and, to some extent, it regulates mass transfer between the lumen and vessel wall. When in a healthy condition, it allows the passage of water and other small solutes through to the intercellular clefts (which hold individual endothelial cells together), while its anionic character appears to help

prevent the migration of like-charged blood particulates (such as the plasma protein albumin and low-density lipoproteins (LDL)). This is supported by evidence of an increase in the rate of passage of these particulates across the endothelium, after enzymatic removal of the glycocalyx[4].

Blood is a complex mixture of formed elements (blood cells and cell fragments) suspended in an aqueous solution called plasma. Also present in the plasma are a variety of trace elements, salts (of sodium, potassium and calcium) and a number of proteins, namely albumin (responsible for the maintenance of plasma volume), globulin (whose important functions include that as an antibody and a trace element transporter) and fibrinogen (important in the clotting process). The formed elements typically constitute just under half the volume of blood (depending on the individual), while blood itself accounts for approximately 7% of body weight in humans[4]. Formed elements consist of three main component categories: red blood cells (RBC), white blood cells (WBC) and platelets. RBCs are packed with the protein haemoglobin which transports oxygen around the body. To maximise their transporting efficiency, they contain no nucleus and exhibit a biconcave disc shape when unstressed, providing a high surface area to volume ratio through which oxygen exchange can occur. They can deform considerably to enable movement through capillaries, whose diameters vary between 4-7μm (diameter of RBCs is typically 7-8μm)[4]. RBCs account for 99% of all the formed elements and play a large part in determining the rheological characteristics of blood.

WBCs are defined as any blood cell containing a nucleus. The principal role of WBCs is to fight infection and disease. There are many different types, of various shapes and sizes, each employing a different immune response mechanism. Although their numbers increase during infection, there are never enough to significantly influence the rheology of blood. To list here each type of WBC and explain their specific function is unnecessary, although Table 1[4,10] gives a brief description of these details. Platelets are disc-shaped cell fragments approximately 1-2μm in diameter[4]. Their function is to assist in the arrest of bleeding, although there are several mechanisms through which this is achieved.

The early stages in the development of atherosclerotic plaques are characterised by the uptake of particulates, carried in the blood, into the artery walls. They consist of patchy streaks of lipid deposits and scar tissue in the sub-endothelial region of large arteries. They begin with an accumulation of LDLs and plasma proteins such as fibrin and albumin[4,11-13] which are transported through the body in the bloodstream. LDLs consist of a protein combined with (usually) cholesterol, a type of sterol lipid, which is a vital constituent of cell membranes and is a precursor to many steroid hormones and bile salts[2]. Fibrin is an insoluble coagulant (formed by the action of the enzyme thrombin on the soluble precursor fibrinogen) which forms the fibrous mesh that is the basis of a blood clot. Many researchers have shown that increased permeability of the endothelial layer is, at least partly, responsible for the elevated concentration of LDLs and plasma proteins in atherosclerotic vessel walls[4,5,11-14].

A key feature in the early stages of plaque formation is the presence within the plaque of foam cells[13]. These are damaged, lipid-laden macrophages (monocyte white blood cells that have migrated from the bloodstream to the vessel tissue). When these foam cells become saturated by lipid, the lipids are simply deposited in an extracellular fashion, leading to the characteristic fatty streaks.

Deposition of platelets onto the vessel wall is another key element in the formation of plaques. Platelets undergo a shape change called 'activation' when subjected to either high shear rates[15] or cyclical stretching[16]. Activation results in the extrusion from its surface of pseudopods that increases the platelet's effective volume by up to eight times[15]. This in turn increases the platelet-boundary collision frequency, increasing the likelihood of deposition[15].

Advanced plaques often contain smooth muscle cells. These cells are absent in healthy intima and their presence indicates the occurrence of the non-atherosclerotic process called intimal hyperplasia[5]. This process is characterised by the proliferation, migration and accumulation of smooth muscle cells and the proteins elastin and collagen into the intimal layer, in the region between the endothelium and the internal elastic membrane. The combination of atherosclerotic and non-atherosclerotic processes involved in arterial plaque formation is not uncommon. This is supported by Nerem et al[5] and Pedley[17], both of whom point out that

atherosclerotic plaques are often associated with, and even superimposed on, regions of intimal hyperplasic growth. It is likely, therefore, that the mechanisms which govern the onset and development of both processes are similar.

The importance of healthy wall tissue (in particular that of the endothelium) is emphasized by considering the functions for which it is responsible. Not only is it the boundary at which blood interacts with the wall – and particulates pass through – but a number of these functions have important anti-atherosclerotic effects. Regulation of vascular tone and diameter is achieved through the secretion of vasoactive chemicals. One of these, Nitric Oxide (NO) is synthesised through shear-stress stimulation of the endothelium and is known also to inhibit the proliferation and migration of smooth muscle cells and the uptake of LDLs and fibrin into the arterial wall[13]. NO also has an anti-clotting effect on platelets through its ability to prevent them from aggregating. Its importance is emphasised by evidence that shows levels of NO in smokers and diabetics (groups particularly prone to atherosclerosis) to be generally low in comparison with a control population[4].

As described previously, the arterial wall is able to undergo a radial expansion ~10% during each cardiac cycle[4]. There is much debate in the literature as to whether *in vitro* experimental analysis of blood flow through arteries should account for this elastic nature. This is a contentious issue since there are significant effects an elastic wall can have on the resulting flow structure and, in particular, the distribution of wall shear stress (WSS). However, stenosis formation, and in particular the deposition of atherosclerotic plaque material, is usually associated with hardening of the vessel wall, thereby reducing its elasticity[7]. It is therefore not unreasonable, as will be done here, to assume a rigid wall condition for *in vitro* analysis of this kind.

The processes described here highlight the importance of arterial health in controlling and preventing the development of atherosclerosis. The role haemodynamics may play in this process has been the subject of a number of studies, the main findings of which are summarised in the following discussion.

1.4: Influence of Local Haemodynamics

As alluded to earlier, those sites which are prone to the development of atherosclerosis and intimal hyperplasia are associated with marked changes in the local haemodynamic environment. This is supported by a number of studies which identify haemodynamics as a causative factor in the progressive development of the disease[6,7,13,15,18-23]. More specifically, WSS is cited as the most important factor, having a critical role throughout[7,13,15,18,20-22]. However, the causative role WSS plays in the various stages of the disease is the subject of intense debate; there is no consensus regarding a relationship between WSS and the overall growth of atherosclerotic plaques and/or intimal hyperplasia. In fact, intimal thickening (caused by hyperplasic growth) and atherosclerotic lesions have been found in regions of both high and low WSS[6,7,24]. Consequently, there is a high probability that WSS plays a number of different roles, depending on the severity and stage of the disease[13].

Sensitivity of the endothelium to haemodynamic forces, particularly WSS, has been demonstrated in a number of studies[14,25-29]. In fact, exposure of the endothelium to elevated levels of WSS has been shown to be highly detrimental to its health and its ability to function correctly[5,12-14,25,30,31]. A number of studies have attempted to quantify this relationship. Fry[14] summarised that endothelial cells suffer erosion when the instantaneous local WSS exceeds approximately 100 Pa. However, since endothelial erosion is strongly dependent on the duration of exposure to WSS, erosion was considered possible at shear stress levels considerably less than this value. Lesser injury was reported at 40 Pa and above[14], at which point endothelial cells begin to deform, yield and swell slightly, increasing the permeability of the endothelium. This concurs well with a separate study[25] in which it was reported that endothelial integrity was compromised at WSS magnitudes of around 38 Pa. A similar study reported endothelial permeability to be enhanced at locations where the WSS environment was in a high state of flux[12]. This is supported by observations made by a number of researchers[32-34] which suggest the oscillatory nature of the flow has an important influence on the transport of macromolecules from the blood to the arterial wall. It is widely accepted that the degradation of endothelial integrity, WSS-induced or otherwise, increases the uptake of plaque material onto the vessel wall[5,12-14].

The activation and deposition of platelets has also been shown to be highly dependent upon local WSS. Using numerical and particle imaging techniques to study Newtonian flow through a model stenosis, Bluestein et al[15] analysed the potential for platelet activation and deposition. Activation was shown to occur when platelets were exposed to either high shear stresses or cyclical elongational stresses (an observation also reported in experiments conducted by Purvis & Giorgio[16]). The high shear regions which exhibited the highest potential for platelet activation were those proximal to the stenosis throat, where the streamlines are forced together, and in the shear layer created between the core jet flow and the recirculation zones distal to the throat. Activation was also shown to increase due to the cyclic elongational/compressive stresses exerted on the platelets, caused by acceleration and deceleration of the flow as it moved through the stenosis. Similarly, Ku[3] and Jung et al[35] concluded that the incidence of platelet activation increased at the throat of the stenosis due, this time, to the elevated WSS in the region. Bluestein et al[15] observed that the deposition rate of activated platelets onto the wall was greatly enhanced where WSS is low, an observation repeated in a number of other studies[24,31,36]. Deposition of other atherogenic particles, such as LDLs and plasma-proteins, was also shown to increase considerably in those regions subjected to low WSS[13,37]. It is thought that the increase in residence time (of particles adjacent to the wall) results in an elevated incidence of contact with, and hence adhesion to, the wall[15,24,31,36]. In addition, the blood's capacity to 'wash away' particles from the wall is greatly reduced due to the low velocity gradients[15]. Bluestein et al[15] reported a peak in the rate of deposition distal to the stenosis where the flow reattached to the wall. Here, the WSS is very low (zero at the stagnation point) and the local flow field induces a high convection rate of particles onto the wall. For the same reason, deposition rates were also observed to be high proximal to the stenosis throat, where local velocity vectors had components normal to the wall.

A number of researchers have attempted to explain the process of intimal hyperplasic growth. As discussed earlier, WSS is 'sensed' by the endothelium which then initiates a response through the secretion of vasoactive agents. The apparent WSS-induced responses suggest the existence of an optimum range of mean (across the cardiac cycle) WSS. A number of researchers have identified this as being critical in

regulating the long-term adaptation of vessel structure[30,31,36]. *In vivo* studies have shown that, given the presence of a healthy endothelium, the artery wall will remodel itself over a period of several months in order to restore mean WSS to its optimum value[30]. If the long-term local mean WSS falls below the accepted range, the diameter is reduced by means of a relative thickening of the intimal layer through hyperplasic growth. This is supported by a number of studies which identify a strong correlation between intimal thickening and regions of low wall shear[13,37]. Calculation of the optimum mean WSS was attempted by several researchers[30,38-40], the results of which are summarised in Table 2. The similarity observed between those values recorded for different kinds of arteries and species suggests WSS is maintained at approximately the same level (1-2 Pa) throughout the cardiovascular tree in many species.

Although there is consensus regarding the effects of WSS when considering a specific process (degradation of the endothelium, deposition of atherogenic particles or hyperplasic growth), there is disagreement as to which process is most important in the early, formative stages of stenotic growth. A number of studies claim that the early stages are characterized by high-shear damage to the intimal layer, in particular the endothelium. Once damaged, it becomes more permeable and hence susceptible to a subsequent increase in the deposition rate of plaque material in low shear regions[5,13,14,30]. Alternatively, some authors suggest the early stages are characterized by intimal thickening and deposition of plaque material in regions of low shear[31,36,41]. The subsequent weakening of the endothelium subjects it to localised peaks in WSS, weakening it further and hence accelerating the development of the disease. In all likelihood, there exists no definitive, sequential course of events which are universal in the development of stenoses. Instead, the numerous processes which are responsible are almost certain to occur in parallel (although at differing rates throughout the vascular tree), particularly since flow rate is constantly varying.

Although not part of the atherosclerotic or hyperplasic processes, the incidence of thrombosis is nevertheless influenced by the presence of stenoses. Acute ischemia (the sudden and total blockage of an artery) is usually brought about by thrombosis.

This is most often caused by the sudden rupture of an atherosclerotic plaque which initiates the natural clotting process of blood.

The long- and short-term effects local haemodynamics have on the cardiovascular system are numerous and have been shown to be critical in the development of stenoses. The influence that arterial geometry inevitably has on the local flow-field has led to many studies which have attempted to model blood flow through simple geometric structures representative of those commonly found *in vivo*. These include bifurcations and anastomoses (both examples of arterial branching), aneurysms and stenoses (see Fig.2). Of these, the most studied have been the end-to side anastomosis and the bifurcation. Fewer studies have concentrated on geometries representative of aneurysms or stenoses. The following summarises previous research which analyzed the geometric effects of stenoses on local flow conditions and, in particular, WSS.

1.5: Previous Studies on Stenotic Geometries

In all circumstances, fluid flow is influenced by the geometry of the domain through which it flows. It is this influence that creates forces such as aerodynamic (in the case of air), hydrodynamic (water) and haemodynamic (blood). As Newton's 3rd law states, these forces are felt by both the fluid and the surface with which it interacts. It follows therefore that complex geometries which represent some part of the cardiovascular tree will induce a change in the local flow-field from what might be expected in a simple straight section of artery. In turn, this change in the haemodynamic environment will exert a change in the force distribution on the walls. For the purposes of this study, a stenosis (called an occlusion when not specifically referring to *in vivo* conditions) is essentially a smooth contraction-expansion in an otherwise uniformly cross-sectional circular pipe. In physiological terms, the growth of a stenosis is invariably non-uniform, making the task of standardising the geometry very difficult. This is illustrated by the numerous designs employed in the various studies reported in the literature. Although the method by which the geometry is defined varies considerably, the severity of the occlusion (S) is consistently defined as the percentage reduction in luminal cross-sectional area, from the straight unobstructed artery to that seen at the throat of the occlusion.

Importantly, Jung et al[35] observed that the shape of the stenosis has less influence on the resulting flow than its overall severity. Although this was written in the context of pulsatile flow, it was thought reasonable to assume that this observation would be applicable to all flow types in stenotic geometries. Because of the various techniques used, and the way in which results are presented, it is not always practical to directly compare quantitative results obtained from different sources. Findings are often discussed therefore in a qualitative fashion when comparisons are sought between different sets of results. With this in mind, the following is an attempt to describe the fundamental findings of the research already conducted.

Although laminar flow is thought to dominate in straight, clean and unrestricted vessels, it is generally accepted that turbulence may be induced in certain areas of the cardiovascular system (e.g. due to the presence of a stenosis), at least for some part of the cardiac cycle (e.g. at peak systole). However, Henry & Collins[42] state clearly that it is not yet possible to numerically simulate the type of transition processes that occur in haemodynamic flows, since it is argued that any simulation would need to be able to model the transition from laminar to turbulent and back again to laminar flow. Although it is not unreasonable to assume that advances in the understanding of the processes involved, and of computing power, will allow more accurate simulations of haemodynamic flows to be made in the future, it is perhaps not surprising that the vast majority of researchers to date have assumed *in vivo* flow conditions to be laminar[e.g. 13,20,22,35,43-46]. This assumption allows the complexity of defining flow parameters in numerical analyses to be reduced significantly.

Most of the available research has concentrated on conditions defined by the application of steady flow rates[7,15,18,20-22,45,47-51]. A large number used numerical simulations, with some attempting to validate results obtained using this technique through comparison with their own experimental results[7,15,49]. Others sought validation by comparing their work with those obtained in previous studies[20-22,47,50]. In these steady flow rate investigations, the scale of the severities used ranged from 25%[50] to 84%[15]. Reflecting its acknowledged importance, most researchers concentrated on the haemodynamic environment induced by the occlusion. Of particular interest were the areas of recirculation, their corresponding stagnation

points and the distribution of WSS. The dependence of these characteristics on severity S, Reynolds number (Re) and rheology were widely reported.

Most authors reported that the length of the recirculating flow region downstream of the occlusion (see Fig.3) increased with Reynolds number[7,18,20,22,47,49]. This result is the consequence of an increase in momentum carried by the fluid (due to the increased flow velocity) which causes the jet to project further past the occlusion before its dissipation forces the flow to reattach to the wall. Importantly, this relationship was observed to occur over a wide range of physiologically relevant Reynolds numbers. This trend was not universally observed however, since a shortening of the recirculation zone was reported in this range by Bluestein et al[15]. In this study, numerical results were obtained using a Newtonian fluid model and Reynolds numbers 300, 900, 1800 and 3600. Observations indicated a decrease in recirculation length between Reynolds numbers 300 and 900, followed by a small increase thereafter. The proposed explanation suggests that this was due to the local elevation of Reynolds number at the throat above a critical value, whereby the shear layer further downstream (between the jet flow and the surrounding fluid) became unstable. This may have been indicative of the flow undergoing transition to turbulence, caused by the high flow velocities in the throat and the rapid expansion of the geometry in the post-stenotic region. This possibility was clearly given some credence by the author since a turbulent model was employed in the numerical analysis. The reason why these results were not observed by other researchers may have been that an area reduction of 84% was used, considerably higher than that which was used in any other study conducted using a steady flow rate.

Numerical analyses conducted by Banerjee et al[18] and Tu & Deville[50] indicate recirculation lengths increase with occlusive severity. This is supported by other studies which were conducted using comparable flow conditions[20,49]. This result is again linked to the increase in momentum, which forces the jet further downstream before reattachment to the wall. In this case however, the momentum increase results from greater acceleration of the flow though the throat, rather than a rise in the overall flow rate. This is significant because the more severe the occlusion, the longer the recirculation zone and hence the greater the range over which WSS magnitudes are perhaps low enough to initiate further stenotic growth.

The majority of authors reported WSS distributions in their analysis. In qualitative terms, their results were comparable, since the main defining features were reported throughout. A peak in WSS was observed at the throat[15,20,22,47-50], while an area of comparatively low and negative WSS was observed in those regions just downstream to the throat. Negative values were recorded in these regions due to the reversed flow direction, indicative of recirculation. The significance of low-magnitude WSS, in terms of its influence on hyperplasic growth and the deposition of plaque material, was discussed in Section 1.4. Bearing this in mind, stenotic growth (be it through hyperplasic or atherosclerotic means) invariably predisposes the area immediately downstream to further growth. This positive feedback means that progression of the disease is accelerated around those areas where it is already established.

Where reported, overall WSS was universally observed to increase with Reynolds number throughout the domain[15,18,21,22,47]. This was due to the elevated velocity gradients in the near-wall region, induced by the increase in flow rate. Similarly, the peak in WSS at the throat increased with severity[18,21,47,50], an observation explained by the increased acceleration of the flow through the vessel's reduced cross-sectional area. The physiological significance of this is that the greater the occlusive severity, the greater the WSS to which the wall at the throat is subjected. As discussed previously (see Section 1.4), elevated WSS leads to injury of endothelial cells and a subsequent reduction in the capacity of the wall to properly perform its required functions. Once again, this positive feedback means injury to the endothelium predisposes the local wall to further degradation and occlusion, in turn leading to further endothelial injury.

The influence that rheological properties have on flow through stenoses has been reported in a number of studies. This is significant because there is much debate in the literature regarding the importance of correctly modelling the rheological characteristics of blood (this is discussed further in Chapter 3). Throughout the literature, the most striking observation is the perceived stabilizing effect non-Newtonian characteristics are shown to have on separated flows. This is manifested in the reduced size of recirculation regions recorded in studies that used both non-Newtonian and Newtonian fluid models. This trend was reported by the majority of

researchers[7,18,20,22,45,47,48], all of whom employed both Newtonian and non-Newtonian fluid models in numerical studies which used a range of mild and acute stenotic geometries. However, this trend was not universally observed; Tu & Deville[50] reported a significant reduction in recirculation length for the Newtonian case.

Where reported[18,20,22,47,50], the effects of the non-Newtonian viscosity of blood on WSS were much less apparent than those observed in relation to recirculation. Only Tu & Deville[50] reported results in which distinct differences were observed between the Newtonian and non-Newtonian cases. Here, the WSS exerted by the Newtonian fluid was significantly higher than that recorded using non-Newtonian models. Although the results presented in the rest of the literature seem to suggest the opposite, they were considered inconclusive since the recorded differences were regarded as negligible. Perhaps the greatest challenge associated with evaluating the influence of rheology on flow characteristics is how best to compare conditions which cannot be described as dynamically similar. This is discussed in detail in Chapter 2.

In comparison to steady-state investigations, research into the nature of haemodynamic flow through stenoses is much scarcer for pulsatile flow. Added to this is the increased complexity of defining parameters which can be interpreted in a global sense, since not only do the effects of geometry and flow rate have to be considered, but also those of oscillation (both frequency and amplitude). The subsequent comparison of work by the various authors is therefore even more challenging than it was for steady-state analysis. The following is therefore an attempt to summarise the work presented in the literature in a qualitative manner.

The majority of investigations have been conducted using numerical rather than experimental procedures[18,35,44-46,48,50,52,53]. Of these, only Deplano & Siouffi[44] used experimental results to validate those obtained numerically. Newtonian fluid models were used throughout, although some researchers also used models aimed at representing the non-Newtonian characteristics of blood. Most employed a waveform representative of that found *in vivo* (characterised by systolic and diastolic acceleration/deceleration, followed by a period of zero net flow rate during the

remainder of the cycle) while some also used a far simpler waveform based on a sinusoidally-evolving flow rate. The scale of the severities studied ranged from 25%[50] to 94%[35], which represents the full range considered clinically relevant (see Section 1.1).

Many studies illustrated the changing flow conditions through the use of streamlines. This provided a means through which the evolution over time of flow structures could be visualised. A core region was observed to develop and become displaced during the cycle, indicating a wave-like motion of the core with peaks and troughs, where recirculation regions were generated between the core flow and the wall (see Fig.4). Although observed in a number of cases[35,46,48,50], the extent of this 'waviness' varied considerably, depending on the geometry and numerical settings employed. The severity of the constriction was found to be particularly influential, with less constricted vessels showing fewer signs of 'waviness'. The wave-like patterns propagated downstream as the cycle progressed until eventually the recirculation regions and the characteristic wave structure disappeared. The whole pattern was found to be repeatable during subsequent cycles. Since 'waviness' is indicative of secondary flow, this observation seems to be consistent with the expectation that flow becomes more three-dimensional with increasing stenotic severity. Further confirmation of secondary flow is provided in Jung et al[35] and Onogi et al[53], where streamwise velocity contours, plotted at various cross-sections and time intervals, showed clear evidence of this.

The temporal and spatial variations in WSS were reported by most authors[18,44-46,48,50], with a spatial peak being universally observed at the throat throughout the cycle. The temporal plots indicated a peak at the time of maximum flow rate and a strong coupling between the temporal variation in WSS and the time-dependent net flow rate. In some cases[44,46,48], the temporal and spatial WSS plots provided further evidence of three-dimensional flow. Peaks and troughs in the WSS distribution distal to the throat (generated by the presence of recirculation regions) were shown to decrease in magnitude further downstream, evidence that the wave gradually weakened as it propagated downstream. Since recirculation regions were created and washed away during each cycle, those areas affected by their presence were subjected to large temporal variations in WSS. The large fluctuation in WSS,

particularly that which was observed in the vicinity of the throat, highlights the elevated susceptibility of such areas to further degenerative processes (see Section 1.4). Deplano & Siouffi[44] compared results obtained experimentally using the same flow conditions as those used in a corresponding numerical analysis. The peaks and troughs observed numerically were not reported in the experimental case since only the mean velocity fields were used in the calculation of WSS. By averaging each of the velocity fields recorded over forty cycles, any effects due to three-dimensional flow were smoothed out.

In those cases where WSS distributions did not indicate the existence of three-dimensional flow features[18,45,50], the evolution of recirculating flow was nevertheless reported. Common to all was the observation that reattachment advanced downstream as the flow accelerated. During the initial stages of deceleration, the length of recirculation increased further, due to the residual momentum carried by the central core flow which required additional reverse flow near the wall in order to maintain continuity.

The variation in pressure throughout the domain at various points in the waveform was also reported by a number of authors[45,46,50]. When the waveform dictated a positive flow rate, a pressure drop across the stenosis was observed by all, followed by a partial recovery in the distal region. Although this trend was reported throughout the cycle, the biggest drop in pressure was observed when flow rate was at a maximum. Significantly, Tu & Deville[50] reported that the pressure drop was smaller when the fluid used was of a non-Newtonian nature. Together with the widespread observation that WSS too is reduced by using non-Newtonian fluids, this again confirms the earlier observation that more stable flow conditions are yielded when using non-Newtonian fluids.

The various studies discussed here have been conducted using a wide variety of stenotic geometries and flow conditions. Both steady-state and pulsatile flow conditions have been investigated using a mixture of experimental and numerical modelling techniques. The study reported in this thesis will attempt to combine all these elements in order to present a comprehensive review of blood flow through a

selection of geometries which represent stenoses typically found *in vivo*. The following therefore details the specific aims and objectives of the present study.

1.6: Objectives of the Thesis

As has been discussed, the prevalence and seriousness of atherosclerosis and related cardiovascular conditions (for example intimal hyperplasia) are such that the research previously conducted into their pathogeneses is substantial. Although development of the disease is dependent upon many cumulative factors, there is strong evidence that suggests the local haemodynamic environment plays a major contributing role at all stages of the disease process. It is vital therefore that stenosis-induced haemodynamic flow is well understood. To date, there have been a number of studies which have attempted to model this, using either experimental or numerical techniques, or a combination of both. The specific objectives of these studies varied considerably, reflecting the wide range of variables associated with research of this nature. This study will aim to quantify those parameters relevant to the development of atherosclerosis and intimal hyperplasia, namely WSS. In addition, the acceptability of using a Newtonian approximation for blood is examined.

The specific tasks which have been carried out and which are described in this thesis can be summarised as follows.

- An experimental analysis of flow through large-scale cylindrical pipes, containing a smooth contraction-expansion typical of a stenotic constriction found *in vivo*, is described. The fluid used was selected according to its ability to represent certain rheological properties of blood. The use of optical instrumentation allowed the velocity field to be recorded under various flow conditions believed to be representative of those found *in vivo*.

- A numerical reconstruction of the experimental analysis is discussed in order to determine the suitability of using Computational Fluid Dynamics (CFD) as an effective modelling tool. This was done by constructing *in vitro*-scale virtual representations of the geometries used in the experimental analysis in conjunction with fluid models that replicated the rheological properties of the

test fluid. Experimental results are compared to those obtained numerically, hence providing a quantitative verification of the numerical techniques employed.

- Further numerical analysis has been conducted using life-size geometries, converted using appropriate scaling laws, and different rheological models which represent blood. These include a non-Newtonian Power-Law model and a Newtonian approximation which is often used in comparable studies. Haemodynamic parameters, relevant to the pathogenesis of atherosclerosis and intimal hyperplasic growth (in particular those affecting conditions at the wall), are quantified and interpreted with respect to physiological concerns. A comparison of results obtained using the different rheological fluid models will provide evidence as to whether the use of a Newtonian approximation for blood is acceptable in studies of this nature.

1.7: Organisation of the Thesis

Having laid the foundations and defined the limits of the proposed study, the following discussion details the steps undertaken to complete the project and meet its objectives.

In Chapter 2, a discussion about dimensional analysis is presented, outlining the principles of dynamic similarity. Parameters, defined using correct scaling of *in vivo* conditions, were established so that an experimental analysis could be conducted using dynamically-similar flow conditions in large-scale *in vitro* models of stenoses. The rheological characteristics of blood are discussed in Chapter 3, including an assessment of the physiological factors which are responsible for these characteristics. Rheologically-similar fluid analogues are identified in order to enable the experimental analysis to be conducted. The apparatus used in the experimental analysis is described in Chapter 4, with particular attention paid to the large-scale *in vitro* models used to represent two different stenotic geometries that might be expected *in vivo*. The discussion also includes a description of the Particle Imaging Velocimetry (PIV) equipment used in the data acquisition process. Chapter 5 describes the experimental results obtained using this apparatus. The analysis

includes those results acquired using correctly scaled physiologically-relevant steady and time-dependent flow rates. A biphasic waveform, representative of one measured *in vivo*, is used for the pulsatile flow rate analysis. Of particular interest is the distribution of WSS in the domain, reflecting its physiological significance. In Chapter 6, the numerical techniques employed in this study are discussed, detailing the processes used, the steps taken to ensure the use of correct computational methods and the results obtained using such procedures. A discussion regarding the validity of using these results is followed by an assessment of the validity of using a Newtonian approximation for blood. Physiologically-relevant quantities, obtained using a fluid model most representative of blood, are then discussed in relation to their influence on the pathogenic processes described previously. Finally, Chapter 7 draws together all the conclusions made in the study and makes suggestions for further work.

2: DIMENSIONAL SCALING AND ANALYSIS

This chapter details aspects regarding the scaling of different fluid flows. What dynamic similarity means, the implications of its requirements and the importance of correctly scaling different flows are all discussed. The procedures used to ensure dynamic similarity is achieved are presented, as are the limitations to which these requirements subject a study such as this. In particular, the ability of flows which use a Newtonian approximation for blood to accurately represent conditions which might be expected *in vivo* is discussed.

2.1: Dynamic Similarity

Dimensional analysis is routinely used in fluid mechanics research as a means to correctly scale fluid flow. It is used most often to allow known flow conditions, found in problems which are unsuitable for the performance of direct analysis, to be recreated on a more manageable scale so that accurate experimental measurements can be made. Using correct dynamic scaling procedures, the balance of forces on the fluid is reproduced in the experimental model so that it is identical to that found in the original case. The method used to ensure dynamic similarity is achieved depends on the definition of a number of dimensionless groups. Each group represents different flow properties, while the number of groups required is determined by the number of variables and dimensions the problem is defined by. (The Buckingham-π theorem[54] states that the number of groups required is equal to the number of defining variables minus the number of defining dimensions). The numerical values of each group must be the same in both the original and experimental cases to guarantee the correct balance of forces. Once this is achieved, flow conditions in both cases are said to be dynamically similar and are hence representative of each other, despite them being defined using different scales. Dynamic similarity is especially useful in studies such as this because flow conditions found *in vivo* can be recreated in an experimental model. Subsequent flow characteristics recorded in the model can therefore be scaled appropriately to reveal conditions which might be expected *in vivo*.

The process of ensuring dynamic similarity is dictated by the individual requirements of the study. Initially, the conditions to be modelled are identified by considering aspects of the flow relating to the geometry of the domain under consideration, the properties of the fluid used and flow rate conditions. Appropriate dynamic scaling is then applied so that a model can be established in which conditions are representative of those found in the original case. Subsequent analysis is then conducted on this model, allowing flow conditions to be investigated in a laboratory setting. The influence on flow conditions, resulting from changes to a single property (be it relating to the geometry, fluid or flow rate) can therefore be quantified, interpreted and discussed accordingly in relation to what can be expected in the original case. Of particular concern in this study are the observed changes in the local haemodynamic environment induced by a change in the geometric severity of the stenosis. In addition, the importance of using a non-Newtonian model to represent blood is also discussed.

In order to ensure the conclusions drawn from any analysis are correct, and that observed changes in the flow are due solely to the change in geometry being investigated, it is essential to maintain dynamic similarity throughout. As discussed in Section 1.4, blood is essentially an aqueous solution in which particulates are suspended. Its rheology varies with shear rate such that viscosity decreases with increasing shear (for more details of blood rheology, see Chapter 3). The problems associated with using a Newtonian assumption for blood, as has been done in many previous studies, are primarily to do with appropriate scaling procedures. Since the true rheology of blood can only be represented by a fluid which shares the same scaling characteristics, those which exhibit Newtonian properties cannot be relied upon to produce dependable results. In this respect, when dynamic similarity is only partially achieved, conclusions become very difficult to draw and the real effects due to a change in geometry are difficult to identify. It is this which highlights the critical importance of using a fluid which accurately represents the rheological properties of blood.

2.2: Definition of Conditions

The principal concern of this study is the distribution of wall shear stress (WSS) in the cardiovascular tree, due to its reported role in the development of atherosclerosis and intimal hyperplasia. Each dimensionless group is therefore derived by considering, in both a spatial and temporal sense, the various parameters which affect WSS. These include those relating to the geometry of the vessel, the fluid used and the waveforms which govern the flow rate conditions. All basic flow quantities affecting WSS, and which are assumed of the original *in vivo* conditions, are summarised in Table 3 (note that the rheological parameters which describe blood in Table 3 were obtained in this study – see Section 3.2). Included are the different rheological assumptions made of blood in this study, both Newtonian and non-Newtonian.

The geometries considered in this study are simplified models of arteries containing a smooth contraction-expansion. Although the smoothness, of both the constriction and the straight section of artery, is not realistic in an anatomical sense, simplification of the geometry was required to ensure results could be readily reproduced by others for comparison. An arterial diameter of 6mm has been assumed for the life-size case, typical of large arteries where atherosclerosis is found to be particularly prevalent, such the femorals and iliacs. For the two *in vitro* models used in this study, the diameter is scaled up to 38mm. The flow rate in large arteries, such as those being modelled here, is pulsatile by nature. The biphasic waveform, obtained *in vivo* by pulsed Doppler ultrasound and shown in Fig.5, was that measured in the femoral artery of a patient who was in a resting condition[55]. All subsequent flow rate definitions to be used in this study were based on this biphasic waveform.

The rheological model for blood used in this study is one which attempts to represent the shear-thinning characteristics observed by previous researchers[56-64]. As will be discussed in more detail in Chapter 3, viscosity is to be approximated using a model based on the Power-Law relationship. The parameters which define this relationship include the Power-Law index n (which describes how viscosity changes with shear rate) and Power-Law consistency κ (which determines the magnitude of the viscosity scale).

$$\eta = \kappa \dot{\gamma}^{n-1} \qquad \text{(Equation 1)}$$

As will be demonstrated in Chapter 3, the value of κ (at normal body temperature, 37°C), is considered to be 18mPa.s^n, while n varies in value depending on the frequency of the time-dependent waveform employed. In steady flows, n = 0.61, while in pulsatile flows, n increases with frequency and is assumed to be 0.67 at frequency f = 1Hz (60 bpm). Additional parameters (η_0 and η_∞) will also be included in an attempt to account for the levelling off of viscosity to constant values at the extremities of the shear rate range.

The elastic nature of blood (see Chapter 3) has been reported in previous studies[65-69] and it should be included in a comprehensive rheological model for blood. However, to further complicate the model used in this study would result in additional problems when attempting to isolate any effects on the flow due solely to viscosity. For this reason, its inclusion is considered beyond the scope of this study and the elastic properties are therefore neglected. The validity of doing this is discussed further in Chapter 3, where a full discussion regarding the viscoelastic nature of blood is presented. In addition, the ability of the test fluid used in the experimental analysis to represent both the viscous and the elastic characteristics of blood is also discussed.

Essentially, the flow under consideration in this study can be defined by a number of parameters which describe the pulsatility of the flow, the rheological properties of the fluid and the geometry of the domain through which this fluid flows. The flow, and in particular WSS, is therefore considered to be a function of each of these parameters. This means that a change in the value of any one of the defining parameters affects the value of WSS. A process of dimensional analysis was conducted enabling a number of dimensionless groups to be defined. This process is described in detail in Appendix A, with the resulting non-dimensional groups being shown below. Since WSS is the flow quantity of interest, the group containing it is expressed as a function of the other six parameters. The relationship between these groups implies that, for two geometries defined by the same shape but using different

scales, non-dimensional WSS will exhibit the same value in both geometries if all the other non-dimensional groups are of the same numerical value in each case.

$$\frac{\tau_w}{\frac{1}{2}\rho \overline{U}_c^{\,2}} \quad \ldots \text{ non-dimensional wall shear stress, } \Gamma \qquad \text{(Equation 2)}$$

is some function of…

$$\frac{\rho d^n \overline{U}_c^{\,(2-n)}}{\kappa} \quad \ldots \text{ Power-Law Reynolds number, } \mathrm{Re_{PL}} \qquad \text{(Equation 3)}$$

$$\frac{\rho d \overline{U}_c}{\eta_0} \quad \ldots \text{ Newtonian Reynolds number in low shear, } \mathrm{Re_0}$$

(Equation 4)

$$\frac{\rho d \overline{U}_c}{\eta_\infty} \quad \ldots \text{ Newtonian Reynolds number in high shear, } \mathrm{Re_\infty}$$

(Equation 5)

$$n \quad \ldots \text{ Power-Law index, n} \qquad \text{(Equation 6)}$$

$$\frac{u_{\max} - u_{\min}}{\overline{U}_c} \quad \ldots \text{ Pulsatility index, P.I.} \qquad \text{(Equation 7)}$$

$$\frac{\omega d}{\overline{U}_c} \quad \ldots \text{ Strouhal number, St} \qquad \text{(Equation 8)}$$

$$\mathrm{T} = f\left(\mathrm{Re}_{PL}, \mathrm{Re}_0, \mathrm{Re}_\infty, n, P.I., St\right) \qquad \text{(Equation 9)}$$

Note that the process of dimensional analysis shown in Appendix A does not dictate that WSS is normalized by dividing it by the dynamic pressure $\left(\frac{1}{2}\rho \overline{U}_c^{\,2}\right)$, only that division by the factor $\rho \overline{U}_c^{\,2}$ is required. However, in order to relate non-

dimensional WSS to a recognisable physical quantity, further division by the factor $\frac{1}{2}$ means WSS is made non-dimensional by dividing it by the dynamic pressure.

The Power-Law Reynolds number given in Equation 3 is often referred to as the Collins-Schowalter Reynolds number[70]. Although non-Newtonian Reynolds number could be defined differently (notably using the Metzner-Reed formulation[71]), the dimensional analysis detailed above indicates the Collins-Schowalter version to be the most appropriate for use in this study.

Each group represents different aspects of the flow. Reynolds number represents the ratio of inertial forces to viscous forces. The greater the Reynolds number, the more influence inertia has on the flow compared to viscosity. This is seen throughout fluid mechanics since, at low Reynolds numbers, viscous forces dominate and the flow is laminar. At high Reynolds numbers, the orderly characteristics of laminar flow break down due to the increased effects of inertia, resulting in turbulent and highly unpredictable flow.

The Power-Law index describes the behaviour of viscosity under varying shear conditions. Its value indicates not only the degree to which viscosity changes with shear rate, but also whether this change is positive or negative.

Oscillatory flow is described by the two remaining dimensionless groups. The pulsatility index represents the magnitude of the cycle amplitude relative to the mean cycle velocity. It therefore describes the relative importance the oscillatory nature of the flow is likely to have in comparison to the net flow rate. Reducing this index to zero equates the waveform to a steady, constant flow rate condition. The other defining aspect of oscillatory flow, frequency, is represented by the Strouhal number. Large Strouhal numbers represent high frequency flows and therefore shorter wavelengths.

2.3: Problems with using a Newtonian Assumption for Blood

The problems associated with using a Newtonian assumption for blood are reflected in the difficulty in the way Reynolds number is defined. Since the relationship between the parameters which define the Reynolds number varies, depending on the degree of non-Newtonian behaviour, there is an inherent inability to compare results obtained using fluids of differing rheological characteristics. This can be explained through a consideration of how Reynolds number is affected by viscosity and what the Reynolds number represents.

When using a Newtonian fluid (n = 1), the Power-Law definition of viscosity (see Equation 1) reduces to the following:

$$\eta = \kappa \dot{\gamma}^{0} = \kappa \qquad \text{(Equation 10)}$$

The nomenclature used to describe Newtonian viscosity is usually different from that which is used to describe the viscosity of non-Newtonian fluids ($\eta \rightarrow \mu$). In keeping with convention therefore, the Reynolds number (defined previously in Equation 3 for Power-Law fluids) is defined as follows for the Newtonian case.

$$\mathrm{Re}_N = \frac{\rho d \overline{U}_c}{\mu} \qquad \text{(Equation 11)}$$

For Newtonian fluids (where n = 1), the Reynolds number is now linearly proportional to both the diameter, d and the cycle mean velocity, $\overline{U}_c$. This is not the case for non-Newtonian fluids where n $\neq$ 1. Therefore, when using a Newtonian fluid to model the behaviour of non-Newtonian fluids, the cause of any change in the observed flow conditions cannot be identified with any certainty. In fact, the effects due to a change in $\overline{U}_c$ cannot be separated from those which result from the difference in the way viscosity is defined. Likewise, diameter, d cannot be de-coupled from viscosity. This principle can be applied for all values of n and therefore explains, in part, why dynamic similarity requires the use of fluids with the same value of n.

Perhaps the most important consequence of this is that calculating appropriate flow rates, which adequately reflect conditions *in vivo*, is highly problematic when using a

Newtonian approximation for blood. One cannot simply equate two Reynolds numbers, which have been defined differently, and assume the corresponding velocities will produce flow conditions which are representative of each other. This is a problem that was encountered in the present study when an attempt was made to assess what impact using a Newtonian approximation for blood would have on important flow characteristics. A computational model (detailed later in Chapter 6) was constructed using a life-scale geometry and a rheological model which used a Newtonian approximation for blood viscosity. Bearing in mind the impossible task of correctly scaling non-Newtonian blood flow using a Newtonian fluid, and the desire not to over-complicate the problem, the flow rates to be used in the study which employed a Newtonian fluid model were simply equated to the flow rates which were measured *in vivo* by Fisher et al[55]. In this respect, no attempt was made to scale the velocities which were measured *in vivo*. While no pretence is made regarding the ability of the resulting flow conditions to accurately represent what might be expected *in vivo*, this is however the simplest way in which a comparison can be made.

The value of Newtonian viscosity which should be used to represent blood is a very subjective matter. Numerous researchers have attempted to identify the viscosity most relevant to the conditions found *in vivo*. Although some authors suggest this characteristic viscosity should take account of the low shear rates found particularly in the centre of the vessel[72], most simply equate the Newtonian viscosity with the high shear rate plateau for blood[30,73-77] (this will be discussed in greater detail in Chapter 3). The latter method is considered to be the most applicable for this study because of the importance of wall conditions in the development of atherosclerosis and intimal hyperplasia. The shear rate in the wall region is generally high, relative to the rest of the flow, due to the high gradients of velocity which are induced by the no-slip condition at the wall. For the most part therefore, a Newtonian approximation for viscosity based on a high shear rate (η_∞) should prove to be the most appropriate for use in this study.

Of critical importance to this study is the distribution of WSS in the stenosed tube. The way in which WSS is defined means that the value of WSS varies greatly depending on the degree of non-Newtonian behaviour the fluid exhibits. For a given

shear rate in the near wall region, the value of the Power-Law index n will greatly influence the resulting value of WSS (τ_w) due to the following relationship.

$$\tau_w = \kappa \dot{\gamma}^n \qquad \text{(Equation 12)}$$

This illustrates the difficulties associated with comparing flows of non-Newtonian fluids with those of a Newtonian fluid. In particular, it demonstrates that even with identical velocity profile characteristics, the corresponding WSS will vary greatly depending on the value of n.

As has been discussed, results obtained using fluids which are defined using different values of n cannot be directly compared. In this respect therefore, any attempt to quantify how representative steady flow rate conditions are of pulsatile conditions is rendered inappropriate in this study since the value of n varies, depending on whether the flow is steady or pulsatile.

2.4: Summary

A discussion regarding the importance of dynamic similarity in studies of fluid flow has been presented. It has been demonstrated that flows based on different scales and fluid characteristics must obey dynamic similarity laws to ensure meaningful comparisons can be made between them. Dimensional analysis was conducted based upon a consideration of the parameters which affect WSS. The dimensionless groups obtained will be used to enable large-scale experimental and numerical studies to be conducted which could be discussed in relation to the conditions found *in vivo*.

A discussion regarding the problems associated with using a Newtonian approximation for blood has also been presented. Dimensional analysis indicates that Newtonian fluids are not dynamically similar to blood because of the rheological differences between them. Related to this, there are certain practical difficulties which include an inability to calculate flow rates which would yield conditions dynamically similar to those found *in vivo*; the difficulty in de-coupling and identifying the effects on the flow of varying different flow characteristics; and what numerical value to assign the Newtonian viscosity.

3: RHEOLOGY

This chapter describes the rheological concerns applicable to this study. A general introduction to rheology is presented which describes the viscosity characteristics of a fluid. The rheological characteristics specific to blood are then described and a mathematical model, based on the Power-Law and which represents the shear viscosity of blood, is proposed for use in this study. The physiological factors which affect the rheology of blood and its relationship with shear rate are also discussed, particularly in relation to the behaviour of red blood cells (RBC). A polymer solution of Xanthan Gum is then proposed for use as a test fluid. The ability of the Xanthan Gum solution to represent certain characteristics of blood rheology is discussed, as are its limitations. These considerations are then taken into account in order to define the role of the test fluid in this study.

3.1: Introduction

Rheology is the study of the flow and deformation of matter. Fluids are defined as either a liquid or gas, whose rheology is characterised by its viscoelastic properties. When subjected to an external force, a purely viscous body will dissipate energy in the form of heat; viscosity is defined as a fluid's tendency to resist flow. A purely elastic body will react by deforming, resulting in energy storage, which, upon release of the force, causes the body to recover its shape; elasticity is defined as the tendency of a fluid to store energy. Since all liquids exhibit properties which are characteristic of both purely viscous and purely elastic bodies, a rheological statement, which describes the strain rate behaviour ($\dot{\gamma}$) of a liquid under the influence of an applied stress (τ), is written in the form of the viscoelastic modulus (η^*), incorporating a description of both properties[78]:

$$\eta^* = \frac{\tau}{\dot{\gamma}} = \eta' - i\eta'' \qquad \text{(Equation 13)}$$

where η' is the viscous component of complex viscosity and η'' is the elastic component of complex viscosity.

Since there are two different viscometric types of flow a fluid can experience, there are equally two distinct categories relating to the viscoelastic properties of a fluid. Shearing flow refers to the type observed in boundary layers or cross-sectional velocity profiles. Under these conditions, fluids tend to move in 'layers' of different velocities, inducing a shearing force on adjacent layers, parallel but opposite to, the direction of the flow. Extensional flow is that which occurs when a fluid is subjected to stresses normal to each other, resulting in the fluid being stretched or pulled apart. Since the flow conditions to be investigated in this study are to be dominated by shearing flow, it was thought reasonable to consider only viscoelastic properties relating to shear. Consequently, the terms viscosity and elasticity will, unless otherwise stated, hereafter relate to shearing flow.

The response of any body (solid or fluid) to the application of a force is described by the relationship between the applied stress (τ) and the strain the body subsequently experiences (e). The complex modulus of rigidity of the body (G^*) describes this relationship mathematically[78]:

$$G^* = \frac{\tau}{e} = G' + iG'' \qquad \text{(Equation 14)}$$

where the elastic character of the response (G') is named the storage modulus and the dissipative (or viscous) character (G'') is named the loss modulus.

Under oscillatory flow conditions (where ω is the frequency), G^* and η^* are related as follows[78]:

$$G^* = i\omega\eta^* \qquad \text{(Equation 15)}$$

Substituting Equations 13 and 14 into 15, viscosity and elasticity are defined as follows:

$$\eta' = \frac{G''}{\omega} \qquad \text{(Equation 16)}$$

$$\eta'' = \frac{G'}{\omega} \qquad \text{(Equation 17)}$$

For the vast majority of fluids, both η' and η'' are functions of shear rate and the frequency of oscillation (ω). Non-Newtonian fluids are defined as those whose

viscosities change under varying rates of shear. The effects of shear upon the behaviour of a fluid vary considerably. Those fluids which undergo a reduction in viscosity with the application of increasing shear are described as shear-thinning, an example of which is ketchup sauce. The adage, 'never shake an upturned (ketchup) bottle', refers to the tendency of the sauce to flow more easily when a high shear stress is applied to it. In contrast, a water and cornstarch mixture is an example of a shear-thickening fluid. When a low shear stress is applied to it, the solution undergoes significant deformation and acts as one might expect a fluid to do so. However, when struck or thrown against a surface, for example, the high shear stress to which it is subjected increases the viscosity, causing it to shatter or bounce. Newtonian fluids are those whose viscosities do not change under the influence of shear; the strain rate response to stress is linear. (Note that there exists a class of fluids called 'Boger Fluids', whose viscosities are constant across the full range of shear rates, but which exhibit a measure of elasticity. As a result, they exhaibit characteristics of both liquids and solids.) They are in fact a special case of non-Newtonian fluids, since the gradient which describes their shear-dependent nature is simply equated to one. This is only an approximation however, albeit a very good one, since the viscosity of even these fluids is not constant at the extremities of the shear scale. It is common practice however, to use the Newtonian assumption for such fluids since the deviation from linearity is negligible. Despite the fact most familiar fluids are Newtonian (examples include air and water) most fluids do in fact exhibit characteristics which define them as being non-Newtonian.

Although not strictly a uniform homogeneous fluid (it is a suspension of particulates in a base solution), blood is nevertheless assumed to be so for the purposes of this study since the arterial scale of interest is many orders of magnitude higher than that of the particles which are carried in blood. The following discussion attempts to summarise its rheological properties and the effects these characteristics have on blood flow. In addition, viscoelastic properties of a potential test fluid are also discussed, with particular attention paid to its ability to represent the non-Newtonian characteristics of blood.

3.2: Blood Rheology

There has been great interest in the study of blood rheology in recent decades. It is universally agreed that blood is a non-Newtonian, shear-thinning fluid when considered over the full range of shear rates. However, there is much debate over the importance these characteristics play on haemodynamics *in vivo*. Some researchers have argued that blood behaves in a Newtonian fashion in the range of shear rates that are physiologically relevant and that consideration of non-Newtonian characteristics is not important[17,79,80]. Although this may be a reasonable approximation in large, clean and unrestricted vessels, this position is questionable when considering flow through complex geometries such as stenoses, bifurcations and anastomoses[7,18]. In such cases, the surrounding geometry induces both large and small spatial gradients of shear, resulting from the formation of distinct flow features such as recirculation, jet flow and shear layers. In addition, large temporal gradients also develop due to the pulsatile nature of blood flow. Indeed, Nerem[13] reasoned that the low shear rates required for blood to behave in a non-Newtonian manner are found in large vessels where the observed flow is pulsatile and/or where the flow is separated from the wall. In these instances, the local shear rate is such that the effects of non-Newtonian viscosity become significant, a conclusion which is drawn by the majority of researchers[e.g. 13,50,81-83]. Considering the geometries and flow rate conditions which are to be used in this study, it was considered necessary to account for the non-Newtonian, shear-thinning characteristics which blood is shown to exhibit. By extension, a comparison between those results obtained using non-Newtonian and Newtonian fluids will attempt to quantify the effects of rheology on the conditions which affect the arterial wall.

There have been numerous studies in the past which have attempted to quantify the shear viscosity of blood. As a result, a large amount of data has been accumulated on the subject; experimental results obtained by a number of researchers[56-64], measured under steady shear rate conditions, are summarised in Fig.6. Most strikingly, the evidence clearly shows that blood possesses significant shear-thinning characteristics. Numerous researchers have used mathematical models in an attempt to describe this shear-dependent viscosity. In the majority of cases, the models used are variations on the same basic formulation, each including terms which provide a description of the gradient observed in Fig.6. For the purposes of this study, the

Power-Law model was considered appropriate and its relative simplicity advantageous. A high-shear plateau is also observed in Fig.6 and has been incorporated into many of the fluid models used by previous researchers[e.g. 18,35,47,50,84]. Although its stated value varies throughout the literature, the range in which it is reported is small. The value used in the present model is 3.5mPa.s. In addition, a low-shear plateau is also included, the value of which is assigned to be 100mPa.s. The shear rates at which the viscosity becomes constant occur at critical values, referred to here as $\dot{\gamma}_{C0}$ (for the low shear plateau) and $\dot{\gamma}_{C\infty}$ (for the high shear plateau). The resulting mathematical model, used in this study to describe the viscous behaviour of blood under steady flow rate conditions, is therefore defined as follows.

If $\dot{\gamma}_{C0} < \dot{\gamma} < \dot{\gamma}_{C\infty} \ldots$ $\eta = \kappa \dot{\gamma}^{n-1}$ (Equation 18)

If $\dot{\gamma} < \dot{\gamma}_{C0} \rightarrow \eta = \eta_0 \ldots$ $\eta_0 = 100mPa.s$

If $\dot{\gamma} > \dot{\gamma}_{C\infty} \rightarrow \eta = \eta_\infty \ldots$ $\eta_\infty = 3.5mPa.s$

Referring to Fig.6, the Power-Law parameters n and κ are assigned the following values in order to represent the steady-shear viscosity of blood (38%<H<45%).

$$n = 0.61$$

$$\kappa = 18mPa.s^n$$

The viscoelastic nature of blood under oscillatory-shear conditions is much less researched than that of steady-shear. This is reflected in Fig.7, which shows the only experimental results of this kind found in the literature[65-69]. Referring specifically to the viscous behaviour (η'), blood again appears to possess shear-thinning characteristics in oscillatory flow. However, the parameters which define the Power-Law relationship between viscosity and oscillatory-shear rate (as indicated on Fig.7) assume different values to those which were assigned to the steady-shear results. In oscillatory-shear, where the frequency of the applied *in vivo* waveform is 1Hz<f<3Hz:

$$n = 0.67$$

$$\kappa = 18mPa.s^n$$

Owing to the observed spread in the viscosity data for blood, it is reasonable to suggest that a range of Power-Law indices are acceptable when attempting to describe its viscosity mathematically. The importance of this flexibility is discussed in greater detail in Section 3.4.2. The shear plateaux observed at the extremities of the shear rate range are again evident, particularly in high-shear. For simplicity, these plateaux are assigned the same values as those applicable for steady-shear.

The elastic behaviour (η'') of blood, over the range of frequencies 1Hz<f<3Hz, is also shown in Fig.7. Despite the presence of a low-shear plateau, it is clearly shown to be a function of shear rate; elasticity decreases with increasing shear over the majority of the shear rate range.

Blood has also been shown to exhibit thixotropic properties[68,85-87]. This property describes the tendency of a fluid to undergo a time-dependent change in viscosity. As has already been discussed, when blood is subjected to a change in the local shear environment, its viscosity changes according to the relationships described previously. However, this change in viscosity does not occur instantaneously; the time required to reach the new equilibrium state demonstrates its thixotropic nature.

When constructing a fluid model, it is clearly desirable to replicate as accurately as possible all aspects of blood rheology. However, the complexity of doing so dictates that this is not practical in the present study. Given the desire to produce a model which describes the rheological properties of blood in a simple yet reliable way, it was thought reasonable to assume viscosity be of primary interest, relegating the effects of elasticity and thixotropy to secondary concerns. In this respect, therefore, a rheological model which accounts solely for the shear viscosity of blood is considered acceptable for the purposes of this study.

3.3: Physiological Factors Affecting Blood Rheology

The processes which influence the rheological properties of blood are driven by its constituent parts. These were discussed briefly in Section 1.3. Of these, few contribute significantly to the rheological properties of blood. The presence of proteins (in particular fibrinogen and globulin) has been shown to fractionally

increase plasma viscosity to 1.2mPa.s[88] from that of water (1.0mPa.s) and that viscosity marginally increases further with greater concentrations[89]. However, plasma is generally considered a Newtonian solution, which reflects the negligible rheological effects of plasma content in comparison to those induced by the presence of RBC. The influence haematocrit (percent concentration of RBC content) has on the rheology of blood is described in detail in Chien et al[64] who concluded that haematocrit has, in fact, a dual-effect on shear viscosity. Not only does the absolute viscosity of blood (measured at a certain shear rate) increase with haematocrit, but so too does the gradient which defines the level of shear-thinning. The former observation is confirmed by the steady-shear data plotted in Fig.6 which shows a clear difference in the viscosity of blood, measured using samples of varying haematocrit. (In those samples where 38%<H<40%, data is plotted in red; in those samples where 44%<H<45%, data is plotted in blue.) In healthy blood, haematocrit varies little (usually in the range 40-45%) and so the data shown in Fig.6 can be considered representative of the shear-dependent nature of healthy blood under steady-shear conditions.

Perhaps not surprisingly, considering the acknowledged influence of haematocrit, the principal mechanism responsible for the rheological properties of blood is the behaviour of RBC under varying rates of shear. Under low-shear conditions, RBCs stack together to form long chains known as aggregates (or rouleaux)[4]. The interaction of these aggregates with one another accounts for both the viscous and (in part) the elastic characteristics of blood[79,90]. It is hypothesised that the aggregates intertwine and get 'knotted-up' with each other, effectively increasing viscosity through their tendency to resist flow. Under high shear conditions, the aggregates untangle themselves and eventually break down into independent cells, the result of which is to reduce viscosity. It is also reported that aggregates are able to undergo a certain degree of elastic distortion before their eventual destruction due to shear occurs[79,90]. On removal of shear stress, the aggregates (if not already broken down) return to their original configurations, recovering elastic energy in the process. In addition, the elastic nature of independent RBCs (through their ability to undergo a shape change) means that, even in the absence of aggregates (where RBCs occur individually), blood still maintains a small measure of elasticity[79,90], although far smaller than that due to the behaviour of aggregates.

The critical shear stress at which aggregates are broken down into individual cells is a precise, basic property of blood[90]. At shear stresses above the critical level, aggregates break down completely, resulting in the reduction of viscosity and the elimination of elastic effects due to the behaviour of aggregates. As a result, this leaves only the deformation of individual RBC as the sole contributor to elasticity[90]. The extent to which aggregates are formed or fragmented in the presence of an oscillatory flow field can be determined by considering the characteristic times of both the flow and aggregation[79]. Aggregation time is a characteristic time relating to the formation of aggregates and is dependent upon haematocrit, plasma composition and shear rate. Sharp et al[79] reported that its value is 10s for normal blood under a constant shear rate of $10s^{-1}$. Characteristic times of the flow include the convective time (the time taken for the fluid to travel a characteristic length, such as the diameter) and the cycle period. For aggregation to occur, aggregation time must be comparable to the convective time and the cycle period. The smaller the ratio of aggregation time to convective time (or similarly the cycle period), the greater the tendency for aggregates to form. Such calculations were performed by Sharp et al[79], using an aggregation time constant of 10s and vessel radii, flow velocities and frequencies all typical of medium to large arteries and comparable to the flow conditions used in this study. It was shown that for normal arterial flow, the two characteristic flow times were at least one order of magnitude lower than the characteristic time of aggregation. In such cases, aggregates do not have sufficient time in which to form and do not therefore exert significant influence on the overall rheology of the blood. Since also shear rates were found to be well above the disaggregation threshold for at least part of the cycle in the medium and large arteries studied by Sharp et al[79], it is assumed that aggregates do not form in normal arterial blood flow. However, the arteries studied were straight healthy ones. This supports the assumptions made by some researchers who argue that a Newtonian approximation for blood is sufficient in such environments. In flow conditions such as those through stenoses however, regions occur where the aggregation time constant approaches the characteristic times of the flow[79]. Such regions may include recirculation zones downstream of a stenosis, where local flow velocities and shear rates are low and where particles experience long residence times. In such conditions, aggregates may be able to form and influence the local rheology,

reinforcing the requirement to account for its non-Newtonian properties in studies such as this. This physical description of the shear-dependent nature of RBC behaviour fits well with experimental findings that confirm the shear-thinning characteristic of blood.

3.4: Rheology of the Test Fluid

One of the problems of investigating the effects of haemodynamics on the development of vascular disease is that blood itself cannot be used as the test fluid in experiments carried out *in vitro*. There are two main reasons for this. Firstly, blood is not transparent, which makes using optical systems such as Particle Imaging Velocimetry (PIV) impossible. Also, the shelf-life of blood, even with the addition of anticoagulants, (which invariably results in a change in rheology) is very short (<24 hours) making consistent and meaningful data collection very difficult indeed. As a result, the need for a transparent fluid with similar rheological properties to blood, which could be used in an experimental analysis, was identified. A comprehensive study of suitable fluid analogues was conducted in a previous study by Gray[91]. An aqueous solution of 0.07%wt Xanthan Gum was suggested as a suitable analogue to use, the rheological characteristics of which are discussed below.

3.4.1: Measurement Procedures

Apparatus capable of measuring both the viscous and elastic properties of a fluid allows a comprehensive study of a fluid's viscoelastic properties to be made. This task was performed here using a rotational rheometer (Rheolyst AR1000-N, TA Instruments). The apparatus works on the principle of placing a fluid sample between a stator (Peltier Plate) and a rotor and measuring the rate of shear the fluid experiences due to the torque the rotor exerts on it. The rotor comes in the form of various geometries, each designed for specific applications and fluid/flow types. Steady-shear viscosity was measured over the shear rate range $0.1s^{-1}$ to $1000s^{-1}$, using a 6cm diameter, 2° cone. A solvent trap was used to minimise evaporation, while the fluid temperature (20°C) was controlled using the Peltier Plate. Both forward and reverse shear rate sweeps were performed so that any shear history present in the fluid could be observed. Oscillatory-shear viscosity was measured

using a 4cm internal diameter, Double Concentric Cylinder geometry, placed inside a Water Jacket. This was then placed on top of the Peltier Plate, maintaining the fluid temperature at 20°C. The viscoelastic characteristics of the fluid under oscillatory-shear conditions were determined using a shear stress sweep, conducted at a pre-determined constant frequency. Measurements were made of the storage (G') and loss (G'') moduli, from which the viscous and elastic properties were calculated using Equations 16 and 17. The oscillatory shear rate, against which these viscoelastic elements would subsequently be plotted, was defined using the conventional equation relating shear rate ($\dot{\gamma}$), shear stress (τ) and the appropriate viscoelastic element (η' or η'').

$$\dot{\gamma} = \frac{\tau}{\eta} \qquad \text{(Equation 19)}$$

Scaling of the oscillatory frequency (ω) was conducted through the use of the Strouhal number St, derived earlier using dimensional analysis. *In vivo* scale parameters were used to calculate the required numerical values of St for the biphasic waveform used in this study. Subsequent calculation of *in vitro* scale parameters, using these values of St, yielded the scaled frequencies appropriate for use in the experimental analysis. These are presented in Table 4 for both geometries used in this study.

3.4.2: Viscous Behaviour

The viscous behaviour of the test fluid under steady-shear conditions is shown in Fig.8. For comparative purposes, the data for that of blood, presented previously in Fig.6, is also included. Similarly, the oscillatory-shear viscosity of the test fluid (obtained using the correctly scaled conditions presented in Table 4) is compared with that of blood (shown previously in Fig.7) in Fig.9. (In the interests of clarity, the viscous and elastic properties are separated and discussed individually.) As discussed previously, the steady and oscillatory shear viscosities of blood were approximated using a combination of the Power-Law expression and limits representing the high- and low-shear plateaux. This was also done for those results obtained using the Xanthan Gum solution. The parameters which define each of these approximations, shown graphically in Figs.8&9, are presented in Table 5.

As discussed previously, flows of Power-Law fluids are dynamically similar only if the Power-Law index, n is the same in each case. Due to the observed spread in the data for blood, it is reasonable to suggest that a range of indices are acceptable when attempting to describe its viscosity. Bearing this in mind, the indices used to describe the viscous behaviour of the test fluid, under steady and oscillatory flow conditions, are considered to be within this range of acceptability. It is tempting therefore to assume that the viscous behaviour of blood can be correctly represented by the Xanthan Gum solution used here. However, dynamic scaling laws (see Chapter 2) dictate that the limits which describe the high- and low-shear plateaux must also be correctly scaled. This is achieved by scaling the limits (η_0 and η_∞) using the Reynolds number definitions in Equations 4&5 (see Section 2.2). Appropriate scaling of the fluid models which describe blood indicates that the Xanthan Gum solution used here does not satisfy these requirements; the limits η_0 and η_∞ are too low in the test fluid. Although not identified, a theoretical fluid (perhaps based on the Xanthan Gum solution used here) with properties which would adequately represent the viscous behaviour of blood is shown in Figs.10&11 for steady and oscillatory shear conditions respectively. This shows that, although the mid-shear regions ($1 \sim 10s^{-1}$ for steady flow, $2 \sim 20s^{-1}$ for biphasic flow) adequately represent blood, the viscous behaviour of the test fluid outside these ranges deviate significantly from that which is required.

Although the Xanthan Gum solution identified by Gray[91] exhibits some properties which are representative of blood (notably the Power-Law indices), the above discussion indicates that it is not suitable for use in the present study as a test fluid from which measured values of velocity and WSS can be converted from the *in vitro*-scale to the life-scale. However, since the results obtained using this test fluid could still be used to validate numerical studies (providing the numerical study is defined using both the same *in vitro* scale as that which defines the experiments and the same viscous parameters which relate to the Xanthan Gum solution), it was decided that the present study would use Computational fluid Dynamics (CFD) to investigate flow at life-scale. Since the Xanthan Gum solution was used only as a means by which numerical techniques could be verified, its viscous properties, being relatively similar to those of blood, are such that it was considered appropriate for use in this study.

3.4.3: Elastic Behaviour

Elastic behaviour of the test fluid was measured across a range of oscillatory shear rates. The results obtained using the frequency applicable to the *in vitro*-scale parameters, defined previously and presented in Table 4, are presented in Fig.12, together with the elastic data for blood over the range of frequencies applicable to the *in vivo* environment ($1Hz<f<3Hz$)[65-69]. The trends observed here for Xanthan Gum are supported by similar, but more extensive, work conducted by Thurston et al[92]. These trends include the presence of a low-shear plateau and a reduction in elasticity with increasing shear rate (in the higher shear region).

Comparing the data obtained here for Xanthan Gum with that reported in the literature for blood, there are a number of similarities worthy of note. These include relatively similar values for both the low-shear plateaux and the shear rates at which elastic linearity ceases to occur. The biggest difference however is the gradient which defines the rate of change of elasticity with shear rate. Despite this, the elastic behaviour of the test fluid generally can be considered to be reasonably similar to that of blood. Since elasticity is considered only a secondary concern in this study, these shortcomings are considered negligible. In this respect, the ability of the test fluid to resemble the elastic characteristics of blood in only the most general of ways (as has been shown here) is considered to be advantageous.

The viscoelastic effects of the Xanthan Gum solution described here are shown to be insignificant when the relaxation time regarding its elastic nature λ_r, is compared to typical flow conditions to be used in the experimental analysis. Referring to Table 4, the diameter of the vessel to be used is approximately 0.038m, while a typical flow velocity is of the order of 0.06m/s. A typical characteristic time of the flow λ_f (the time taken for a fluid particle to travel one diameter) is therefore ~0.6s. Bewersdorff et al[93] conducted studies on the relaxation times of aqueous Xanthan Gum solutions of varying concentrations. For 0.05%XG, it was found that, over a wide range of shear rates considered applicable to this study, λ_r~0.01s. (Although no data was available for an aqueous solution of 0.07%XG, use of this value was considered valid for the purposes of this study, since the relaxation times reported over the range of concentrations and shear rates were all of this order of magnitude.) Since

viscoelastic effects only become significant when λ_r and λ_f are comparable, it is assumed that the use of a rheological model which represents solely the viscous behaviour of the test fluid is an acceptable compromise between suitably representing its rheological characteristics and maintaining simplicity of the model.

3.5: Summary

A brief discussion regarding the rheology of blood has been presented. The physiological mechanisms responsible for its varying rheology have been summarised, highlighting those properties responsible for its viscoelastic characteristics.

A suitable fluid analogue was identified for use in the experimental analysis. The chosen analogue, 0.07%XG, was shown to have certain rheological properties representative of blood. However, limitations regarding its use as a test fluid, which can be used to model blood flow, have also been summarized; it has been shown that the solution cannot be considered dynamically similar in every sense to blood and can therefore not be used to accurately model blood flow in the geometries to be used in this study. Its primary use in this study however, is to enable experimental measurements to be made, against which numerical techniques can be verified later. Given that this does not require the use of a fluid with properties dynamically similar in every sense to those of blood, the Xanthan Gum solution described in this chapter was considered appropriate for use in this study. The following chapter reviews the apparatus required, and the techniques employed, to enable the experimental analysis to be conducted.

4: EXPERIMENTAL MODEL

This chapter describes both the apparatus and the method used to perform an experimental analysis of non-Newtonian fluid flow through occluded pipes. All the major components of the test rig are described, including the procedures undertaken to calibrate the pumps, the flowmeter and the optical devices used to record the data. Geometric features of the two test sections, used to represent typical clinical examples of stenosed arteries, are also described. In addition, a brief description of how the data acquisition system works, and the methods used to generate the experimental results described later in Chapter 5, are also presented.

4.1: General Construction and Operation

The experimental rig consisted of a reservoir, two pumps which produced the required flow rate waveform, a settling chamber, a straight entry pipe, the stenotic test section and a pipe returning fluid to the reservoir (see Fig.13). The fluid is first pumped from the reservoir into the settling chamber using the time varying main pump. A 'trim' pump then returns some fluid back to the reservoir from the settling chamber at a constant rate, to 'downshift' the waveform and allow reverse flow. This permits the reproduction of physiologically representative waveforms where negative flow is observed in diastolic arterial blood flow. The settling chamber includes a flow straightener and is conical in shape to ensure the flow through the entry length is one-dimensional. The time-varying flow rate was measured immediately downstream of the settling chamber using an electromagnetic (EM) flowmeter. This data was relayed back to a PC which also controlled the pumps. This provided the opportunity to check the measured flow rate against that which was required. The test fluid, having passed through the settling chamber and the straight entry pipe (47 pipe diameters in length), then entered the test section. Flow patterns in a 2D plane through the centreline of the test section were recorded using a Particle Imaging Velocimetry (PIV) system. Once through the test section, the fluid was returned to the reservoir via u-PVC plastic tubing, similar to that which carried the fluid to the pumps and settling chamber.

The test section was manufactured using borosilicate glass. This is significant since the test section was housed in a rectangular refraction box and immersed in pure glycerine (see Fig.14). The refraction box consisted of glass walls through which optical instruments could operate. Glycerine was used to fill the refraction box because of the similarity in its refractive index to that of borosilicate glass (identical to four significant figures). This effectively caused the outer surface of the test section to appear invisible since light would not be refracted at the boundary between the glycerine and glass. There were no problems with refraction through the glass walls of the refraction box because the optical instruments were positioned perpendicular to the walls of the box. Due to its hydrophilic nature, the possibility of the glycerine's refractive index changing over time had to be considered. Gray[91] observed that the refractive index a small distance below the surface remained unchanged over many months. The refraction box was therefore overfilled with glycerine, ensuring the test section was kept well below the surface of the glycerine.

A similar problem of refraction at the inner surface of the stenosis tubing could not be overcome using this technique however. The refractive index of the test fluid could not be matched exactly with that of the borosilicate glass. However, the difference was generally small and so the problem was overcome using a target to calibrate the effect of refraction at the glass-fluid boundary by measuring the observed diameter in the test section and comparing this with the known diameter.

The rig also included bleed taps located in the plastic piping, just downstream of the test section, to allow air to be bled from the system. A mixing loop was also included, independent of the test section, to enable thorough mixing of the test fluid. A pressure release valve, located immediately downstream of the main pump and returning fluid to the reservoir, was also installed for safety purposes. In the interests of clarity, none of these features are shown in Fig.13.

4.2: Electromagnetic Flowmeter

The flow rate of the fluid entering the test section was measured using a Fischer & Porter electromagnetic (EM) flowmeter. This type of flowmeter was chosen because it has been demonstrated to be unaffected by changing fluid properties such as

density, viscosity and the velocity profile[94]. Other commonly used flowmeters, such as vortex shedding, ultrasonic and orifice plate devices, are dependent upon these fluid properties. Since the test fluid would have to be replaced on a regular basis, there could be no guarantee that such fluid properties would be identical in all cases. For this reason the EM flowmeter was chosen as the most suitable for use in this application. The only requirement for the EM flowmeter to work properly is that the conductivity of the fluid be at least 20μS/cm. This condition is satisfied by the fluid that was to be used in this study.

The EM flowmeter was also chosen for its fast response time. In the pulsatile experiments undertaken in this study, the flow rate generated by the main pump required updating 100 times per cycle. The flowmeter was therefore required to update the measured flow rates at the same frequency. Since the time period of the desired waveform was to be of the order of a few seconds, the Fischer & Porter flowmeter (which has an excitation frequency of 50Hz) was considered ideal for this application.

4.3.1: Flowmeter Calibration

To ensure the experimental rig obtained realistic quantitative results, it must be shown that the actual flow rate achieved in the rig was the same as the flow rate indicated by the EM flowmeter. Calibration of the EM flowmeter was achieved using a method which involved pumping water through the EM flowmeter and into a bucket. Water was collected in the bucket for a set time and then weighed. The volumetric flow rate was calculated and compared with the mean EM flowmeter reading. This process was repeated for the entire range of main pump input voltage, 0 – 10V, in 0.5V increments. The resulting data is presented in graphical form in Fig.15. The response of the meter is clearly linear with a calibration factor of 1.0355, offset by –0.09. This calibration equation was used in all subsequent experiments.

4.3.2: Flowmeter Tolerances

So that the level of certainty in the recorded flow rate could be established, it was considered necessary to calculate the tolerance to which the flowmeter was able to operate in both steady and pulsatile flow experiments. In steady flow experiments,

the flow rate would be determined by calculating an average from a set of data signals received from the EM flowmeter. In order to determine how many data signals would have to be collected to ensure an acceptable mean value was obtained, 1000 data signals were measured by the EM flowmeter and recorded by the PC at approximately 0.1s intervals with the main pump running at a steady flow rate. The overall mean of the 1000 signals and the progressive mean were calculated and plotted on the same chart. This procedure was conducted at four different flow rates, which represent the full range to be used in the analysis. Referring to Fig.16 (where flow rate is 4.58lpm), the mean flow rate takes only 200 samples to converge within 1% of the final average of 1000 samples, while an error of only 0.5% is achieved after approximately 500 samples. This level of tolerance was typical of that which was obtained at the other three flow rates that were investigated in this manner. It was decided therefore that, in steady flow rate experiments, the measured flow rate would be recorded 500 times and the resulting mean would be used to define the flow.

In pulsatile flow, the average of a set of data signals was not calculated. Instead, each data reading was treated on its own, its value assumed to be representative of the instantaneous flow rate. However, there is an uncertainty associated with each reading and this was estimated by calculating the standard deviation of the data set collected above. Values which fell within one standard deviation of the mean accounted for 68% of the readings, while those which fell within two standard deviations of the mean accounted for 95% of the readings. It was therefore possible to attribute uncertainties to a given percentage (68% or 95%) of the measured flow rate readings. Table 6 summarises the uncertainties associated with the four flow rates for which this analysis was conducted.

4.3: Pumps

Two positive displacement pumps were used to produce the desired time-varying waveform. A variable speed 'main' pump was used to provide the main flow, while a much smaller 'trim' pump provided a constant reverse flow. This trim pump effectively 'downshifts' the waveform, allowing negative flow rates to be generated. Both pumps were controlled using a PC interfaced to the rig with a PC30AT card.

The desired outputs were regulated using a PASCAL programming code. The required waveform was first read from a string of 100 discrete flow rate values, converted into a voltage reading by a calibration equation in the PASCAL code and sent to the pumps at regular intervals (every 100^{th} of a time period) via a 0-10V digital-to-analogue converter. The interval at which signals were sent to the pumps was controlled using an adjustable delay function in the PASCAL code. This enabled the time period of the waveform to be controlled accordingly.

The same PC and PASCAL code was used for recording measured flow rates from the EM flowmeter. The EM flowmeter produced a current in the range 0-20mA which was put through a 500Ω resistor and read as a voltage by the PC30AT interface card. This voltage (0-10V) was then sent to the PC, in which the calibration equation converted it into a flow rate reading. In steady state experiments, a mean value was calculated using all the flow rate data received during acquisition of optical data. In pulsatile experiments, flow rates were recorded and stored in an array. Flow rates recorded in successive cycles, at identical points in the waveform, were then averaged and compared with the required waveform.

Both pumps were driven by voltages sent to them by the controlling PC. The magnitude of the voltage determined the speed at which the pump operated and hence the volumetric flow rate. Calibration of this relationship was determined by plotting the EM flowmeter output (measured in litres per minute) against the user-defined voltage that was sent to the pump (OpVoltsM for the main pump and OpVoltsT for the trim pump). Typical examples of the data generated for the main and trim pumps are shown in Figs.17&18. The third order equations which represent these data were inserted into the PASCAL programme to allow conversion of user-defined flow rates into voltages (to drive the pumps) and vice versa (to convert voltages sent from the flowmeter into flow rate values to be recorded by the PC).

4.4: Test Section

The test section was required to have certain characteristics which would enable it to be used in a laboratory environment where the effects of geometry on the resultant flow field could be studied. These characteristics include appropriate scaling of the

geometry and the ability for it to be used in conjunction with flow visualisation techniques (see Section 4.5). The former is discussed below, while the latter was achieved through the selection of borosilicate glass as the production material. This is a transparent glass which exhibits a refractive index within 4 significant figures of that of glycerine. The benefits of this near-perfect match were discussed previously in Section 4.1.

By their very nature, stenoses are irregular growths which can be located anywhere in the cardiovascular system. While certain areas have been identified with an increase in prevalence, there is no doubt that the severity, exact location and uniformity of atherosclerotic growths cannot be predicted. While it is impractical to replicate the shape and dimensions of stenoses and their host arteries for every physiological eventuality, an attempt is made in this study to examine the effects of severity. It was decided therefore that a simple contraction-expansion geometry would suffice. The shape of the constriction is shown in Fig.19.

Severity S, is consistently defined in the literature as the percentage reduction in cross-sectional area caused by the stenosis. This can be written in the form:

$$Severity, S = \frac{A_0 - A_N}{A_0} \times 100\% \qquad \text{(Equation 20)}$$

where the cross-sectional areas A_0 and A_N refer to those measured in the unrestricted vessel and at the stenosis throat respectively. The severities considered for use in the present study (51% and 84%) represent approximately the top and bottom end of the scale judged to be clinically significant by Gray et al[2]. They are also somewhere near the limits of the range in which other researchers have conducted previous studies[35,50]. They were chosen to enable atherogenic parameters to be quantified, and the suitability of using numerical techniques to be assessed, at the limits of these scales.

The likelihood of separated flow reattaching to the wall asymmetrically was considered a realistic possibility. Of particular concern in this study is that such asymmetry could lead to the reattachment points, and hence the jet, moving around the azimuth over time. This phenomenon was observed by Khezzar et al[95], who

conducted an experimental study of Newtonian flow through both axisymmetric and asymmetric round sudden expansion geometries. (Although the geometries to be used in this study are not of the same type as those used by Khezzar et al[95], the flow characteristics in both types of geometry are comparable.) Khezzar et al[95] reported that, at low Reynolds numbers in the axisymmetric case, the central core of the flow remained well-structured, stable and symmetrical. As Reynolds number was increased however, the core was observed to oscillate, leading also to the reattachment points oscillating around a mean. In the asymmetric geometries, the flow was also observed to oscillate, this time reattaching to the wall asymmetrically and then returning to symmetry at some point further downstream. (Note that Khezzar et al[95] observed unsteadiness to occur at lower Reynolds numbers in the asymmetric geometry compared to the symmetric case. It was therefore considered important that any asymmetry in the geometry be minimised.) It was decided that, in the present study, the stenosis geometry would be defined such that a small amount of asymmetry was present; the centreline of the constriction was offset from that of the pipe by a set distance (see Fig.19). This was done in an attempt to control the azimuth position of the mean reattachment point (reattachment was assumed to commence initially at the azimuth position relating to the minimum height of the stenosis, (see Fig.20)). In doing so, the two dimensional plane in which flow data is recorded could be set such that any asymmetry in the flow is observed; the plane of data acquisition was set such that it dissected the minimum and maximum reattachment lengths ($\theta = 0,2\pi$ and $\theta = \pi$ respectively in Fig.20). For both geometry types used in this study, the offset distance was approximately 1% that of the internal diameter of the pipe.

As was discussed previously in Section 1.3, the elastic nature of the arterial wall is ignored for the purposes of this study; the *in vitro* analysis conducted here assumes a rigid wall condition. This assumption is supported by the observation that atherosclerosis is usually associated with hardening of the vessel wall, thereby reducing its elasticity[7]. This is a favourable outcome since it allows considerable simplification of the problem.

4.5: The PIV System

The Particle Imaging Velocimetry (PIV) system is a flow visualisation technique which works using the principle of tracking illuminated particles through a transparent test section. The main components include a laser (a pulsed Nd:YAG, NewWave Research Minilase III, wavelength 532nm), a high performance digital camera (Dantec DoubleImage 700) and an operating PC. The PC uses a software package called FlowManager which provides an interface through which the settings controlling the hardware can be altered and the received signals can be processed into a velocity vector map.

A two dimensional plane of illumination is achieved by directing the laser beam through a cylindrical lens to produce a sheet of laser light. The laser is then positioned so that the light sheet illuminates the centre-plane of the test section. Visualisation of the flow is achieved by seeding the fluid with reflective particles (Dantec fluorescing polymer particles, typically 75μm in diameter). The very short period in which the particles are illuminated means they appear stationary. A digital image of the illuminated field is obtained by positioning the camera perpendicular to the light sheet, its focal point set to ensure the particles appear as sharp bright dots. Synchronization of the laser and camera to record a pair of images a set time interval apart, is coordinated by the processor. A velocity vector map is then produced by first identifying the position of each seeding particle in the two images. The displacement of each particle is divided by the known time interval between images in order to calculate the velocity of each particle in the domain and to hence generate a velocity vector map.

Before full-scale use of the testing equipment could be started, a number of necessary setup procedures were identified and undertaken. These included the definition of a coordinate system, calculation of a scale factor and an assessment of the effects of refraction at the inner surface of the test section. A normal Cartesian coordinate system was adopted while the origin was defined as lying on the centreline of the straight tube, at an axial position where the diameter of the tube is at its minimum.

Due to the mismatch in the refractive indices of the glass tubing and the test fluid inside, refraction at the boundary between these media causes the image to be distorted in the direction tangential to the curvature of the pipe. This was observed to occur mainly in the radial direction, although small effects were also observed in the axial direction in the occluded region, due to the gradual narrowing of the cross-section. In addition to these refractive effects, the scale factor (which defines the number of camera pixels per millimetre observed in the image) was also measured using a target with a millimetre scale. This target was inserted into the test section and the pipes filled with the test fluid. Using an image from the CCD camera, scale factor calibration was conducted by recording the pixel position of each axial increment on the geometric centreline of the pipe, across a 100mm distance. These measurements were recorded across a region which included both the occlusion and a straight section of pipe. The data obtained for the 51% severity case are shown in graphical form in Fig.21. Refraction in the axial direction, due to the narrowing of the pipe can be detected in this plot, but was judged to be of minor concern in both geometries used. The resulting scale factor was inserted into the FlowManager programme where it was used to convert all subsequent images into the metric scale. This procedure was conducted upon insertion of each new geometry.

In the radial direction, refraction effects caused the observed diameter to be smaller than the true diameter. Although not insignificant, this disparity was sufficiently small to warrant its correction through the use of a linear scale. Using the same CCD camera image that was used to calibrate the scale factor, the pixel position of each radial increment at three axial locations on the target was recorded and converted into the metric scale using the scale factor calculated previously. This data was then plotted against the real metric dimensions of the target; the gradient relating this data is defined as the correction factor. Again this procedure was repeated for each new geometry used. An example is shown in Fig.22 for the 51% severity case. The correction factor was introduced into the FlowManager programme where it was used to correct distorted images recorded by the CCD camera.

The most important parameters to be defined in the data acquisition setup were identified to be the timing interval between the two images in a pair and the size and percentage overlap of interrogation areas. The effects of these parameters are related

and the determination of each must therefore be made with appropriate consideration of the others. The image captured by the CCD camera is broken down into a grid-like structure consisting of squares called interrogation areas. The size of an interrogation area is defined by the number of pixels in each dimension and determines both the level of resolution and the range of measurable velocities the system is able to compute. Large interrogation areas are able to produce a wide range of measurable velocities but at low resolution. Alternatively, many small interrogation areas are able to produce velocity vector maps with high resolution yet only a narrow range of recordable velocities. Since the expected velocities were small, interrogation areas of 16×16 pixels were employed. The time interval between image pairs was calculated so that particles moving with the maximum velocities in the domain would move approximately a quarter of the length of the interrogation areas.

In order to compute the displacement (and therefore velocity) of a seeding particle, the particle needs to be identified and located in the same interrogation area in each of the two images in a pair. Due to its movement between successive images, it is likely that a particle will have moved from one interrogation area to a neighbouring one. For this reason, an overlap of adjacent interrogation areas was required, enabling correct identification of more particles in a given image pair. An overlap of 25% was used, reflecting the recommended maximum displacement of particles between images. Using such settings, seeding particles should always remain within at least one interrogation area in the two images which constitute a pair. These settings provide a reasonable compromise between spatial resolution and a wide range of measurable velocities.

Noise in the computation is produced by signal dropout and is manifested in the velocity vector map as 'wrong' vectors, random in both magnitude and direction. Signal dropout is where a seeding particle identified in one image is not identified in the same interrogation area in the corresponding image belonging to that pair. In other words, a particle seen in an interrogation area in image A is not seen in the same interrogation area in image B. A considerable number of 'stray' particles are therefore observed which are not correctly paired with particles in the corresponding image. This gives rise to incorrectly paired particles which produce 'wrong' vectors

in the velocity vector map. Signal dropout is affected by the timing interval between images in a pair, the size and overlap of the interrogation areas, the seeding density and out-of-plane (3-dimensional) motion of the flow.

The seeding density is closely linked to the size of the interrogation areas since it is recommended that at least 5 particle pairs are required in each area to ensure the production of good data[96]. Out-of-plane motion produces signal dropout for the same reasons as those relating to a poor choice of timing interval and interrogation area size. In this instance however, particles move through (perpendicular to) the laser sheet as opposed to across (parallel to) it. To reduce signal dropout, the thickness of the laser sheet was increased so that out-of-plane motion would be restricted to a quarter of the sheet thickness. This is in line with good practice[96] and suggests that the worst case scenario would see a maximum of 50% of particles drop out.

Once all these conditions were satisfied, the rig was filled with test fluid. One hundred image pairs were recorded for each required flow rate condition and processed using the following technique. Firstly, a 'mean image' was produced, representing the average luminosity of each pixel in the domain throughout the recorded data set. Subtraction of this 'mean' from each image in the data set significantly reduced environmental noise by effectively filtering out any received light not originating from the illuminated seeding particles. This was aided by also attaching a filter to the CCD camera lens which permitted only light with the same wavelength as that emitted by the laser (and hence reflected by the seeding particles) to penetrate. These images were then processed using an algorithm which produced a velocity vector map for each image pair. Velocity vectors outside the flow region (generated by noise) were then deleted using a mask which defined the boundaries of the flow domain. This mask was prepared using an image which enabled the outline of the domain to be accurately determined. Erroneous vectors within the flow domain, generated by signal dropout, were then removed from these raw velocity vector maps in an attempt to increase the signal to noise ratio. There are a number of algorithms which can be used to do this. Some of these attempt to replace false vectors with 'corrected' ones, whose values are predicted using those of neighbouring vectors. However, this practice was considered risky because of the

potential for introducing flow structures unrepresentative of the real flow and, conversely, eliminating flow features that do actually occur, particularly small ones. For this reason, it was decided that only Range Validation would be used. This is an algorithm that simply rejects velocity vectors with magnitudes above a certain user-defined threshold. This threshold was set at a value 25% greater than the maximum velocity expected in the flow domain at that instance. This slight over-compensation means that only velocity vectors that are definitely false will be removed. The final step in this process involved the calculation of a mean velocity vector map. This was done by averaging, for every point in the flow domain, the calculated velocities in each of the 100 individual velocity vector maps. A velocity map of this type was generated for each flow condition investigated and the velocity data exported from these were used to produce the results presented in Chapter 5.

4.6: Summary

An experimental rig was used to enable a large-scale, *in vitro* analysis of Power-Law fluid flow through models of arterial stenoses. Two test sections were constructed; one representing a mild yet significant degree of luminal narrowing and another much more severe constriction. An interface was established through which user-defined, time-dependent flow rates required in the rig could be set and subsequently measured. Two-dimensional flow visualisation and measurement was achieved through the use of PIV technology.

The results obtained using this setup are described in detail in the following chapter. Steady flow rate experiments are presented first, providing a foundation upon which further discussions regarding a more physiologically-representative time-dependent waveform can be developed. Of particular concern throughout will be factors which affect wall conditions due to their established importance in further degrading arterial health and accelerating the development of stenoses.

5: EXPERIMENTAL RESULTS

This chapter describes the steady and time-dependent experimental results obtained using the test fluid, apparatus and data acquisition methods described previously.

5.1: Introduction

The apparatus described in Chapter 4 was used to investigate non-Newtonian fluid flow through large-scale model stenoses. The fluid used was the Xanthan Gum solution described in Chapter 3. The geometries employed were circular pipes with smooth occlusions, representing arterial stenoses defined by a reduction in cross-sectional area of 51% and 84%. The nature of the local flow fields present in each of these geometries were studied under both steady and pulsatile flow rate conditions. A process of dimensional analysis enabled the scaling of these flow rate conditions such that the numerical values of the relevant dimensionless groups, representing different aspects of the flow, were identical in the model to those that would be expected at life-scale. Velocity measurements were made in a two-dimensional plane through the centre of the tube, proximal and distal to the occlusion, using Particle Imaging Velocimetry (PIV). The results presented in this chapter include velocity vector maps and axial velocity profiles, both of which illustrate the structure of the local flow field. The velocity gradients at the wall are then used to obtain the distribution of wall shear stress (WSS) along the walls of the geometries.

Before a discussion of the results can take place, the conditions used in the model to simulate those found in the cardiovascular system are discussed first.

5.2: Experimental Conditions

Experimental investigations of flow through the model stenoses were conducted with special consideration given to the physiological waveform recorded *in vivo*[55] (see Fig.5). Appropriate scaling of this waveform was conducted using the dimensional analysis described in Chapter 2. The characteristic lengths used in the Reynolds number scaling procedure were the vessel diameters. The *in vivo* diameter was 6mm. Since the tubes used in the *in vitro* study were found to have slightly different

diameters in the sections of the pipe proximal and distal to the occlusions (34.7:37.7mm in the 51% occlusive geometry and 37.0:38.1mm in the 84% occlusive geometry), a decision on which diameter to use as the characteristic length was required. Although the difference was not considered important, the diameters of the pipes in the distal sections were employed in the scaling technique, since the majority of the flow field under consideration was distal to the occlusion. The applicable scaling parameters for both the *in vivo* case and the *in vitro* cases are summarised in Table 7. Using these parameters and the scaling procedure described in Chapter 2, the *in vivo* biphasic waveform in Fig.5 was scaled for use in the experimental analysis.

A number of positions in the cycle were identified as being characteristic of the *in vivo* biphasic waveform. These include the peak systolic flow rate and the cycle mean flow rate. Two intermediate flow rates were also considered; halfway between the peak systolic flow rate and the peak diastolic flow rate (Intermediate 1) and half the peak systolic flow rate (Intermediate 2). The Power-Law Reynolds numbers relating to these characteristic flow rates, calculated using parameters which define the Power-Law fluid under steady flow rate conditions ($n = 0.61$, $\kappa = 41 mPa.s^n$), were found to be $Re_{PL} = 74$ for the cycle mean flow rate condition, $Re_{PL} = 180$ for the Intermediate 1 condition, $Re_{PL} = 235$ for the Intermediate 2 condition and $Re_{PL} = 617$ for the peak systolic flow rate condition. These characteristic conditions were used to conduct a steady flow rate analysis of non-Newtonian fluid flow through the occluded geometries.

5.3: Steady Flow Experiments

Results for the steady state experiments are presented in this section. Of particular interest are the reported effects of Reynolds number and stenosis severity (S) on the resultant flow fields. The experiments were conducted using flow rates which were judged to be characteristic of the biphasic waveform described in Section 2.2 (see Fig.5). The two geometries used in the experiments represent arteries within which stenoses have developed due to atherosclerotic or intimal hyperplasic growth. They are referred to here by the severity of their constrictions and represent examples of mild (S = 51%) and serious (S = 84%) clinical cases. The fluid used in these

experiments was the Xanthan Gum solution described in Chapter 3.

The results are presented here in various forms. The velocity vector maps generated by PIV are useful mainly for qualitative purposes and for highlighting important flow features such as regions of recirculation and stagnation points. The numeric data which describes these velocity vector maps was exported to enable more quantitative results to be presented.

Of primary interest are the velocity profiles and the WSS distributions. The axial velocities were normalized using the bulk flow velocity which was calculated using the volumetric flow rate and the cross-sectional area of the vessel distal to the occlusion. The volumetric flow rate was measured 100 times by the EM flowmeter while simultaneously acquiring the PIV data. These measurements were recorded on a PC and then averaged to give the mean flow rate. The bulk velocity was also used to calculate the bulk dynamic pressure for each flow rate investigated. These dynamic pressures were then used to convert the calculated WSS into non-dimensional values (see Chapter 2).

The extent of the flow domain to be visualised was dependent upon the field of view the camera was able to obtain. A decision regarding these limits was based on a consideration regarding the amount of flow that could be observed and the resolution that the camera was able to achieve; a compromise had to be sought. The limits were defined such that five diameters in the axial direction was considered sufficient to enable a detailed study to be made of the flow, in a sufficiently large area of the domain, while maintaining resolution at an adequate level. The distribution of the field of view was chosen in light of the need to concentrate on the flow in the post-occlusive region, since it is here that disturbances due to the presence of an occlusion are greatest. The selected distribution encompassed approximately one diameter upstream and four diameters downstream of the occlusion throat.

5.3.1: Overview – Steady Flow

The flow can be visualised using time-averaged velocity vector maps. These were calculated using the individual velocity vector maps which were derived using the 100 data sets recorded by the PIV system for each flow rate condition. In order to

establish whether a sample size of 100 was sufficient for the time-averaged results to be considered representative of, for example, 100,000 samples, velocity profiles were plotted using a sample size of 10, 25, 50 and 100 samples. This was done for both geometry types and was conduced at some location downstream of the occlusion, since it is here where the flow is affected by the occlusion. Referring to Fig.23a (considered to be the best case scenario – least severe geometry and lowest Reynolds number used in this study), the time-averaged velocity profiles one diameter downstream of the occlusion are shown to converge as the sample size is increased. However, even with a sample size of just 10, the velocity profile is shown to be representative of that which was obtained using 100 samples. This confirms that a sample size of 100 is sufficient to enable the time-averaged results to be considered representative of those which would be obtained using a much larger sample size. A similar analysis was conducted using the 84% severity geometry and $Re_{PL} = 617$ (see Fig.23b), In this case however, the profiles were obtained two diameters downstream of the occlusion instead of one because of the increased length of the occlusion in the 84% case. Fig.23b shows that a greater sample size is required before convergence is achieved using these conditions. The velocity profiles indicate a sample size of 10 to be insufficient for reliable data analysis to be conducted, However, a comparison between the profiles obtained using 50 and 100 samples indicates that 100 samples is enough to enable a quantitative analysis to be made with confidence.

The time-averaged velocity vector maps, generated for the Reynolds numbers identified in Section 5.2, are presented in Fig.24 and Fig.25 for the 51% and 84% severity cases respectively. The nature of the observed flow fields (e.g. recirculation length) is shown to be highly dependent on both Reynolds number and, more significantly, occlusive severity. General flow features, such as recirculation regions, can be interpreted from these velocity vector maps, but are identified more readily using another form of PIV data output.

For a given flow condition, flow structures can be visualized by recording a long exposure image of the flow. In doing this, the seeding particles are tracked over time and their movement is shown as streaks, effectively recording the path followed by each particle as it travels through the domain. This process was conducted for each

flow rate investigated, examples of which are displayed in Fig.26. In Fig.26a (S = 51%) recirculating flow is readily identified in the near-wall region downstream of the occlusion. The stagnation points, which define the limits of recirculation, are also clearly visible. By comparison, none of these features are recognisable in Fig.26b (S = 84%). The clarity with which recirculation can be identified provides an indication of the level of stability in the flow, since, in highly time-dependent flow, seeding particles are unable to follow constant fixed paths through the domain. The flow distal to the occlusion in Fig.26a can therefore be regarded as being more stable than that which is observed in Fig.26b, despite the flow upstream of the occlusion being steady and fully-developed in both cases. Stable flow fields, in which recirculating flow is readily identified (such as in Fig.26a), were observed at all Reynolds numbers in the 51% severity geometry and at Re_{PL} = 74 in the 84% geometry. For $Re_{PL} \geq 180$ in the 84% severity case, the long exposure images of the flow resembled that which is shown in Fig.26b, indicating significant unsteadiness downstream of the occlusion. This unsteadiness is illustrated more clearly through the use of contour maps which plot the ratio of the standard deviation of the velocity vector data to the mean local velocity.

$$\frac{\sigma}{\overline{u}_{(x,r)}} \qquad \text{(Equation 21)}$$

These plots, presented in Fig.27 and Fig.28 for the 51% and 84% occlusive severity cases respectively, indicate a number of important features. Referring to Fig.27, the flow field is shown to be highly repeatable. This is particularly so in the region proximal to the throat of the occlusion (where the flow assumes fully developed, laminar conditions), in the throat region (where the flow is accelerated) and in the central core region downstream of the occlusion (where the effects of the wall are not felt). This high level of repeatability implies that the recorded velocity vector quantities showed very little variation throughout the recorded data sequence. This is confirmed by comparing a sample of the 100 velocity vector maps from which each mean velocity vector map was derived. An example of this comparison is shown in Fig.29 for both the 51% and 84% occlusive severity geometries. In each case, Re_{PL} = 180. In the 84% geometry, there is clearly a much greater degree of variability in the velocity vector field, with a significant fluctuation in the position where the flow reattaches to the wall. This does not occur in the 51% case, where the flow field is

shown to be highly repeatable. Referring to Fig.27&28, the localized elevated levels of variability indicate the presence of shear layers and stagnation points. These stagnation points represent the locations where the flow separates and reattaches to the wall. There are two reasons for the high levels of variability shown in these areas. Firstly, since the standard deviation is normalized using the local mean velocity, those points at which the mean velocities are small will be represented here as having large variations in the data set. However, these regions do undoubtedly show significant variations in the data that are the result of axial, radial and circumferential movement of the jet (and hence the shear layers and stagnation points). The shear layers and stagnation points are therefore considered to be inherently unstable, causing the jet to 'flicker' and the point of flow reattachment to oscillate around a mean.

These normalized standard deviation plots confirm that instability in the flow increases with Reynolds number. Referring to Fig.27, the majority of the flow is shown to be highly repeatable for all Reynolds numbers investigated. They are considered repeatable enough to enable them to be described as steady. Despite this however, instability in the shear layers is clearly observed to increase with Reynolds number (compare Fig.27a and Fig.27d). This observation is supported further by the plots shown in Fig.28 for the 84% severity case, where the trend is even more noticeable. In Fig.28a, the central jet and recirculation regions are shown as distinct, well defined features, separated by two definite shear layers. (These 'two' shear layers are in fact a cross-sectional slice through a three-dimensional shear surface.) At higher Reynolds numbers however (e.g. Fig.28d), the distinction between these features becomes less well defined, indicating greater movement of the jet over time. In addition, the normalized standard deviation increases throughout the whole distal section of the domain, particularly in the shear layer but also even in the central core region, indicating greater levels of instability.

The relationship between occlusive severity and instability is shown clearly by comparing tests, conducted using different geometries, in which the Reynolds number is comparable (e.g. Fig.27c and Fig.28c). The first and most significant observation is that the degree of variability is noticeably greater in the more severely constricted geometry. Movement of the jet, the shear layers and the reattachment

points is therefore considerably higher in the 84% severity case, indicating an inverse relationship between stability and occlusive severity. This trend is shown to occur throughout the range of Reynolds numbers used here. The highly stable flow observed for all Reynolds numbers in the 51% severity geometry is only seen in the 84% severity case at the lowest Reynolds number investigated. For Reynolds numbers of 180 and above, unsteadiness was observed in the 84% severity case, even though a steady driving flow rate was applied. This is illustrated by the high levels of fluctuation encountered, particularly in the vicinity of the shear layers.

The tendency of instability to increase with severity can be explained by considering how the flow is affected by the presence of an occlusion. As flow progresses through the contracting section of the geometry, the fluid is deflected towards the centreline of the pipe. At this point, the flow experiences strong two-dimensional characteristics due to the enforced radial velocity as the flow is accelerated through the contraction. In the expansion section, flow again develops a radial component of velocity (this time away from the centreline), driving the flow once more towards the wall. The increase in cross-sectional area, and the consequential required deceleration of the flow, results in the need of the fluid to dissipate momentum. Perturbations present in the flow are exaggerated by this process, leading to instability and asymmetry in the resulting flow field. The more severe the occlusion (and, similarly, the higher the Reynolds number), the greater the required dissipation of momentum distal to the occlusion. Instability is therefore dependent upon both Reynolds number and the severity of the occlusion encountered, results which have both been demonstrated here experimentally.

In experiments characterised by low Reynolds numbers and geometries of low occlusive severity, the resulting flow conditions have been shown to be highly stable. In such cases, fluid travels smoothly through the domain, remaining largely two-dimensional and encountering little three-dimensional motion. As a result, a high degree of flow stability was observed in these cases. As Reynolds number was increased, the flow became more unsteady. This was manifested as an increase in the movement or 'flickering' of the jet, the adjoining shear layers (which separate the jet from the areas containing recirculating flow) and the points of flow reattachment. Occlusive severity has also been shown to be highly influential in the level of

instability present in the flow. In severely constricted geometries, jet movement was observed to be highly significant, resulting in large fluctuations in the position of shear layers and stagnation points. These observations indicate significant local unsteadiness.

Although velocity vector maps, particle tracking and standard deviation plots provide an effective aid to understanding the general flow structure and characteristics, they are limited in their capacity to display results in a meaningful and quantitative manner. The following sections provide details of how data provided by the PIV apparatus was used to present results in a more suitable format.

5.3.2: Velocity Profiles – Steady Flow

To examine how axial velocity varied throughout the domain, velocity profiles were plotted. These were derived using the data exported from the time-averaged velocity vector maps shown in Figs.24&25. The profiles were plotted at intervals of approximately half a (distal) diameter in the axial direction. The data provided by the PIV apparatus was assigned an axial and a radial coordinate to identify its pixel position within the flow domain. The size of the interrogation area (16x16 pixels) was such that velocity vectors were produced every 8 pixels in both the axial and radial directions. Velocity profiles were therefore calculated using the velocity vectors located nearest to each of the defined intervals and were sited according to their position relative to these intervals.

Conversion of the pixel coordinates into a standard metric length scale was achieved by multiplying the pixel position by the scale factor which defined the number of pixels per millimetre. The refraction correction factor was also used to account for the refraction caused by the curvature of the glass in the radial direction. (As discussed in Section 4.5, refraction due to curvature of the glass in the axial direction in the occlusive region was considered to be insignificant.) For comparative purposes, these axial and radial coordinates were then normalized by dividing by the diameter and radius respectively, therefore enabling the data to be plotted without dimensions. For the same reason, velocities were normalized using the bulk flow velocities and, in the 51% severity case, an additional factor of 5 was used to make the data easier to view and interpret (hence the reference vector representing $5\overline{U}$ on

Fig.30). For the 84% stenotic severity case, this additional scaling factor was increased to 15, reflecting the higher velocities recorded using this geometry. The resulting velocity profiles are shown in Fig.30 for the 51% severity case and in Fig.31 for the 84% severity case.

Consider the velocity profiles plotted in Fig.30 and Fig.31 for both geometry types. There are a number of common features which are applicable in both geometries and across the full range of Reynolds numbers studied. Firstly, the velocity profiles indicate that, in the regions proximal to the occlusions, flow is of a fully-developed, laminar nature. This is confirmed by the comparison between the experimental results obtained in this region and the theoretical velocity profile for fully-developed laminar flow of a non-Newtonian fluid[97]:

$$u(r) = \overline{U}\left(\frac{3n+1}{n+1}\right)\left\{1-\left(\frac{r}{R}\right)^{\frac{(n+1)}{n}}\right\} \qquad \text{(Equation 22)}$$

These comparisons are shown in Figs.32&33 for the 51% and 84% severity occlusive geometries. Note that in Fig.33, the calculated profiles do not resemble the fully-developed, laminar flow condition as well as one would expect. This is because, contrary to the 51% case, they were measured at a point where the diameter had already begun to decrease due to the occlusion (reduction in area ~7%), forcing the flow to accelerate and hence the profile to flatten. However, their relatively close match suggests that, if these measurements were taken further upstream, away from the influence of the occlusion, the profiles would resemble the fully-developed, laminar profile condition much more clearly. As flow is accelerated through the occlusions, the profiles flatten. This is particularly noticeable in Fig.31 and is due to the increased effect of inertial forces which dominate in this high-velocity region. This phenomenon is shown to be positively dependent on both Reynolds number and the severity of the constriction, and is the result of the increased inertia which is carried by the fluid under such conditions and the thinning of the boundary layer under the strong positive pressure gradient. As the flow progresses past the throat, the flow separates from the vessel walls, resulting in a jet surrounded by areas of recirculation. Further downstream, the jet diverges as its momentum is dissipated, reattaching to the wall at a point beyond which the profiles slowly begin to once again resemble that of fully-developed, laminar flow.

Of particular interest to this study are those characteristics which exhibit clear Reynolds number dependence. Figs.27&28 showed that instability is one such characteristic. The coupling mechanism that exists between Reynolds number and instability dictates that the strength and significance of the perturbations increase with Reynolds number. By definition, these perturbations divert the flow field away from a symmetrical and wholly stable condition. Although small perturbations were present in all cases, Figs.27&28 illustrated that the flows in which instability was significant enough to cause unsteadiness were those where the geometry is defined by an occlusive severity of 84% and where $Re_{PL} \geq 180$. For the same geometry, Fig.28a indicated that, at $Re_{PL} = 74$, a highly stable flow field develops in which a core jet is surrounded by long regions of stable recirculating flow. This is confirmed by the velocity profiles in Fig.31a which can be regarded as being highly representative of the instantaneous condition. However, at $Re_{PL} \geq 180$, the highly transient nature of unsteady flow results in the time-dependent complexities being averaged and smoothed-out in the time-averaged profiles plotted in Fig.31b-d. The variability in the velocity data distal to the occlusion in these circumstances was identified previously in relation to the standard deviation plots (Fig.28). The three-dimensional nature of the flow in these circumstances may also be responsible for the apparent lack in continuity at some locations in the velocity profile plots shown in Fig.31. The tendency of the jet to 'flicker' and skew towards the wall, at a position not in the observed plane, means that conservation of momentum may not necessarily be observed in the two-dimensional plane in which the velocity data was recorded. This is supported by performing a simple calculation of the two-dimensional flow rate at various locations along the length of the domain. This was done by integrating the axial velocity profiles in Fig.30&31 using Simpson's Rule[98]. For the 51% severity case, the two-dimensional flow rate at the neck was typically ~10-15% greater than that at the end of the domain (3.5 diameters downstream of the throat). In comparison, the two-dimensional flow rate was typically ~40-50% greater at the neck than at the end of the domain in the 84% severity case, indicating a much greater tendency of the flow to exhibit three-dimensional characteristics (and hence be skewed towards the wall at a position not in the observed plane) in the more severely occluded geometry. Although continuity is not maintained in the two-dimensional plane shown here, if the entire three-

dimensional domain is considered, continuity will clearly be maintained.

Although not immediately obvious, asymmetry was also observed to increase with Reynolds number. Referring to Figs.30&31, flow is axisymmetric in both geometry types under low Reynolds number regimes. Only at high Reynolds numbers was asymmetry noticeable (see particularly Fig.30d and Fig.31d distal to the occlusion).

Another aspect of the flow which is shown to be dependent on Reynolds number is the length of recirculation. A meaningful relationship between these parameters can only be made for those flows in which steady conditions apply. The behaviour of recirculation regions is described in the following discussion of WSS.

5.3.3: Wall Shear Stress – Steady Flow

The physiological significance of WSS, with regard to its role in the pathogenic processes of atherosclerotic plaque development and intimal hyperplasic growth, was identified and discussed in Chapter 1. Because of this significance, it was deemed essential to employ a method which could be used to quantify WSS. Since it cannot be measured directly, an estimate was made using velocity gradients at the wall and the power law relationship between shear stress and shear rate.

$$\tau = \kappa \dot{\gamma}^n \qquad \text{(Equation 23)}$$

The rheological quantities n, κ, η_0 and η_∞, for the Xanthan Gum solution under steady experimental conditions, were identified previously (see Table 7). If the shear rate at the wall is in the range where viscosity is governed by non-Newtonian behaviour ($\dot{\gamma}_{C0} < \dot{\gamma} < \dot{\gamma}_{C\infty}$), WSS is calculated using the values of n and κ given in Table 7. However, if $\dot{\gamma} < \dot{\gamma}_{C0}$, the Power-Law parameters assume the values n = 1 and $\kappa = \eta_0$. Similarly, if $\dot{\gamma} > \dot{\gamma}_{C\infty}$, n = 1 and $\kappa = \eta_\infty$.

Shear rate was derived using the assumption that the velocity gradient in the near wall region is linear. If the no slip condition at the wall is assumed, shear rate is determined using the following equation, where u_w is the component of local velocity parallel to the wall and δ is the perpendicular distance from the velocity vector to the wall.

$$\dot{\gamma} = \frac{u_w}{\delta} \qquad \text{(Equation 24)}$$

At this point it must be emphasized that this method provides no more than an approximation of the local WSS. The linear velocity gradient assumption can only be considered valid if δ is sufficiently small. For the most part therefore, velocity vectors which lay within 1mm of the wall were used. Assuming the velocity gradient in this region to be linear invariably introduces a degree of uncertainty in the WSS estimates. This uncertainty however, could not be quantified here, although an attempt to do so is made in Chapter 6. Perhaps a much greater source of uncertainty lay in the identification of the exact location of the wall when constructing the mask (see Chapter 4). There are two important factors to consider in this respect. The pixelated nature of the image from which the mask was derived meant resolution of the wall position in the image was limited to half a pixel (~±0.058mm or typically ±5.8% of δ). A much more significant, although less quantifiable, uncertainty is caused by the incorrect identification of the pixel which defines the wall position. Although extreme care was taken while conducting this task (it is assumed that, for the most part, the correct pixel was identified) human error was inevitably introduced. Given each pixel is typically 12% of δ (δ = 1mm), then defining the wall position incorrectly would result in a significant error in the value of δ and, by default, $\dot{\gamma}$ and WSS.

For comparison purposes, the WSS distributions were plotted without dimensions by dividing WSS by a quantity suitably representative of the flow. The process of dimensional analysis described in Chapter 2 suggested that dynamic pressure, calculated using the bulk flow velocity, should be used for this exercise. The axial position of the velocity vector used to calculate WSS was normalized using the (distal) diameter. These results are shown in Fig.34 for the 51% severity case and in Fig.35 for the 84% severity case. Estimates of WSS are shown for both the upper and lower surfaces of the geometry.

Consider the WSS distributions plotted in Fig.34 for 51% occlusive severity. The general shape for all Reynolds numbers investigated using this geometry is characterised by a number of common features. Initially, a near-constant value in the

straight proximal section of the tube is observed. This is indicative of fully developed, steady flow which results in a constant near-wall velocity gradient along the length of the domain. (It would be expected that, in a straight section of pipe where the flow is fully-developed, WSS would be constant. It is likely therefore that the variability in the data proximal to the occlusion in Fig.34 is the result of small-scale irregularities in the geometry.) As the flow approaches the occlusion, WSS falls marginally where the pipe diameter begins to decrease and the streamlines begin to converge towards the centreline. As the diameter continues to narrow, the flow is accelerated resulting in a rapid increase in WSS which rises to a peak at the point where the diameter reaches a minimum (see Chapter 1 for the physiological significance of elevated WSS). As the flow progresses and the diameter increases, WSS decreases due to deceleration of the flow. Separation occurs at some point in the expansion region. This is indicated here at the point where WSS assumes a negative value. The stagnation point which defines reattachment is represented here by the point where the WSS again crosses the horizontal axis. The near-wall region bound by these stagnation points is characterised by an area of recirculating fluid (see Fig.36). Fluid caught in this recirculation 'bubble' moves very slowly and is often trapped for long periods (see Chapter 1 for the physiological significance of long residence times in the near-wall region). As the flow progresses beyond the recirculation zone, WSS increases until a plateau is reached, at which point a steady fully developed flow condition is resumed.

An indication of the validity of these results is given by comparing the experimental values of WSS in the fully-developed region with the theoretical values which might be expected. The theoretical calculation of shear rate at the wall is derived through the differentiation of Equation 22 with respect to radius 'r'. The subsequent use of Equation 23 enables the calculation of the theoretical WSS in fully-developed flow. This process was conducted for all four flow conditions discussed above and shown in Fig.34. For $Re_{PL} = 74$, the theoretical value of dimensionless WSS proximal to the occlusion (in the fully-developed region) was calculated to be 0.14. This compares very favourably to the values shown graphically in Fig.34a, indicating that the magnitude of experimental WSS in this region is acceptable. Likewise, the theoretical value of dimensionless WSS proximal to the occlusion was calculated to be 0.059 for $Re_{PL} = 180$, 0.047 for $Re_{PL} = 235$ and 0.020 for $Re_{PL} = 617$. Referring

to Fig.34, these theoretical values of WSS compare favourably to the experimental values indicated. This process demonstrates that the experimental values of WSS in the fully developed region proximal to the occlusion are of an acceptable magnitude, hence providing a certain degree of validity to the experimental WSS results presented here.

Consider now the WSS distributions for 84% occlusive severity plotted in Fig.35. For the most part, the general shape can be described in the same way as in the 51% severity case. However, there are a number of important differences. Once again, the practice of time-averaging flow fields means that in those cases where instability was observed ($Re_{PL} \geq 180$), WSS distributions are only representative of the instantaneous condition. Referring to Fig.28, instability is observed only in the distal region, regardless of Reynolds number. The flow is shown to be highly stable upstream of the stenosis, in the vicinity of the occlusion and for approximately one diameter downstream of the throat. As a result, the distribution of WSS in these areas is highly representative of the instantaneous conditions. However, the unsteadiness observed further downstream of the occlusion ($x/d > 1$) means that the WSS in this region oscillates around the time-averaged value plotted here.

There are some important quantitative results which can be returned from these plots. Perhaps most significant in physiological terms is the behaviour of the WSS in the throat region, since it is here that it is observed to reach a maximum. Referring to Fig.37, the peak WSS is appreciably higher in the 84% severity case compared to the 51% case (typically by a factor of 2.6), due to the greater acceleration experienced by the flow in the more severe occlusion. The apparent inverse relationship observed in Fig.37 may, at first, be surprising, since greater flow rates would be expected to produce higher velocities and hence greater WSS. This is indeed the case, as would be apparent were the data to be plotted with units. However, the inverse relationship originates from the method used to convert WSS into dimensionless quantities. By dividing WSS (derived from the component of local velocity parallel to the wall) by the square of the mean velocity (in the form of dynamic pressure), it is the latter term which becomes dominant in the dimensionless expression for WSS. As a result, non-dimensional WSS is greatest at low Reynolds number flows where the flow is dominated by viscous forces.

The most prominent flow feature to be observed was the recirculation zone. The relationship between Reynolds number and the length of recirculation is shown in Fig.38 for both geometries used here. In both cases, the axial position of separation was observed to change very little across the range of Reynolds numbers measured. The position where the flow is observed to reattach to the wall, however, is shown to be highly dependent upon Reynolds number. In the 51% severity case, reattachment advances downstream with increasing Reynolds number. This is due to the increased momentum carried by the jet as Reynolds number increases, which results in it travelling further downstream before the dissipation of momentum forces the flow to reattach to the wall. It would be expected that this same principle would be applicable in the 84% severity case. However, due to the unsteadiness which is characteristic of flow in this geometry, the reattachment points shown in Fig.38 do not represent the limits of well-defined, stable structures of recirculating flow. Due to the considerable 'flickering' of the jet, they are instead merely indications of the mean positions at which the flow reattaches to the wall. The inherent unsteadiness of the flow means that this point will move considerably in both the axial direction and around the azimuth. The apparent tendency of this point to move towards the throat with increasing Reynolds number is a consequence of unsteadiness setting in earlier with increasing Reynolds number.

Of further interest is the clear dependence on Reynolds number of asymmetry. This was discussed earlier with respect to the asymmetry observed in the velocity profiles and is further supported by Fig.38. In this case, the difference in the measured length of recirculation on the two opposing walls is used as a measure of flow asymmetry. Fig.38 shows that, as Reynolds number is increased, asymmetry increases in both the 51% and 84% cases.

5.3.4: Summary – Steady Flow

A steady state experimental analysis of flow through model stenoses was conducted. The flow rates employed were representative of a waveform measured *in vivo*. Measurements were made in a two-dimensional cross-sectional plane through the model geometry using optical velocimetry. Velocity vector maps were used to generate velocity profiles and estimates of local WSS. Variance in the data was used

as an indication of the level of stability in the flow field.

Flow conditions were shown to be highly dependent upon both the flow rate (Reynolds number) and the severity of the occlusion. In the low severity (51%) geometry, the flow was observed to be highly stable at all Reynolds numbers. However, in the more occlusive geometry (S = 84%), instabilities were much more evident, leading to the flow becoming more asymmetric. This trend was also observed for increasing Reynolds number. Instabilities were manifested here as 'flickering' of the jet and the subsequent movement of shear layers and reattachment points which resulted in an increase in the normalized standard deviation of the local velocity field.

5.4: Unsteady Experiments – Biphasic Flow

Steady flow through model stenosis geometries was studied and discussed in Section 5.3 in order to assess the effects of Reynolds number and occlusive severity on the local flow field. However, the usefulness of that study is limited due to its unrealistic representation of the pulsatile nature of blood flow. To account for this pulsatility, the biphasic waveform, measured by Fisher et al[55] and shown in Fig.5, was scaled accordingly, using techniques detailed in Chapter 2. The defining parameters relating to the scaled waveform are shown in Table 4. The range of flow rates investigated in the steady state experiments reflect those observed in the biphasic waveform used in this section. The six positions, identified in Fig.5 and relating to those points in the flow cycle where flow data was to be recorded, were chosen to enable a clear picture of the changing flow conditions to be compiled. Experimentation was conducted using the same fluid and geometries as those which were used in the steady state investigations.

The following discussion describes a mixture of qualitative and quantitative results, presented for each of the characteristic positions in the biphasic waveform. Velocity vector maps provide a clear representation of the changing flow field, highlighting important features such as the acceleration of flow through the occlusion and areas of recirculation. Standard deviation maps illustrate the level of variation in the recorded data. They provide an indication of how repeatable the observed flow field is in

successive cycles while also highlighting the presence of shear layers and stagnation points. Velocity profile plots illustrate clearly the spatial distribution of axial velocity and the way it changes over the course of a cycle. The spatial distribution of wall shear stress (WSS), at key points in the waveform cycle, is also discussed, providing a clear picture of those areas which could be susceptible to arterial degradation.

5.4.1: Overview – Biphasic Flow

The flow field is visualised using velocity vector maps, similar to those presented earlier for steady flow. They were derived by averaging 100 individual velocity vector maps which were generated for each of the stated positions in the biphasic waveform and are presented here in Fig.39 and Fig.40 for the 51% and 84% severity cases respectively. They are averaged over the 100 cycles and can, therefore, only be considered representations of the instantaneous flow field at the given waveform position, particularly when that flow field is unsteady and varies between cycles. The velocity vectors were scaled, as indicated in the Figures, in order to make them easier to view and interpret. Their value here is mainly qualitative, since they provide the reader with a picture of the changing flow conditions, without actually presenting numerical quantities related to the flow.

Consider the velocity vector maps shown in Fig.39 for the 51% stenosis case. In general, the flow field becomes increasingly dominated by the central jet during the systolic phase of the cycle. During systolic acceleration (see Fig.39a), the flow is driven by an increasingly positive pressure gradient which flattens the axial velocity distribution in the radial plane. In Fig.39b, the flow rate peaks and is momentarily steady, neither increasing nor decreasing. The resultant velocity vector field closely resembles that of a steady flow rate condition (compare with Fig.24). During systolic deceleration (Fig.39c), momentum is retained by the core flow region, even though net flow rate is decreased, causing vortices to form near the wall. Since the faster moving fluid in the central core takes longer to slow down, the slower moving fluid near the wall is drawn into recirculation to replace it, leading to a phase lag between the core and the near-wall regions. The result is a progressive lengthening of recirculation (see Fig.39a-c). When the flow rate is reduced to zero in Fig.39d, these features still remain and a complex flow field is observed, characterised by

highly recirculating flow. At peak diastole (see Fig.39e), these complexities are washed out of the domain (in the proximal direction), resulting in a relatively stable flow field. At the end of diastole (see Fig.39f), the residual momentum in the core (this time having been generated during diastole) again leads to a phase lag between the core and the near-wall regions resulting in a similar flow field (although reversed) to that observed at the end of systolic deceleration (Fig.39d).

The consistency in the recorded data is illustrated by the normalized standard deviation plots shown in Fig.41 and Fig.42 for the 51% and 84% severity cases respectively. Indirectly, these indicate the level of 'stability' present in the transient flow field (i.e. the consistency between the 100 individual velocity vector maps). An illustration of the level of repeatability in successive cycles is given in Fig.43. These velocity vector maps (shown for both the 51% and 84% severity geometries) are a sample of the 100 which were used to produce the mean velocity vector maps shown in Fig.39&40. They confirm that flow in the 51% severity geometry is much more stable and repeatable than that in the 84% case.

Referring to the standard deviation plots in Fig.41, the flow-fields measured at each position in the waveform are shown to be highly repeatable from one cycle to the next throughout the duration of the cycle. The variability in velocity data is shown to be greatest in the shear layers and around the stagnation points. As discussed previously, this is due partly to the very low local mean velocities in these areas which, when used to normalize the local standard deviation, yield large values. Any small deviation from the mean local velocity is therefore magnified in a normalized plot such as this. These plots confirm the tendency of recirculating flow to advance downstream during systole and also the development of complex flow fields at the end of systole (d) and diastole (f). However, since consistency in the data is generally high, it can be assumed that the velocity vector maps shown in Fig.39 are very good representations of the flow field at each of the specified positions in the cycle.

Consider now the velocity vector maps in Fig.40, produced for the 84% severity case. There are a number of issues relating to plausibility that need to be addressed; the most noticeable regarding that of continuity. Since an incompressible fluid was

used in the experiments, the continuity law (which states that the flow rate through all three-dimensional cross-sectional planes be equal), must be obeyed. The data presented here may, in some instances, appear to disobey this law. In those regions where the flow deviates significantly from the illuminated plane (for example, where the jet first reattaches to the wall elsewhere in the tube), discontinuities may occur naturally. However, there are discrepancies (particularly in Fig.40a), the extent of which cannot be explained by such phenomena. Referring to those planes with axial locations -40mm and +20mm in Fig.40a (0mm is defined as being at the throat of the occlusion), continuity is clearly not obeyed; it cannot reasonably be argued that three-dimensional flow is the source of such a large discrepancy in the flow rate across the observed two-dimensional plane.

Further evidence of the erroneous nature of the flow in Fig.40a is provided in the normalized standard deviation plot (see Fig.42a), where the level of variance in the velocity vector field is clearly unacceptable. As discussed previously, a certain amount of variance is expected, particularly in the vicinity of shear layers and stagnation points. However, consistency is expected to be very high around the throat of the occlusion. Acceleration of the flow in the contraction region forces the flow to become highly two-dimensional, increasing the consistency in the local flow field. This is clearly not the case in Fig.42a. Having identified the results in Fig.40a as being unreliable, it was decided that all related data would subsequently be omitted from discussion.

In contrast, there are much greater levels of repeatability observed in the throat region in Fig.42b,c&e. The relatively high levels of variance observed at the throat in d) and f) are due to the zero (or near zero) net flow rates recorded at these time instants. Similarly, the high levels of variance observed around the shear layers and stagnation points can, in part, be attributed to the low local velocities. In addition, unsteady phenomena, such as shear layers and stagnation points, naturally show significant movement in successive cycles. It is reasoned that the relatively high levels of variance observed in Fig.42b, approximately two diameters downstream of the throat in the centre of the pipe, is the result of flow being accelerated to very high velocities at this point in the cycle which leads to unsteadiness distal to the occlusion.

The main conclusion to draw from the above concerns (regarding the 84% severity geometry) is that there is great deal of unsteadiness and unpredictability in the flow. However, there are certain features which can be described in a specific manner. During systole, flow is dominated by the core region in the vicinity of the throat, especially so for approximately one and a half diameters downstream. Instability in the shear layers initiates unsteadiness and highly three-dimensional flow patterns, manifested here by the high levels of variance in the recorded data and by issues relating to continuity. Diastolic acceleration washes away these features initially. At peak diastole, the flow field resembles those which were observed in the low-Reynolds number steady flow rate experiments described previously (see Fig.25a). As was observed in the 51% severity case, residual momentum in the core region accounts for the phase lag between the core and the near-wall regions. In order to maintain continuity and balance the residual momentum in the core, 'jetting' of the flow in the opposite direction was observed near the wall.

5.4.2: Velocity Profiles – Biphasic Flow

Velocity profiles were plotted in order to visualise the distribution of axial velocity, in both the radial and axial directions, and how it changes over the course of the waveform cycle. These profiles are shown in Figs.44&45 for the 51% and 84% occlusive severity geometries respectively. Profiles were plotted approximately every half diameter. The normalized scaling of axial velocities was achieved in this instance through the use of the cycle mean velocities, $\overline{U}_C$. Further scaling was applied to allow easier interpretation of the results. Due to the cyclic nature of the applied flow rate, these scaling factors varied (see Figures for details).

Consider the velocity profiles for the 51% severity case in Fig.44. Because of the high degree of consistency between the 100 separate measurements, these profiles are a very good representation of the flow conditions that exist at the points in the cycle indicated. The first point to make is to confirm the earlier observation that systolic flow is dominated by core flow and that it becomes increasingly so as the systolic phase progresses. The blunt profiles observed in Fig.44a are caused by the increasing pressure gradient, which prevents the flow from becoming fully-developed and forces it to move in a more uniform, bulk manner. At peak systolic

flow (see Fig.44b), the flow rate is momentarily constant and the profiles are more characteristic of fully-developed steady flow rate conditions (compare with Fig.30). Acceleration of flow through the occlusion induces a jet surrounded by regions of recirculation. During systolic deceleration, (see Fig.44c) the flow field becomes increasingly dominated by this jet, since the residual momentum carried by it is balanced by recirculating flow near the wall. Progressive lengthening of the recirculation regions during systole is indicated here by the advancement downstream of negative flow near the wall. As flow rate is reduced to zero (see Fig.44d), there is still evidence of this structure remaining, with near-wall regions experiencing strong reverse flow in comparison to the more positive axial velocities found in the centre of the tube. The highly complex flow-field observed in Fig.44d is therefore the exaggerated product of those features created during the systolic phase. Although the net flow rate is zero, these complexities mean that relatively high local velocities are observed throughout the domain. As the cycle progresses (see Fig.44e), diastolic acceleration reduces the complexities in d), although the general features observed previously (characterised by more positive axial velocities in the centre of the domain) are still evident. Deceleration of the flow towards a net flow rate of zero (see Fig.44f) resulted in a marked reduction in velocity (particularly in the centre of the pipe) and in the overall flow complexity. It is assumed that, for the remainder of the cycle, the flow can be represented by the conditions observed in Fig.44f, perhaps with even weaker features due to the natural dissipation of energy which would occur when the applied flow rate is zero.

Although points d) and f) are assumed to represent conditions at which the net flow rate is zero, this does not appear to be the case. This is particularly noticeable at the throat of the occlusion. The most likely explanation for this is that data was recorded at an instant fractionally too late in the cycle. This proved to be very difficult to avoid, due to the inherent difficulty in recording data at an instant in time, especially when the waveform is discretized. On reflection, it would have been more appropriate to delay the point at which data for point f) was recorded to reduce the possibility of inaccurately timing its acquisition. Another possible reason for the apparent non-zero flow rate is that the elastic properties of the fluid resulted in a recoil action. This is a likely explanation of the positive net flow rate observed at point f), since there was no positive flow rate applied beyond this point.

Consider now the velocity profiles in Fig.45 for the 84% severity case. Referring to Fig.45a-c in particular, there are concerns regarding continuity in some areas (particularly around two diameters distal to the throat). As discussed previously, the results relating to point a) were shown to be sufficiently unreliable such that they be omitted from further discussion. During systole, the flow is dominated by a rapid acceleration through the throat which induces strong recirculation features and very high gradients of velocity. Rapid deceleration of the flow and the subsequent dissipation of momentum in the distal region make the flow highly unstable, resulting in high levels of variance (see Fig.42b&c). The three-dimensional nature of the flow under these circumstances may be responsible for the apparent lack of continuity in some areas. This lack of continuity is confirmed by the approximate calculation of flow rate (in the observed two-dimensional plane) using Simpson's Rule[98]. For the 84% severity geometry at peak systole (Fig.45b), the two dimensional flow rate two diameters distal to the throat is shown to be only ~10% that at the throat. Similarly, at the mid-point in systolic deceleration (Fig.45c), the flow rate two diameters distal to the throat is ~25% that at the throat. Towards the end of the domain however, continuity is at least partially recovered in both cases; at 3.5 diameters downstream of the throat, flow rate was increased to ~40% that at the throat for both flow conditions. This partial recovery in two-dimensional continuity towards the end of the domain, and the reduced variance shown in Fig.42b&c in the same region, indicates that the flow structure becomes much less three-dimensional further downstream, tending towards a more stable condition.

Contrary to what might be expected, the complexities observed in Fig.44d do not, at first, appear to be replicated in Fig.45d, at least not to the same extent. This may be due to the unsteadiness in the latter case which would lead to these complexities being averaged and hence smoothed out. This is supported by Fig.42d, which indicates significant variance in the data throughout the domain, rather than being concentrated in shear regions as in Fig.41d. During diastole (see Fig.45e), the profiles resemble those more characteristic of steady flow rate conditions (compare with Fig.31). This is maintained throughout diastole until the zero flow rate condition is achieved (see Fig.45f). This is supported by Fig.42e&f which show variance only in those areas where low velocities intensify the normalized standard

deviation. It is expected that for the remainder of the cycle, the flow-field will be much the same as that depicted in Fig.45f due to the absence of any driving flow rate.

5.4.3: Wall Shear Stress – Biphasic Flow

As highlighted previously, WSS has been shown to be a key parameter in physiological terms, due to its role in the pathogenic process of atherosclerotic plaque development and intimal hyperplasic growth. A method was proposed in Section 5.3.3 which provided the means by which an estimate of WSS could be made. Details of this technique were discussed previously, as were its limitations. The same method was used again here, the only difference being the way in which the data is presented. Normalization of WSS was achieved using the dynamic pressure (see Chapter 2) which, in this instance, was calculated using the mean cycle velocities.

Consider the WSS distributions plotted in Figs.46&47 for the 51% and 84% severity geometries respectively. Estimates of WSS are shown for both the upper and lower surfaces of the geometry. For comparative purposes, the distributions recorded at each of the time intervals on the waveform are displayed together. (Note that WSS conditions relating to the mid-point in systolic acceleration are not plotted for the 84% case because of the previously-discussed reliability issues regarding this data.) In general, the behaviour in both cases can be summarised in a similar fashion to that which was described previously for the steady flow experiments. The way in which WSS is shown to change during the cycle however, is clearly unique to the time-dependent waveform used. All these aspects are discussed here, beginning with those common to both geometries.

At any given point in the cycle, WSS is shown to peak at the throat. The reduced cross-sectional area results in acceleration of the flow and hence high local velocity gradients. Clearly, the more severe the reduction in area, the more acceleration the flow experiences and hence the much greater WSS shown in Fig.47 compared to Fig.46. In addition to the elevation of velocity gradients in this region, WSS is also increased in areas which experience shear rates greater than $\dot{\gamma}_{C\infty}$ (the critical value

above which viscosity is Newtonian, η_∞) due to the use of Newtonian parameters, instead of Power-Law parameters, in the calculation of WSS. The consequence of using Newtonian parameters under such conditions is that the fluid is more viscous compared to what would be the case were Power-Law parameters to be used. These conditions were observed at peak systole in the 84% severity occlusion (see Fig.47).

As expected, WSS was shown to vary considerably through time; the throat in particular experienced very large fluctuations in WSS, the maximum WSS being recorded at peak flow rate. The considerably higher range of WSS observed in Fig.47 during the cycle was again due to the much greater reduction in area at the throat.

Very low WSS was recorded along the length of the vessel during the last two-thirds of the cycle, while zero (or near-zero) WSS conditions could be expected throughout the domain during the last third of the cycle, when the applied net flow rate was zero. In Fig.46, very low WSS were also recorded throughout the cycle in the region approximately one diameter downstream of the end of the expansion zone. These observations could have physiological implications, regarding the tendency of particulates to adhere to the wall and of hyperplasic growth to develop (see Chapter 1).

Observations unique to the 51% severity case (see Fig.46) include a steady WSS in the region proximal to the stenosis and a small decrease in WSS just prior to the beginning of the contraction zone. It is expected that these characteristics would be replicated in the 84% stenosis case; they could not be observed here because no straight entry length was present in the featured domain due to the desire to concentrate on the flow distal to the occlusion.

Referring to Fig.46, there is a marked difference in WSS at the first and third cycle positions. Although this may have been partly the result of a difference in flow rate (the waveform suggests it should be equal at these time instants, although this could not be guaranteed), the velocity profiles (see Fig.44a&c) certainly indicate that it is largely the result of a difference in the structure of the flow. The profiles in the

vicinity of the throat in Fig.44a (when flow is dominated by a positive, driving pressure gradient) are clearly less pointed than those in Fig.44c (when flow is dominated by residual momentum in the core region). This results in higher shear rates near the wall during acceleration and hence higher WSS.

Despite these similarities, the level of stability present in the flow has been shown to be highly dependent upon which geometry is considered. As discussed earlier, flow in the 51% severity case was shown to be highly stable, both throughout the cycle and between successive cycles; the WSS distributions (see Fig.46) are therefore considered highly representative of those which can be expected in successive cycles. By comparison, unsteadiness was shown to occur distal to the throat in the 84% severity case, particularly in systolic flow. As a result, the WSS distributions, relating to this part of the cycle and in this region, can be regarded only as mean values; instantaneous values will oscillate around the mean value indicated here.

In the 51% severity occlusion, Fig.46 clearly indicates the lengthening of recirculation during the initial stages of the cycle. This continues during systole until recirculation is experienced in the entire distal section of the domain studied. During systolic acceleration, this occurs due to the increasing pressure gradient. During systolic deceleration, the residual momentum in the core causes the lengthening of near-wall recirculation. By comparison, the mean reattachment point observed in the 84% severity occlusion is shown to migrate towards the throat during deceleration due to increasing unsteadiness.

5.4.4: Summary – Biphasic Flow

A biphasic waveform, representative of that found *in vivo* and scaled accordingly for use *in vitro*, has been used in an experimental study of flow through model stenoses. Analysis of a two-dimensional cross-section of the flow yielded velocity field data from which velocity profiles were generated and estimates of local WSS were made. Variance in the data was used as an indication of the level of repeatability in the flow field in successive cycles.

Flow conditions were shown to be highly dependent upon both the severity of the occlusion and the pulsatile nature of the biphasic waveform. In addition to

intensifying characteristics such as local WSS, highly constricted geometries induce more unsteadiness and flow which is more three-dimensional. The result is a mean flow field which does not represent accurately that which exists at any given instant. However, it is reasonable to consider the mean conditions in a study of this kind, since it is their effects over time which are of interest in relation to physiological concerns. By comparison, less severe constrictions exhibited flow which is remarkably stable, even during peak flow rate conditions. The result is a highly repeatable flow pattern, in both a spatial and temporal sense.

5.5: Summary – Experimental Results

An experimental analysis of cardiovascular flow was conducted using simplified large-scale model geometries representative of typical stenoses found *in vivo*. An aqueous Xanthan Gum polymer solution was employed as a test fluid in which seeding particles were suspended. Particle imaging apparatus generated two-dimensional velocity vector maps, recorded in the centre plane of the test section. This data was used to study the effects of the occlusion on the local flow field, in particular those which affect conditions at the wall. Both steady and pulsatile flow rate conditions, representative of those recorded *in vivo* and scaled using dimensional analysis, were investigated, the results of which have been described in this chapter.

The local flow field was shown to be highly dependent upon both the flow rate conditions and the severity of the occlusion encountered. The most significant observation was that of a highly coupled relationship between occlusive severity and flow stability. In the geometry where the reduction in pipe diameter was low, consistent, stable and mostly two-dimensional flow fields were observed throughout the range of Reynolds numbers investigated, including for the duration of the biphasic waveform. Small scale instabilities, however, were observed in this geometry. In steady flow rate conditions, instabilities caused the jet, shear layers and stagnation points to 'flicker' and move around the azimuth; a tendency observed to increase with Reynolds number. Although very different flow structures were generated in the biphasic waveform experiments, similar behaviour was observed in successive cycles at each of the pre-determined points in the waveform. These instabilities were manifested here as a decrease in the level of consistency in the flow

field recorded over time.

This relative stability was not reproduced in the highly constricted geometry. In steady flow rate experiments, stability was only observed downstream of the occlusion at the lowest Reynolds number investigated. At all other Reynolds numbers, significant time-dependent flow conditions were observed which resulted in highly three-dimensional flow and unsteadiness. In the biphasic waveform experiments, stability was observed for the duration of the cycle upstream of the occlusion and, at some low Reynolds number conditions, throughout the domain. However, considerable unsteadiness was observed downstream of the constriction during systole in particular.

WSS was shown to be highly dependent on Reynolds number, the waveform cycle and the local domain geometry. Generally, WSS increased throughout the domain with increasing Reynolds number. It was observed to peak at the throat of the occlusion, its magnitude increased with the severity of the occlusion due to the accelerating effects of reducing the pipe diameter.

6: COMPUTATIONAL FLUID DYNAMICS

This chapter provides a detailed discussion of the numerical methods employed to simulate fluid flow in occluded pipes. The results generated from the analysis using fluid models representative of the Xanthan Gum solution used in the experiments are presented and compared against the experimentally-observed flow conditions described in Chapter 5. An assessment is made regarding the suitability of using such numerical techniques to model both steady and pulsatile non-Newtonian fluid flow in pipes that contain a contraction-expansion. Extending the study further, the numerical models developed are then used to simulate blood flow through life-scale occluded pipes to represent stenosed arteries. This is done using two different fluid models to represent the viscous behaviour of blood; one based on the Power-Law approximation described in Chapter 3 and another using the assumption that blood behaves as a Newtonian fluid. An assessment is then made regarding the suitability of using this Newtonian approximation for blood in haemodynamic studies. A discussion regarding the physiological implications of the resulting wall shear stress (WSS) distributions is also presented.

6.1: Introduction

Computational Fluid Dynamics (CFD) refers to the numerical solution of the governing equations which describe fluid flow. These equations, referred to as the Navier-Stokes equations (see Appendix B), are solved using computational methods to simulate fluid flow from which quantitative predictions of important flow parameters can be obtained.

CFD was used in this project to assess the suitability of using numerical techniques in the study of blood flow in complex geometries such as arterial stenoses. The potential benefits beyond the scope of this project, should its use be validated, are enormous. On an individual basis, non-invasive three-dimensional mapping of localized parts of the cardiovascular tree is currently possible using a technique called angiography. The data collected in an angiogram could potentially be used to build a three-dimensional model of a diseased vessel through which the patient's

own conditions of blood flow could be tested numerically using CFD. An assessment could then be made to determine the level of risk to the patient, with regard to acute life-threatening events (see Chapter 1), and to enable effective preventative treatment to be administered to reduce associated health risks.

Although computing power and the associated computing time may inhibit mass exploitation of this technique at present, it is not unreasonable to expect such practices to become commonplace in the future, as computing power increases and the availability of CFD packages becomes more widespread. To ensure such a technique is robust and reliable however, the validity of its use needs first to be established.

A typical CFD software package consists of a geometry and grid generation programme (in this case, Gambit©) and software which solves the Navier-Stokes equations and allows the subsequent analysis of results (in this case Fluent©). In the geometry/grid generator, a virtual three-dimensional model of the bounded domain, through which fluid flow is to be investigated, is generated in the form of a mesh. This mesh consists of many finite volume blocks called cells. The model is then exported to the flow equation solver where boundary conditions and known fluid properties and flow characteristics are defined. The Navier-Stokes equations are then solved in an iterative process for each of the cells, starting at the inlet boundary and sweeping through the domain. Iteration is continued until the solutions to each equation in every cell are within predetermined tolerance values (10^{-3} for the continuity and momentum equations), at which point convergence is achieved.

In order to ensure the results obtained were not affected by the nature of the computational grid being used, a guarantee of grid independence was required. Due to the finite volume approach employed by such computations, all results obtained through CFD simulations are inevitably approximations. The true mathematical solutions could theoretically be obtained by employing an infinite number of elements whose sizes were reduced to zero. By definition, this is not possible in this type of finite simulation and so an acceptable approximation of the solution was sought for each flow condition. Firstly, a coarse grid was generated and used, with the relevant steady flow rate conditions, to find an approximate solution. The grid

was then refined, based on this initial solution, using a technique known as gradient adaption, where the velocity gradient between adjacent cells is calculated. Cells which experienced a velocity gradient exceeding a user-defined maximum were halved in size, resulting in a finer mesh in regions of high shear rate. Further computation of the solution was then conducted and the resulting flow solution compared with that of the previous solution, obtained with the coarser grid. This process was repeated until solutions obtained from successively refined grids were judged to be negligibly different to each other. The solution is then considered to be independent of the grid.

This procedure, for determining the grid structure necessary to generate a solution independent of the grid, is only wholly suitable for steady flow conditions. In time-dependent solutions, the flow conditions change with respect to time. This was simulated by dividing the time period of the waveform into discrete time steps, the solutions to which were solved iteratively using the same process as that used in the steady cases. Since the solutions for unsteady flows are time-dependent, the grid structure would ideally be adapted and refined for each time step. This was not possible however since only one grid structure can be used at a time in the computational process. For this reason, a steady flow condition characteristic of the unsteady regime in question was simulated, and adaption performed, until grid independence was achieved. The steady condition employed was that which corresponded to the mean flow rate of the time-dependent waveform. This grid was then used in the relevant time-dependent simulation.

In order to ensure the solutions governed by time-dependent flow rates were unaffected by initiation of the solution, the computation of several time periods was performed. It was found that the results became unaffected by initiation of the solution after approximately one quarter of a cycle. The results presented in this chapter are therefore those which were recorded in the second cycle. (Note that each biphasic cycle required approximately 3-4 weeks of computing time. For steady-state simulations, convergence to a final grid-independent solution required approximately 1 week of computing time. These time scales illustrate how computing time limits the number of simulations which can be performed, particularly those which use the time-dependent biphasic waveform.)

6.2: Definition of Conditions

Due to the very large and adaptable nature of FLUENT©, practice was required to ensure the correct flow variables and computational method settings were used. Control settings determine which solution methods are employed and the order of accuracy to which the Navier-Stokes equations are solved. In all simulations conducted in this study, the flow was defined as laminar. The lack of an algorithm which could account for the structure of turbulence in a turbulent flow using a non-Newtonian fluid meant that using any of the available turbulence models could not be relied upon to produce physically-meaningful results. Unless otherwise stated, all Navier-Stokes equations were solved to second order accuracy.

Computational models of both the geometries used in the experimental analysis (see Chapter 4 for geometry definitions) were constructed for use in the numerical analysis. There are several factors that were considered with regard to how this would be done. These include the difficulties associated with mapping the internal surface of a tube in three dimensions, particularly one with small-scale irregularities. To construct models based on these three-dimensional maps would produce grid structures too large and complicated to allow efficient computation, and a comprehensive analysis, to be made. It was decided therefore that slightly simplified representations of the experimental models would be constructed, based on the defining characteristics of the geometry in question (i.e. the manufacturing irregularities were overlooked). These include the mean proximal diameter, the diameter at the throat of the occlusion, the offset distance between the centreline of the throat and the unrestricted pipe, the mean distal diameter and the rate of change of diameter in the occlusion. The contraction-expansion sections were defined in the same way as was done so for the geometries used in the experimental analysis (see Fig.19). An entry length of approximately fifty diameters was considered sufficient to allow the flow in the vicinity of the occlusion to be influenced solely by the reduction in area, rather than boundary conditions at the inlet of the domain. Similarly, an exit length of twenty diameters was considered sufficient to allow flow conditions downstream of the occlusion to be modelled adequately. Referring to Fig.48, the numerical models constructed were considered acceptable representations of the geometries used in the experimental analysis. (These computational models were constructed using the same scale as in the experimental case but could be scaled

according to requirements.) For the 51% severity geometry, the coarse un-refined grid structure consisted of 673335 cells. Following the adaptation procedures required for grid independence to be achieved, the number of cells was increased to between 815988 and 902788, depending on the flow conditions under consideration. For the 84% severity geometry, the coarse un-refined grid structure consisted of 667008 cells. Adaption increased this to between 740599 and 818670.

The non-Newtonian fluid model used in the numerical simulations is a modified version of the Power-Law model, limited at the shear rate extremes by both high- and low-shear plateaux. The variation of viscosity with shear rate, as quantified by this model, was shown previously in Fig.8 (steady-shear) and Fig.9 (oscillatory-shear) for both blood and the Xanthan Gum solution used in the experimental analysis. The defining parameters of both these non-Newtonian fluid models and of the Newtonian approximation for blood used in the numerical analysis presented in this chapter are shown in Table 5.

Both steady and time-dependent flow rate conditions were investigated here. The biphasic waveform (see Fig.5) was used for the latter case, while flow rates characteristic of this waveform (see Table 8) were used in the simulation of steady flow.

6.3: Validation of CFD

The principal purpose of conducting the analysis described in Section 5 was to obtain experimental data against which numerical results could be compared. The validity of using CFD as an effective tool for modelling flows of this nature could then be assessed. This was done primarily by comparing the WSS distributions and velocity profiles obtained experimentally with those done so here using CFD. This section describes the results obtained using the numerical techniques outlined previously and an evaluation of the suitability of using CFD in further related work.

The geometries used in this exercise were the experimental (*in vitro*) scale models described in Section 6.2. The non-Newtonian fluid model was defined using the

appropriate parameters relating to Xanthan Gum. These varied depending on whether the flow under consideration was steady or pulsatile (see Table 5). Appropriate flow rates and waveforms were used to replicate the various conditions observed in the experimental analysis.

In the interests of clarity, the results obtained using steady flow rates are discussed first, followed by those which represent biphasic flow.

6.3.1: Steady Flow

The steady flow experiments described in Section 5.3 were reproduced here using numerical techniques. Flow conditions were defined using the same Reynolds numbers as those used in the experimental analysis (see Table 8) and a fluid model representative of the Xanthan Gum solution, under steady flow rate conditions (see Table 5).

An initial assessment of steady flow in a straight, circular section of pipe was conducted in order to help verify the methods and settings to be used. This was done by comparing the velocity profiles in an area where the flow was considered to be fully-developed, with the theoretical velocity profile for laminar flow of a non-Newtonian fluid described by Equation 22 (see Section 5.3.2). This assessment was conducted using the Reynolds numbers identified, and the model geometries described, in Section 6.2. Under steady flow rate conditions, the fluid model was defined using a Power-Law index value of n = 0.61. Under these conditions, the long entry length (~fifty diameters) allowed sufficient room for the flow to become fully-developed. This was confirmed by analysis which showed no discernable difference (centreline velocities were the same to within 1%) between the axial velocity profiles measured 40 diameters downstream of the inlet plane and those measured 45 diameters from the inlet plane. Further supporting evidence that an entry length of 50d is sufficient to ensure the flow becomes fully-developed is provided by the relationship which governs the entry length of Newtonian fluid flow[99]:

$$\frac{L_e}{d} \approx 0.06\,\mathrm{Re}_N \qquad \text{(Equation 25)}$$

Although this cannot be applied exactly to non-Newtonian flows, it can however be regarded as a suitable guide. For the highest Reynolds number case used here (Re_{PL} = 617), the above equation suggests an entry length of ~38d is sufficient for fully-developed flow to be realised. (Likewise, for the maximum Newtonian Reynolds number that is to be used in this study (Re_N = 644), the required entry length is ~39d.)

Consider the velocity profile plot shown in Fig.49. This data was recorded 40 diameters downstream from the inlet plane and approximately 10 diameters upstream from the occlusion. For comparative purposes, velocities were normalized using the bulk flow velocity, while radial positions were normalized using the pipe radius. There is clearly strong agreement between the numerical results and the theoretical profile, defined using Equation 22. Although just one example is shown here (S = 51%, Re_{PL} = 235), this level of agreement was observed in each geometry and over the whole range of Reynolds numbers used; the percentage difference between the centreline velocities was typically less than 1%. This quick assessment confirms the correct use of control settings and the ability of the numerical model to recreate fully-developed laminar flow in a straight section of a cylindrical pipe.

Extending this analysis further to include flow conditions affected by the reduction in pipe diameter, the following discussion compares the numerical results in the vicinity of the occlusion with those obtained experimentally.

51% Severity – Steady Flow

Consider the velocity profiles plotted in Fig.50 for the 51% severity geometry. The data was plotted using the same format as was used to present the equivalent experimental data. In order to effectively compare numerical results with those obtained experimentally, both sets of data are presented here together. The most significant observation to make is that agreement between the two data sets is generally favourable, both across the full range of Reynolds numbers investigated and throughout the domain. Proximal to the stenosis, the profiles assume the fully-developed, laminar conditions observed experimentally, while the acceleration of

flow in the throat region is shown to flatten the profiles. Similarly, the extent to which these profiles are flattened is also shown to increase with Reynolds number. The momentum increase generated by the acceleration in the throat is carried downstream, resulting in a jet of fluid which separates from the wall near the throat and reattaches at some point further downstream; the length of the enclosed recirculating flow is again found to be dependent upon Reynolds number. Beyond reattachment, the flow again begins to revert back to the full-developed, laminar conditions that exist proximal to the stenosis. Overall, the numerical techniques employed here are shown to be capable of modelling these characteristics.

The only cause for concern is the apparent discrepancy between the two data sets in Fig.50d. Although these differences are not large, they do appear to get progressively worse towards the end of the domain, particularly in relation to continuity. The asymmetry in the experimental results (also evident in the numerical results, albeit to a lesser extent) indicates that the jet is 'skewed'. There is therefore a likelihood that, should the jet have skewed towards the wall at some azimuth position not in the observed two-dimensional plane, continuity may not have been maintained in this plane (although if the whole three-dimensional domain were considered, continuity would be observed). It may be reasonable, therefore, to assume the numerical results are more accurate than would appear so initially. This is supported by the considerably better agreement observed further upstream. However, referring to the full range of Reynolds numbers investigated, there does seem to be a slight deterioration in agreement between experimental and numerical results with increasing Reynolds number. This would appear to be indicative of the dependence on Reynolds number of the magnitude of instabilities in the flow (there is evidence of this in the normalized standard deviation plots shown in Fig.27). These differences were not however, thought significant enough to warrant any major concerns regarding the ability of CFD to effectively model the experimental velocity distributions in this geometry.

Consider now the WSS distributions shown in Fig.51 for the 51% severity geometry. For comparative purposes, the numerical results are again plotted with the corresponding experimental results for both the upper and lower surfaces of the

geometry. The most significant observation to make is that, overall, the numerical model predicts the general shape of the distribution very well. WSS conditions in the recirculation region appear to be predicted satisfactorily, both in terms of its magnitude and the relationship between Reynolds number and the recirculation length (see Fig.52), as do conditions further downstream. Numerical predictions of WSS conditions upstream of the occlusion are also considered acceptable. The data appears to differ noticeably only at the throat where the numerical model appears to consistently over-predict WSS (see also Fig.53). There are likely to be a number of reasons for this. Firstly, the way in which the numerical model was constructed meant that the small-scale irregularities present in the experimental model were not reproduced numerically. As a result, the numerical values of WSS given here can therefore not be regarded as being truly accurate representations of the experimentally-obtained WSS values. In addition to this, it has been shown that the WSS values derived from experimental data includes a considerable level of uncertainty (see Section 5.3.3). The exact location of the wall was found to be particularly difficult to determine in the occlusive region, leading to an error in the calculation of the normal distance between the velocity vector and the wall which, in turn, results in an error in the calculated value of WSS.

However, it is likely that these factors are only partly responsible for the discrepancy observed in the peak WSS values shown in Fig.51; the most significant cause results from the inaccuracy of the linear velocity gradient assumption used to calculate experimental WSS from the near-wall velocity vector. Given the considerable flattening of the velocity profile in the throat region, caused by acceleration of the flow, it is likely that the velocity vector used to calculate experimental WSS in this region was not close enough to the wall for the linear velocity gradient to be wholly accurate. The required compromise between the resolution and range of velocities which could be measured using PIV meant that velocities could not be resolved as close to the wall in the experimental case as could be done so numerically. The idea that PIV-derived estimates of WSS were seriously affected by the inaccurate assumption of a linear velocity gradient (between the wall and the velocity vector used to calculate wall shear rate) is supported by the data coloured green in Fig.53. This data was obtained using the same CFD files that were used to calculate the WSS

values coloured blue in both Fig.51&53. For the data coloured green in Fig.53 however, shear rates were calculated using velocity vectors located at the same spacial positions as those velocity vectors used in the calculation of PIV-derived WSS. Referring to Fig.53, there are a number of points worth noting. Firstly, the linear velocity gradient assumption, used in the PIV-derived estimation of WSS, is inadequate since it yields a shear rate – and by default, a WSS - value that is too small. Most importantly however, the flow in the throat region is modelled much better numerically than is initially apparent and, consequently, CFD is a far more effective tool than PIV for modelling the WSS distributions required of this study.

84% Severity – Steady Flow

Consider the velocity profiles plotted in Fig.54 for the 84% severity geometry. Again, the numerical results are plotted together with the experimental data to enable an effective comparison to be made. In the lowest Reynolds number condition (Fig.54a), the numerical procedure is shown to be particularly capable at reproducing the velocity profile distribution observed experimentally. Numerical analysis correctly simulates all the major features of the flow; the acceleration of flow through the occlusion, its separation in the expansion zone and the stable regions of recirculation distal to the occlusion.

By comparison, Fig.54b-d suggests that, at higher Reynolds numbers ($Re_{PL} > 180$), CFD is much less capable of reproducing the profiles generated by the time-averaged experimental results. This is not the case throughout the whole domain however. Proximal to the occlusion, where the flow was shown previously to be fully developed (see Fig.49), the agreement is especially good. Acceleration of the flow through the contraction part of the occlusion, and the resulting flattening of velocity profiles, is also clearly adequately modelled numerically. As the pipe diameter increases, and the flow decelerates, agreement between the two data sets is initially satisfactory, although the tendency of CFD to 'skew' the jet away from symmetry quickly becomes apparent. This is manifested here in the off-centre peak in axial velocity and the distinct asymmetry in the cross-sections of recirculating flow. These characteristics do not appear in the experimentally produced velocity profiles. There

are a number of issues that this raises. The way in which experimental results are presented ensures that any unsteadiness in the flow field (Fig.28 indicates there is substantial variation at Re_{PL} > 180) is averaged out over time. The highly asymmetrical patterns suggested here by CFD may therefore be more representative of an instantaneous flow field than might initially be apparent. There are however limitations as to how reliable these numerical results are. Defining the flow as being steady forces the numerical solver to generate a time-independent solution, suppressing any transient tendencies such as those observed distal to the occlusion in Fig.28b-d. In fact, the difficulty with which convergence was achieved under these conditions (less accurate solution methods were required in order to make the solutions converge) indicates an inherent unsteadiness in the flow field. Although unsteady simulations were conducted, the time-dependent solutions produced did not show the amount of transient behaviour observed experimentally. The reason for this may require further investigation, although it is worth noting that, in both the steady and the unsteady simulations, the flow field in the immediate vicinity of the occlusion (±1D) was found to be highly representative of that observed experimentally.

Consider now the WSS distributions shown in Fig.55 for the 84% severity geometry. Only at Re_{PL} = 74 (Fig.55a), where the flow field was shown previously to have a high degree of stability (see Fig.28a), can the WSS distributions plotted here be compared fully. The ability of CFD to simulate fully this condition, using a steady state solver with the Navier-Stokes equations solved to second order accuracy, confirms that the stable flow field observed experimentally is reproduced here numerically. Although a steady state solver was used for all Reynolds numbers, the results for Re_{PL} > 74 were generated with the Navier-Stokes equations solved only to first-order accuracy. This was necessary to ensure convergence of the solutions. In doing so, the difficulty in getting the solution to converge as a steady state one is demonstrated, implying a certain degree of unsteadiness in the flow. This corresponds well with experimental findings. For these conditions therefore (Re_{PL} > 74), the numerical WSS distributions shown in Fig.55b-d are regarded only as indicative of an instantaneous flow field.

The general shape throughout the range of Reynolds numbers studied here represents well those which were observed in the experimental case. The sharp rise and fall of WSS in the occlusion region is reproduced sufficiently well numerically, as is the behaviour of WSS downstream of the occlusion. The most important aspect worth discussion is the apparently severe inability of CFD to reproduce the magnitude of WSS at the throat (see also Fig.56). Acceleration of the flow in this region means that the velocity gradient close to the wall is elevated further than in other regions of the flow. The ability of CFD to use the cell closest to the wall in the calculation of shear rate (typically <0.1mm for the *in vitro*-scale geometries) means that it is calculated very precisely. Conversely, the experimental calculation of shear rate was performed using velocity vectors which, by comparison, were much further away from the wall. As discussed previously, in relation to the 51% severity geometry, the linear velocity gradient assumption may not be sufficiently good to enable an accurate prediction of WSS to be made using PIV data. The inaccuracy of the linear velocity gradient assumption means that shear rate is likely to be under-estimated using the experimental procedure. Not only will this have a direct consequence on the calculated value of WSS (through the relationship between shear stress and shear rate), there will also be an indirect consequence of using Power-Law rheological parameters in the calculation of WSS instead of Newtonian ones (since the calculated shear rate may be less than the critical value ($\dot{\gamma}_{C\infty}$) at which the viscosity assumes Newtonian characteristics). Both these effects will suppress the experimental value of WSS. Referring to Fig.56, the data coloured green was obtained using the same CFD files that were used to present the data coloured blue in Fig.54-56. For the data coloured green however, the velocity vectors used in the calculation of shear rate were located at the same spacial locations as those used to calculate the experimentally-derived WSS values shown in Fig.55&56. This procedure was conducted preciously for the 51% geometry and the same conclusions which were drawn then can also be made here. The highly favourable comparison between the data coloured red and green in Fig.56 indicates that the WSS conditions observed experimentally at the throat are reproduced very well numerically, provided velocity vectors at the same spatial locations are used in the calculation. Most significantly, these results indicate that the linear velocity gradient does not extend as far as the radial position of the velocity vector used in the calculation of experimental WSS.

As a result, the predicted wall shear rate is under-estimated, leading to an under-estimation of WSS in the throat region. These results indicated that the experimental data is inadequate for use in the calculation of WSS and that CFD is a far more effective tool than PIV for the analysis of WSS in this geometry.

Another concern is the apparent inability of CFD to model the mean reattachment point. This is most likely to be because of the way in which flow conditions were defined. Although the flow field observed experimentally showed signs of unsteadiness, the numerical settings were defined such that a wholly steady condition was enforced. In addition, the Navier-Stokes equations were, in some instances, solved using first order approximations, compared with the usual practice of using (more accurate) second order approximations.

6.3.2: Biphasic Flow

The experiments described in Section 5.4, representing the time-dependent biphasic waveform recorded *in vivo*[55] and scaled using dimensional analysis, were reproduced here using numerical techniques. To ensure the flow is unaffected by the initiation of the solution, two periods of the waveform were simulated; the results presented here relate to the second cycle. The fluid model used in this instance is that which represents pulsatile flow of the Xanthan Gum solution used in the experimental analysis in Chapter 5; the parameters which define the viscous behaviour under such conditions are presented in Table 5.

51% Severity – Biphasic Flow

Consider the comparison of velocity profiles for biphasic flow through the 51% occlusive severity geometry in Fig.57. To facilitate an easy and effective comparison between the two data sets, numerical and experimental results are presented together and in the same format as was used to present the experimental results in Chapter 5. In general, the numerical results represent those obtained experimentally rather well, particularly during systolic flow. The blunt profiles observed during systolic acceleration (Fig.57a) are reproduced numerically, as is the extreme level of flattening at the throat. However, recirculation does not seem to

extend as far downstream as was observed experimentally, although by the end of the domain, the difference between the two data sets is shown to reduce significantly.

Very good agreement is also observed at peak systole (Fig.57b). The momentarily constant pressure gradient (neither increasing nor decreasing) leads to the velocity profiles closely resembling those which are characteristic of steady flow rate conditions (compare with Fig.50). Acceleration-induced flattening of the profile in the throat region is reproduced especially well by CFD, as is the subsequent entrainment of fluid into the regions of recirculation near the wall distal to the occlusion. Divergence of the numerical results away from the experimental ones, towards the end of the domain, can be attributed to the increased variance in the experimental data observed in this region (see Fig.41b). The further downstream the flow gets from the stabilizing influence of the occlusion, the greater the instabilities, which lead to a reduction in the consistency of the flow field between successive cycles. As a consequence, the experimental results in this area are more influenced by the time-averaged approach used to present the data.

During systolic deceleration (Fig.57c), the observed retention of momentum in the core region, distal to the occlusion, is reproduced to an even greater extent in the numerical model. The recirculation of fluid near the wall is therefore also more significant, resulting in CFD displaying features which are more pronounced than those observed experimentally. Again, there is a considerable degradation in the ability of CFD to accurately represent those results obtained experimentally towards the end of the domain. It is supposed that this is once again due to the smoothing effects of averaging data in successive cycles, and that the flow field predicted by CFD is, in fact, typical of a real-time condition that might be observed experimentally.

When the flow rate is reduced to zero at the end of systole (Fig.57d), the complex flow field evident in the experimental case is modelled to a certain degree here using CFD. Most strikingly however, is the far greater difference in the level of agreement between the two sets of results compared with that observed during systolic flow. The momentum retained in the flow during systolic deceleration is still evident here and is responsible for the distinct bodies of fluid shearing past each other and the

high velocity gradients which separate them. The level of variance in the experimental data (see Fig.41d) suggests that the highly complex patterns observed numerically would be smoothed out over successive cycles so that the mean velocity profiles would be more like those observed experimentally.

The complex flow structures in Fig.57d were partly washed away during diastolic acceleration due to the increasing pressure gradient. At peak diastole (Fig.57e), there remains evidence of these complexities although their magnitude has been reduced. The flow is still significantly asymmetrical and the numerical profiles are again distinctly different from the time-averaged experimental ones. However, it might be expected that averaging the numerical flow field over the course of many cycles will produce time-averaged velocity profiles more representative of those obtained experimentally.

At the end of diastole (Fig.57f), the velocity profiles obtained numerically are shown, in general, to agree very well with the time-averaged experimental profiles. Although more asymmetry is observed in the numerical case, the profiles are nevertheless highly representative and it is assumed that these asymmetries would be reduced if averaging of the flow field was conducted over the course of many cycles.

In general, the velocity profile plots discussed here show that CFD is adequately capable of modelling the transient flow fields observed experimentally in the 51% severity geometry using the biphasic waveform. Although, in general, there is significantly more asymmetry observed numerically in comparison to the experimental results, it is supposed that this is due to the way in which the results are presented. In the numerical case, the results presented here are instantaneous, representing the flow field at a moment in time, while in the experimental case, the flow fields of successive cycles are averaged, and the profiles plotted therefore relate to these averaged flow fields. If the asymmetry observed numerically is real, and the asymmetric nature of the flow field varies from one cycle to the next (as has been shown experimentally), then over the course of many cycles the asymmetry will be reduced and the velocity profiles will be smoothed out to yield more symmetrical and less exaggerated profiles which would be more representative of those obtained experimentally.

Consider now the comparison between experimental and numerical WSS distributions (for both the upper and lower surfaces) shown in Fig.58 for biphasic flow through the 51% occlusive severity geometry. The numerical results are presented alongside those obtained experimentally in order for an effective comparison to be made. There are a number of important observations to make. Firstly, the magnitude of WSS proximal to the occlusion, and its behaviour over the course of the biphasic cycle, is generally modelled well using CFD. There is also a clear indication of the trend that was observed experimentally of a small reduction in WSS as the flow approaches the occlusion. As was the case for steady flow, it is the magnitude of WSS at the throat of the occlusion (arguably the most important region under consideration) during systolic flow that shows the biggest discrepancy between experimental and numerical results. The apparent over-estimation of numerical WSS in this region is between 30% (systolic deceleration) and 100% (peak systole) of the equivalent experimental results. This may be partly explained by uncertainty in the calculation of experimental WSS due to the difficulty in determining the wall position (see Section 5.3.3). However, a complete reliance on this source of uncertainty would appear to be a less convincing argument when the magnitudes of WSS at the throat over the remainder of the cycle are compared. Referring to the velocity profiles discussed previously (Fig.57a-c), there is, importantly, very close agreement between numerical and experimental results at the throat of the occlusion (arguably more so than anywhere else in the domain). It would therefore be expected that the WSS in this region would also show good agreement. Given the extreme flattening of the profiles in this region, the most reasonable conclusion to draw is that the velocity vector used to calculate experimental WSS in this region was not close enough to the wall for the linear velocity gradient to be wholly accurate (the implications of this were discussed previously for steady flow rates). Given the ability of CFD to use the velocity vector in the cell closest to the wall (typically <0.1mm for the *in vitro*-scale geometries) for the calculation of WSS, this problem would not be encountered numerically. For steady flow conditions (see Section 6.3.1), an attempt was made to illustrate the effects of inaccurate usage of the linear velocity gradient assumption in the calculation of experimentally-obtained WSS. The same procedure that was used then is employed here. Using the same CFD flow-field data that was used to calculate the numerical WSS values shown in Fig.58,

WSS was calculated again using velocity vectors situated at the same spatial positions as those used in the experimental estimation of WSS. At peak systole (where the greatest discrepancy between PIV- and CFD-derived values of WSS is observed in Fig.58), the resulting non-dimensional WSS value at the throat of the stenosis was calculated to be ~1.15. This compares very favourably with the experimental value for non-dimensional WSS (~10% difference), indicating that the WSS environment at the throat is reproduced much more accurately than is initially apparent when considering Fig.58. As concluded previously for steady flow rates, this also suggests that CFD is a far more effective tool than PIV for modelling the WSS environment in studies such as this.

For the remainder of the flow, WSS was modelled satisfactorily, the only difference between experimental and numerical results worthy of note being the behaviour of WSS towards the end of the domain at peak systole. This discrepancy is most likely to be caused by the unsteadiness observed in this region at this point in the cycle.

84% Severity – Biphasic Flow

Consider the comparison of velocity profiles for biphasic flow through the 84% occlusive severity geometry in Fig.59. Again, the numerical results are presented together with those which were obtained experimentally and are done so using the same format that was used to present the results in Chapter 5. [Note that, in Fig.59a (systolic acceleration), there is no experimental data against which the numerical results are compared. This is because of the previously discussed reliability issues regarding the experimental data at this point in the cycle (see Section 5.4.1). However, the numerical results obtained at this cycle position are presented and discussed here in relation to the development of the flow as the cycle progresses.]

There are a number of points to make regarding the comparison between the numerical and experimental velocity profiles. In general, the numerical methods appear to reproduce the profile characteristics in the immediate vicinity of the occlusion ($-1<x/d<1$) in a satisfactory manner. This is observed throughout the cycle, although it is particularly evident during systolic flow, especially in the region proximal to the occlusion. This is a region which, during systole, experienced high levels of consistency in the experimental data (see Fig.42) due to acceleration of the

flow as the pipe cross-section decreased. This reduction in luminal area reduces tangential velocity components in the flow, making it highly two-dimensional and hence consistent. It also leads to a flattening of velocity profiles at the throat of the occlusion, an observation reproduced here numerically. Further evidence of the flattening effect (on velocity profiles) of accelerating flow, can be inferred from the shape of the profiles proximal to the occlusion during systolic acceleration (Fig.59a). Compared with those in the same region at peak systole (Fig.59b), these profiles appear more blunt, because of the positive pressure gradient experienced during systolic acceleration, as opposed to a momentarily zero pressure gradient at peak systole. Although no experimental data is available in Fig.59a, this trend appears to be modelled here using CFD.

Only when the flow progresses beyond the expansion region ($x/d > 1$) do the numerical and experimental results appear to diverge significantly. It is of great significance that the divergence of these results occurs when the variance in the experimental data is high. This high level of variance (see Fig.42a-c) is indicative of the unsteady nature of the flow in this region which was caused by the rapid expansion in cross-sectional area that preceded it. The averaging method used to present the experimental data causes the flow field to be 'smoothed-out'; only the mean flow condition, at the cycle position in question, over successive cycles is presented. Although the numerical profiles in this region are perhaps more representative of the instantaneous condition than the mean experimental profiles against which they are compared, the inability of CFD to model the unsteady behaviour observed experimentally suggests that CFD is not a suitable tool for modelling the unsteady flow conditions distal to the 84% severity occlusion during systole.

At the end of systolic deceleration (see Fig.59d) the almost flat experimental profiles are again likely to be the result of averaging unsteady data (see the high levels of variance in Fig.42d). These same problems are observed again at peak diastole (Fig.59e), although there is good agreement between numerical and experimental results in the throat region, where consistency in the experimental data is high (see Fig.42e) due to the acceleration of flow through the occlusion.

The numerical profiles shown in Fig.59f, relating to the end of diastolic flow and the beginning of the zero net flow rate condition which defines the remainder of the cycle, are observed to be highly representative of the experimental results. This is shown to be the case throughout the domain, despite the small scale which is used to present the data. Referring to Fig.42f, this may at first appear to breach the pattern reported previously, regarding the relationship between consistency in the experimental data and agreement between the numerical and experimental velocity profiles. However, it is supposed that the complexities observed in Fig.59d, the likes of which might be expected at the end of diastole, are not observed in Fig.59f because of the natural reduction in the transient nature of the flow due to the low flow rates that preceded this point in the cycle. It is supposed therefore that the normalized standard deviation plot in Fig.42f exhibits high levels of (normalized) inconsistency because of the very low velocities recorded throughout the domain at this time. It follows therefore that both velocity profile data sets shown in Fig.59f are realistic representations of the flow field at this point in the cycle.

In general, the velocity profile plots presented here in Fig.59 show CFD to be, at best, adequate in its ability to reproduce the experimental results obtained using the biphasic waveform in the 84% severity geometry. In the vicinity of the occlusion ($-1<x/d<1$), CFD is clearly shown to be highly capable of modelling those conditions observed experimentally due to the high levels of stability present in this region. However, in those regions where unsteadiness was observed experimentally (distal to the occlusion), CFD appears to be much less capable of correctly modelling flow conditions. Since averaging of the experimental data 'smoothed-out' the local flow field where unsteadiness was high (greatly reducing the magnitude of local mean velocities), it might be expected that significant asymmetric flow would be observed numerically. In successive cycles, any asymmetry or waviness would likely be 'smoothed out', resulting in a mean velocity profile distribution more representative of the experimental results. However, highly symmetric flow was predicted using CFD, suggesting this to be unlikely. In this respect, the inability of CFD to model the unsteadiness observed experimentally is demonstrated.

Consider the comparison between experimental and numerical WSS distributions (for both the upper and lower surfaces) shown in Fig.60 for biphasic flow through the

84% occlusive severity geometry. The numerical and experimental results are presented alongside each other in order to facilitate an effective comparison. [Note the absence of experimental data for systolic acceleration. This is because of the reliability issues related to this data (see Section 5.4.1). However, referring to the numerical results in Fig.60, similar trends to those reported for the 51% severity occlusion (see Fig.60) are observed. These include a return to constant WSS distal to the occlusion (at $x/d \approx 3.0$ for the 84% case compared with $x/d \approx 1.4$ for the 51% case) and a peak in WSS at the throat.] The conclusions to be drawn from this comparison are similar to those made earlier for the 51% severity occlusion. The most significant result is again the apparent over-estimation, by CFD, of WSS at the throat during systolic flow. On this occasion however, the numerical values of WSS at the throat are as much as ~300% (at peak systole) that which was predicted experimentally. Given the accuracy at which WSS is predicted in other parts of the domain, and the extremely good correlation observed in the velocity profile plots in the throat region (see Fig.59), it is reasoned that the discrepancies between the values of WSS at the throat during systole can be explained in the same way as was done so previously; the wall shear rate (calculated using the linear velocity gradient assumption) is under-estimated in the experimental case. This affects the calculation of WSS both directly, through the relationship between shear rate and shear stress, and indirectly, through the influence of shear rate on the viscosity parameters to be used in the calculation of WSS. Evidence that CFD is able to model the WSS environment in the throat more effectively than is initially apparent, is provided by conducting the same calculations that were performed previously using the 51% geometry; estimates of WSS were made, at the throat of the stenosis and at the peak systolic flow rate condition (where the greatest discrepancy between experimental and numerical values of WSS are observed in Fig.60), using the same CFD flow field data that was used to present the data shown in Fig.59&60. This time however, estimates of WSS were made using data relating to the velocity vectors located at the same spacial locations as those used to estimate WSS experimentally. The velocity gradient was assumed to extend linearly in this region. The dimensionless WSS values obtained using this technique were ~4.7. The difference between this value and the equivalent experimentally-obtained value for WSS is ~20%, significantly better than the 300% difference observed in Fig.60. This indicates that the linear velocity gradient assumption is grossly inadequate for use in conjunction with the

experimental data and that, as a result of doing so, wall shear rate is significantly under-estimated using the experimental data. Since CFD enables velocity vectors which are much closer to the wall (compared with PIV) to be used in the calculation of WSS, this result confirms the previous conclusion that CFD is a far more effective tool than PIV for modelling the WSS environment in the types of geometry investigated here.

All other aspects of this comparison can be summarised in the same way as in the 51% severity occlusion case. Although there are some issues relating to the inability of CFD to replicate the direction of mean experimental WSS distal to the occlusion, its magnitude in this region is, however, very well modelled numerically despite the previously discussed issues regarding the ability of CFD to model unsteadiness. This is the case for the duration of the cycle.

Also noteworthy is the significant difference in the position of flow separation. In all circumstances where separation occurs, this point is further downstream in the experimental case than in the numerical one. This is possibly due to the idealised way in which the numerical domain was defined; it is not an exact reproduction of the geometry used in the experimental analysis.

6.3.3: Validation of CFD – Summary

It has been demonstrated that the numerical techniques used here vary significantly in their ability to accurately reproduce the results observed experimentally, depending on both the flow rate conditions and the geometry employed. For the steady flow rate case, comparison between experimental and numerical data, through the use of velocity profiles and WSS distributions, indicates that CFD is very good at modelling the experimentally observed flow fields in the low occlusive geometry (S = 51%). This is the case throughout the domain and over the full range of Reynolds numbers studied. However, in the geometry where the occlusion is highly constrictive (S = 84%), the ability of CFD to reproduce the experimental conditions reported in Chapter 5 was found to be less satisfactory. Those conditions observed proximal to, and in the immediate vicinity of, the occlusion were modelled very well due to the flow being highly stable and two-dimensional. However, the unsteadiness observed experimentally distal to the occlusion could not be reproduced numerically.

In this respect, the flow fields produced by CFD cannot be considered representative of those observed experimentally. However, given that the most physiologically-significant parameter studied here is WSS (due to its reported role in the many atherogenic processes), the ability of CFD to acceptably predict mean WSS was therefore considered the most important issue. Although CFD has been shown to be incapable of modelling the unsteadiness distal to the occlusion in the 84% case, its ability to effectively model the mean experimental WSS distribution suggests that, for steady flow rate conditions, CFD is indeed a suitable tool for modelling the most atherogenically-important flow parameter, WSS.

For the time-dependent biphasic waveform case, the ability of CFD to reproduce the conditions observed experimentally has again been shown to be highly dependent upon the severity of the occlusion. Using the 51% area reduction geometry, the change in velocity profile characteristics during the cycle was modelled adequately throughout the domain, particularly so near the occlusion but also further downstream where the flow is inherently unstable. Most importantly however, WSS distributions were shown to be acceptably modelled throughout the cycle. For the 84% severity geometry, the inability of CFD to model the unsteadiness recorded experimentally was demonstrated. Despite this, the WSS distributions predicted by CFD for this geometry were found to be representative of the mean distributions recorded previously using experimental techniques. In all cases – using steady and time-dependent flow rate conditions and both geometry types – CFD consistently predicted higher values of WSS at the throat of the occlusion compared to that calculated experimentally. It is assumed that this discrepancy was due to the inaccuracies in the assumptions made to calculate experimental WSS, particularly regarding the linear velocity gradient.

Although there are a number of limitations regarding the ability of CFD to model all aspects of the flow correctly (in particular the unsteadiness observed distal to the occlusion in the 84% severity geometry), its usefulness in modelling the mean WSS distribution over time has been demonstrated. By extension therefore, CFD was used to study blood flow in life-scale occlusive geometries in order to quantify the effects of stenoses in relation to physiological concerns. These findings are presented below.

6.4: In Vivo-Scale Numerical Simulations

An assessment regarding the suitability of using CFD as an effective tool for modelling non-Newtonian fluid flow in occluded pipes has been conducted. In order to extend this study further, to establish specifically the nature of blood flow in stenotic arteries, numerical simulations were conducted using the same geometries that were employed previously, this time scaled to represent life-size arterial cases. Two different rheological models were used to represent blood, both of which were based upon the viscosity measurements reported in the literature and shown in Figs.6&7. The first is a modified Power-Law model which includes limits at the extremities of the shear rate range (see Section 3.2). This model is considered to be a good mathematical model of blood viscosity over the full range of shear rates. The second is a Newtonian approximation (μ = 3.5mPa.s), based upon the common assumption that blood flow in arteries occurs under sufficiently high shear conditions for the fluid to be Newtonian.

Initially, a discussion will be presented regarding the suitability of using the Newtonian approximation for the viscosity of blood. This will be done by comparing the results obtained using the Newtonian approximation with those that were obtained using the more accurate modified Power-Law model. The physiological significance of these results will then be discussed, with particular attention paid to those which relate to the conditions which affect the wall, namely WSS. Both these discussions will concentrate on the results obtained using the biphasic waveform, since it is these results which are most relevant to the conditions which are found *in vivo*.

Given that new fluid models and newly scaled geometries were to be used in this analysis, it was considered appropriate to repeat the verification of fully-developed velocity profiles conducted in Section 6.3.1. Profiles obtained using the characteristic steady flow rate conditions, identified in Table 8, were selected at two points in the domain (40 and 45 diameters downstream of the inlet plane) where the pipe is straight, unaffected by the occlusion and at a distance from the inlet considered sufficient to ensure the flow is fully-developed. In all cases, a comparison of the profiles obtained at 40 and 45 diameters downstream of the inlet plane showed no discernable difference (centreline velocities were the same to within

1%), indicting the flow to be fully-developed at both these positions. This procedure was conducted using the Reynolds numbers identified in Table 8 and both of the viscous models considered to be representative of blood. A selection of these results (obtained 40 diameters downstream of the inlet plane and 10 diameters upstream of the occlusion) is shown in Fig.61. (For confirmation that continuity is satisfied, i.e. the volumetric flow rates of the fully-developed Newtonian and non-Newtonian profiles are the same, see Appendix C.) The results presented for Re_{PL} = 74 and Re_N = 140 correspond to the mean cycle flow rate condition and Re_{PL} = 617 and Re_N = 644 correspond to peak flow rate. Comparing these profiles with the fully-developed profiles described by Equation 22 (see Section 5.3.2), there are a number of important points for discussion.

Consider first the profiles obtained using the modified Power-Law fluid model (Fig.61a). As has been discussed previously, the viscous behaviour of this fluid is described using both the Power-Law relationship between viscosity and shear rate and Newtonian approximations of viscosity at the extremities of the shear rate range. This has been shown to be a very good approximation for the steady-shear viscosity of blood over the full range of shear rates (see Fig.6). Using this model, blood viscosity can only be described by the Power-Law relationship if the local shear rate lies within the following range:

$$\dot{\gamma}_{C0} < \dot{\gamma} < \dot{\gamma}_{C\infty}$$

If the local shear rate lies beyond these limits, the local viscosity is defined as Newtonian ($\eta = \eta_0$ if $\dot{\gamma} < \dot{\gamma}_{C0}$ or $\eta = \eta_\infty$ if $\dot{\gamma} > \dot{\gamma}_{C\infty}$). Referring to Equation 1 (see Section 2.2), the values of $\dot{\gamma}_{C0}$ and $\dot{\gamma}_{C\infty}$ vary, depending on the value of both n and κ. For blood flow under steady flow rate conditions (where n = 0.61 and κ = 18mPa.s^n), these critical shear rates assume the following values.

$$\dot{\gamma}_{C0} = 0.0123 s^{-1}$$

$$\dot{\gamma}_{C\infty} = 66.6 s^{-1}$$

Referring now to Fig.61a, neither the profiles in the lower Reynolds number (Re_{PL} = 74) nor in the higher Reynolds number scenarios (Re_{PL} = 617) fit the fully-developed profile which would be expected of a fluid which obeys fully the Power-Law model.

In fact these profiles seem to confirm that the modified Power-Law model (used here to represent blood viscosity) is a hybrid of the Power-Law and Newtonian models (the profiles lie somewhere between the two ideal cases). This is further confirmed by the contour maps of shear rate given in Fig.62. These plots show regions which exhibit local shear rates below (shaded blue) and above (shaded green) the critical shear rate at which the viscosity changes from the Power-Law relationship to the high-shear Newtonian condition ($\dot{\gamma}_{C\infty}$). At a distance of 40 diameters from the inlet (where the profiles shown in Fig.61 are recorded), the local shear rate distribution indicates the fluid in the centre of the pipe is governed by Power-Law parameters while in the remainder of the domain, the fluid is described by Newtonian parameters.

A comparison between the two shear rate maps in Fig.62 also illustrates why the two profiles relating to Re_{PL} = 74 and Re_{PL} = 617 in Fig.61 are different; the higher the Reynolds number, the greater the volume of fluid which conforms to the Newtonian, rather than the Power-Law, relationship. Consequently, the greater the Reynolds number, the more Newtonian-like the velocity profiles become (compare the respective fully-developed profiles in Fig.61a).

Referring now to the velocity profiles generated using the entirely Newtonian fluid model (Fig.61b), CFD is shown to reproduce highly acceptable profile characteristics. The maximum velocities, recorded at the geometric centreline, are shown to be within 2% of that which is suggested by the parabolic laminar profile (see Equation 22 in Section 5.3.2).

The ability of CFD to model correctly, and accurately, fully-developed characteristics of the flow, defined by these two fluid models under steady flow rate conditions, has been demonstrated. Extending this study further to include specifically the characteristics of more physiologically-relevant conditions, these fluid models were used in the *in vivo*-scale geometries with the flow rate varying according to the biphasic waveform used previously. The following discussion addresses the validity of using the Newtonian approximation for blood under these conditions.

6.4.1: Validity of Using a Newtonian Approximation for Blood

As discussed previously in Chapter 1, there is much debate in the literature as to the importance of the non-Newtonian characteristics of blood with regard to the way it affects flow through the cardiovascular system. Since there are many different features within this system (for example straight and curved sections, sites of arterial branching and narrowing and indeed the size of the artery in question), there exists, in all likelihood, no absolute rule which can be applied to all areas of concern. For this reason, the following discussion can only be considered applicable to blood flow in the types of geometry studied here.

The two fluid models considered representative of blood were used to simulate physiologically-relevant time-dependent flow rate conditions in the two simplified models of stenotic arteries. Considering first the modified Power-Law fluid model, the critical limits of shear rate, which define the transition of viscosity from the Power-Law to the Newtonian relationship, assume the following values under biphasic flow rate conditions (where n = 0.67 and κ = 18mPa.s^n):

$$\dot{\gamma}_{C0} = 0.0055 s^{-1}$$

$$\dot{\gamma}_{C\infty} = 143 s^{-1}$$

Note the difference between these values and those calculated previously for the steady flow rate condition. This difference is the direct consequence of the different values of the index n used in Equation 1 (see Section 2.2). As discussed in Chapter 3, the value of n was shown to vary, depending on whether the fluid was subjected to steady or oscillatory shear rates. Because of its dependence on shear rate, the easiest way with which to determine whether the local viscosity is Newtonian or governed by the Power-Law, is to examine the shear rate distribution throughout the domain. The following discussion describes, therefore, the contour maps of shear rate, generated at each position in the biphasic cycle identified previously.

Contour Maps of Shear Rate – Biphasic Flow

Shear rate maps for both the 51% and 84% severity occlusions are shown in Figs.63&64 respectively. The way they are presented means that those areas which

experience shear rates greater than $\dot{\gamma}_{C\infty}$ (and, by definition, whose rheology is Newtonian, $\eta = \eta_\infty$) are coloured according to the magnitude of the local shear rate relative to the rest of the domain over the whole cycle. Areas which experience shear rates less than $\dot{\gamma}_{C\infty}$ are coloured grey in order to highlight regions where the rheology is described by the Power-Law approximation. No significant areas were found to exhibit shear rates below the critical value which defines the low-shear, high-viscosity condition ($\dot{\gamma}_{C0} = 0.0055 s^{-1}$).

Referring to the 51% occlusive severity case in Fig.63, the high shear regions (coloured here in red/yellow) near the wall in the throat are clearly visible during systole (Fig.63a-c). These are caused by the high gradients of velocity which result from the combination of zero velocity at the wall (satisfying the no-slip condition) and acceleration of the flow to the high velocities encountered at the throat. Also visible are the shear layers which project from the throat and separate the high-velocity core region from the low-velocity recirculating flow distal to the occlusion. Since the local shear rate is high in these areas ($> \dot{\gamma}_{C\infty}$), rheology of the fluid is defined using the Newtonian approximation, $\eta = \eta_\infty$. However, there are clearly regions which experience shear rates below $\dot{\gamma}_{C\infty}$ (coloured grey), where the rheology is defined using Power-Law parameters. During systole, these are found in either the central core region or in the area of recirculating flow distal to the occlusion. Although the velocity of fluid in the central core is high compared to elsewhere in the domain, layers of fluid travel at similar velocities, leading to low gradients of velocity and hence low shear rates. In the recirculation region, shear rates are generally low because of the small velocities encountered. Note the lengthening of recirculation regions as the systolic phase progresses (see Fig.63a-c). This is due, during systolic acceleration, to the increasing pressure gradient and, during systolic deceleration, the residual momentum carried by the central core. Residual momentum in the core means that, to ensure continuity, fluid near the wall (which is able to dissipate momentum more readily than elsewhere in the domain due to its proximity to the wall) is drawn backwards.

The distribution of shear rates below the critical value ($\dot{\gamma}_{C\infty}$) for the remainder of the cycle is much more widespread; indeed at the end of diastole (Fig.63f) the entire domain is shown to be subject to shear rates below $\dot{\gamma}_{C\infty}$. It is presumed that the low shear environment, indicated by Fig.63f, applies until acceleration of systolic flow occurs at the beginning of the next cycle.

Despite the prevalence of low shear rates ($< \dot{\gamma}_{C\infty}$), in both significant portions of the domain and throughout the duration of the cycle, the most important point to make is that they exist predominantly in regions which are not adjacent to the wall. Apart from the last third of the cycle (where net flow rate is zero), flow adjacent to the wall experiences shear rates greater than $143s^{-1}$ ($\dot{\gamma}_{C\infty}$) for almost the entire length of the domain. This implies that the fluid in this region is Newtonian ($\eta = \eta_{\infty}$).

Referring now to the shear rate map shown in Fig.64 for the 84% occlusive severity case, similar observations to those made for the 51% case are applicable here. The greater magnitude of shear rates (compare keys in Figs.63&64) observed in the 84% severity geometry is due to the acceleration of flow to much greater velocities in the more severe constriction. Areas of high shear are again observed adjacent to the wall in the throat of the occlusion and in the shear layers which divide the high-velocity jet from the areas of recirculation downstream of the occlusion. Note the shear layer projecting upstream from the occlusion at peak diastole (Fig.64e). This shear layer is in the opposite direction to those seen in systolic flow (see Fig.64a-c) because of the reversal in the direction of net flow rate. This shear layer was not observed in the 51% severity case because of the combination of low flow rate and the relatively small reduction in area compared to the 84% case. Reverse flow in the 51% case was therefore observed to travel smoothly through the occlusion without separating from the wall. In the 84% case, separation did occur, leading to the creation of a three-dimensional shear plane (seen here as two distinct shear layers). Shown clearly here (particularly in Fig.64a-c&e) is the increase in shear rate in the centre of the domain as the flow accelerates through the contraction part of the occlusion. This is due to the convergence of streamlines in this region, which leads to an increase in the local gradients of velocity.

Low shear rates again dominate in the central core and in areas of recirculation. Recirculation is once more observed to lengthen, and indeed expand radially (indicated here by the expansion of low shear regions in this area), during systole (Fig.64a-d). A further expansion of areas in which $\dot{\gamma} < \dot{\gamma}_{C\infty}$ occurs throughout the remainder of the cycle, eventually covering almost the entire domain at the end of diastole (Fig.64f). However, and most importantly, they are again observed to dominate mainly in regions not adjacent to the wall. By definition therefore, for the majority of the cycle, fluid adjacent to the wall has a constant Newtonian viscosity ($\eta = \eta_{\infty}$).

To show how the flow field is affected by the shear-thinning characteristics that govern blood rheology in areas of low shear, a comparison between the velocity profiles, obtained using both the modified Power-Law and the Newtonian fluid models, is presented below.

Velocity Profiles – Biphasic Flow

Axial velocity profile plots, for both the 51% and 84% severity occlusions, are shown in Figs.65&66 respectively. They are presented in the same format, using the same scaling of velocities, as those described previously in Section 5.3.2. For both the Newtonian and the modified Power-Law fluid models used here to represent blood, the general features of the flow in both geometries can be summarised in a similar fashion to those which were described previously in Section 6.3.2. These include a flattening of the profiles during systolic acceleration (due to the increasing pressure gradient); a flow field typical of a steady flow rate condition at peak systole (due to a momentarily zero pressure gradient); lengthening of recirculating flow during systole (due to the increasing Reynolds number during systolic acceleration and by the retention of momentum in the core region during deceleration which draws fluid near the wall backwards in order to maintain continuity); a complex flow field at the end of systole (dominated by the exaggeration of flow features developed during systole); reverse net flow at peak diastole (with features developed previously still present) and a relatively stable flow field at the end of diastole.

Despite clearly being similar in many respects, further analysis of the velocity profile plots shown in Figs.65&66 illustrates how the flow is affected by the difference between the two rheological models used to represent blood. It has been shown previously in Fig.61 how the value of n (Power-Law index) affects the velocity profiles; the smaller the value of n, the more blunt the fully-developed profile becomes. Although time-dependent flow does not achieve fully-developed status, the relationship between the shape of velocity profiles and n is still maintained. This effect is shown particularly in Fig.65d&e where shear rates below $\dot{\gamma}_{C\infty}$ (where the viscosity between the two fluid models diverges) dominate (see Fig.63d&e). The profiles relating to the Newtonian model are observed to be more pointed in comparison to those of the modified Power-Law model.

Despite these small differences, the velocity profiles shown in Figs.65&66 illustrate how similar the flow fields, generated using the two rheological models for blood employed in this study, are to each other. Referring to the WSS distributions (for both the upper and lower surfaces) for the 51% and 84% severity geometries, Figs.67&68 show only those results obtained using the modified Power-Law fluid model. Although not shown here, the WSS distributions obtained using the Newtonian fluid model exhibited no distinguishable difference when compared to those results shown in Figs.67&68. Given that, for the Newtonian fluid model, WSS is defined using the Newtonian parameters n = 1 and $\kappa = \eta_{\infty}$ (= 3.5mPa.s), this result confirms the earlier observation that, for the modified Power-Law model, WSS is defined using these same Newtonian parameters if the local shear rate at the wall is greater than $\dot{\gamma}_{C\infty}$. More significantly, it also demonstrates that, for large parts of the biphasic cycle, flow in the near-wall region experiences shear rates greater than $\dot{\gamma}_{C\infty}$ and that, consequently, it can be defined as Newtonian. This is a highly significant result since it confirms the validity of employing Newtonian fluid models in *in vivo*-scale haemodynamic studies of blood flow in geometries such as those used in this study. The implications of this result are summarised below.

Validity of Using a Newtonian Approximation for Blood – Summary

WSS is considered the most critical parameter under consideration in this study. This is because of its accepted role in the various stages of stenosis formation (see

Chapter 1). Because of the amount of speculation in the literature regarding the importance of the non-Newtonian character of blood, the ability of the Newtonian fluid model used in this study to accurately reproduce the WSS environment in life-scale arterial stenoses is discussed here.

The contour maps of shear rate produced using the more representative modified Power-Law fluid model (see Figs.63&64) illustrated clearly the range of shear rates which can be expected throughout the domain as the cycle progresses. Most importantly, they highlighted those areas in which the local viscosity is defined by either Power-Law or Newtonian parameters. Although there are clearly significant portions of the domain in which the fluid exhibits non-Newtonian characteristics, the velocity profiles shown in Figs.65&66 illustrate that the overall flow field is altered very little by the introduction of Power-Law parameters.

Referring specifically to the local wall environment, fluid in this region has been shown to mostly exhibit Newtonian properties. This was observed to be the case throughout the length of the domain under consideration and for the vast majority of the non-zero net flow rate portion of the cycle. As a result, using the approximation that blood has constant viscosity was shown to have a negligible effect on the calculated WSS environment when results obtained using the two fluid models were compared. Use of the Newtonian approximation for blood (μ = 3.5mPa.s) is therefore considered valid for modelling blood flow in life-scale geometries, provided the objective is to study the behaviour of WSS.

Overall, it has been shown that there are certain applications for which the use of a Newtonian approximation for blood viscosity is acceptable. These are namely for investigating the processes which occur at or very near to the wall.

In addition, the unsteadiness observed experimentally distal to the occlusion in the 84% stenosis geometry indicates that only areas in which the flow is steady (such as proximal to, and in the immediate vicinity of, the occlusion) can numerical results be relied upon to generate flow conditions which are truly representative of the instantaneous conditions which might be expected *in vivo* (see Section 6.3.3). Since unsteadiness was observed only in the 84% geometry and not in the 51% geometry,

further research is required to establish the occlusive severity at which unsteadiness is initiated.

6.4.2: Physiological Concerns

As discussed previously, there is general consensus in the literature that WSS plays a major role in the pathogenesis of stenosis formation. The processes which lead to this degradation in arterial health, and the influence WSS has upon them, were detailed previously in Chapter 1. Some of these processes were shown to be associated with exposure to high magnitudes of WSS (such as shear-induced injury to the endothelium) while others are associated with exposure to low magnitudes of WSS (such as the deposition of particulates that are carried in the bloodstream). In order to address how the results presented in this thesis might be used to quantify the prevalence of these physiological processes, each is considered individually in the following discussion.

Although the Newtonian approximation used in this study to represent blood viscosity has been shown to be quite capable of modelling the general flow characteristics that were predicted using the more representative modified Power-Law fluid model, the results referred to here are those which were obtained using the modified Power-Law fluid model. In doing so, those processes which occur in the presence of low as well as high shear rates can be addressed, since this model has been shown to be a very good approximation for the viscosity of blood over the full range of physiologically-relevant shear rates. The WSS distributions obtained using this fluid model and measured at the cycle positions studied in this thesis are shown in Figs.67&68 for the 51% and 84% occlusive severity geometries respectively.

Localized Injury to the Endothelium

Endothelial cells line the internal surface of the artery and, as such, amount to a barrier between the artery wall and the bloodstream. When in a healthy condition, it forms a semi permeable membrane, through which water and small solutes such as glucose are able to pass. The transport of larger molecules however, such as LDLs and the plasma proteins albumin and fibrin, is prevented. Since these materials often accumulate in the early stages of atherosclerotic plaque formation, integrity of the

endothelium is extremely important in regulating the transport of these materials into the vessel wall and therefore the development of the disease.

Shear stress has been shown by previous researchers to be the main destructive mechanism through which the endothelium is damaged[5,12-14,25,30,31]. The scale of endothelial injury varies greatly depending on the local WSS environment. A number of researchers identified critical WSS values which relate to different stages of damage to the endothelium. Fry[14] studied the erosive nature of WSS and observed that, when the instantaneous local WSS exceeded approximately 100Pa, endothelial cells were eroded from the surface of the artery wall. Appropriate scaling of this value (according to its definition in Equation 2 (see Section 2.2.) and the flow properties relevant to this study and presented in Table 3) yields a dimensionless WSS value of 31.5. Referring to the WSS results presented here for the 84% severity geometry (see Fig.68), the dimensionless WSS at the throat of the occlusion is shown to peak at approximately 37. This suggests that, given such a severely constricted artery, erosion of the endothelium will certainly occur at the throat of the stenosis for at least a short duration of the cycle when systolic flow rate is near the maximum.

Referring now to the WSS distributions shown in Fig.67 for the 51% severity geometry, the peak magnitude of dimensionless WSS (= 5.3) is much less than the erosion threshold proposed by Fry[14]. This suggests that extensive erosion of the endothelium does not occur in mildly stenosed arteries such as this and that endothelial erosion is associated with advanced stages of stenosis formation; it does not initiate the accumulation of atherosclerotic plaque material or hyperplasic growth of the intima. Since the prevalence of endothelial erosion has been shown to be dependent on the severity of the stenosis, there clearly exists a critical percentage reduction in luminal area which elevates the local WSS to such a level that erosion of the endothelium occurs. It is suggested that this critical severity could be investigated in a subsequent related study.

Erosion of the endothelium however, is not the only process by which its integrity is compromised. As discussed in Section 1.4, if the local WSS is elevated above approximately 38-40Pa (in this case, a dimensionless value of ~12), endothelial cells

deform, swell and yield slightly[14,25], resulting in an increase in the permeability of the endothelium[5,12-14,25]. Referring to Fig.68, this condition is satisfied, at the throat of the 84% severity occlusion, for the majority of systolic flow and for what amounts to a considerable duration of the entire cycle (~25%). In the 51% case however (see Fig.67), WSS was not observed to reach this magnitude at any position in the domain or at any point in the cycle. Again this suggests that injury to the endothelium is not an initiating factor in the development of arterial stenoses in an otherwise straight section of artery, but is perhaps important in its latter stages.

Further susceptibility to an increase in endothelial permeability was reported in the literature where the WSS environment experiences a high state of flux[12,32-34]. Due to the pulsatile nature of the waveform used, the WSS environment was observed to be highly oscillatory in the present study, particularly at the throat of the stenoses, providing yet more confirmation that this region is especially prone to endothelial damage.

It has been suggested, in the above discussion, that injury to the endothelium is not an initiating factor in the development of arterial stenoses. Although the results presented in this study appear to indicate this to be the case in arteries which, in their original unstenosed state, are large, straight and at a significant distance from other features in the cardiovascular tree (such as bifurcations), it is not unreasonable to imagine areas where the local geometry elevates WSS to such levels as to cause at least small-scale injury to the endothelium. In fact, sites of elevated WSS have been observed in various geometric configurations by previous researchers. Most notably, these tend to be at sites of arterial branching. In a distal end-to-side anastomosis, WSS was shown, in numerous studies[e.g. 19,91,100-103], to peak opposite the junction between the host artery and the bypass graft, where the flow impinges on the wall. Elevated levels of WSS were also observed where the bypass graft was sown onto the side of the host artery. In bifurcations, the apex of the arterial division (sometimes referred to as the flow divider) has been shown to be susceptible to very high magnitudes of WSS[e.g. 19,80,104] because of the impingement of flow onto the wall in this region. Other regions which have been shown to exhibit elevated levels of WSS are sites of extreme curvature[e.g. 8] due to acceleration of the flow in this region.

Given the highly localized nature of WSS distribution, it seems reasonable to assume that endothelial injury may occur at various stages of stenosis formation. For example, in an area that is pre-disposed to high levels of WSS (due, for example, to the local geometric environment), endothelial injury may be an initiating factor in the subsequent deposition of atherosclerotic material. Alternatively, it may require the formation of a stenosis through a different cascade of pathogenic processes before the local WSS environment has a detrimental effect on the health of the endothelium.

Hyperplasic Growth of the Intima Leading to Intimal Thickening

Intimal hyperplasia is the process whereby smooth muscle cells proliferate, migrate and accumulate, together with the wall proteins elastin and collagen, in the region between the endothelium and the internal elastic membrane (see Fig.1). As discussed in Chapter 1, this process is thought to be a response to a change in the local WSS environment. Given the presence of a healthy endothelium (through which WSS can be 'sensed'), the artery wall remodels itself in order to restore the cycle mean WSS to an optimum value[17,30]. This quantity was calculated, by several researchers[30,38-40], to be 1-2Pa (see Table 2). If the local mean WSS falls below this range, the luminal diameter is reduced (and hence WSS increased) through hyperplasic growth of the intima.

Appropriate scaling of the lower limit of this range (1Pa), using the flow properties relevant to this study, yields a dimensionless value of ~0.3. Referring to the 51% stenotic case in Fig.67, there are clearly regions in which the local WSS is consistently below this threshold for the duration of the cycle. Most noticeably, this is shown to be the case in the region just distal to the stenosis throat, where recirculation occurs during systole. Similarly, this region (particularly x/d~1) is also shown to exhibit very low magnitudes of WSS in the 84% stenotic geometry (see Fig.68).

This WSS-induced adaptation of the wall (through intimal hyperplasic growth) occurs in the presence of a healthy endothelium. However, as has already been discussed, there is a strong likelihood that injury to the endothelium will occur, hence inhibiting this adaptive process. Given the role intimal hyperplasia is shown to have

in the formation of stenoses, this would appear to be a favourable outcome. However, if the endothelium is damaged, its ability to synthesize NO is severely limited[4,13]. Since NO inhibits the proliferation and migration of smooth muscle cells[13], intimal hyperplasia is therefore clearly possible (and perhaps extensive) in the presence of an endothelium which has undergone damage.

Deposition of Atherosclerotic Material onto the Vessel Wall

Stenoses are formed through either hyperplasic growth of the intima, deposition of atherosclerotic material onto the artery wall or through a combination of these processes. Deposited particulates include platelets (which often previously undergo a shear-induced metamorphic change called 'activation'), plasma-proteins (such as fibrin and albumin) and LDLs. The activation of platelets has been shown to occur in the presence of either high absolute shear rates[3,15,35] or where cyclical elongational stresses are high[15,16]. High shear rates are experienced in the near-wall region in the throat of the stenosis, in the shear layers which separate the core flow from recirculating flow and where the streamlines are forced together in the contraction part of the stenosis. Cyclical elongational stresses occur in the stenotic region due to the acceleration/deceleration of the flow as it travels through the stenosis. The incidence of platelet activation (and therefore, their subsequent deposition) is therefore clearly high in the vicinity of stenoses relative to an unstenosed section of artery.

There is wide agreement in the literature that deposition of atherosclerotic material occurs most readily where WSS is low[13,15,24,31,36,37], through a combination of long residence time (of the particles near the wall) and the non-capacity of local blood flow to 'wash away' particles adjacent to the wall. It is reasonable to assume therefore that the deposition rate of atherosclerotic material is greatest in those areas already identified as being susceptible to low magnitudes of WSS (e.g. in the recirculation regions).

Physiological Concerns – Summary

The results presented here, using *in vivo*-scale geometries and a fluid model representative of blood, were discussed in relation to the physiological processes which result in the formation of stenoses. In particular, the impact of the local WSS

environment on the health of the endothelium was discussed, reflecting the importance of the endothelium in regulating the transport of atherogenic particles onto the wall. Bearing in mind the pathogenic processes responsible for injury to the endothelium (see Chapter 1), endothelial injury was thought to be most likely at the throat of the stenosis, particularly during systole.

The relative likelihood of atherogenic particles being deposited onto the vessel wall was also discussed. Areas which exhibit consistently low magnitudes of WSS (and therefore high levels of particulate deposition) were found to be in the expansion planes of the stenoses, where the flow separates from the wall during systole. This region was shown to be subject to low magnitudes of WSS throughout the cycle. Conversely, the rate of particulate deposition is thought to be lowest in those areas where WSS is high (such as at the throat of the stenosis).

The tendency of the intima to undergo hyperplasic growth was also discussed in relation to the local WSS environment. Since this process also occurs mainly in the presence of low magnitudes of WSS, the pattern of its occurrence is likely to be similar to that of the deposition of atherogenic particles.

An interesting, and important, observation to make is that these results seem to confirm the pattern of WSS behaviour, observed by other researchers[15,18,20-22,47-50], which suggests that the formation of stenoses is a self-propagating phenomenon; the more severe the stenosis, the greater the rate at which the processes which lead to their growth occur.

6.5: Computational Fluid Dynamics – Summary

Computational Fluid Dynamics has been used to investigate the nature of non-Newtonian fluid flow in occluded pipes. Finite volume domains, representative of the geometries used in the experimental analysis described in Chapter 5, were constructed. Fluid properties were defined using the appropriate parameters relating to the Xanthan Gum solution used in the experiments, while the flow rate conditions used *in vitro* were employed here in the numerical analysis. The ability of CFD to reproduce the conditions observed experimentally was assessed by comparing the

structure of the flow (through the use of velocity profiles) and the WSS environment. In the mildly occluded geometry (S = 51%), CFD was shown to be highly capable of modelling the flow characteristics observed experimentally. This was the case for both steady and pulsatile flow rate conditions. In the most severely occluded geometry (S = 84%), CFD was demonstrated to be unable to model the unsteadiness observed distal to the occlusion in the experimental results during systole. However, the flow proximal to, and in the immediate vicinity of, the occlusion was modelled sufficiently well to enable the flow characteristics in these areas to be studied.

Once the extent to which CFD could be used to model non-Newtonian fluid flow in occluded pipes had been quantified, the study was extended to enable *in vivo* conditions to be modelled. The geometries constructed previously were scaled to *in vivo* proportions and the fluid model defined such that blood was represented by both a Newtonian approximation and a more realistic model based on the Power-Law relationship between viscosity and shear rate. Comparison between the results yielded using these two fluid models enabled an assessment to be made regarding the validity of using a Newtonian approximation to represent the viscosity of blood. The overall flow field was shown to be affected very little by the introduction of Power-Law parameters in low-shear conditions. Most important, however, was the observation that fluid in the near-wall region was shown to mostly exhibit Newtonian properties. The use of a Newtonian approximation for blood viscosity was therefore considered valid providing the objective is to study those processes which occur at or near the wall.

The results yielded using the more accurate fluid model (based on a modified version of the Power-Law) were then discussed in relation to the physiological processes which drive the formation of stenoses. Permeability of the endothelium was identified by previous researchers to be WSS dependent. It was inferred therefore that the resistive nature of the endothelium to the deposition of atherosclerotic material was reduced, in general, where WSS was observed to be high and, in particular, at the throat of the stenosis.

Similarly, the deposition of atherosclerotic material and the hyperplasic growth of the intima were observed by previous researchers to occur most readily in areas

which are subjected to low magnitudes of WSS. The most notable location where this condition is satisfied was found to be in the expansion plane of the stenosis, where the flow separates from the wall during systole; WSS was observed to be low in this region throughout the cycle.

7: CONCLUSIONS

The objective of this thesis was to conduct a study on the influence of arterial stenoses on local haemodynamics. This was done using two techniques. Initially, a large-scale experimental analysis was conducted, in which the test fluid exhibited certain rheological characteristics that are similar to blood. Flow rate conditions (both steady and pulsatile) were set such that they were suitably scaled representations of the flow rate conditions found *in vivo*. Particle Imaging Velocimetry (PIV) was employed to produce maps of the local velocity fields. From this data, conclusions could be drawn regarding certain flow characteristics, such as the structure of, and level of stability preset in, the observed flow field. The velocity data was also used to produce estimates of the local wall shear stress (WSS) along the length of the test sections. Whilst it was recognised that the large scale *in vitro* measurements could not be used to represent life-scale flows (primarily because of the inability of the test fluid to capture all the requirements of dimensional analysis, particularly the scaling of the high-shear viscosity), their use as reference data, against which numerical results could be compared, was however considered valid. Consequently, a numerical study was conducted by constructing three-dimensional models of the geometries used *in vitro*. Flow conditions and fluid properties were set in order to replicate those used in the experimental analysis. The results obtained using this numerical procedure were then compared with those from the experimental analysis in order to verify the use of CFD in studies of this nature, as well as its limitations.

Extending this numerical study further, the *in vitro*-scale geometries were scaled to life-scale dimensions, while the fluid was defined such that its viscous properties were representative of blood. This was done in two ways. Firstly, the viscous behaviour of blood was modelled, over the shear rate range considered applicable to this study, using a modified version of the Power-Law relationship which included limiting values of viscosity at the extremities of the shear rate range. Secondly, a Newtonian fluid model was used, in which the viscosity was defined as that which is observed in the high-shear range. Appropriate flow rate conditions were set according to the physiologically-relevant waveform found *in vivo*.

Two main assessments were conducted using the results obtained in the *in vivo*-scale study. Initially, the validity of using the Newtonian approximation for blood was evaluated. This was done by studying the difference in the flow structures (particularly those in the vicinity of the wall) produced using the two viscous models considered representative of blood. The parameter most of interest in this regard was the WSS, its influence on the various atherogenic processes having already been identified.

Finally, the physiological implications of the *in vivo*-scale results were evaluated, with particular attention paid to the effects the observed WSS environment might be expected to have on pathogenic processes which lead to further growth of the stenosis.

7.1: Main Conclusions

By comparing experimental results with the numerical results obtained using *in vitro*-scale geometries and fluid properties representative of the Xanthan Gum solution, it was concluded that the ability of CFD to predict the general flow characteristics observed experimentally differs greatly depending on the severity of the stenosis. In the 51% severity case, general flow features were modelled very well using numerical techniques. However, the unsteadiness observed experimentally downstream of the more severe stenosis could not be modelled numerically. In this respect, further work is required to establish modelling techniques which could be introduced, in order to satisfactorily model the unsteady nature of flow in highly-constricted geometries. Despite these limitations however, perhaps the most significant result is that CFD is capable of modelling the mean WSS distributions. In fact, it is reasoned that CFD is more suitable than PIV-based experimental techniques for the analysis of WSS, owing to the ability of CFD to use conditions much closer to the wall compared with experimental results which rely on measurements made using PIV.

In vivo-scale numerical studies of blood flow through stenosed arteries led to the conclusion that a Newtonian approximation for blood viscosity is acceptable for use

in geometries such as those used in this study. This was established first by examining the distribution of local shear rate magnitude. Although significant portions of the domain experienced sub-critical shear rates (i.e. where the shear rate was low enough for the fluid to be defined by Power-Law parameters), there were significant areas (most importantly those near the wall), where the local viscosity of the fluid was constant. Furthermore, the two sets of velocity profiles, relating to the two fluid models used to represent blood (i.e. the modified Power-Law model and the Newtonian model), were very similar, again implying that the Newtonian assumption is valid. Most important however is the proven ability of CFD to accurately predict the local WSS environment. A comparison between the WSS distributions, obtained using the two fluid models used to represent blood, showed no discernable difference, suggesting the use of a Newtonian approximation for blood is acceptable for modelling the conditions at the wall. However, to fully model the flow conditions throughout the domain, it is suggested that a fluid model which accounts for the viscoelastic effects of blood is used, an aspect which has not been addressed in this study.

7.2: Limitations of this Study and Recommendations for Future Work

There are a number of issues regarding the limitations of the present study. These relate mainly to the various assumptions made of the rheological characteristics of both the test fluid (used in the experimental analysis) and blood. In both cases, only the rheological characteristics in shearing flow, not extensional flow, were discussed, since it was reasoned that the flow in arteries is dominated by shearing flow. However, owing to the pulsatile nature of blood flow, it is not unreasonable to assume blood is subjected to a certain degree of extensional flow. In addition, the elastic characteristics of both the test fluid and blood, although discussed, were not accounted for in the fluid models used in the numerical analysis; only the viscous effects were modelled. It is therefore recommended that a comprehensive fluid model, which accounts for all the rheological characteristics of blood, should be developed and used in future studies.

Perhaps the most notable limitation regarding the use of CFD was its apparent inability to model the unsteadiness distal to the occlusion in the most severely

constricted geometry. This was observed to be the case in both steady and pulsatile simulations. Since unsteadiness was observed only in the most severe constriction, further work is required to determine what occlusive severity is required to initiate unsteadiness. In addition, it is suggested that further studies are conducted in order to establish more suitable numerical settings that allow the unsteadiness to be modelled accurately.

Further suggestions for future studies include accounting for the elastic effects of the arterial wall. This aspect was discussed briefly in this project but, for the sake of simplicity, was not incorporated into either the experimental or numerical studies conducted here. Although it is desirable to simplify the problem in order to investigate the effects of particular changes in its definition, the elastic nature of the wall may have a significant effect on the local flow field around a stenosis.

It is suggested that further numerical studies incorporate the various atherogenic processes described in this thesis. Mechanisms which account for the transport of particulates onto the vessel wall could be included. This would require further study to establish the tendency of various atherogenic particles to adhere to the wall across a range of WSS. Likewise, the susceptibility of endothelial erosion could also be included.

REFERENCES

1 National Statistics, (2006), *"Health - Mortality: Circulatory diseases – leading cause group"* [online]. Available: http://www.statistics.gov.uk/CCI/ nugget.asp?ID=1337, [Accessed 16th July 2007)

2 Gray, H.H., Dawkins, K.D., Morgan, J.M., Simpson, I.A., *"Lecture notes on Cardiology"*, Blackwell Science, 4th Edition, ISBN 0-86542-864-6, (2002)

3 Ku, D.N., "*Blood flow in arteries*", Annual Review of Fluid Mechanics 29, pp.399-434, (1997)

4 Levick, J.R., *"An introduction to cardiovascular physiology"*, Arnold, 4th Edition, ISBN 0-340-80921-3, (2003)

5 Nerem, R.M., Cornhill, J.F., *"The role of fluid mechanics in atherogenesis"*, Journal of Biomechanical Engineering 102, pp.181-189, (1980)

6 Hayashi, K., Yanai, Y., Naiki, T., *"A 3D-LDA study of the relation between wall shear stress and intimal thickness in a human aortic bifurcation"*, Journal of Biomechanical Engineering 118, pp.273-279, (1996)

7 Quintella, E.F., Souza Mendes, P.R., Azevedo, L.F.A., Naccache, M.F., *"Visualization and computation of the flow of a highly shear-thinning liquid past the axisymmetric contraction-expansion: Application to blood flow through stenotic vessels"*, American Society of Mechanical Engineers, Fluids Engineering Division (Publication) FED 255, pp.131-140, (2001)

8 Wahle, A., Lopez, J.J., Olszewski, M.E., Vigmostad, S.C., Chandran, K.B., Rossen, J.D., Sonke, M., *"Analysis of the interdependencies among plaque development, curvature and wall shear stress in coronary arteries"*, Functional Imaging and Modelling of the Heart 2005, Lecture Notes in Computer Science 3504, pp.12-22, (2005)

9 Ballyk, P.D., Steinman, D.A., Ethier, C.R., *"Simulation of non-Newtonian blood flow in an end-to-side anastomosis"*, Biorheology 31, pp.565-586, (1994)

10 Mehta, A., Hoffbrand, V., *"Haematology at a glance"*, Blackwell Science, 1st Edition, ISBN 0-632-04793-3, (2000)

11 Hodgson, L., Tarbell, J.M., *"Solute transport to the endothelial intercellular cleft: The effect of wall shear stress"*, Annals of Biomedical Engineering 30, pp.936-945, (2002)

12 Karner, G., Perktold, K., "*Effect of endothelial injury and increased blood pressure on albumin accumulation in the arterial wall: A numerical study*", Journal of Biomechanics 33, pp.709-715, (2000)

13 Nerem, R.M., *"Vascular fluid mechanics, the arterial wall and atherosclerosis"*, Journal of Biomechanical Engineering 114, pp.274-282, (1992)

14 Fry, D.L., *"Certain histological and chemical response of the vascular interface to acutely induced mechanical stress in the aorta of the dog"*, Circulation Research 24, pp.93-108, (1969)

15 Bluestein, D., Niu, L., Schoephoerster, R.T., Dewanjee, M.K., "*Fluid mechanics of arterial stenosis: Relationship to the development of mural thrombus*", Annals of Biomedical Engineering 25, pp.344-356, (1997)

16 Purvis, N.B., Giorgio, T.D., "*The effects of elongational stress exposure on the activation and aggregation of blood platelets*", Biorheology 28, pp.355-367, (1991)

17 Pedley, T.J., "*High Reynolds number in tubes of complex geometry with application to wall shear stress in arteries*", Journal of Biological Fluid Dynamics, pp.219-241, (1995)

18 Banerjee, R.K., Cho, I.Y., Kensey, K., *"Effect of the non-Newtonian viscosity of blood on steady and pulsatile flow in stenosed arteries"*, Advances in Bioengineering 20, pp.103-106, (1991)

19 Kleinstreuer, C., Hyun, S., Buchanan, J.R.Jr., Longest, P.W., Archie, J.P.Jr., Truskey, G.A., *Haemodynamic parameters and early intimal thickening in branching blood vessels"*, Critical Reviews in Biomedical Engineering 29(1), pp.1-64, (2001)

20 Moayeri, M.S., Vali, A., *"Effects of non-Newtonian properties of blood on flow characteristics through a stenosis"*, Iranian Journal of Science and Technology 20 (1), pp.25-43, (1996)

21 Pralhad, R.N., Schultz, D.H., "*Modelling of arterial stenosis and its applications to blood disease*", Mathematical Biosciences 190, pp.203-220,

(2004)

22 Tandon, P.N., Rana, U.V.S., Kawahara, M., Katiyar, V.K., "*A model for blood flow through a stenotic tube*", International Journal of Biomedical Computing 32, pp.61-78, (1993)

23 Young, D.F., *"Fluid mechanics of arterial stenoses"*, Journal of Biomechanical Engineering 101, pp.157-175, (1979)

24 Freidman, M.H., Bargeron, C.B., Duncan, D.D., Hutchins, G.M., Mark, F.F., *"Effects of arterial compliance and non-Newtonian rheology on correlations between intimal thickness and wall shear"*, Journal of Biomechanical Engineering 114, pp.317-320, (1992)

25 Fry, D.L., *"Acute vascular endothelial changes associated with increased blood velocity gradients"*, Circulation Research 22, pp.165-197, (1968)

26 Fry, D.L., *"Response of arterial wall to certain physical factors"*, in Porter, R., Knight, J., *"Atherogenesis: Initiating Factors"*, CIBA Foundation Symposium 12, Associated Scientific Publishers, Amsterdam, pp.93-120, (1973)

27 Flaherty, J.T., Ferrans, V.J., Pierce, J.E., Carew, T.E., Fry, D.L., *"Localizing factors in experimental atherosclerosis"*, in Likoff, W., Segal, B.L., Insull, W., *"Atherosclerosis and coronary heart disease"*, Grune & Stratton, New York, pp.40-83, (1972)

28 Flaherty, J.T., Pierce, J.E., Ferrans, V.J., Patel, D.J., Tucker, W.K., Fry, D.L., *"Endothelial nuclear patterns in the canine arterial tree with particular reference to hemodynamic events"*, Circulation Research 30, pp.23-33, (1972)

29 Fry, D.L., *Certain chemorheologic considerations regarding the blood vascular interface with particular reference to coronary artery disease"*, Circulation 40, pp.38-57, (1969)

30 Zarins, C.K., Zantia, M.A., Giddens, D.P., Ku, D.N., Glagov, S., *"Shear stress regulation of artery lumen diameter in experimental atherogenesis"*, Journal of Vascular Surgery 5(3), pp.413-420, (1987)

31 Zarins, C.K., Giddens, D.P., Bharadvaj, B.K., Sottiural, V.S., Mabon, R.F., Glagov, S., "*Carotid bifurcation atherosclerosis: Quantitative correlation of plaque localization with flow velocity profiles and Wall Shear Stress*", Circulation Research 53, pp.502-514, (1983)

32 Chien, S., Usami, S., Fan, F.C., Skalak, R., Weinbaum, S., Caro, C.G., *"Effect*

of mechanical disturbances on uptake of macromolecules by the arterial wall", Proceedings of the Specialists Meeting of the Ohio State University Columbus Ohio, pp.16-1 - 16-4, (1978)

33 Caro, C.G., Nerem, R.M., *"Transport of ^{14}C-4-Cholesterol between serum and wall in the perfused dog common carotid artery"*, Circulation Research 32, pp.187-205, (1973)

34 Nerem, R.M., Mosberg, A.T., Schwerin, W.E., *Transendothelial transport of ^{131}I-Albumin"*, Biorheology 13(1), pp.71-77, (1976)

35 Jung, H., Choi, J.W., Park, C.G., "*Asymmetric flows of non-Newtonian fluids in symmetric stenosed artery"*, Korea-Australia Rheology Journal 16(2), pp.101-108, (2004)

36 Caro, C.G., Fitz-Gerald, J.M., Schroter, R.C., "*Atheroma and arterial wall shear. Observation, correlation and proposal of a shear dependant mass transfer mechanism for atherogenesis*", Proceedings of the Royal Society of London Series B Biological Sciences 177(1048), pp.109-159, (1971)

37 Giddens, D.P., Zarins, C.K., Glagov, S., *"Response of arteries to near wall fluid dynamic behaviour"*, Applied Mechanics Review 43(2), pp.S98-S102, (1990)

38 Kamiya, A., Togawa, T., *"Adaptive regulation of wall shear stress to flow change in the canine carotid artery"*, American Journal of Physiology – Heart and Circulatory Physiology 239(1), pp.H14-H21, (1980)

39 Lipowsky, H.H., Zweifach, B.W., *"Network analysis of microcirculation of cat mesentery"*, Microvascular Research 7, pp.73-83, (1974)

40 Whitmore, R.L., *"Rheology of the circulation"*, Permagon Press, London, pp.90-108, (1968)

41 Wahle, A., Lopez, J.J., Olszewski, M.E., Vigmostad, S.C., Braddy, K.C., Brennan, T.M.H., Bokhari, S.W., Bennett, J.G., Holper, E.M., Rossen, J.D., Chandran, K.B., Sonka, M., *"Relationship between plaque development and local haemodynamics in coronary arteries"*, Proceedings of The International Society for Optical Engineering (SPIE) 5746, pp.223-232, (2005)

42 Henry, F.S., Collins, M.W., *"Numerical modelling of blood flow"*, Advances in Hemodynamics and Hemorheology 1, pp.67-112, (1996)

43 Davis, P.F., Tripathi, S.C., *"Mechanical stress mechanisms and the cell: An*

endothelial paradigm", Circulation Research 72, pp.239-245, (1993)

44 Deplano, V., Siouffi, M., *"Experimental and numerical study of pulsatile flows through stenoses: Wall shear stress analysis"*, Journal of Biomechanics 32, pp.1081-1090, (1999)

45 Ishikawa, T., Guimaraes, L.F.R., Oshina, S., Yamane, R., *"Effect of non-newtonian property of blood on flow through a stenosed tube"*, Fluid Dynamics Research 22, pp.251-265, (1998)

46 Tutty, O.R., "*Pulsatile flow in a constricted channel*", Journal of Biomechanical Engineering 114, pp.50-54, (1992)

47 Cho, K., Kensey, K.R., "*Effects of the non-Newtonian viscosity of blood on flow in a diseased arterial vessel. Part 1: Steady flows*", Biorheology 28, pp.241-262, (1991)

48 Neofytou, P., Drikakis, D., "*Effects of blood models on flows through a stenosis*", International Journal for Numerical Methods in Fluids 43, pp.597-635, (2003)

49 Noguchi, Y., Wishah, M.I., "*Three-dimensional CFD modelling of blood flow through asymmetric stenosis*", Computational Methods and Experimental Measurements XI, pp.567-574

50 Tu, C., Deville, M., "*Pulsatile flow of non-Newtonian fluids through arterial stenoses*", Journal of Biomechanics 29(7), pp.899-908, (1996)

51 Tura, A., Cavalcanti, S., *"Stenosis-induced flow disturbances in an artery segment assessed by numerical simulation"*, Advances in Fluid Mechanics 26, pp.145-154, (2000)

52 Chakravarty, S., Mandal, P.K., *"Effect of surface irregularities on unsteady pulsatile flow in a compliant artery"*, International Journal of Non-Linear Mechanics 40, pp.1258-1281, (2005)

53 Onogi, K., Kohge, K., Minemura, K., *"Numerical simulation of blood flow through stenosed vessel"*, American Society of Mechanical Engineers, Pressure Vessels and Piping Division 491(2), pp.93-102, (2004)

54 Buckingham, E., *"On physically similar system; illustrations of the use of dimensional equations"*, Physics Review 4, pp.345-376, (1914)

55 Fisher, R.K., How, T.V., Carpenter, T., Brennan, J.A., Harris, P.L., "*Optimising Miller cuff dimensions. The influence of geometry on anastomotic*

flow patterns", European Journal of Vascular and Endovascular Surgery 21(3), pp.251-260, (2001).

56 Wells, R.E., Schmid-Schonbein, H., Goldstone, J., "*Flow behaviour of red cells in pathologic sera: Existence of a yield stress in the absence of fibrinogen*", Theoretical and Clinical Hemorheology, pp.358-365, (1971)

57 Cokelet, G.R., "*The rheology of human blood*", Ph.D. Thesis, (1963)

58 Rand, P.W., Lacombe, E., Hunt, H.E., Austin, W.H., "*Viscosity of normal human blood under normothermic and hypothermic conditions*", Journal of Applied Physiology 19(1), pp.117-122, (1964)

59 Schmid-Schonbein, H., Wells, R.E., "*Red cell aggregation and red cell deformation: Their influence on blood rheology in health and disease*", Theoretical and Clinical Hemorheology, pp.348-355, (1971)

60 Wells, R.E., Merrill, E.W., "*Shear rate dependence of the viscosity of while blood and plasma*", Science 133, pp.763-764, (1961)

61 Ditzel, J., Kampmann, J., "*Whole-blood viscosity, hematocrit and plasma protein in normal subjects at different ages*", Acta Physiologica Scandinavica 81, pp.264-268, (1971)

62 Schmid-Schonbein, H., Wells, R.E., "*Rheological properties of human erythrocytes and their influence upon the 'Anomalous' viscosity of blood"*, in 'Reviews in Physiology' 63, pp.146-218, (1971)

63 Chien, S., "*Shear dependence of effective cell volume as a determinant of blood viscosity*", Science 168, pp.977-979, (1970)

64 Chien, S., Usami, S., Taylor, H.M., Lundberg, J.L., Gregersen, M.I., "*Effects of hematocrit and plasma proteins on human blood rheology at low shear rates*", Journal of Applied Physiology 21(1), pp.81-87, (1996)

65 Thurston, G.B., *"Frequency and shear rate dependence of viscoelasticity of human blood"*, Biorheology 10, pp.375-381, (1973)

66 Anadere, I., Chmiel, H., Hess, H., Thurston, G.B., *"Clinical blood rheology"*, Biorheology 16, pp.171-178, (1979)

67 Thurston, G.B., "*Viscoelasticity of human blood*", Biophysical Journal 12, pp.1205-1216, (1972).

68 Thurston, G.B., *"Rheological parameters for the viscosity, viscoelasticity and thixotropy of blood"*, Biorheology 16, pp.149-162, (1979)

69 Thurston, G.B., "*Non-Newtonian viscosity of human blood: Flow-induced changes in microstructure*", Biorheology 31(2), pp.179-192, (1994)

70 Collins, M., Schowalter, W.R., *"Behaviour of non-Newtonian fluids in the entry region of a pipe"*, American Institute of Chemical Engineers Journal 9(6), pp.804-809, (1963)

71 Metzner, A.B., Reed, J.C., *"Flow of non-Newtonian fluids – correlation of the laminar, transition and turbulent flow regions"*, American Institute of Chemical Engineers Journal 1(4), pp.434-440, (1955)

72 Gijsen, F.J.H., Allanic, E., van de Vasse, F.N., Janssen, J.D., *"The influence of the non-Newtonian properties of blood on the flow in large arteries: Unsteady flow in a 90° curved tube"*, Journal of Biomechanics 32, pp.705-713, (1999)

73 Keynton, R.S., Rittgers, S.E., Shu, M.C.S., *"The effect of angle and flow rate upon haemodynamics in distal vascular graft anastomoses: An in vitro study"*, Journal of Biomechanical Engineering 113, pp.458-463, (1991)

74 Kute, S.M., Vorp, D.A., *"The effect of proximal artery flow on the haemodynamics at the distal anastomosis of a vascular bypass graft: Computational study"*, Journal of Biomechanical Engineering 123(3), pp.277-283, (2001)

75 Moore, J.A., Steinman, D.A., Prakash, S., Johnston, K.W., Ethier, C.R., *"A numerical study of blood flow in anatomically realistic and simplified end-to-side anastomoses"*, Journal of Biomechanical Engineering 121, pp.265-272, (1999)

76 Rowe, C.S., Carpenter, T.K., How, T.V., Harris, P.L., *"Local haemodynamics of arterial bypass graft anastomoses"*, Proceedings of the Institution of Mechanical Engineers 213(H), pp.401-409, (1999)

77 White, S.S., Zarins, C.K., Giddens, D.P., Bassiouny, H., Loth, F., Jones, S.A., Glagov, S., *"Haemodynamic patterns in two models of end-to-side vascular graft anastomoses: Effects of pulsatility, flow division, Reynolds number and hood length"*, Journal of Biomechanical Engineering 115, pp104-111, (1993)

78 Schowalter, W.R., *"Mechanics of non-Newtonian fluids"*, Pergamon Press Inc., 1st Edition, ISBN 0-08-021778-8, (1978)

79 Sharp, M.K., Thurston, G.B., Moore, J.E. Jr., "*The effect of blood viscoelasticity on pulsatile flow in stationary and axially moving tubes*",

Biorheology 33(3), pp.185-207, (1996)

80 Zhao, S.Z., Xu, X.Y., Hughes, A.D., Thom, S.A., Stanton, A.V., Ariff, B., Long, Q., *"Blood flow and vessel mechanics in a physiologically realistic model of a human carotid arterial bifurcation"*, Journal of Biomechanics 33, pp.975-984, (2000)

81 Grigioni, M., Daniele, C., Morbiducci, U., Del Gaudio, C., D'Avenio, G., Balducci, A., Barbaro, V., *"A mathematical description of blood spiral flow in vessels: application to a numerical study of flow in arterial bending"*, Journal of Biomechanics 38, pp.1375-1386, (2005)

82 Liepsch, D., Moravec, S., *"Pulsatile flow of non-Newtonian fluid in distensible models of human arteries"*, Biorheology 21, pp.571-586, (1984)

83 Moravec, S., Liepsch, D., *"Flow investigations in a model of a three-dimensional human artery with Newtonian and non-Newtonian fluids: Part 1"*, Biorheology 20, pp.745-759, (1983)

84 Davies, P.H., Mazher, A.H.K., Giddens, D.P., Zarins, C.K., Glagov, S., *"Effects of non-Newtonian fluid behaviour on wall shear in a separated flow region"*, First World Congress of Biomechanics, University of California San Diego (1), pp.301, (1990)

85 Gregersen, M.I., Usami, S., Chien, S., Dellenbach, R.J., *"Characteristics of torque-time records on heparinized and defibrinated elephant, human and goat blood at low shear rates 0.01sec^{-1}): effects of fibrinogen and dextran (Dx 375)"*, 4th European Conference on Microcirculation, Cambridge, 1966, Bibl. Anat. 9, pp.276-281, (1967)

86 Healy, J.C., Joly, M., *"Rheological behaviour of blood in transient flow"*, Biorheology 12, pp.335-340, (1975)

87 Huang, C.R., Siskovic, M., Robertson, R.W., Fabisiak, W., Smitherberg, E.H., Copley, A.L., *"Quantitative characterisation of thixotropy of whole human blood"*, Biorheology 12, pp.279-282, (1975)

88 Nichols, W.W., O'Rourke, M.F., *"McDonald's blood flow in arteries"*, Arnold, 4th Edition, ISBN 0-34064614-4, pp.17-21, (1990)

89 Walburn, F.J., Schneck, D.J., *"A constitutive equation for whole human blood"*, Biorheology 13, pp.201-210, (1976)

90 Thurston, G.B., "*Elastic effects in pulsatile blood flow*", Microvascular

Research 9, pp.145-157, (1975)

91 Gray, J.D., *"Non-Newtonian scaling of blood flow in a femoral bypass"*, Ph.D. Thesis, University of Liverpool, (2002)

92 Thurston, G.B., Pope, G.A., "*Shear rate dependence of the viscoelasticity of polymer solutions: II. Xanthan Gum*", Journal of Non-Newtonian Fluid Mechanics 9, pp.69-78, (1981).

93 Bewersdorff, H.W., Singh, R.P., *"Rheological and drag reduction characteristics of Xanthan Gum solutions"*, Rheologica Acta 27, pp.617-627, (1988)

94 Higham, E.H., *"Electromagnetic flow rates"*, in Mylroi, M.G., Calvert, G., *"Measurement and instrumentation for control"*, Peter Peregrines, ISBN 0-86341-024-3, (1984)

95 Khezzar, L., Whitelaw, J.H., Yianneskis, M., *"Round sudden-expansion flow"*, Proceedings of the Institution of Mechanical Engineers 200(C6), pp.447-455, (1986)

96 *"FlowMap Particle Image Velocimetry Instrumentation: Installation and User Guide"*, Dantec Dynamics, Denmark, (1998)

97 Barnes, H.A., Hutton, J.F., Walters, K., *"Rheology Series, Volume 3: An introduction to rheology"*, Elsevier, ISBN 0-444-87140-3, pp.33-34, (1989)

98 Stroud, K.A., *"Engineering mathematics"*, Macmillan Press Ltd., 4th Edition, ISBN 0-333-62022-4, pp.750, (1995)

99 White, F.M., *"Fluid mechanics"*, McGraw-Hill International Editions, 4th Edition, ISBN 0-07-116848-6, pp.331, (1999)

100 Cole, J.S., Watterson, J.K., O'Reilly, M.J.G., *"Numerical investigation of the haemodynamics at a patched arterial bypass anastomosis"*, Medical Engineering and Physics 24, pp.393-401, (2002)

101 Hofer, M., Rappitsch, G., Perktold, K., Trubel, W., Schima, H., *"Numerical study of wall mechanics and fluid dynamics in end-to-side anastomoses and correlation to intimal hyperplasia"*, Journal of Biomechanics 29(10), pp.1297-1308, (1996)

102 Keyton, R.S., Evancho, M.M., Rodway, N.V., Gobin, A., Rittgers, S.E., *"Intimal hyperplasia and wall shear in arterial bypass graft distal anastomoses: An in vivo model study"*, Journal of Biomechanical Engineering

123, pp.464-473, (2001)

103 Longest, P.W., Kleinstreuer, C., *"Particle-hemodynamics modelling of the distal end-to-side femoral bypass: effects of graft calibre and graft-end cut"*, Medical Engineering and Physics 25, pp.843-858, (2003)

104 Chua, L.P., Zhang, J., Zhou, T., *"Numerical study on the steady flow characteristics of proximal anastomosis models"*, International Communications in Heat Mass Transfer 30(7), pp.945-954, (2003)

TABLES

Table 1: Components of whole human blood, their function, size and concentration[4,10]

Constituent	Function	Size	Typical number per litre
Plasma	The base fluid in which the formed elements, waste products, nutrients and proteins are dissolved and suspended.	-	-
Erythrocytes (Red Blood Cells)	Nucleus-less, haemoglobin filled cell with flexible membrane, responsible for the transport of O_2 and CO_2 around the body. Percentage concentration of these cells in the blood determines the degree of shear-thinning behaviour.	8×2 μm diameter, biconcave disc	$3.9 – 6.5 \times 10^{12}$
Leucocytes (White Blood Cells)	Any blood cell that contains a nucleus. Protects the body against foreign particles and involved in antibody production.	Various	$4 – 11 \times 10^{9}$
• Granulocytes	• Destroys bacteria and parasites by ingestion	-	-
➢ Neutrophils	➢ Capable of ingesting and killing bacteria; provides an important defence against infection.	9.4 μm	$2.5 - 7.5 \times 10^{9}$
➢ Eosinophils	➢ Poorly understood; capable of ingesting foreign particles, involved in allergic responses and host defence against parasites.	9.4 μm	$40 - 400 \times 10^{6}$
➢ Basophils	➢ Poorly understood; capable of ingesting foreign particles.	9.4 μm	$10 - 100 \times 10^{6}$

• Lymphocytes ➢ B-Lymphocytes (B-cells) ➢ T-Lymphocytes (T-cells) ▫ Helper T-cells ▫ Cytotoxic T-cells • Monocyte	• Main player in the immune response mechanism. ➢ Produce antibodies which kill circulating foreign particles. ➢ Responsible for identifying and destroying infected cells. ▫ Key role in recognizing the presence of foreign bodies; stimulates production of Cytotoxic T-cells. ▫ Destroys cancerous and virus-infected cells targeted by the Helper T-cells. Will also destroy an allograft. • Ingests foreign particles such as bacteria and tissue debris.	6–14 μm diameter - - - - 7.4 μm diameter	$1.5 – 3.0 \times 10^9$ $0.5 – 1.0 \times 10^9$ $1.0 – 2.0 \times 10^9$ - - 2.2×10^9
Thrombocytes (Platelets)	Initiate the arrest of bleeding through blood clotting.	1-2μm diameter, irregular disc shape	$150 – 400 \times 10^9$

Table 2: Optimum mean WSS for various arteries

Author	Subject	Optimal mean WSS (Pa)
Kamiya & Togawa[38]	Carotid artery, dog	1.5
Whitmore[40]	Large arteries, dog	1.5 – 2.0
	Terminal arterial branch, dog	1.4 – 2.2
Lipowsky & Zweifach[39]	Mesenteric capillary bed, cat	1.0
Zarins et al[30]	Iliac arteries, monkey	1.5 – 1.6
	Aorta, monkey	1.2

Table 3: *In vivo* properties which affect wall shear stress

Geometry:	
Diameter, d	6 mm
Fluid (Blood):	
Density, ρ	1050 kg/m^3 [2]
Newtonian viscosity, μ	3.5 mPa.s
Non-Newtonian viscosity:	
Power law index, n	0.61 (Steady)
	0.67 (Pulsatile)
Power law consistency, κ	18 mPa.s^n
Pulsatility:	
Time period, T	1s[55]
Angular frequency, ω	6.283rad/s[55] (1Hz)
Cycle mean velocity, $\overline{U}_C$	77.8mm/s[55]
Peak to peak amplitude of waveform, $\hat{u}$	421mm/s[55]

Table 4: Scaling parameters for biphasic flow

	In Vivo, Blood	*In Vitro, Xanthan Gum*	
		51% Severity	84% Severity
Diameter, d (mm)	6.0	37.7	38.1
Cycle mean velocity, $\overline{U}_C$ (mm/s)	77.4	59.2	59.0
Oscillatory frequency, ω (rad/s)	6.28	0.765	0.755
f (Hz)	1	0.122	0.120
Strouhal number, St	**0.487**	**0.487**	

Table 5: Scaled viscosity parameters

	Steady		**Biphasic**	
	Blood	*0.07%wt XG*	*Blood*	*0.07%wt XG*
n	0.61	0.61	0.67	0.67
κ (mPa.s^n)	18	41	18	41
η_0 (mPa.s)	100	42	100	32
η_∞ (mPa.s)	3.5	3.8	3.5	4.0

Table 6: Uncertainty of flowmeter signal for average readings after 500 data points (steady flow experiments) and single readings (pulsatile flow experiments)

		Percentage uncertainty		
		Steady Experiments	Pulsatile Experiments	
Flow rate (lpm)	1 Std. Dev. (lpm)	After 500 readings	For 1 Std. Dev. (68% of data)	For 2 Std. Dev. (95% of data)
4.59	0.140	< ± 0.915	± 3.05	± 6.10
9.48	0.150	< ± 0.024	± 1.58	± 3.16
14.40	0.167	< ± 0.048	± 1.16	± 2.32
19.42	0.172	< ± 0.019	± 0.885	± 1.77

Table 7: Scaling parameters

		In Vivo, blood	In Vitro, *Xanthan Gum*	
			S = 51%	*S = 84%*
d (mm)		6.00	37.7	38.1
ρ (kg/m^3)		1050	995	995
n	Steady	0.61	0.61	0.61
	Pulsatile	0.67	0.67	0.67
κ (mPa.s^n)	Steady	18	41	41
	Pulsatile	18	41	41
η_0 (mPa.s)	Steady	100	42	42
	Pulsatile	100	32	32
η_∞ (mPa.s)	Steady	3.5	3.8	3.8
	Pulsatile	3.5	4.0	4.0

Table 8: Flow rates characteristic of the biphasic waveform,

	In Vitro scale, Power-Law fluid model representing Xanthan Gum			In Vivo scale, Power-Law fluid model representing blood			In Vivo scale, Newtonian fluid model representing blood		
	d (mm)	$\overline{U}$ (mm/s)	Re_{PL}	d (mm)	$\overline{U}$ (mm/s)	Re_{PL}	d (mm)	$\overline{U}$ (mm/s)	Re_{N}
Mean flow rate	37.7 - 38.1	65.2	74	6.0	77.8	74	6.0	77.8	140
Intermediate 1	37.7 - 38.1	124	180	6.0	147	180	6.0	147	265
Intermediate 2	37.7 - 38.1	150	235	6.0	179	235	6.0	179	322
Peak systolic flow rate	37.7 - 38.1	300	617	6.0	358	617	6.0	358	644

FIGURES

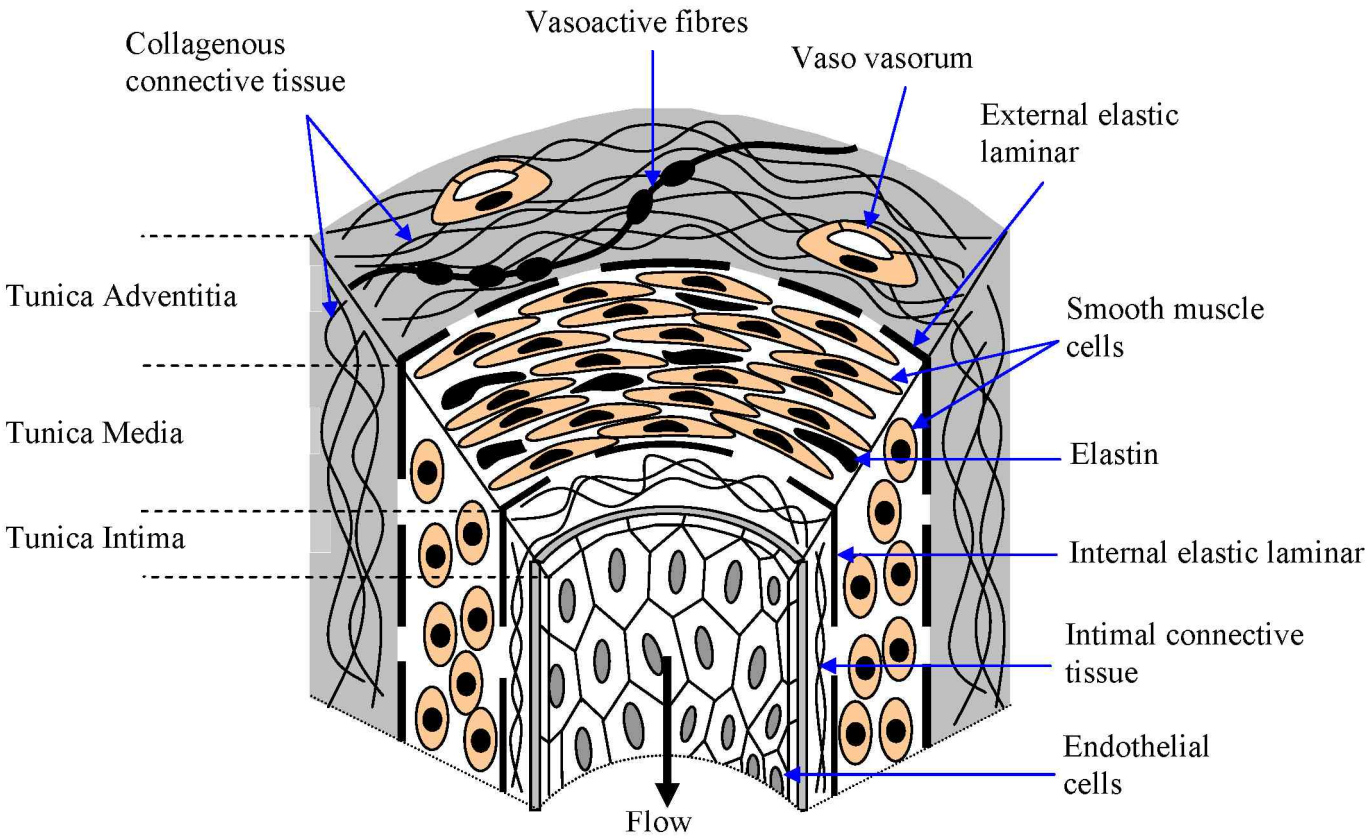

Fig.1: Wall structure of a muscular artery[4].

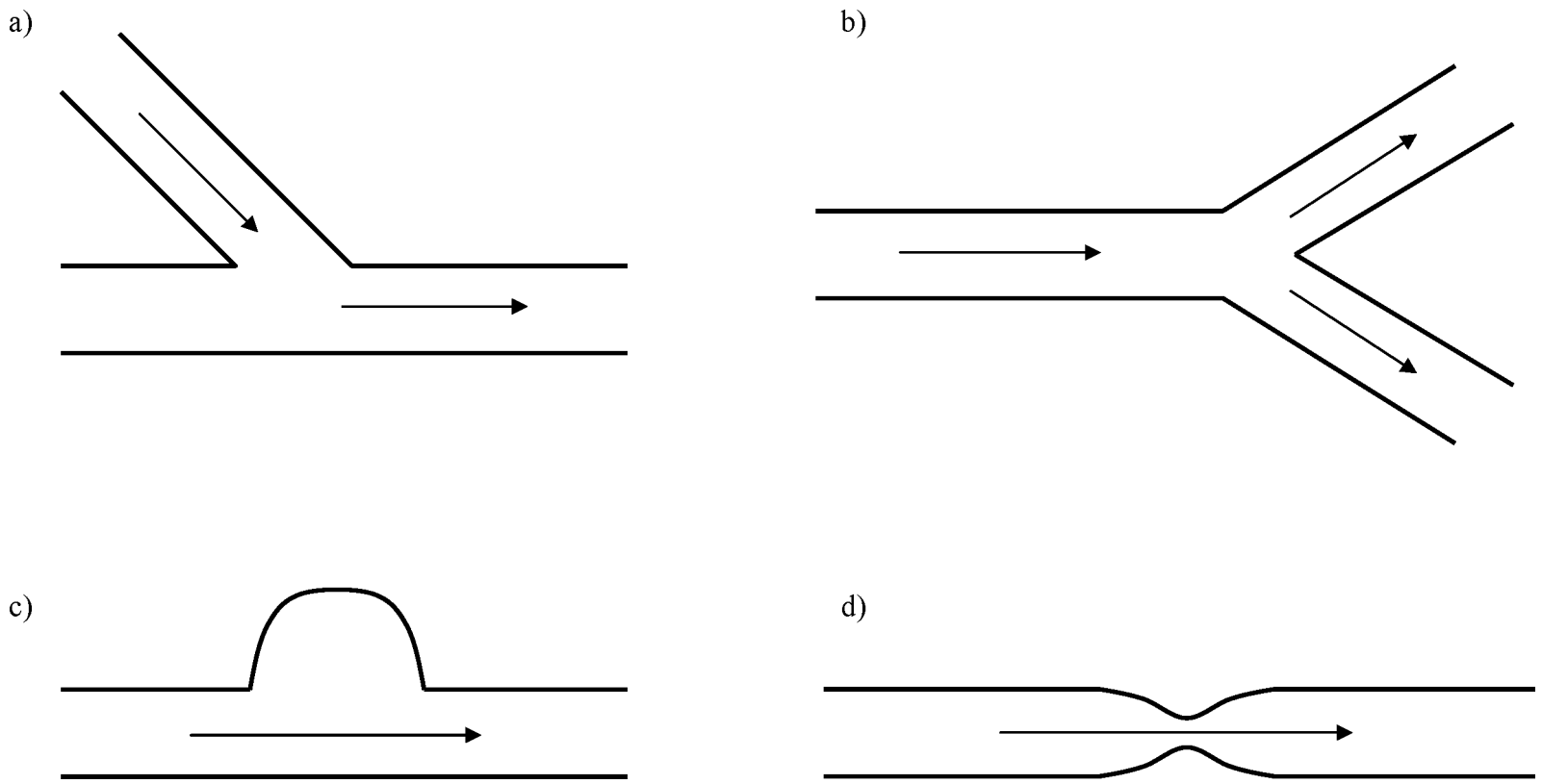

Fig.2: Schematic representations of various arterial geometries with flow direction indicated; a) distal anastomosis; b) bifurcation; c) aneurysm; d) stenosis.

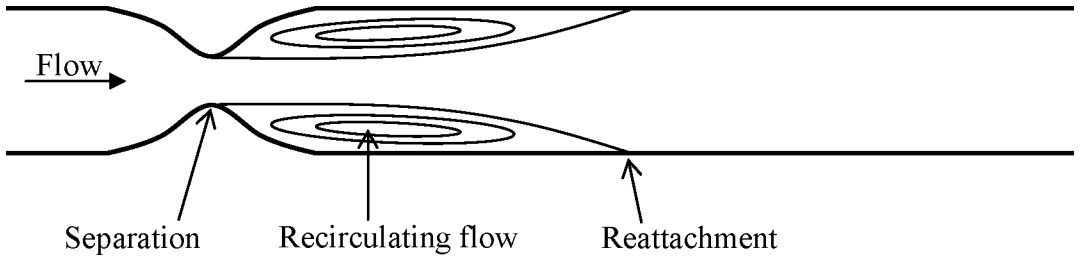

Fig.3: Recirculating flow through an occlusion.

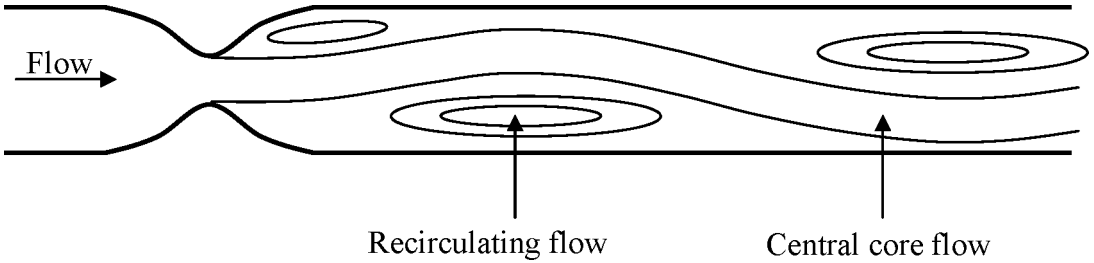

Fig.4: Example of waviness observed distal to a stenosis in unsteady flow.

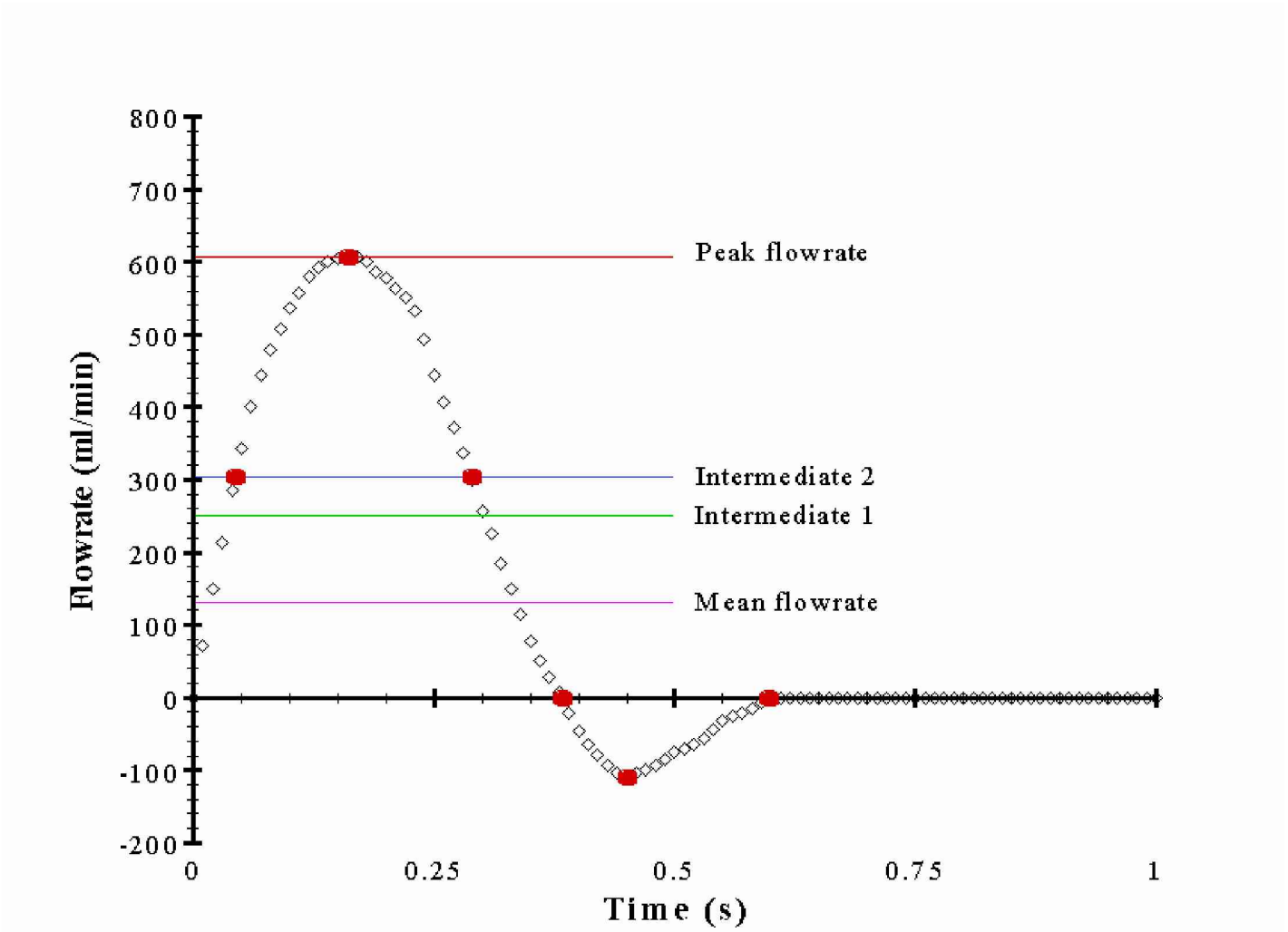

Fig.5: Physiological biphasic flow waveform recorded in the femoral artery under resting conditions[55].

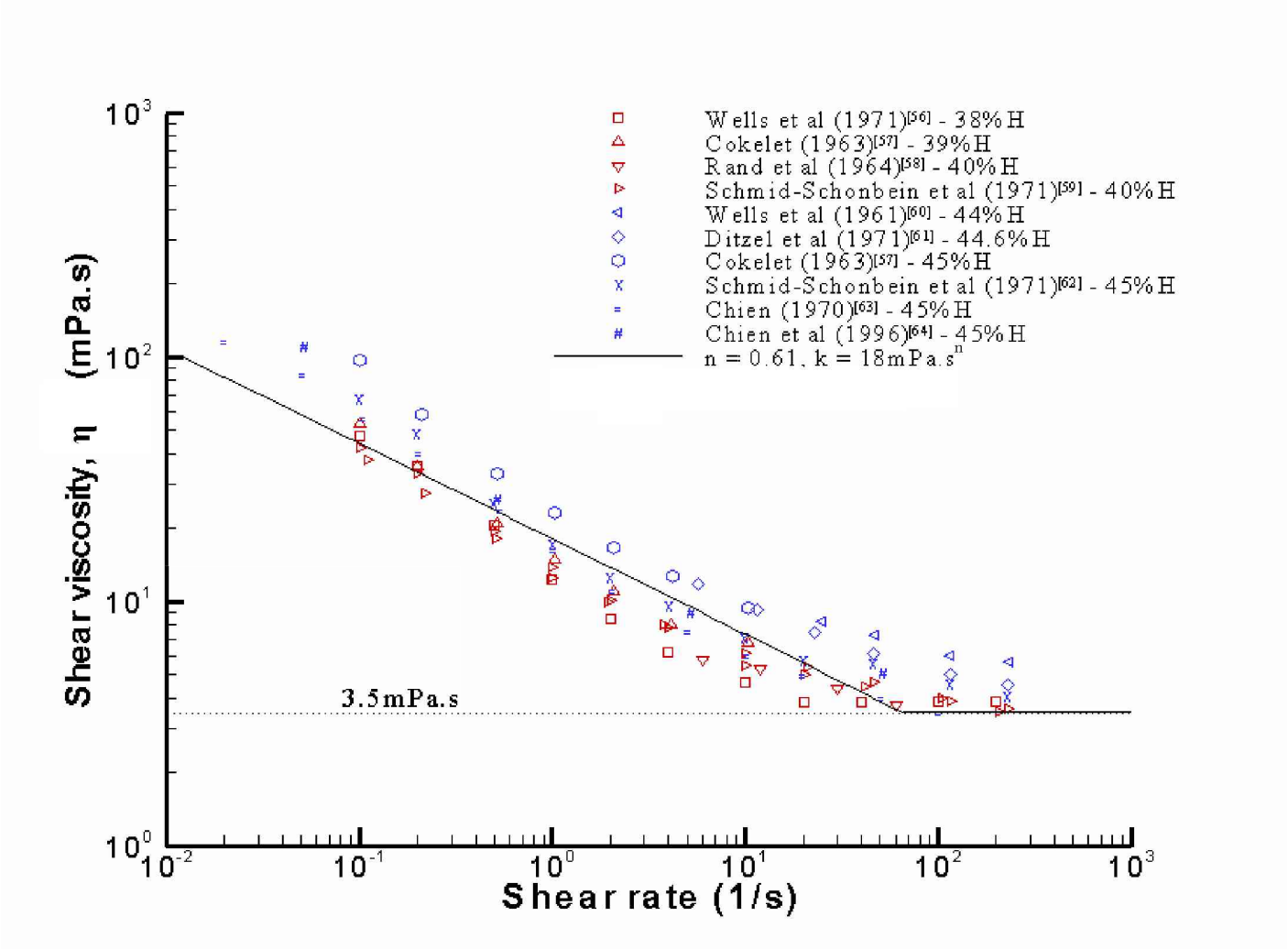

Fig.6: Steady-shear viscosity of blood.

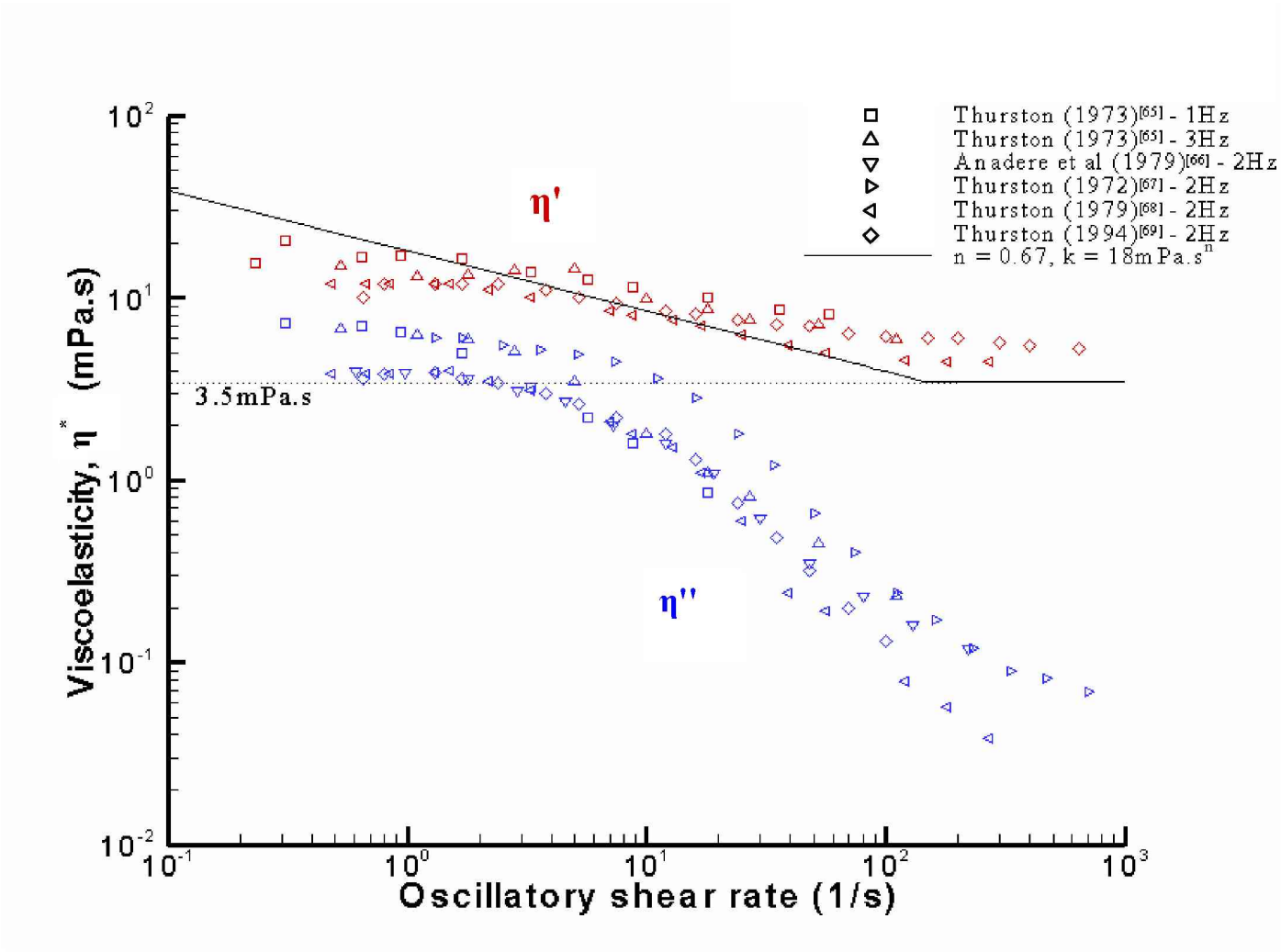

Fig.7: Shear rate dependent viscoelasticity of blood in oscillatory flow conditions (43%<H<50%, 22˚C<T<25˚C).

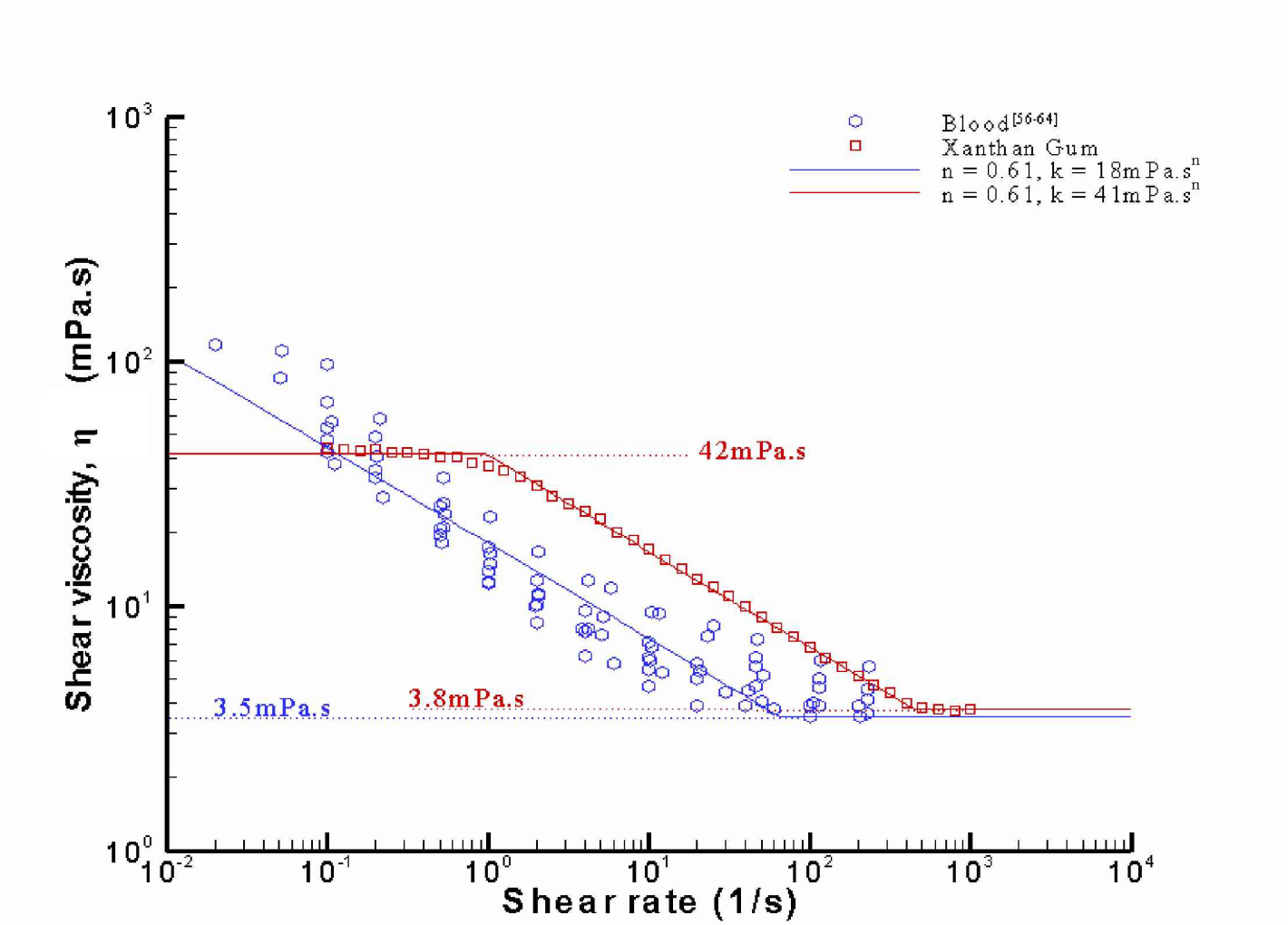

Fig.8: Comparison between the steady-shear viscosity of blood and the Xanthan Gum solution used in the experimental analysis.

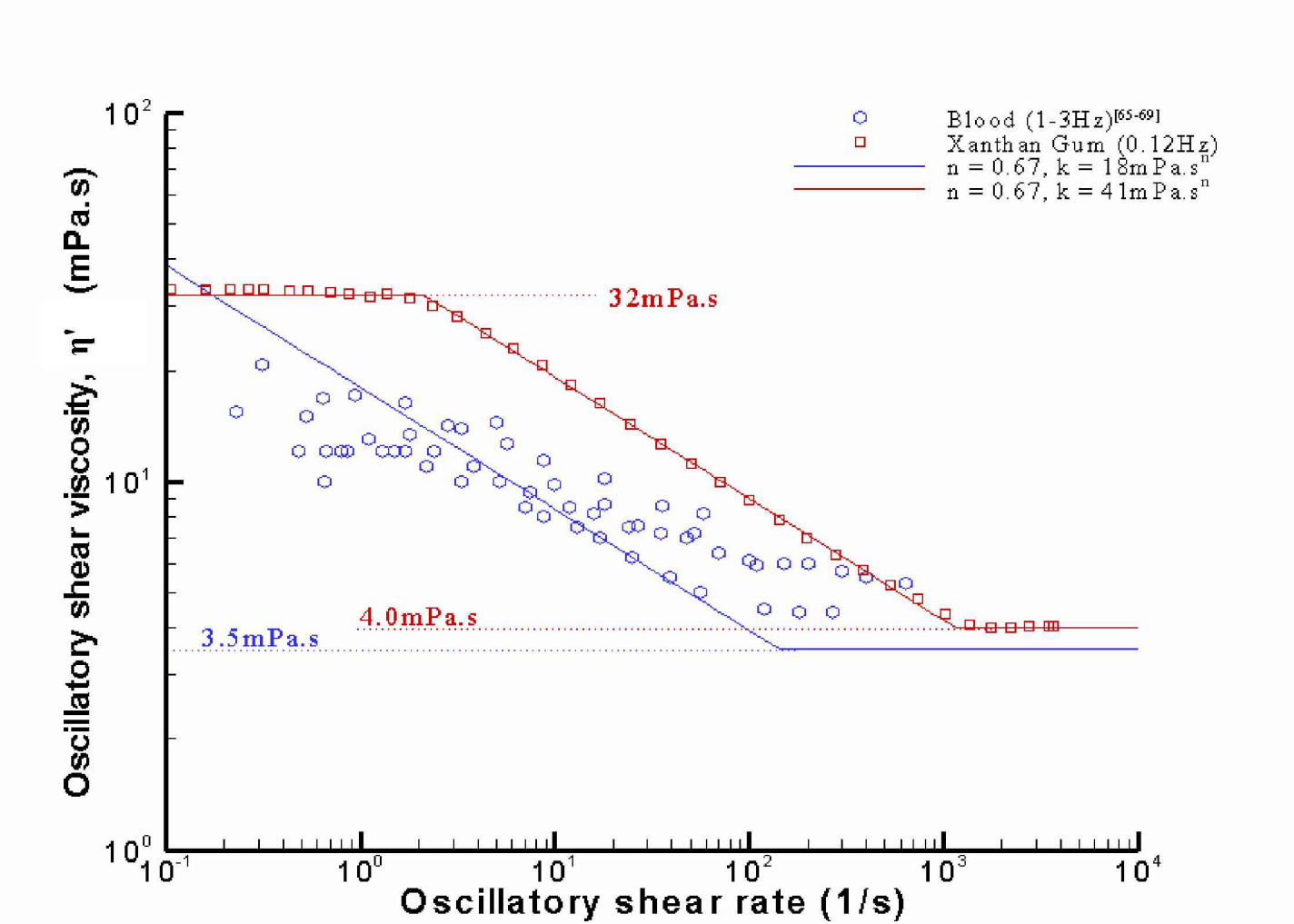

Fig.9: Comparison between the oscillatory-shear viscosity of blood and the Xanthan Gum solution used in the experimental analysis.

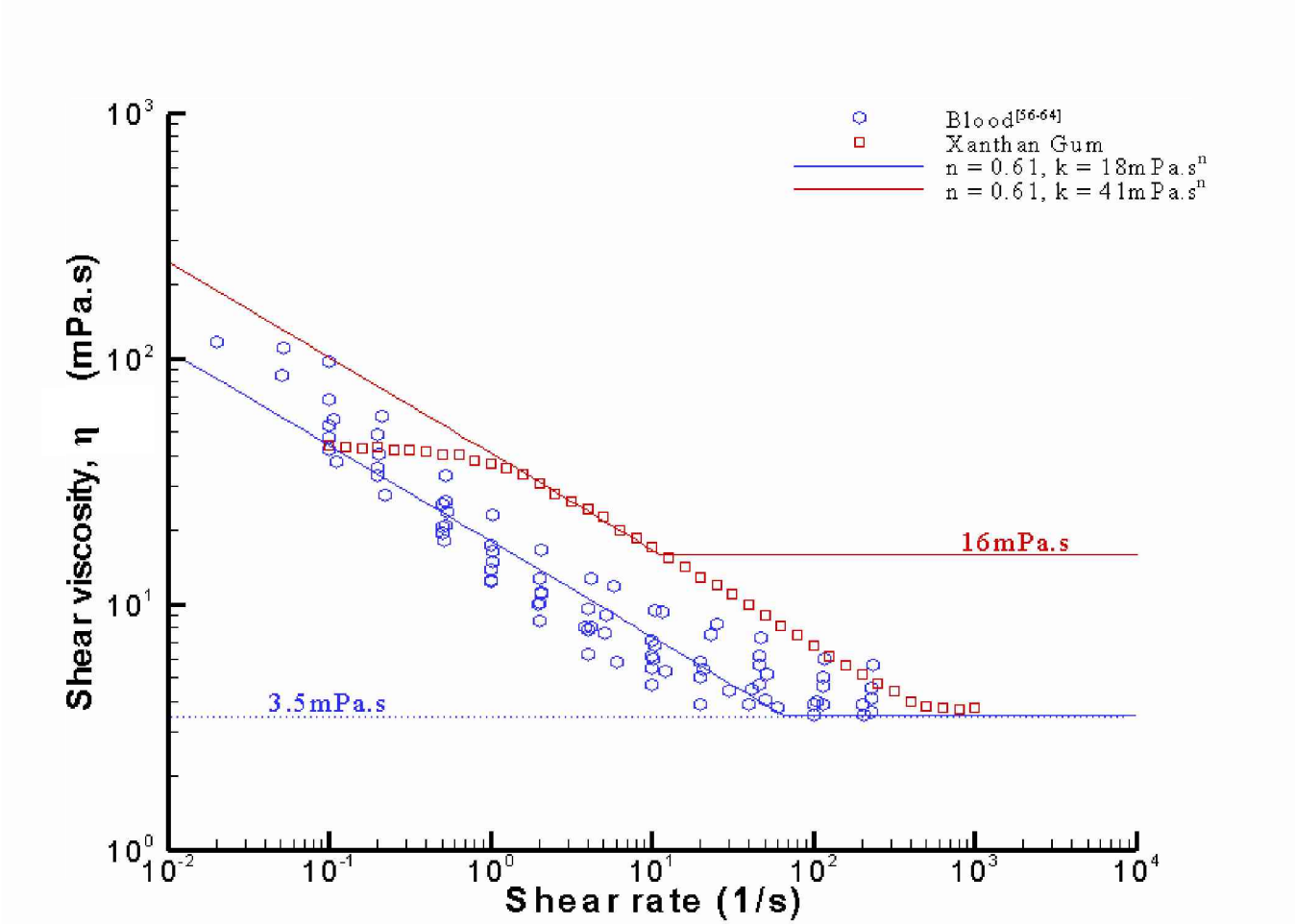

Fig.10: Steady-shear viscosity of blood, the Xanthan Gum solution used in the experimental analysis and a hypothetical fluid which could be used to represent blood.

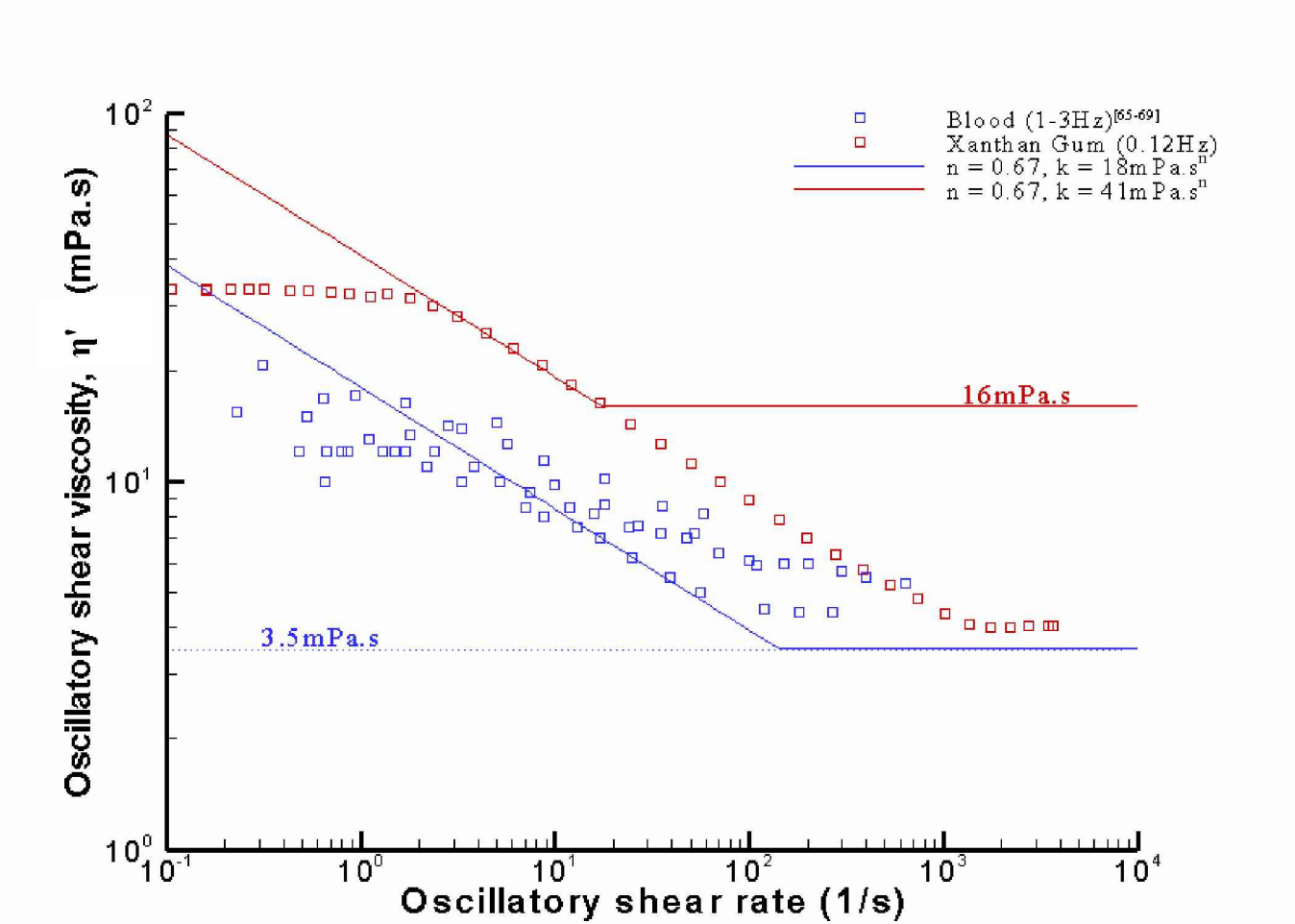

Fig.11: Oscillatory-shear viscosity of blood, the Xanthan Gum solution used in the experimental analysis and a hypothetical fluid which could be used to represent blood.

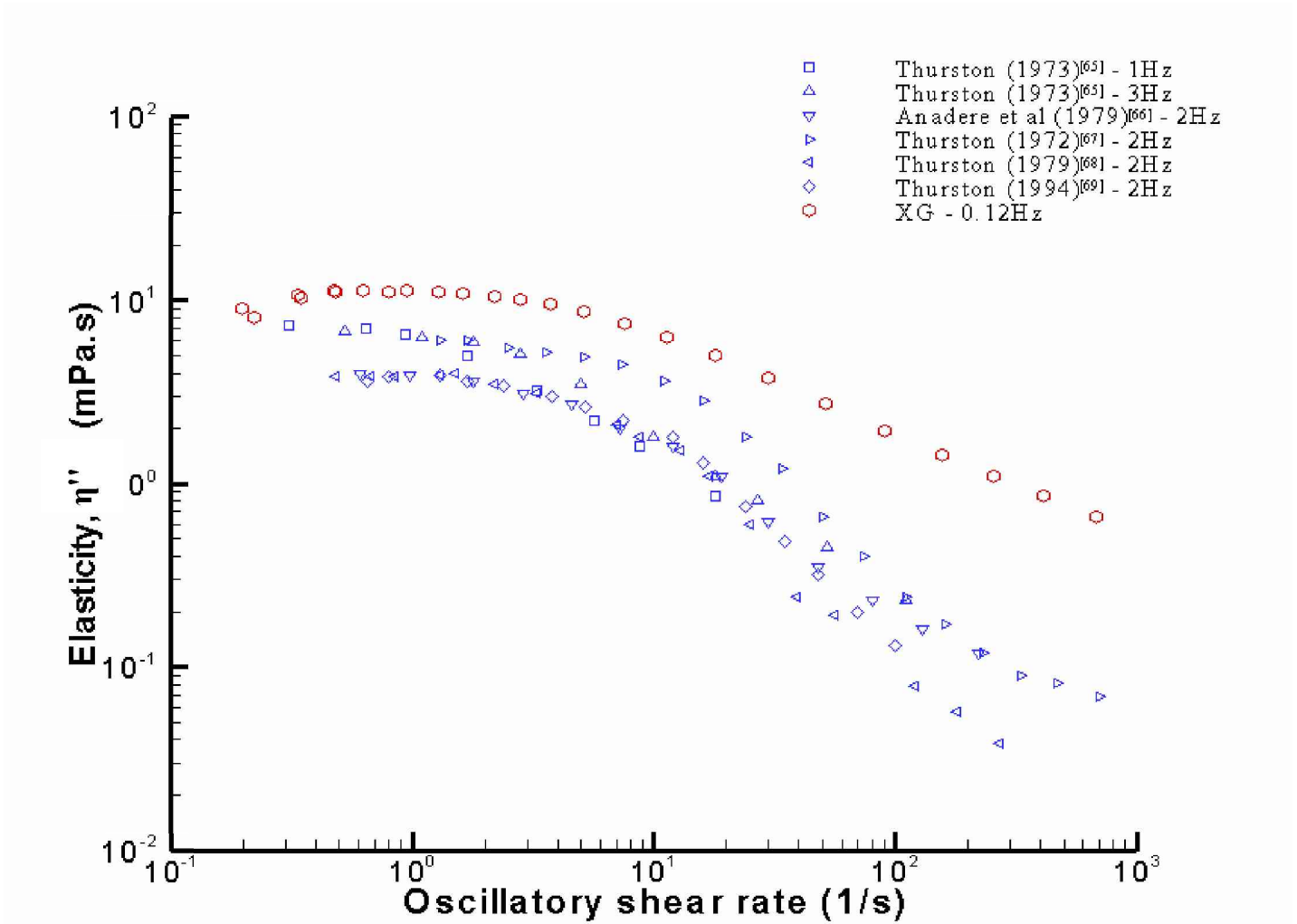

Fig.12: Comparison between the elasticity of blood at various oscillatory frequencies (43%<H<50%, 22°C<T<25°C) and 0.07%wt XG (0.12Hz).

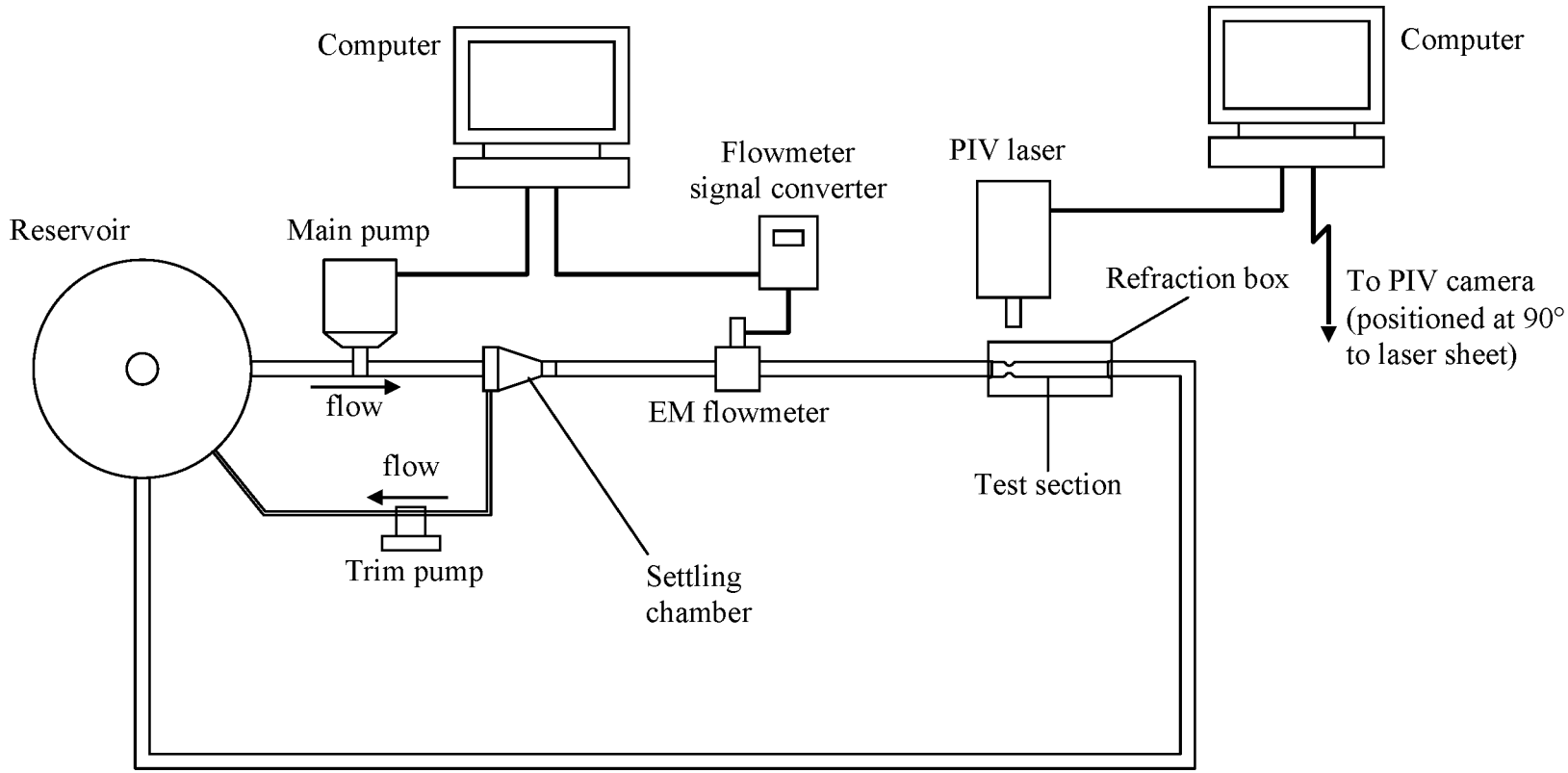

Fig.13: Schematic diagram of experimental apparatus.

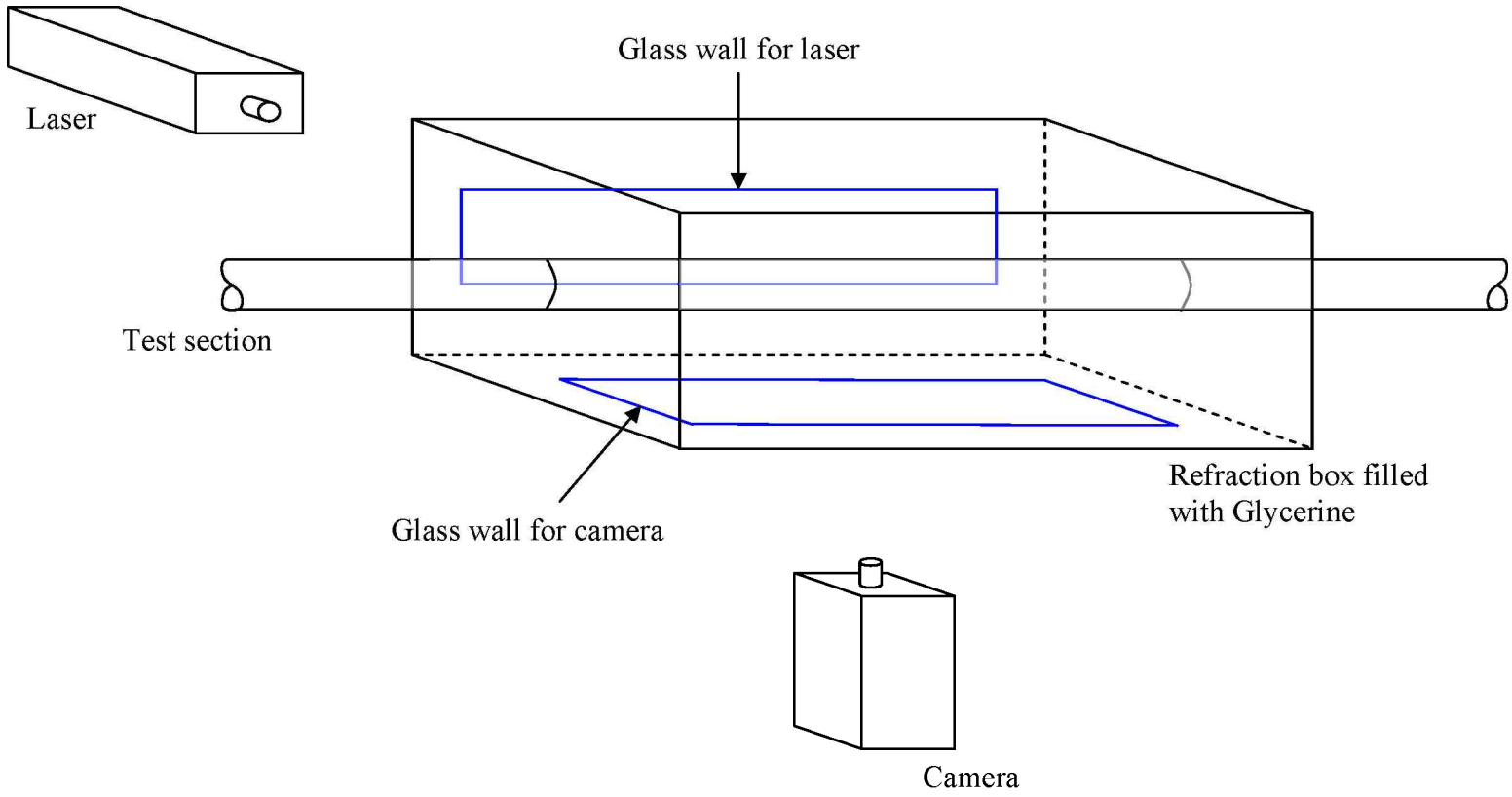

Fig. 14: Refraction box setup.

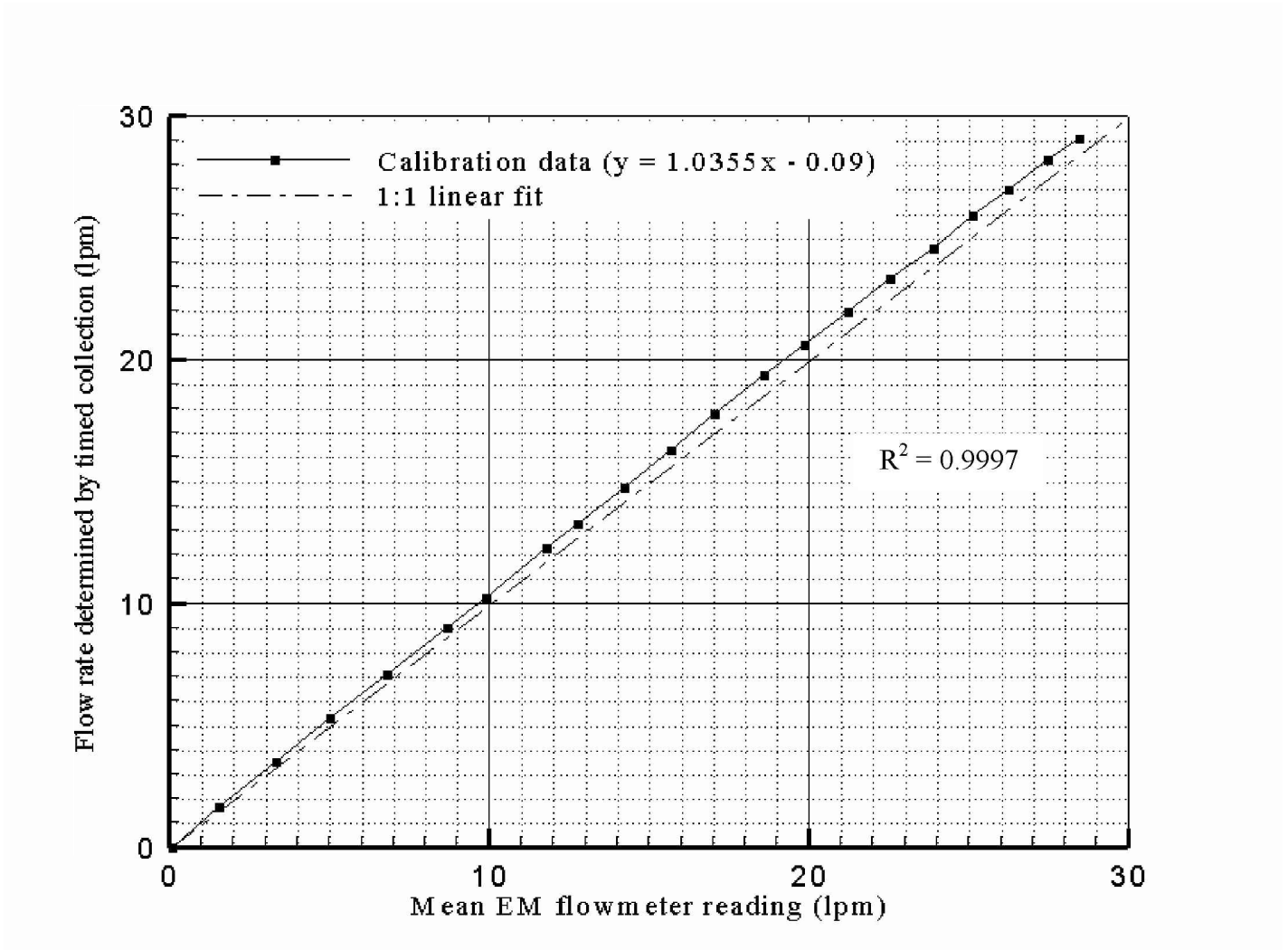

Fig.15: Calibration of electromagnetic flowmeter.

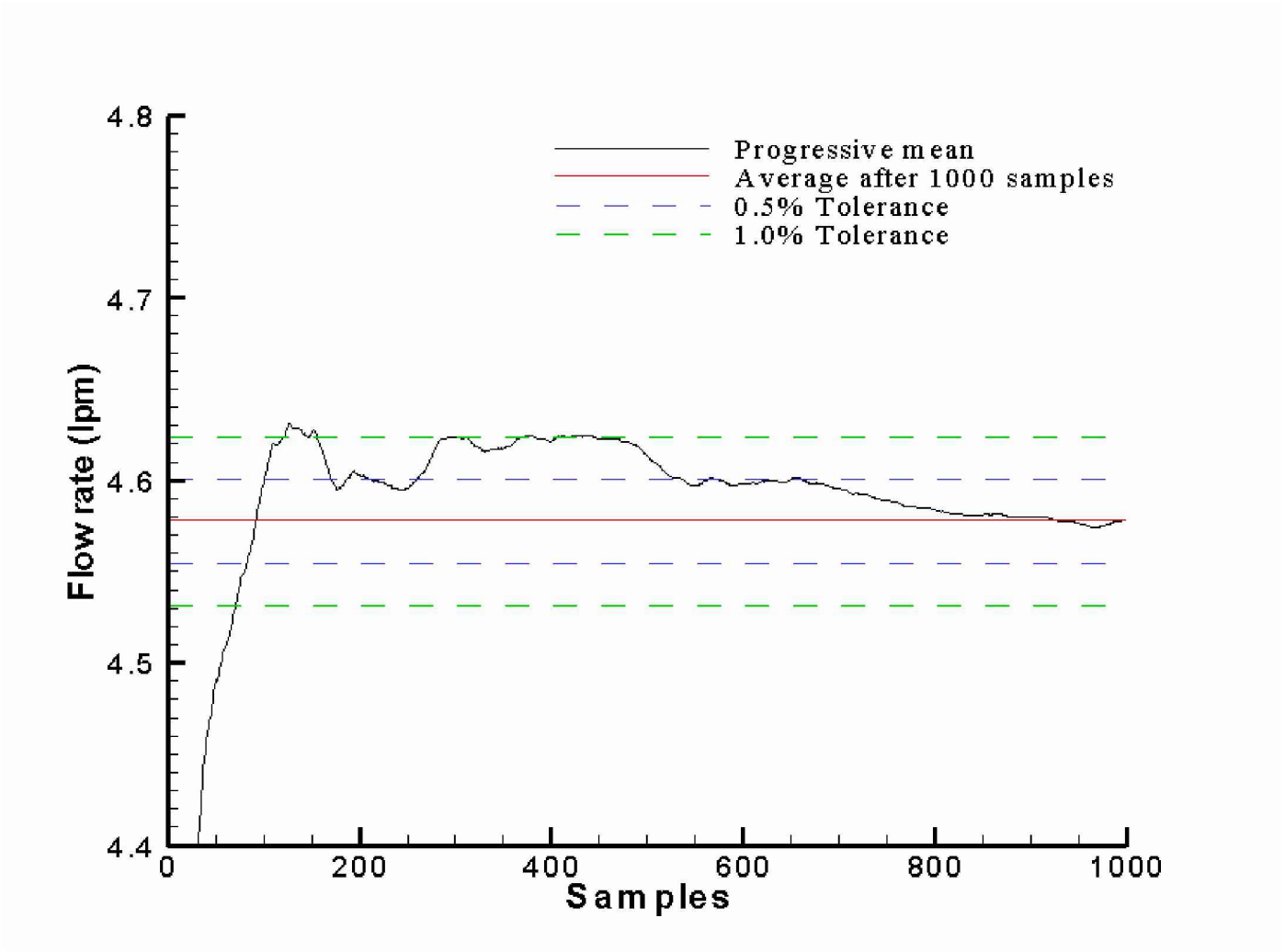

Fig. 16: Electromagnetic flowmeter: Convergence of flow rate with increasing sample count. Flow rate = 4.58lpm.

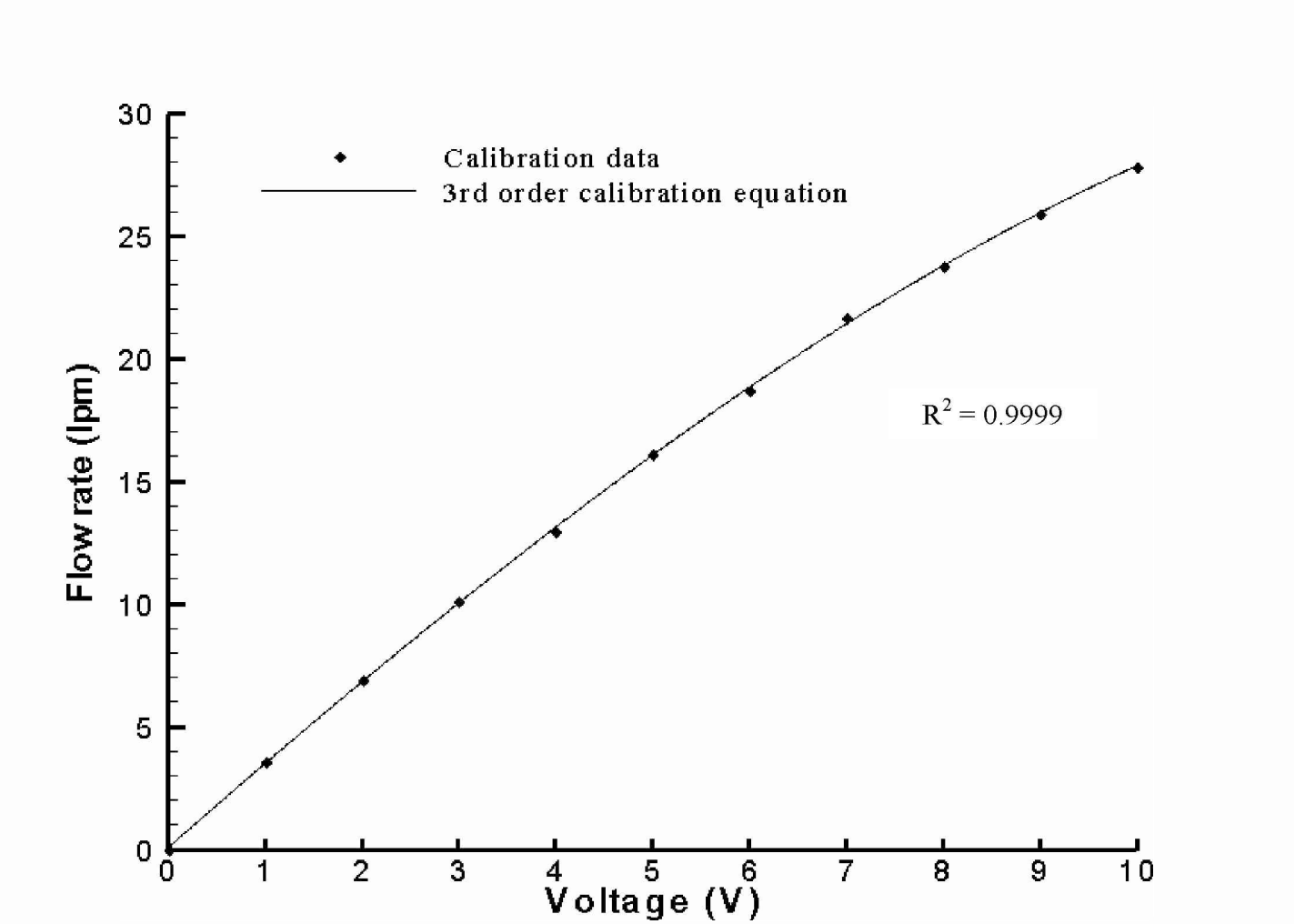

Fig.17: Calibration of the main pump used in the experimental analysis (51% severity).

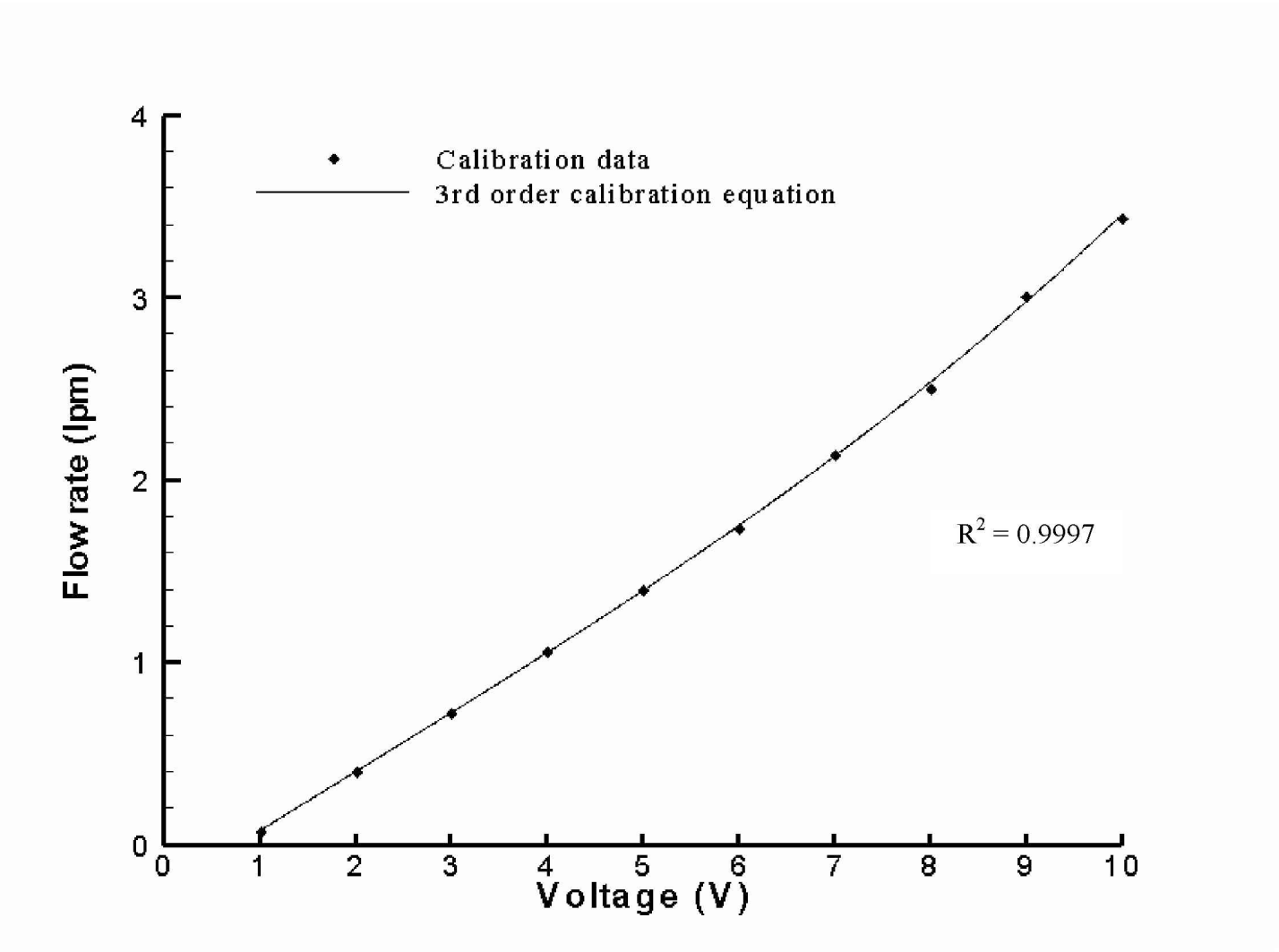

Fig.18: Calibration of the trim pump used in the experimental analysis (51% severity).

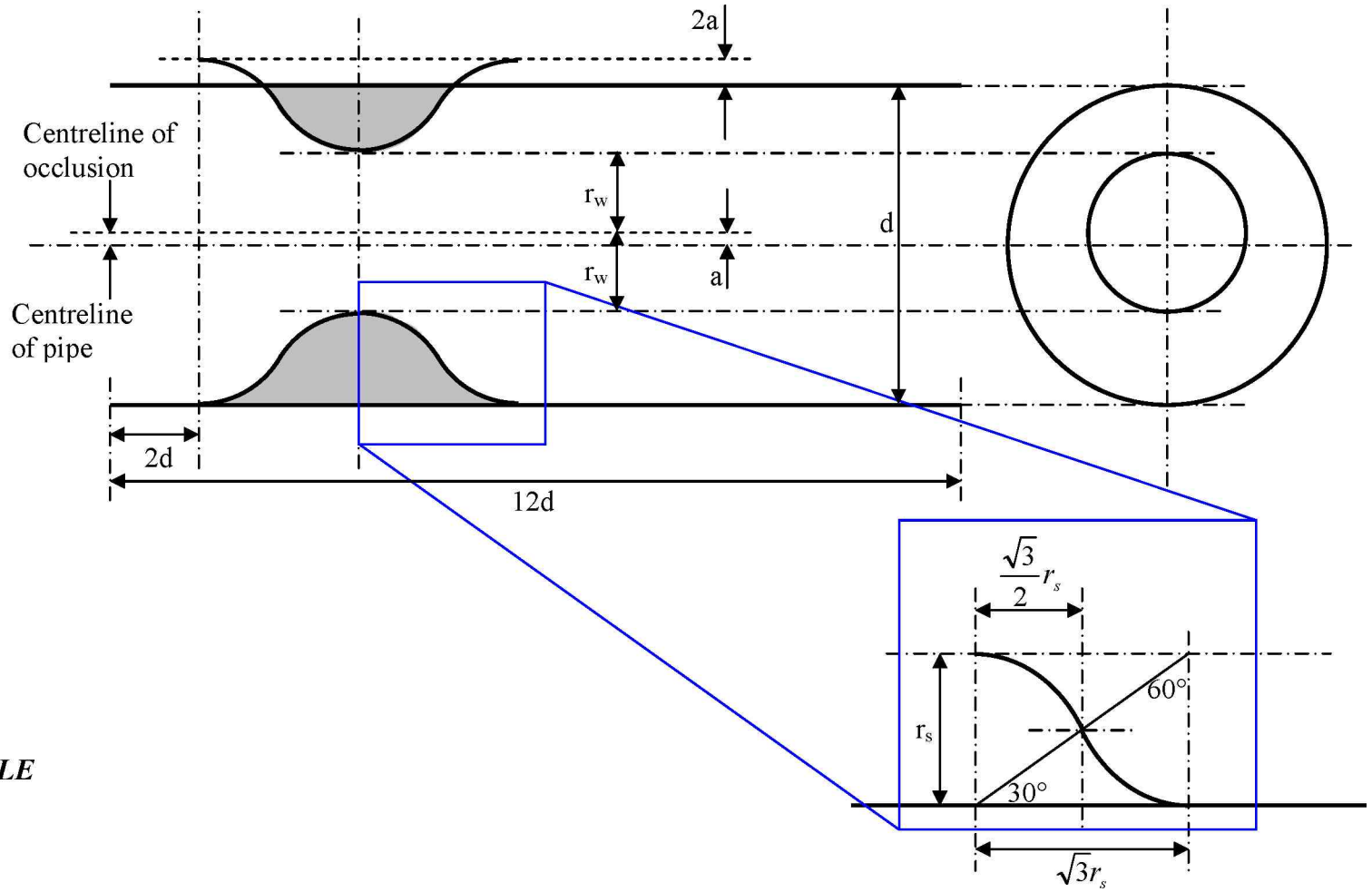

NOT TO SCALE

Fig.19: Schematic of the stenosis test section.

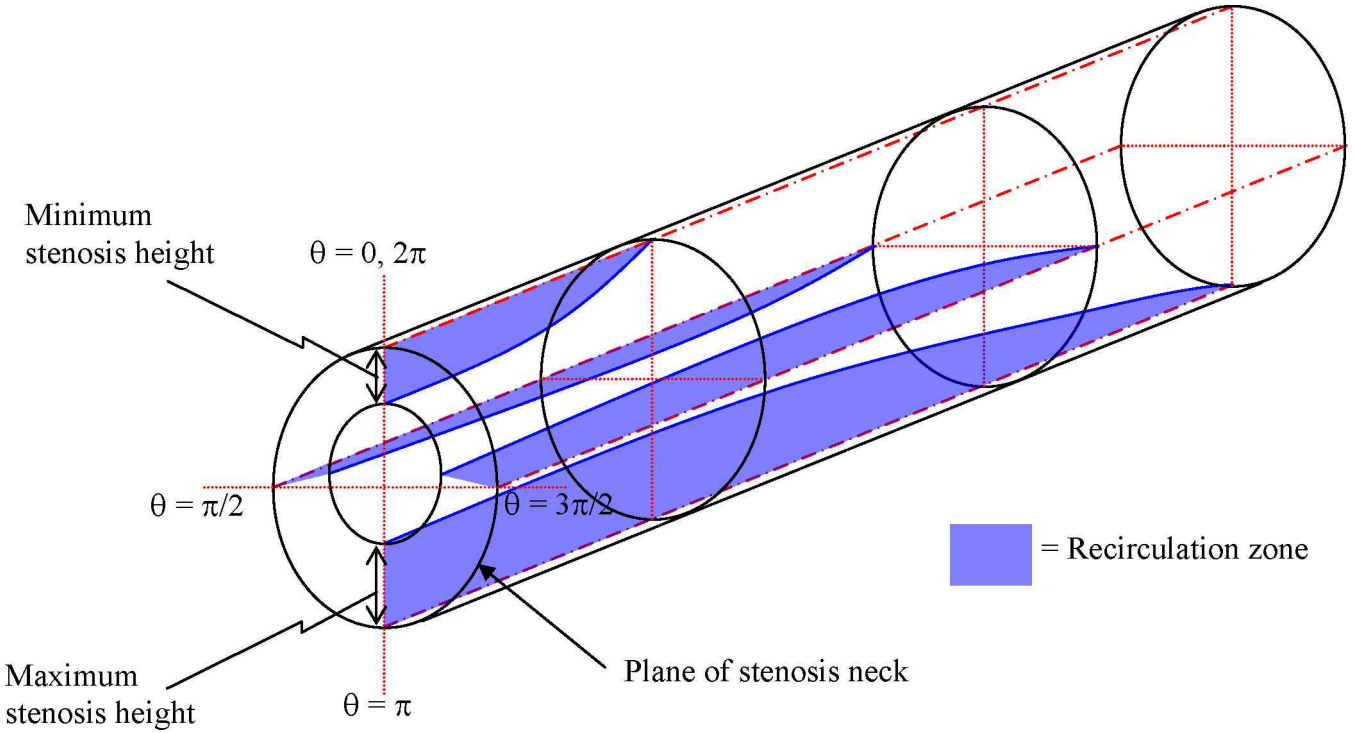

Fig.20: Attachment points and areas of recirculation in an asymmetric stenosis.

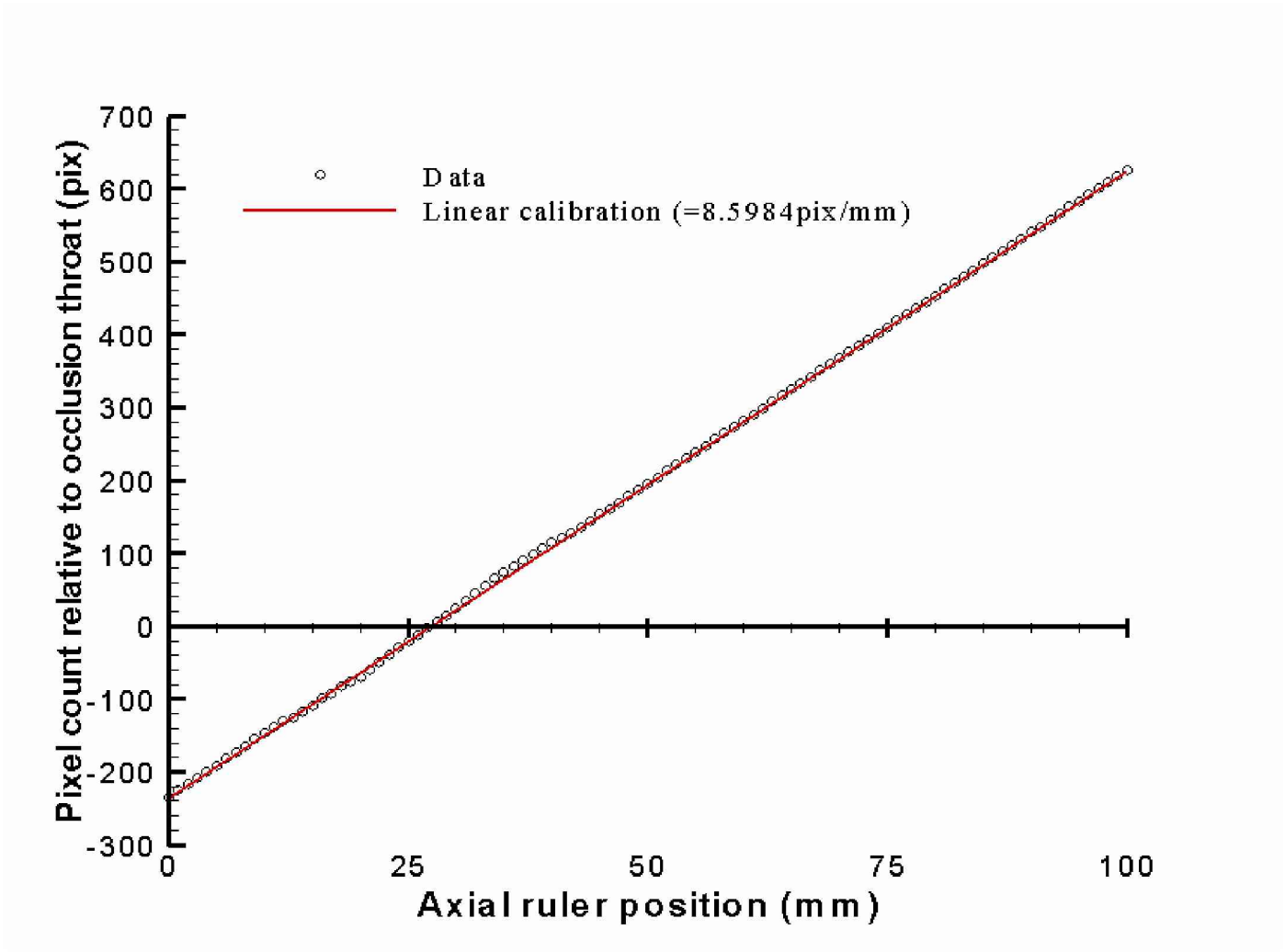

Fig.21: Calibration of the scale factor, defining the number of camera pixels per millimetre (51% severity).

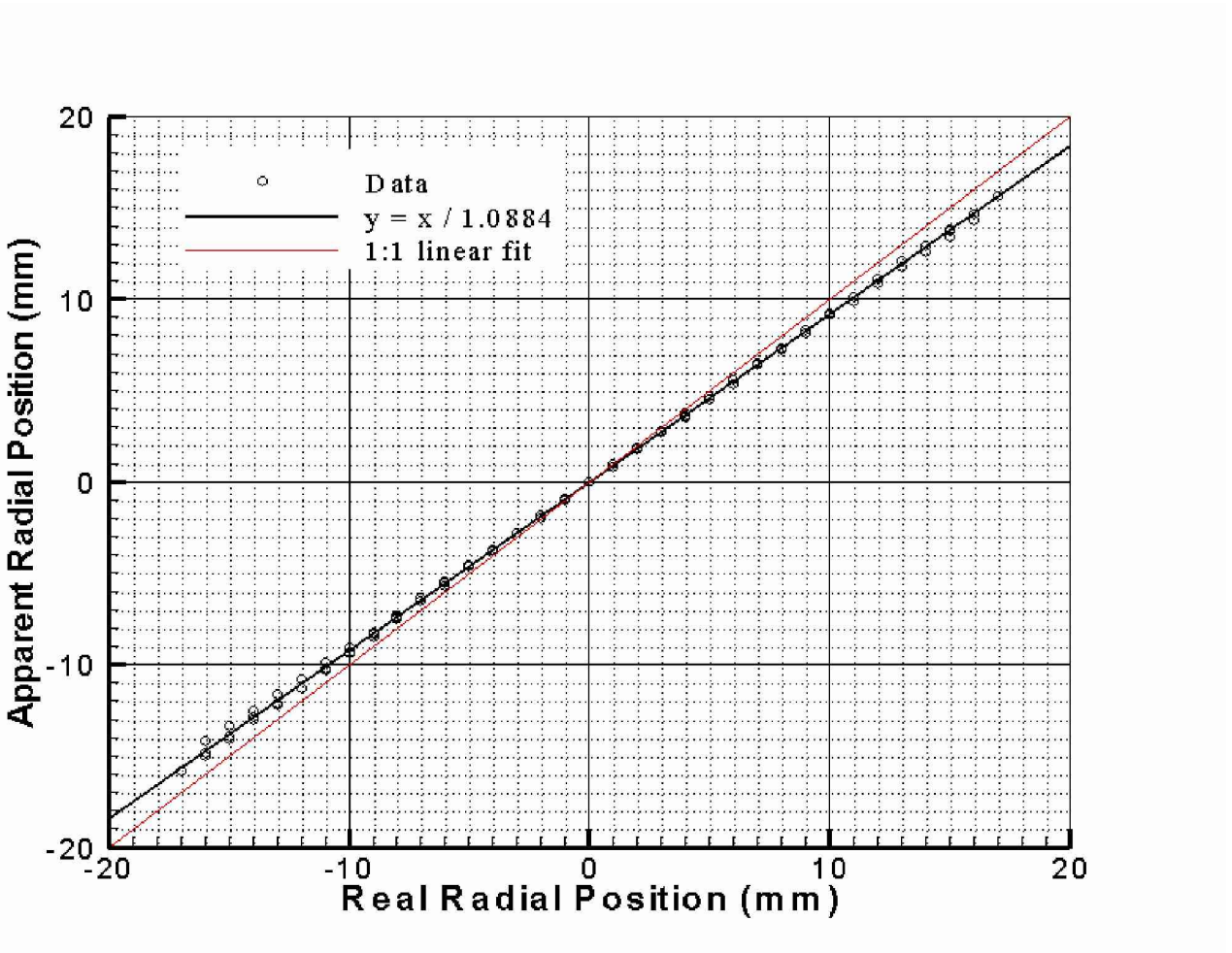

Fig.22: Estimation of the correction factor, introduced to account for the effects of refraction at the boundary between the glass test section and the test fluid (51% severity).

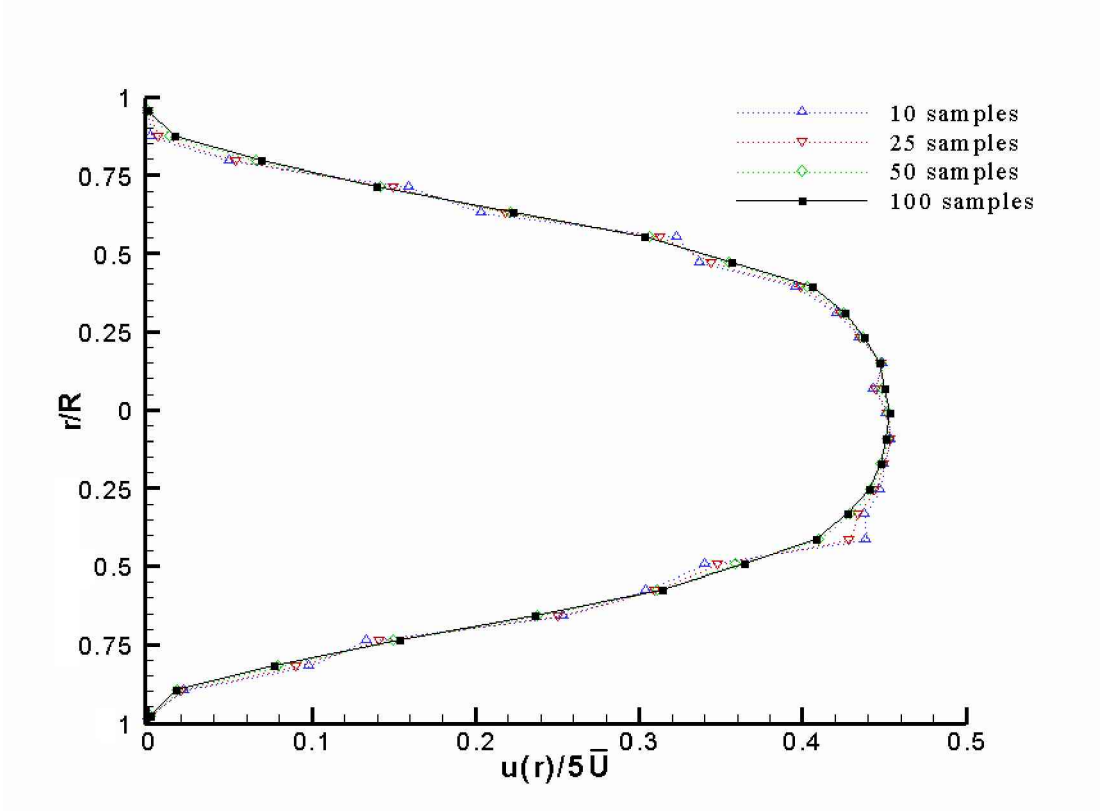

Fig.23a: Velocity profiles one diameter distal to the occlusion in the 51% severity occlusion, Re_{PL} = 74. Sample size of 10, 25, 50 and 100.

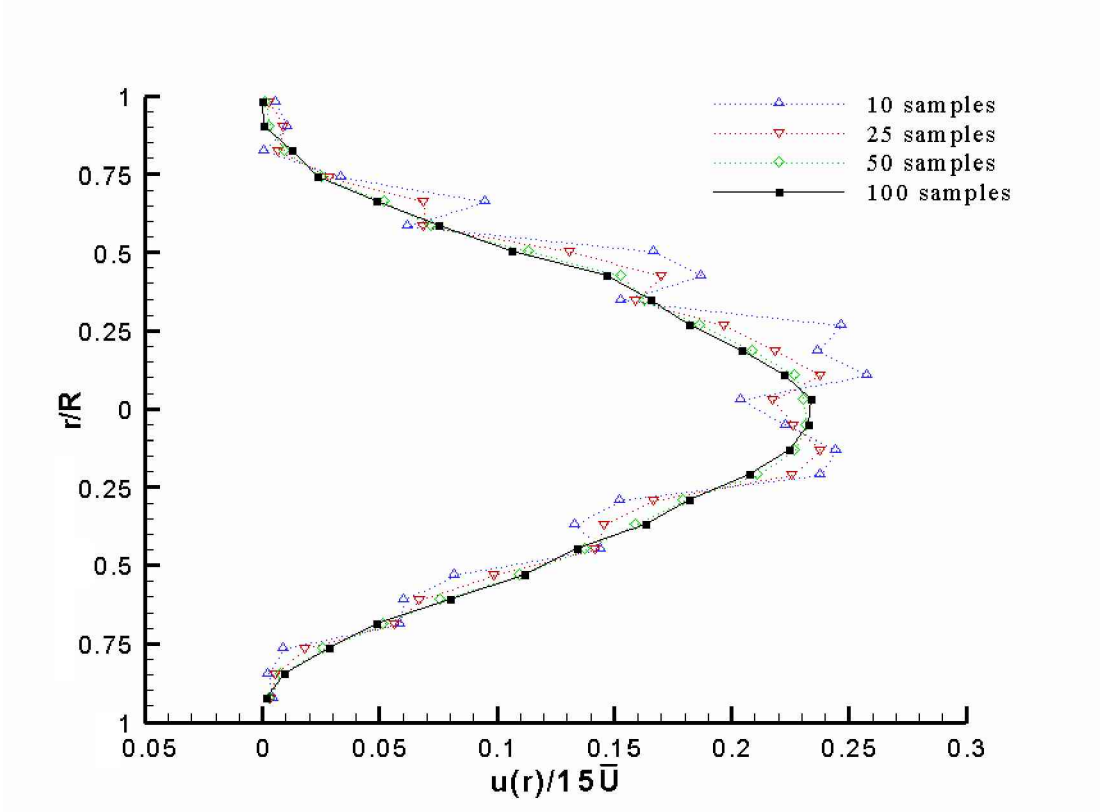

Fig.23b: Velocity profiles two diameters distal to the occlusion in the 84% severity occlusion, Re_{PL} = 617. Sample size of 10, 25, 50 and 100.

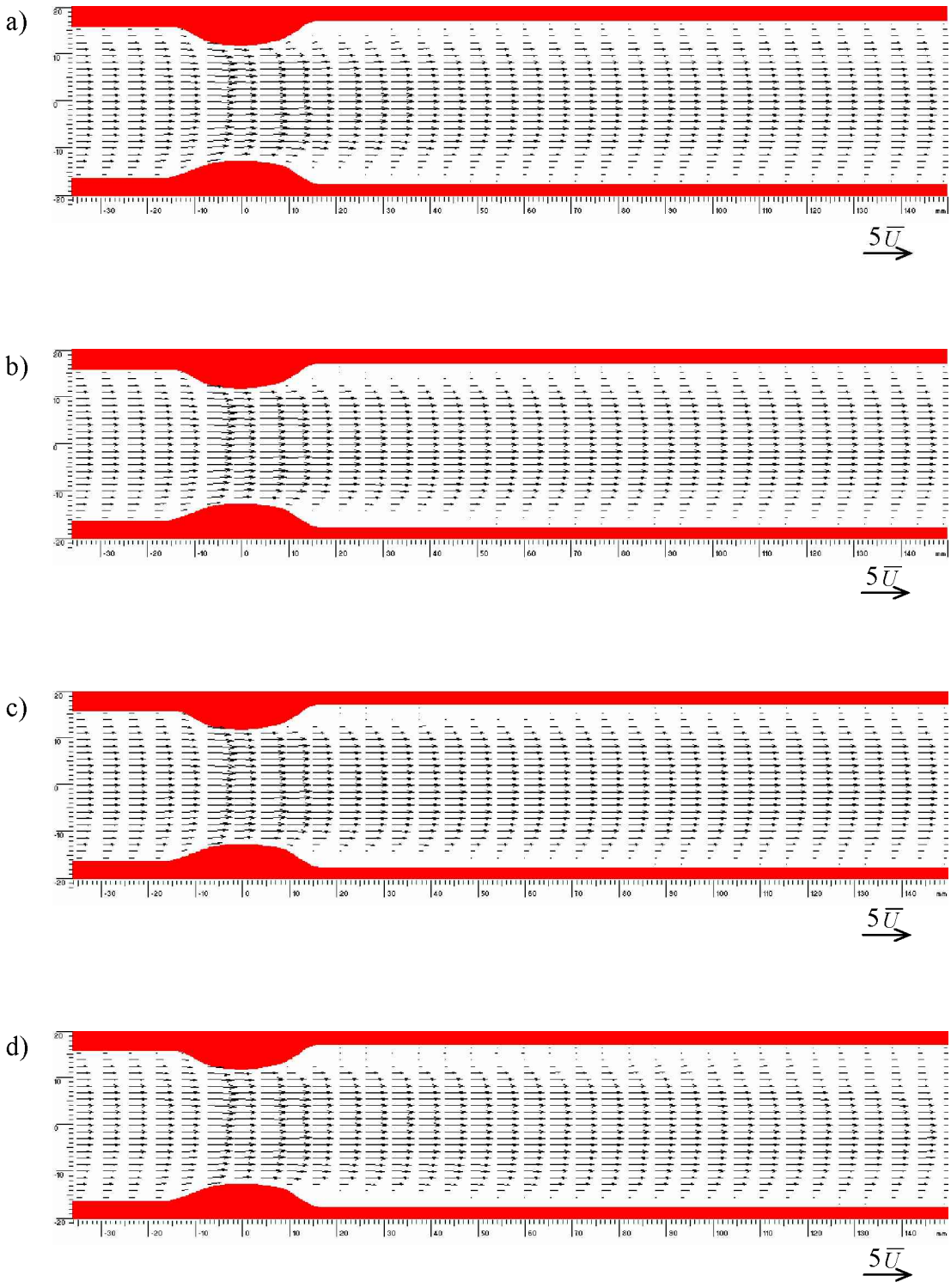

Fig.24: Mean velocity vector field (calculated from 100 raw PIV data sets) for 51% occlusive severity. a) Re_{PL} = 74, b) Re_{PL} = 180, c) Re_{PL} = 235 and d) Re_{PL} = 617.

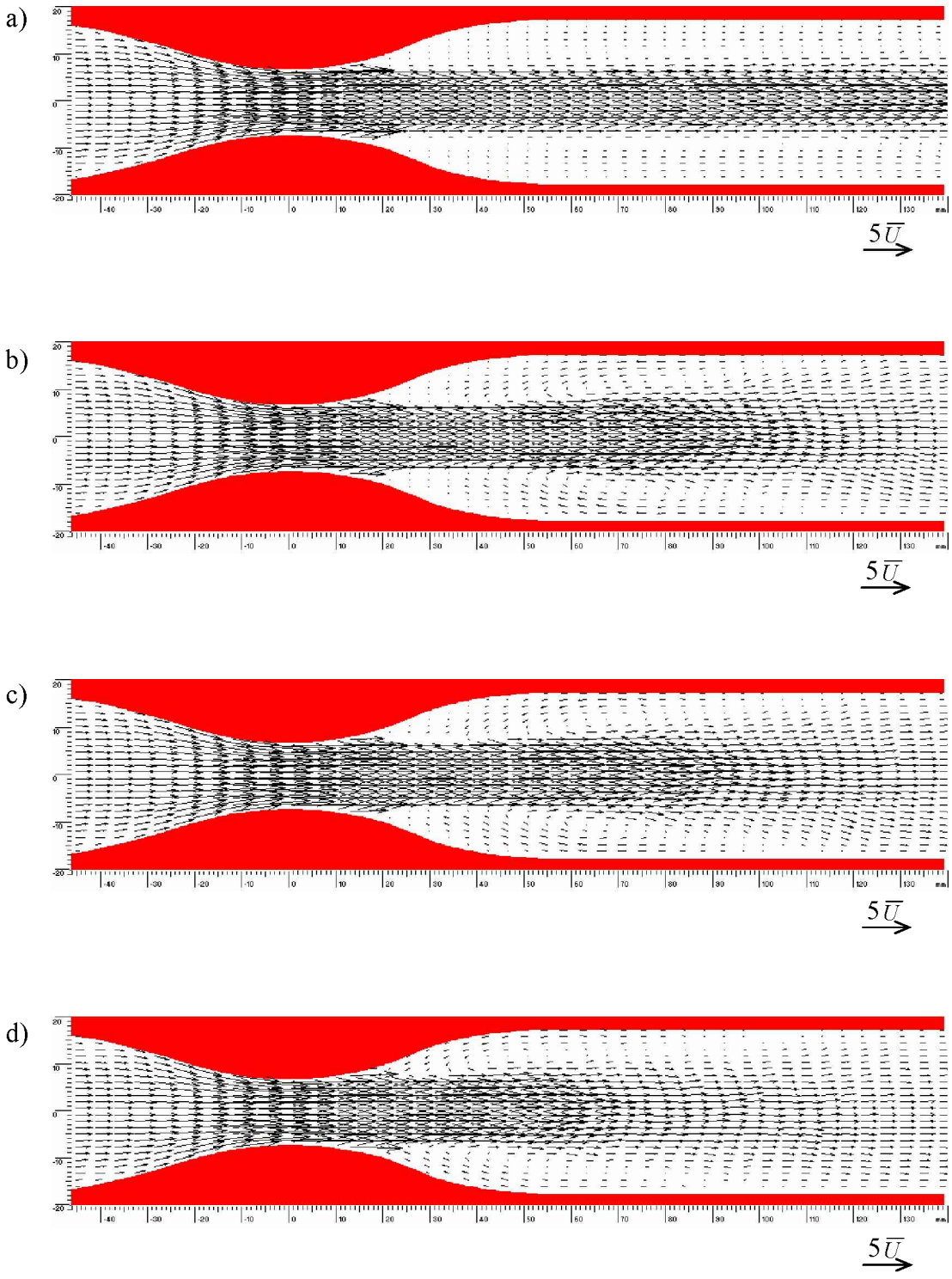

Fig.25: Mean velocity vector field (calculated from 100 raw PIV data sets) for 84% occlusive severity. a) Re_{PL} = 74, b) Re_{PL} = 180, c) Re_{PL} = 235 and d) Re_{PL} = 617.

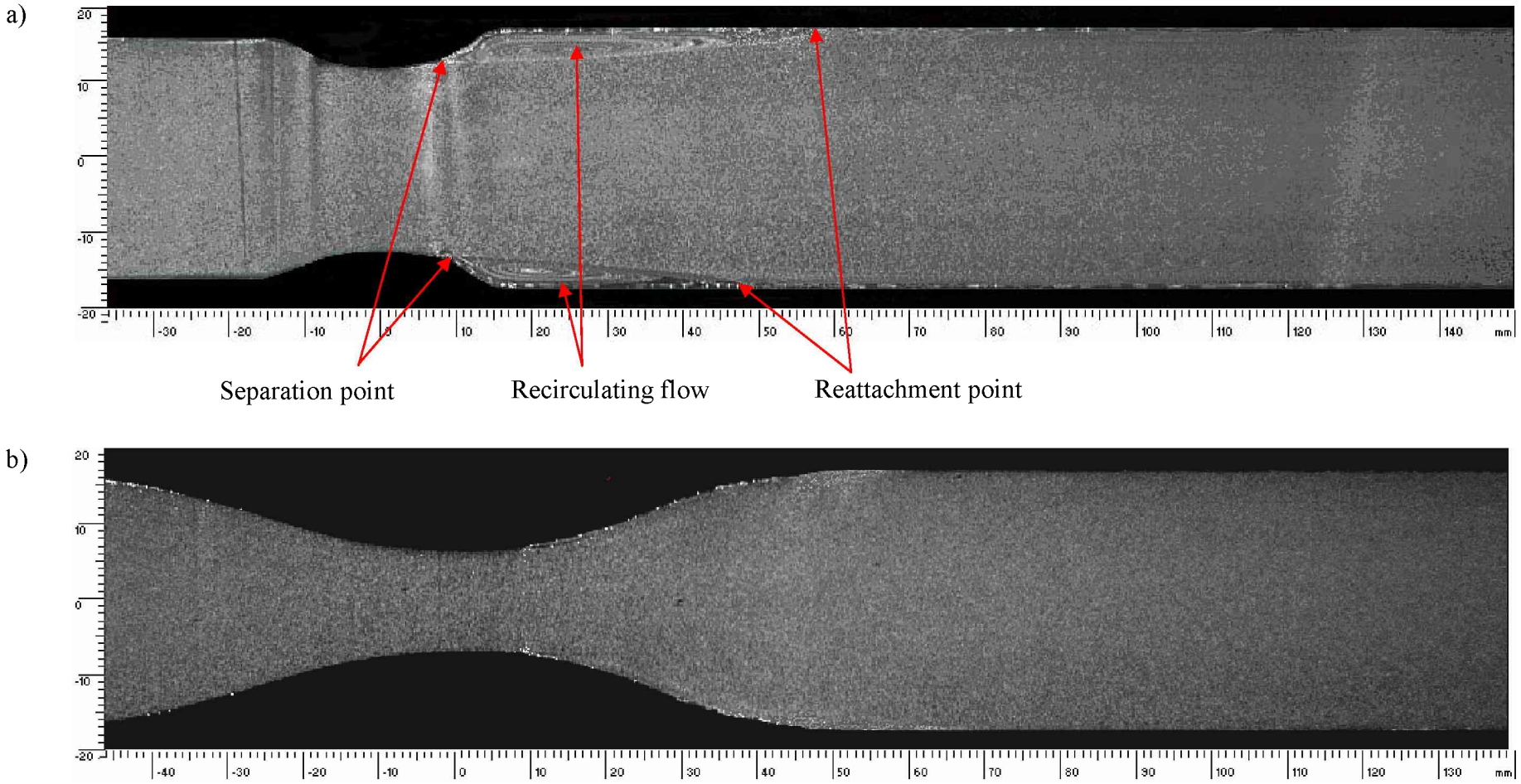

Fig.26: Visualisation of the flow in the test section, a) 51% occlusive severity, Re_{PL} = 180, b) 84% occlusive severity, Re_{PL} = 180.

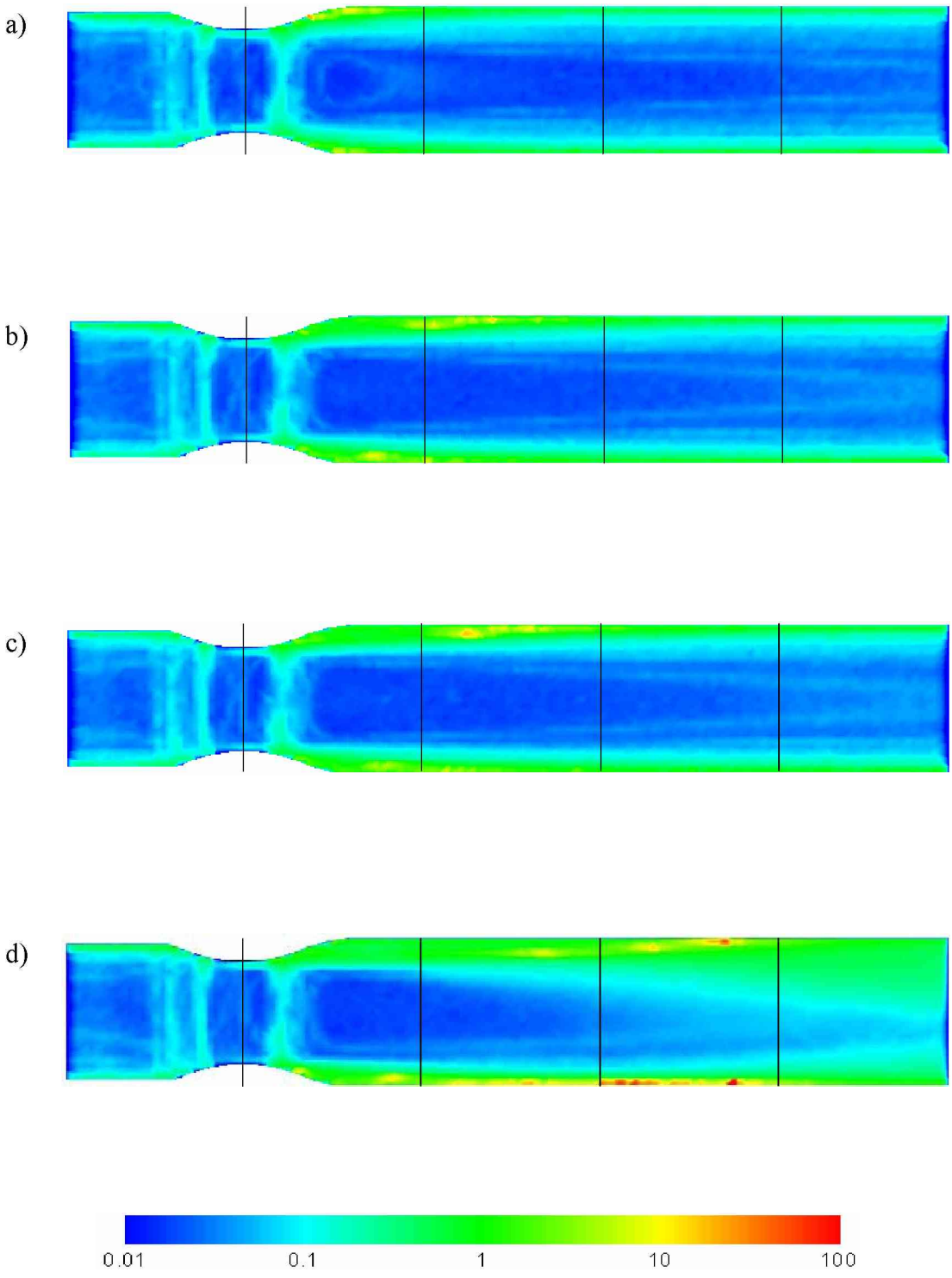

Fig.27: Normalized standard deviation maps of PIV data (51% occlusive severity) for a) Re_{PL} = 74, b) Re_{PL} = 180, c) Re_{PL} = 235 and d) Re_{PL} = 617. Intervals shown every diameter.

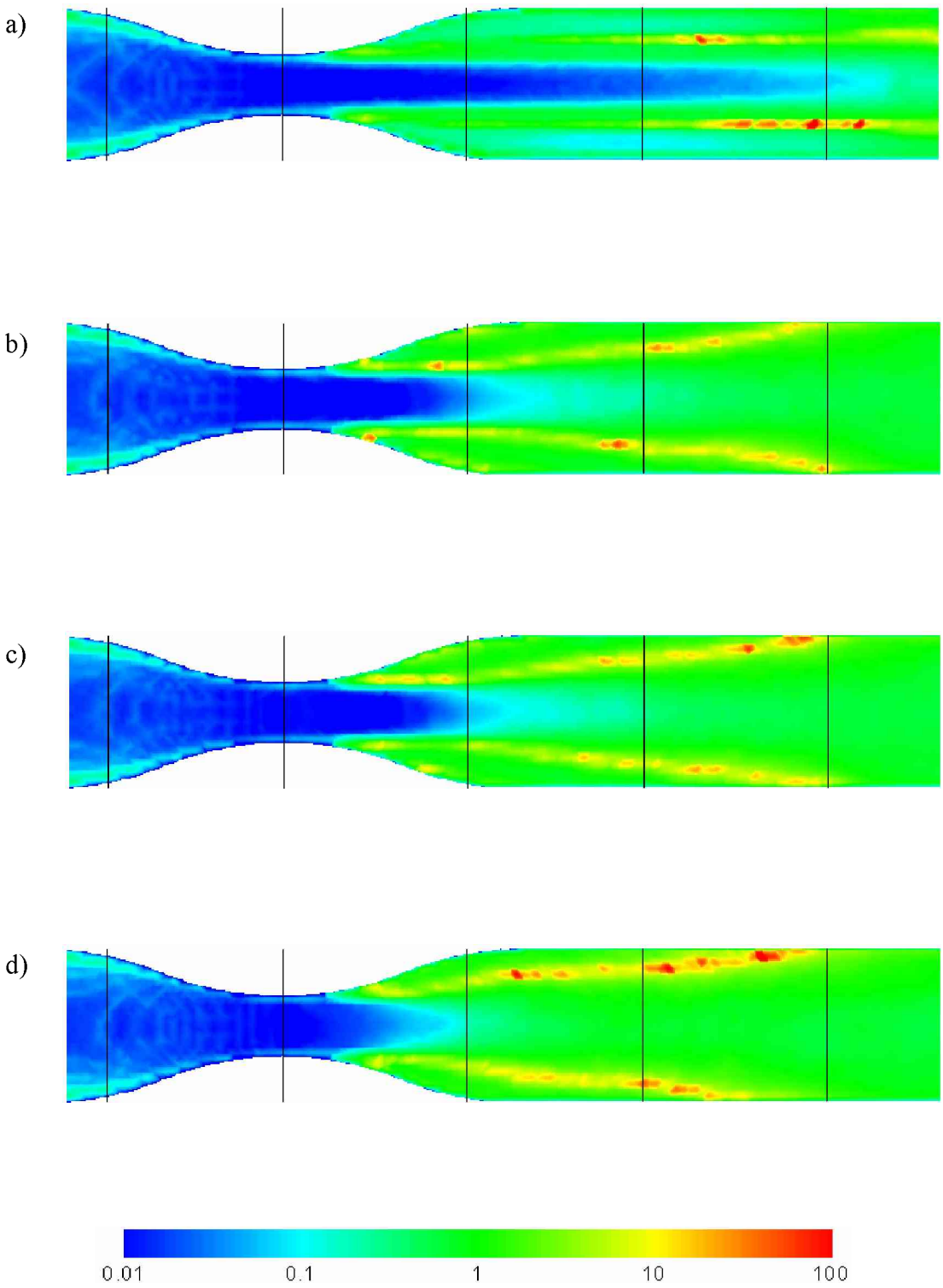

Fig.28: Normalized standard deviation maps of PIV data (84% occlusive severity) for a) Re_{PL} = 74, b) Re_{PL} = 180, c) Re_{PL} = 235 and d) Re_{PL} = 617. Intervals shown every diameter.

a)

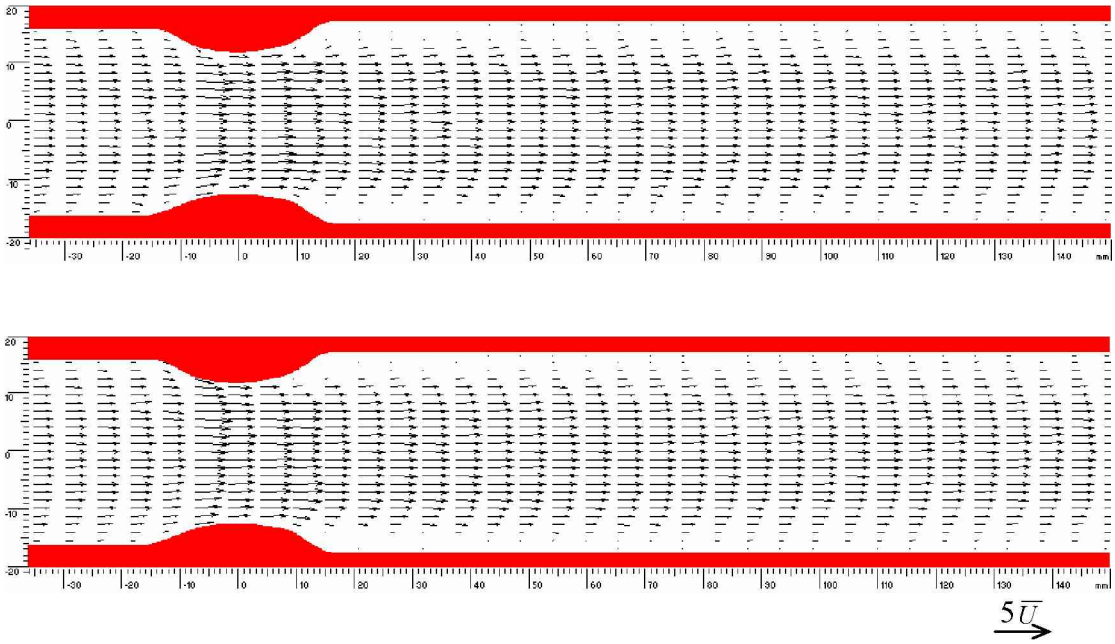

b)

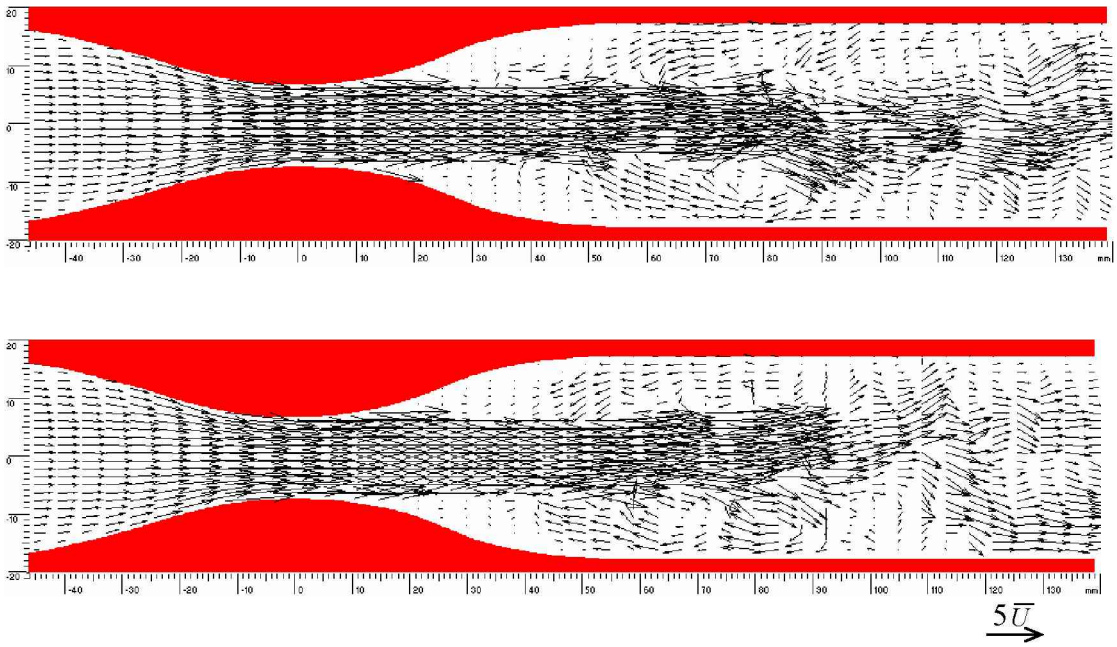

Fig.29: Comparison between the individual vector maps used to calculate the mean vector maps shown in Fig.26b and Fig.27b. Re_{PL} = 180. a) 51% occlusive severity, b) 84% occlusive severity.

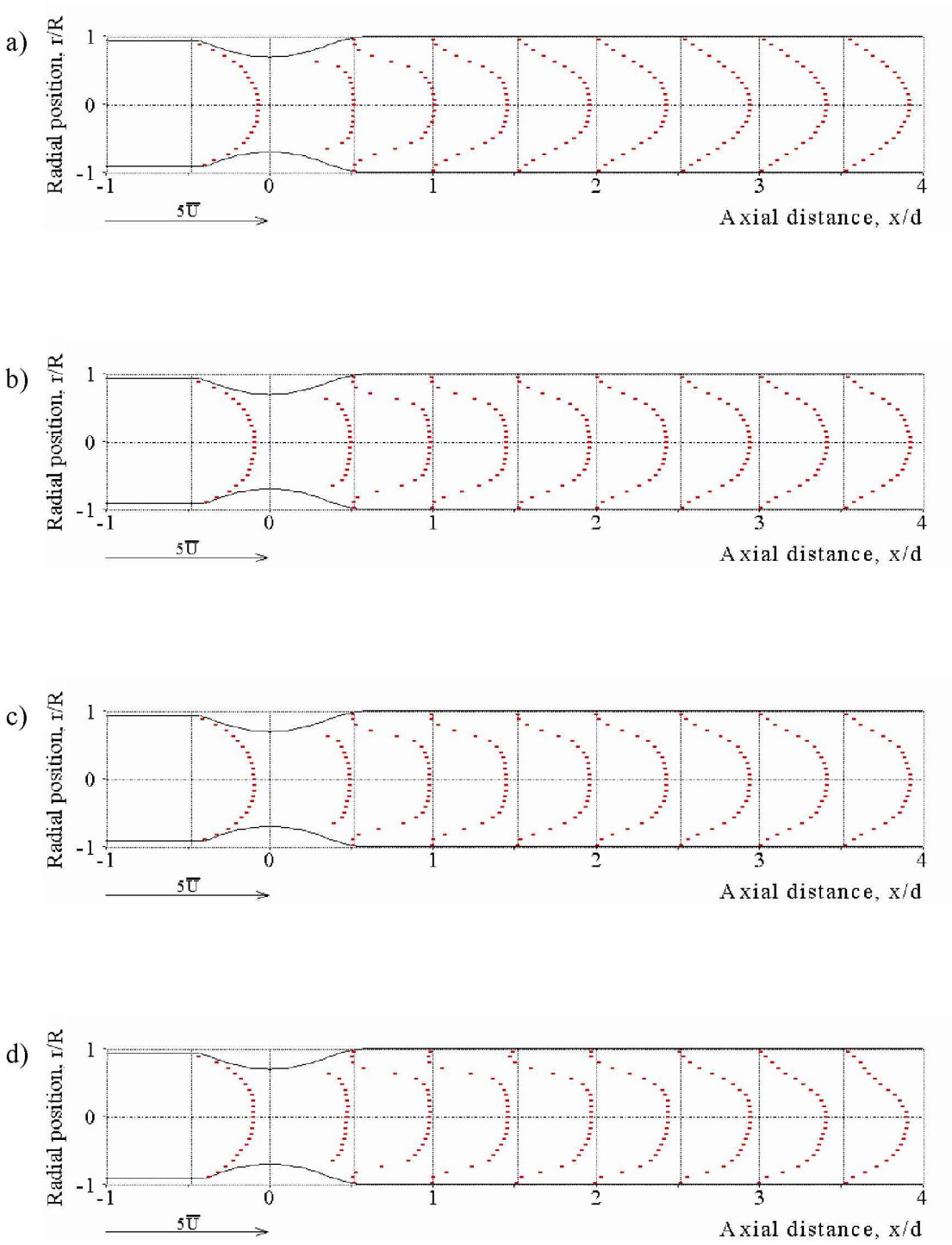

Fig.30: Velocity profiles, derived from PIV data (51% occlusive severity), for a) Re_{PL} = 74, b) Re_{PL} = 180, c) Re_{PL} = 235 and d) Re_{PL} = 617.

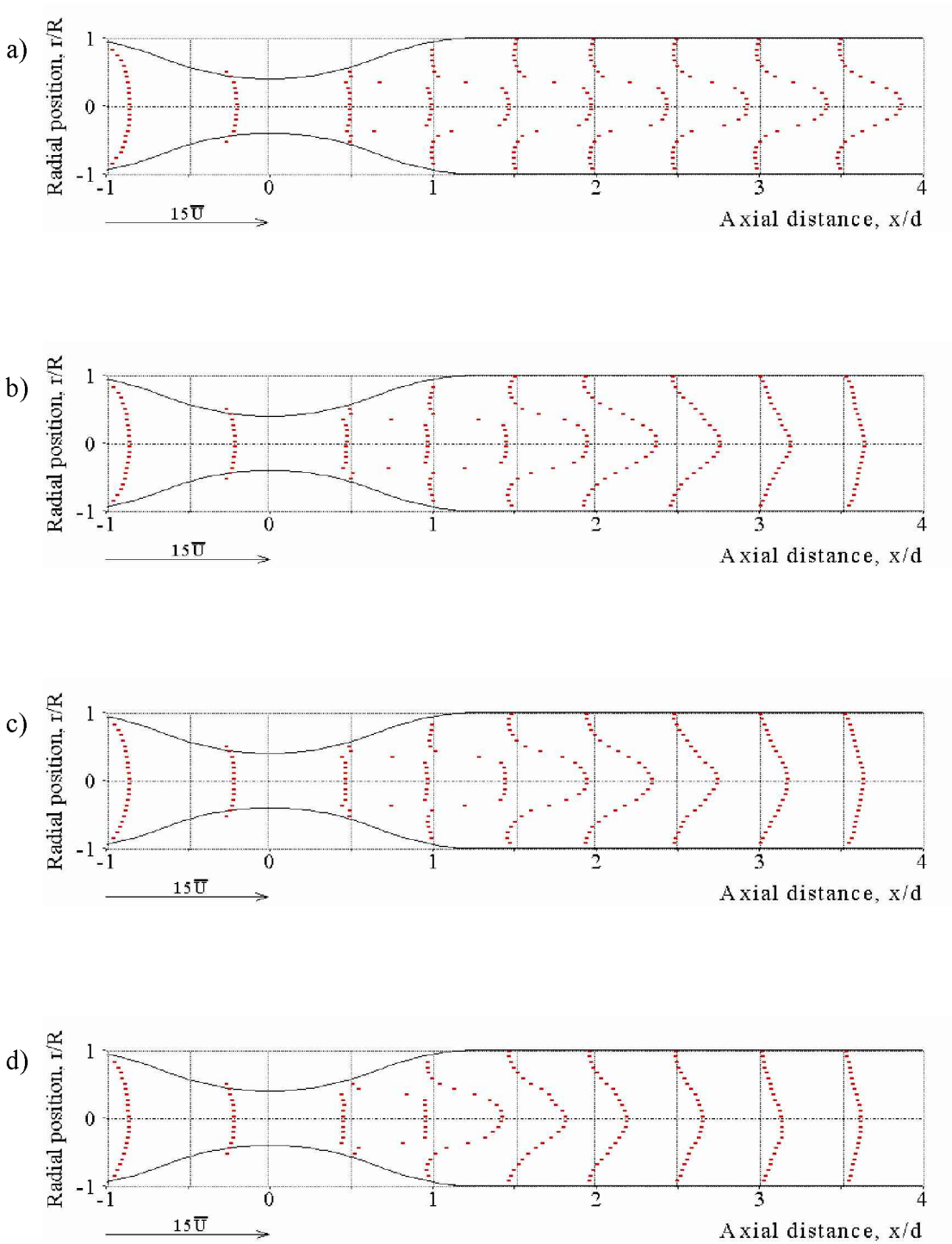

Fig.31: Velocity profiles, derived from PIV data (84% occlusive severity), for a) Re_{PL} = 74, b) Re_{PL} = 180, c) Re_{PL} = 235 and d) Re_{PL} = 617.

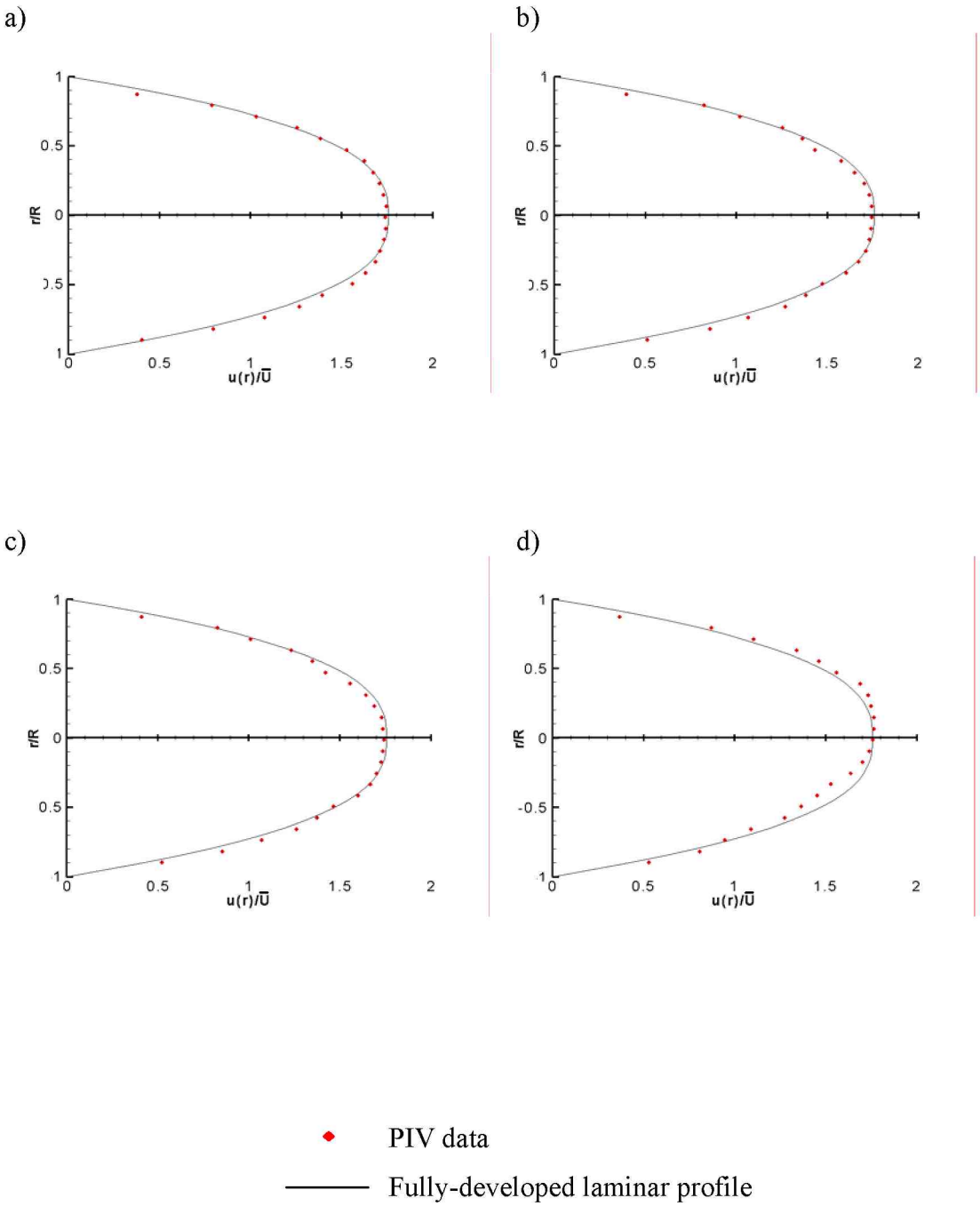

Fig.32: Fully-developed laminar velocity profile (n = 0.61) and PIV velocity profiles, measured at 0.93 diameters upstream of stenosis neck (51% occlusive severity) and normalized with the bulk velocity; a) Re_{PL} = 74, b) Re_{PL} = 180, c) Re_{PL} = 235 and d) Re_{PL} = 617.

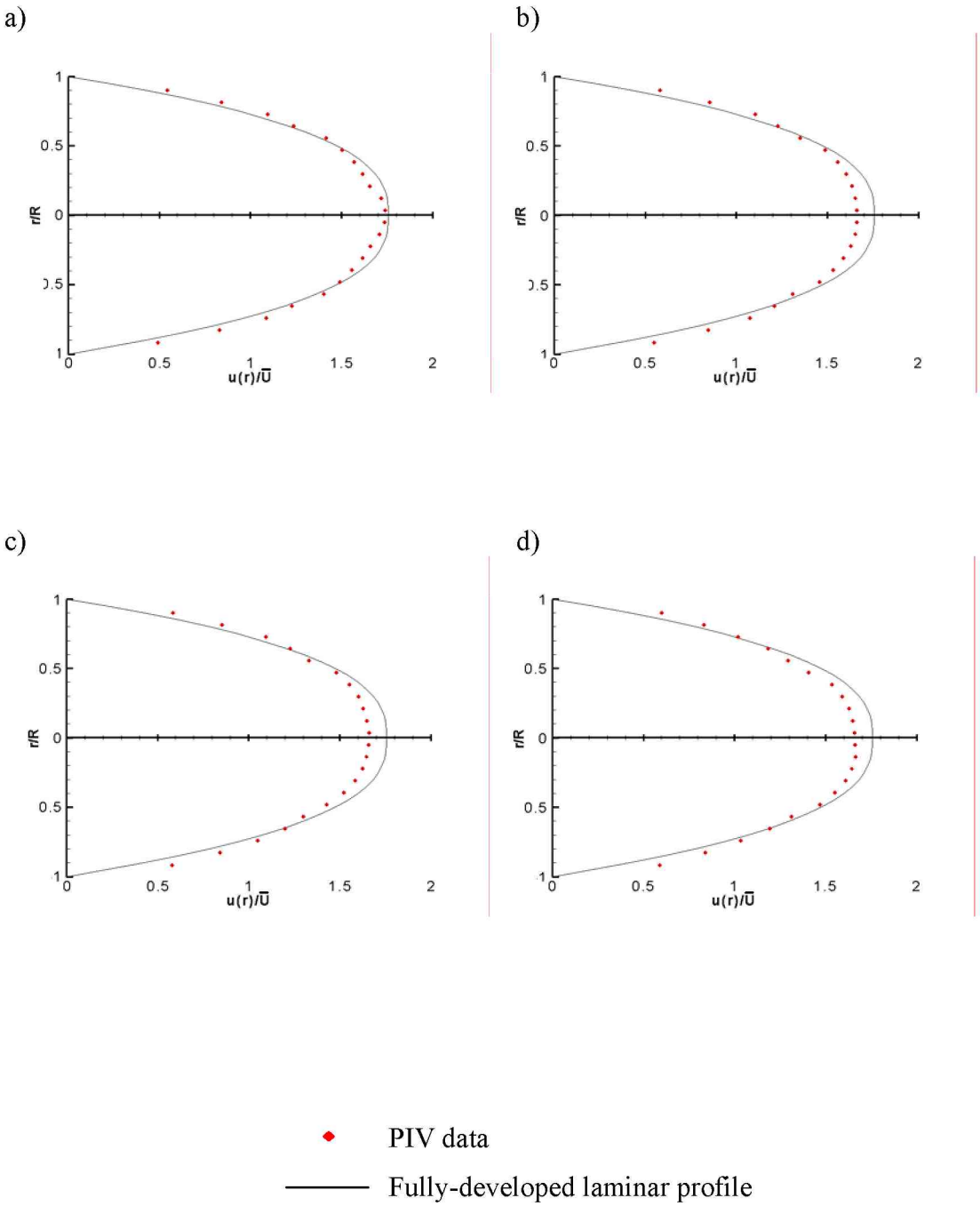

Fig.33: Fully-developed laminar velocity profile (n = 0.61) and PIV velocity profiles, measured at 1.18 diameters upstream of stenosis neck (84% occlusive severity) and normalized with the bulk velocity; a) Re_{PL} = 74, b) Re_{PL} = 180, c) Re_{PL} = 235 and d) Re_{PL} = 617.

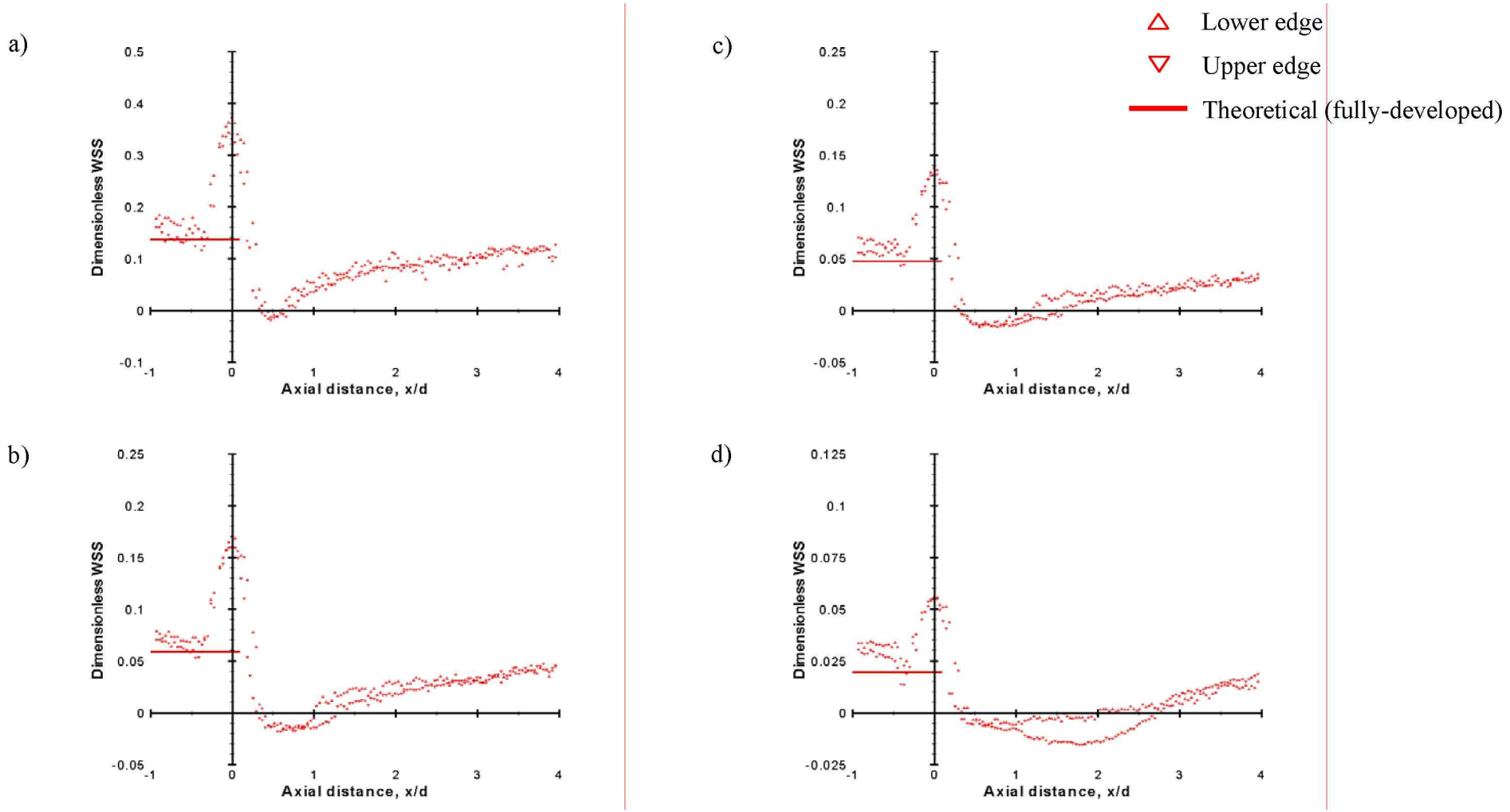

Fig.34: Wall shear stress distributions, derived from PIV data (51% occlusive severity); a) Re_{PL} = 74, b) Re_{PL} = 180, c) Re_{PL} = 235 and d) Re_{PL} = 617.

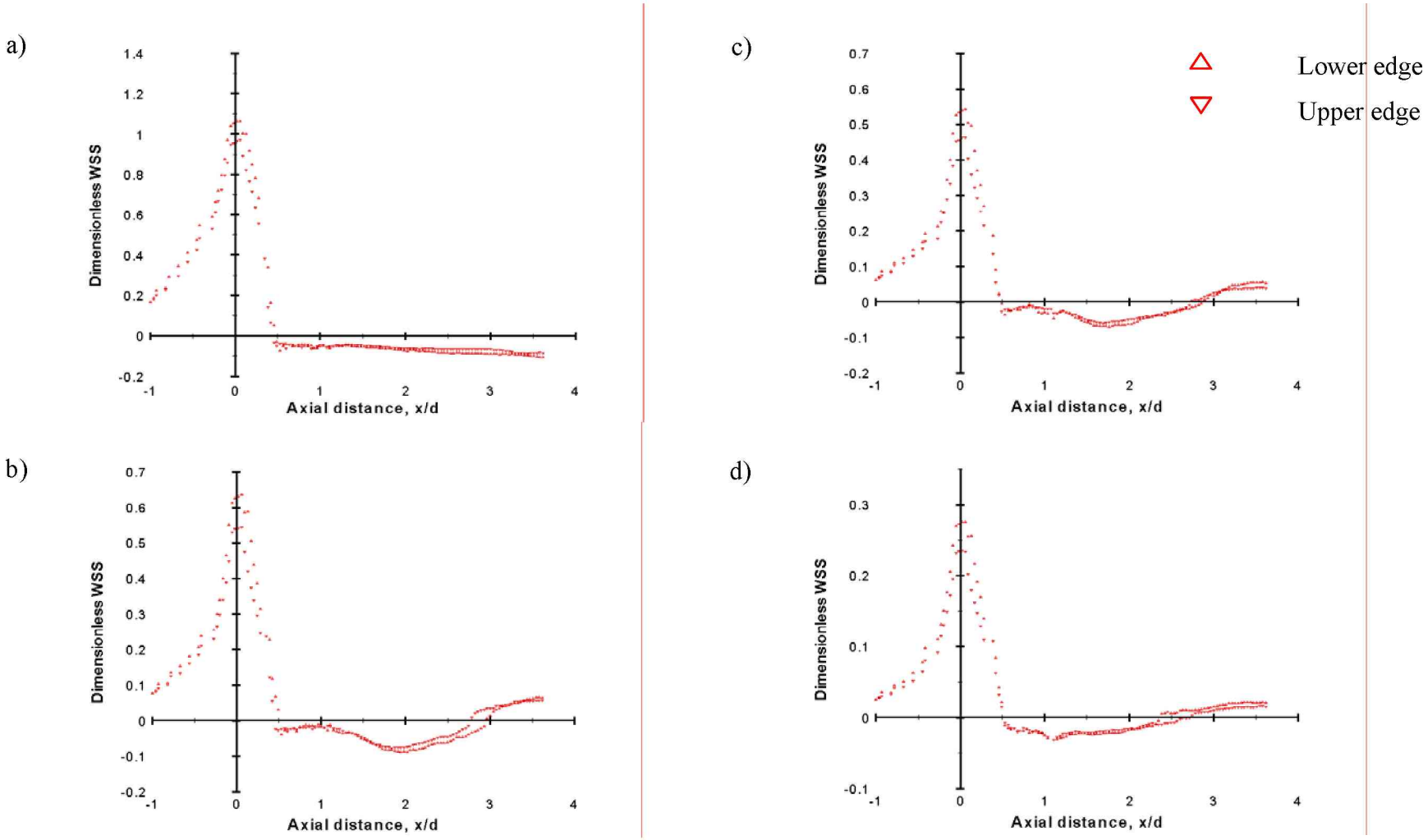

Fig.35: Wall shear stress distributions, derived from PIV data (84% occlusive severity); a) Re_{PL} = 74, b) Re_{PL} = 180, c) Re_{PL} = 235 and d) Re_{PL} = 617.

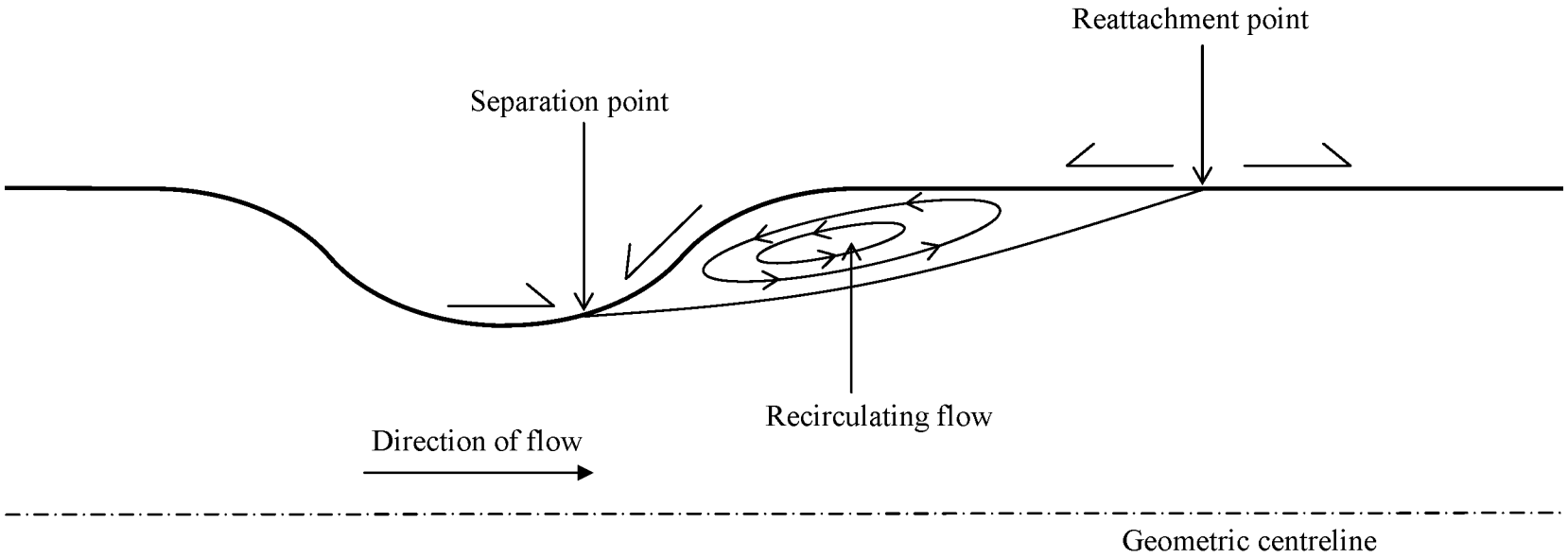

Fig.36: Schematic representation of recirculating flow.

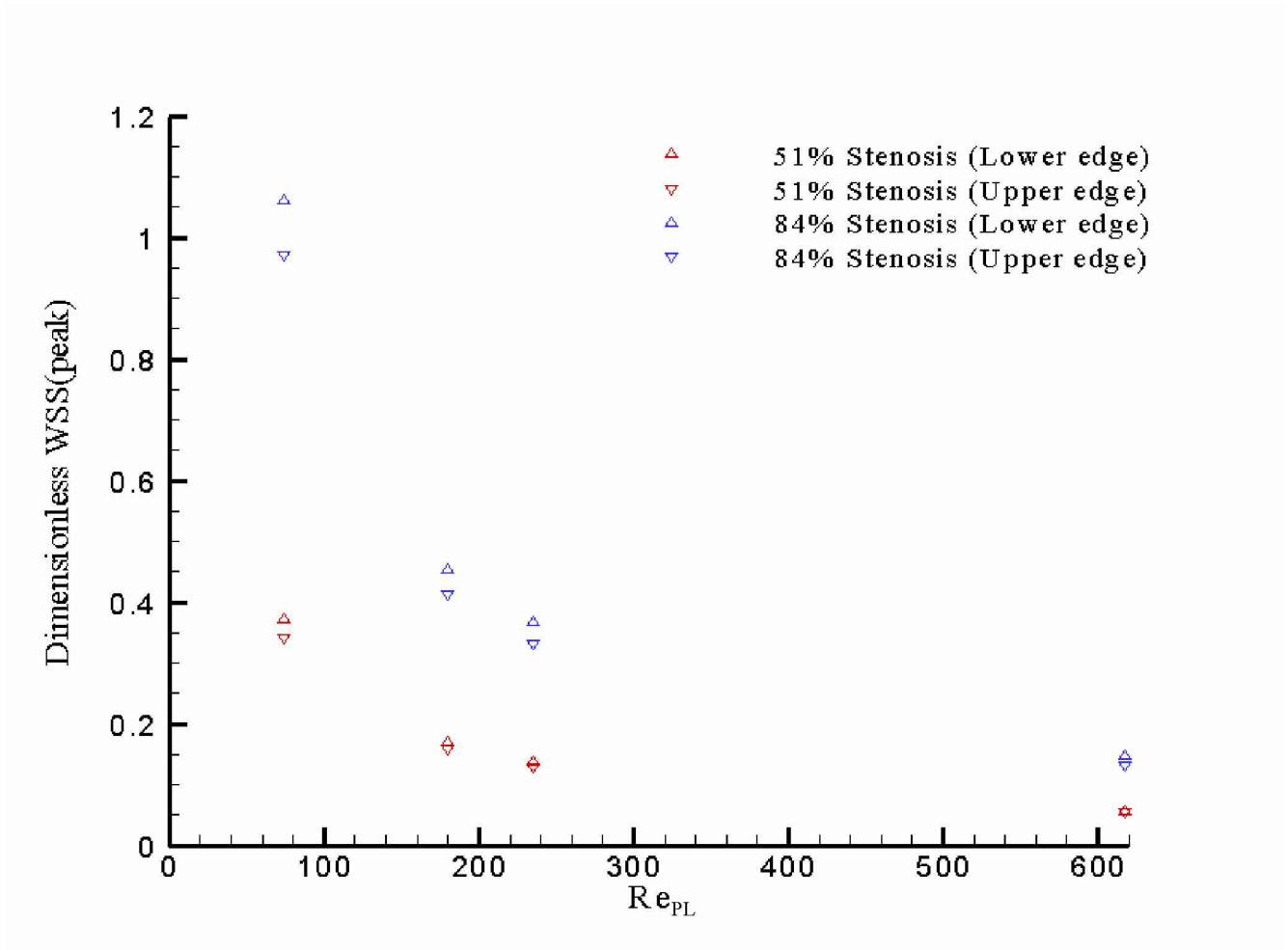

Fig.37: Variation of dimensionless peak wall shear stress, at the throat of the occlusion, with Reynolds number under steady flow conditions – experimental results.

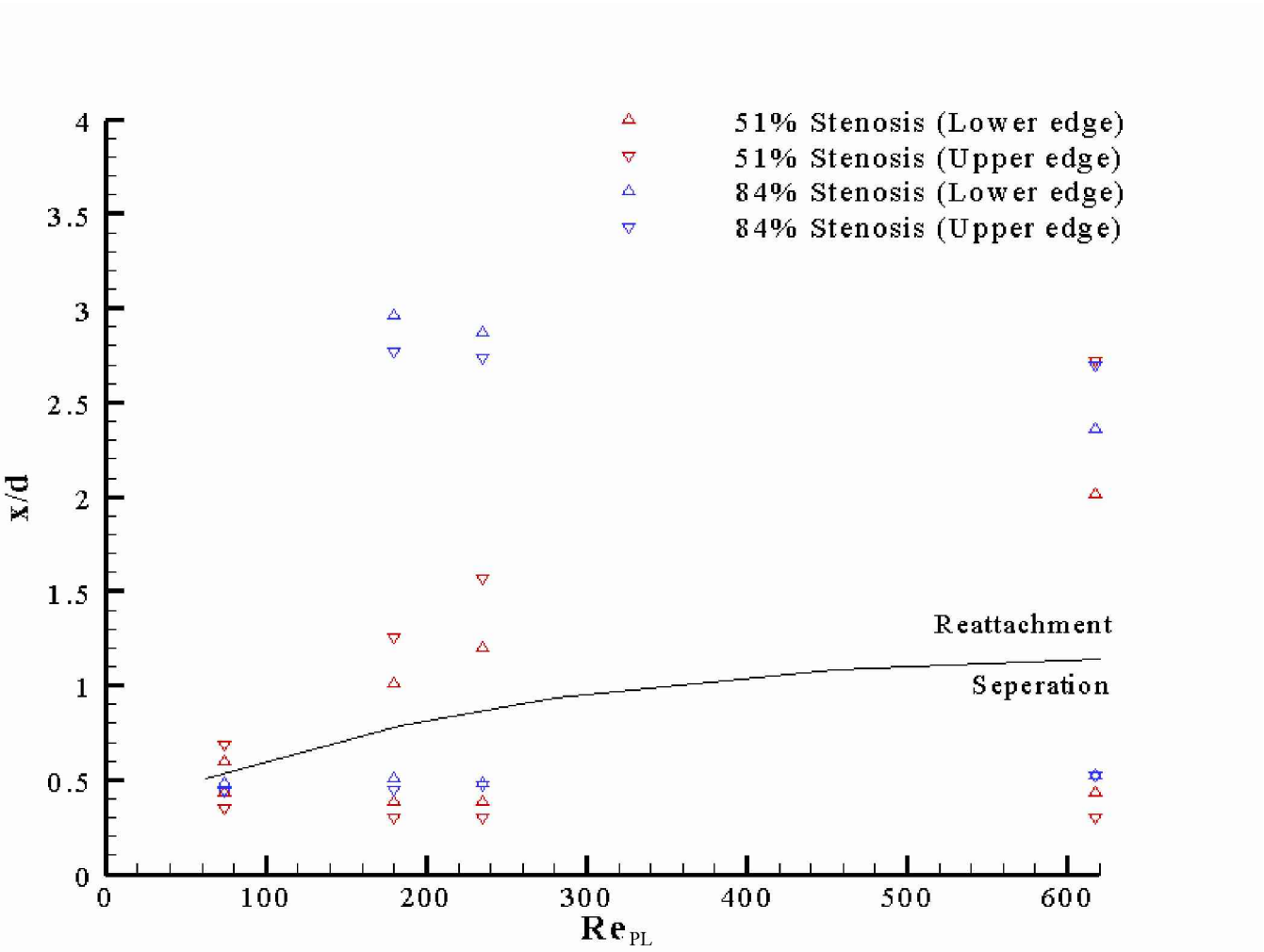

Fig.38: Variation of separation and reattachment points with Reynolds number under steady flow conditions – experimental results.

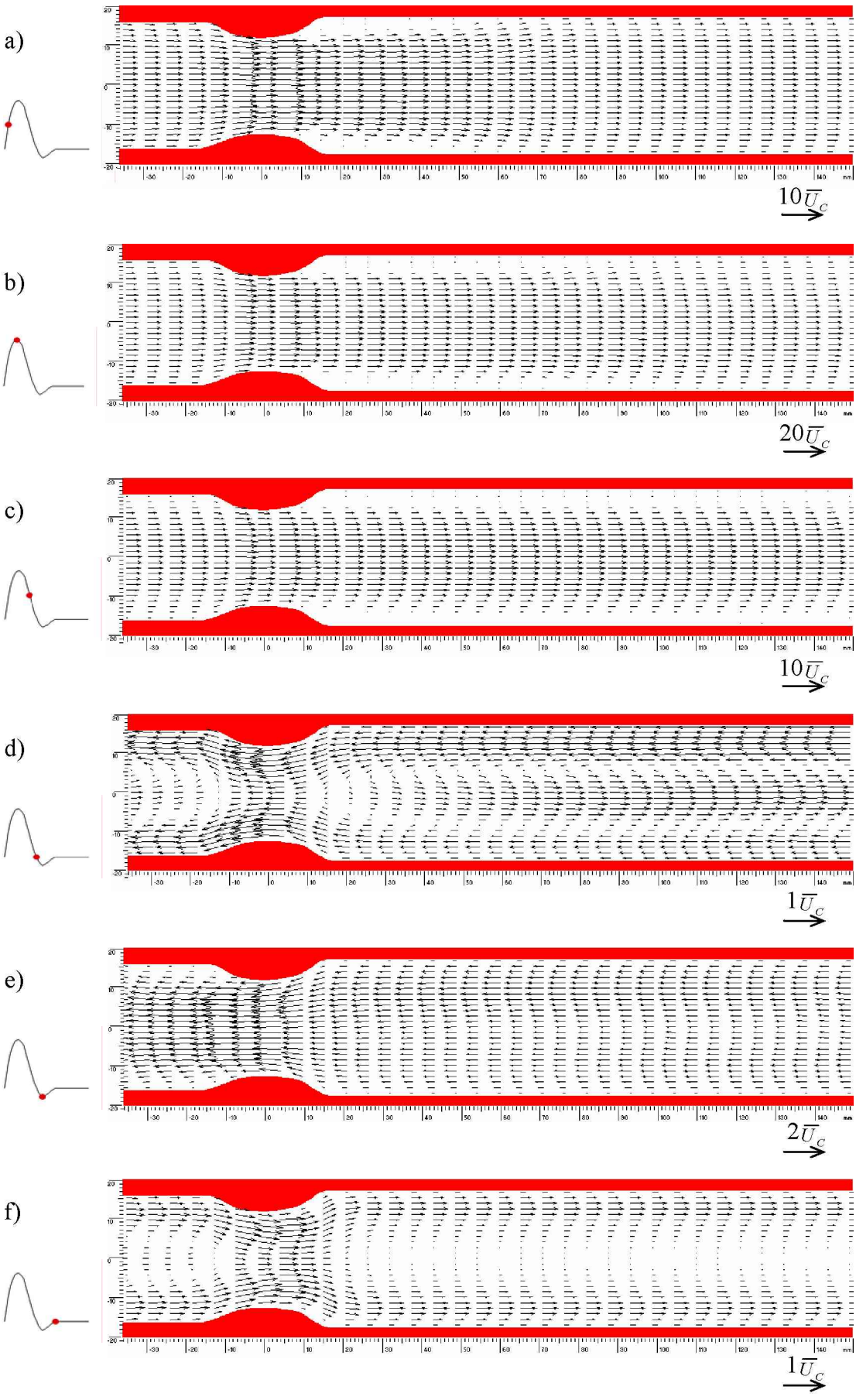

Fig.39: Mean velocity vector field (PIV data, 51% occlusive severity), biphasic flow.

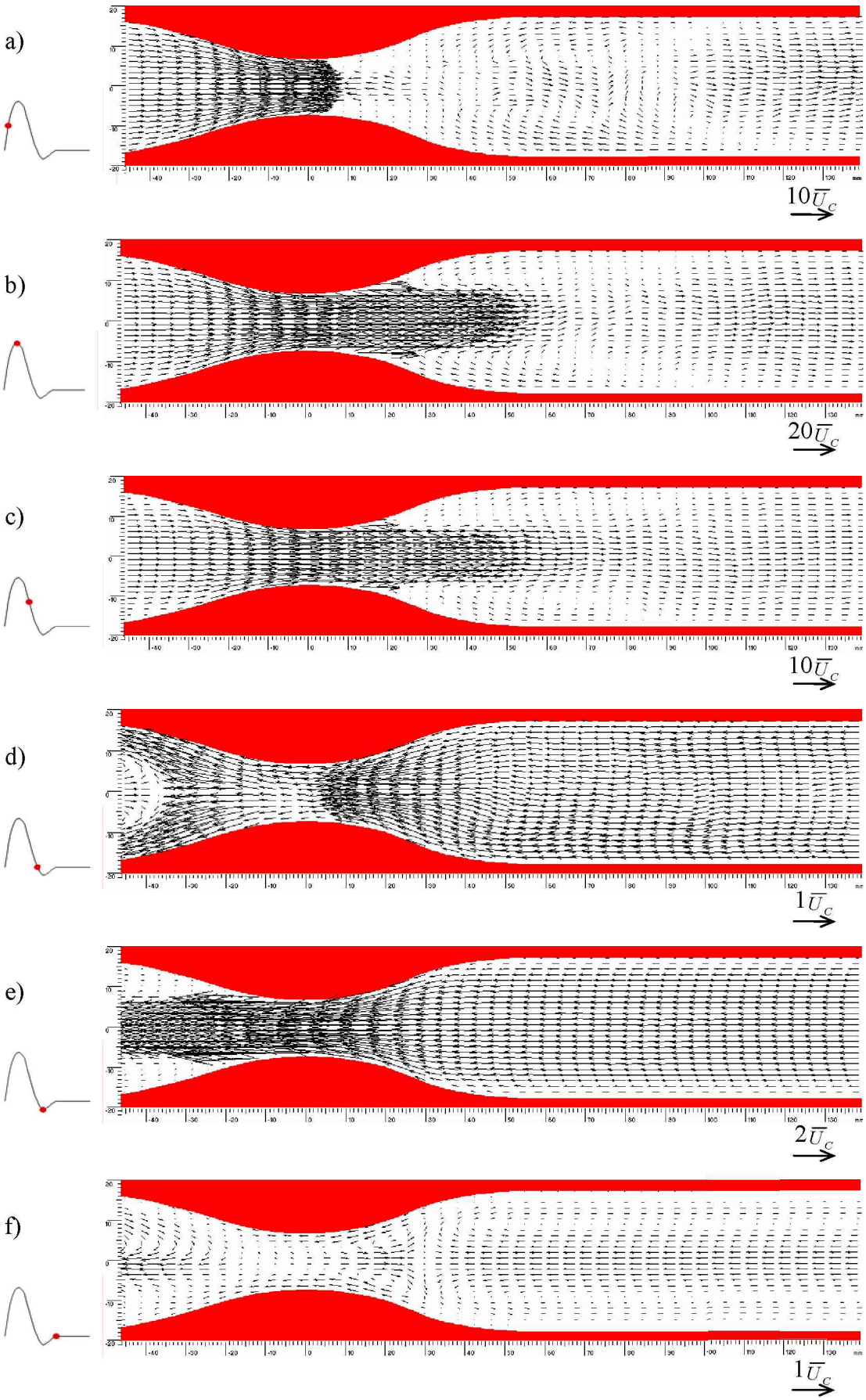

Fig.40: Mean velocity vector field (PIV data, 84% occlusive severity), biphasic flow.

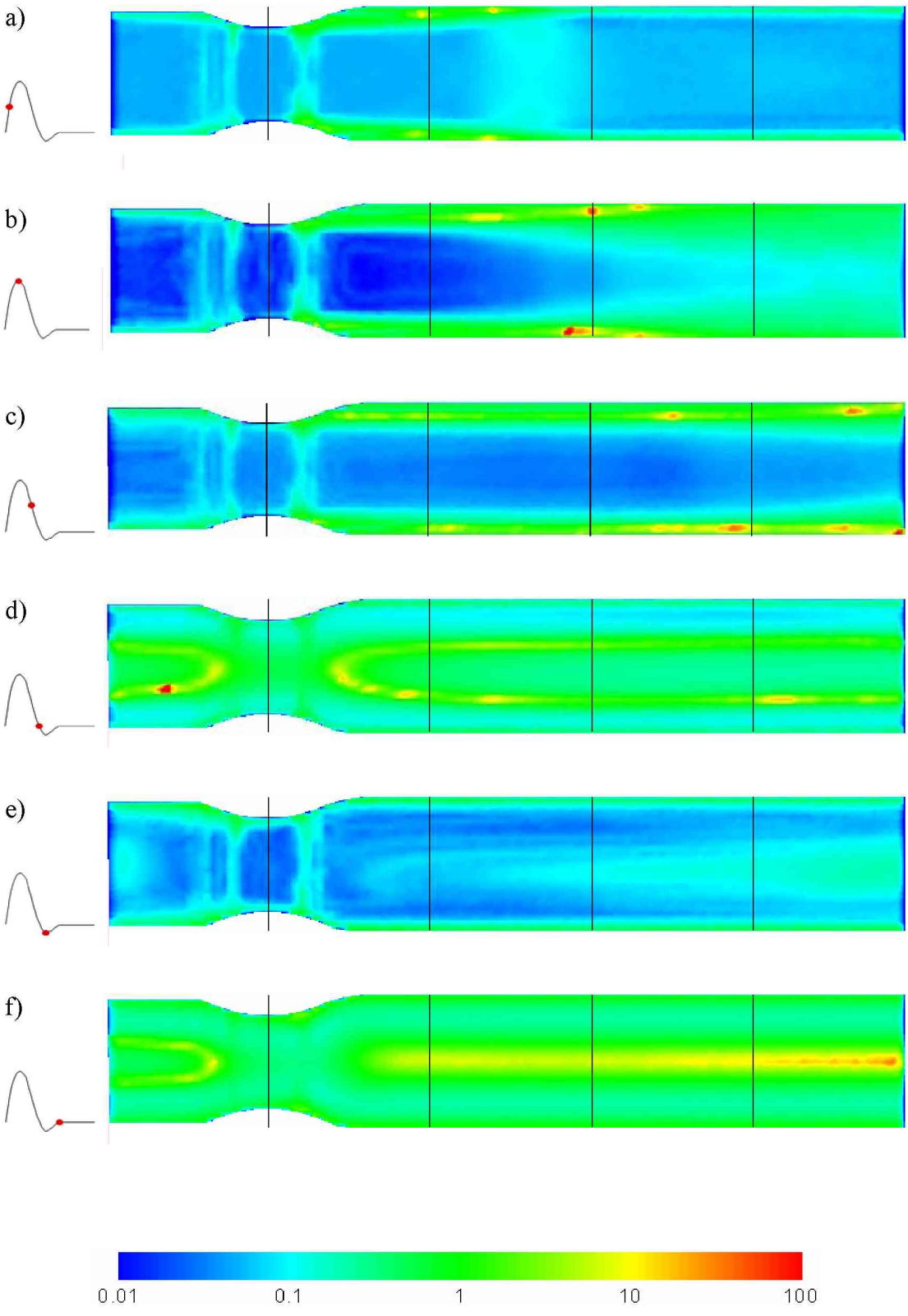

Fig.41: Normalized standard deviation maps of PIV data (51% occlusive severity), biphasic flow. Intervals shown every diameter.

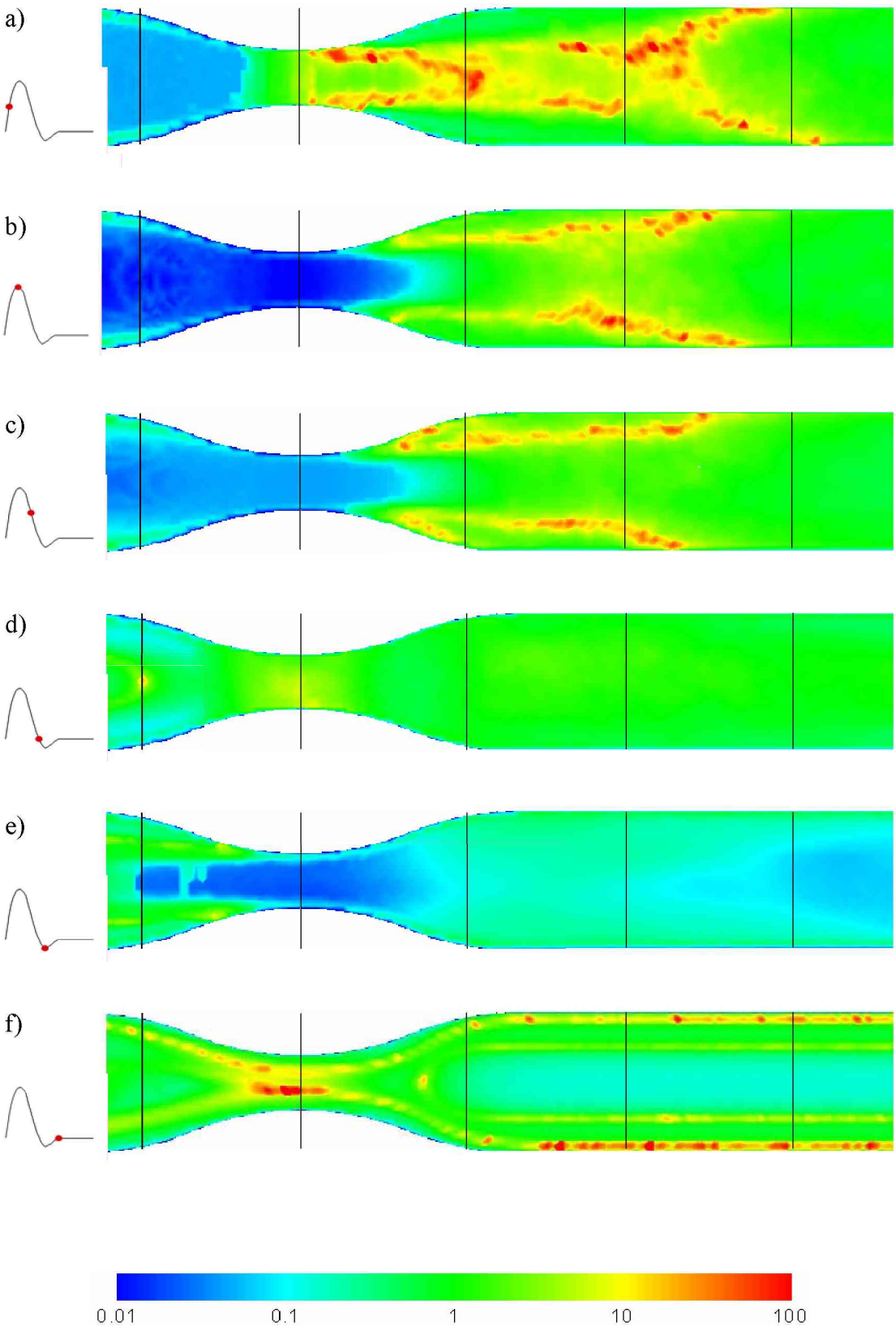

Fig.42: Normalized standard deviation maps of PIV data (84% occlusive severity), biphasic flow. Intervals shown every diameter.

a)

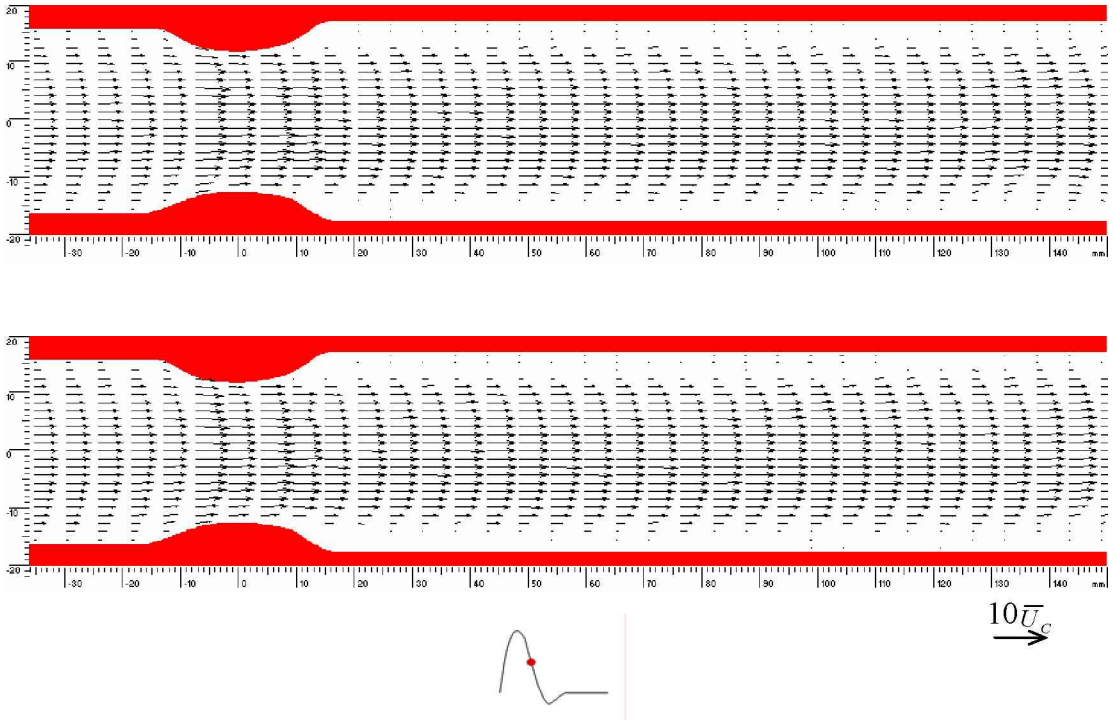

b)

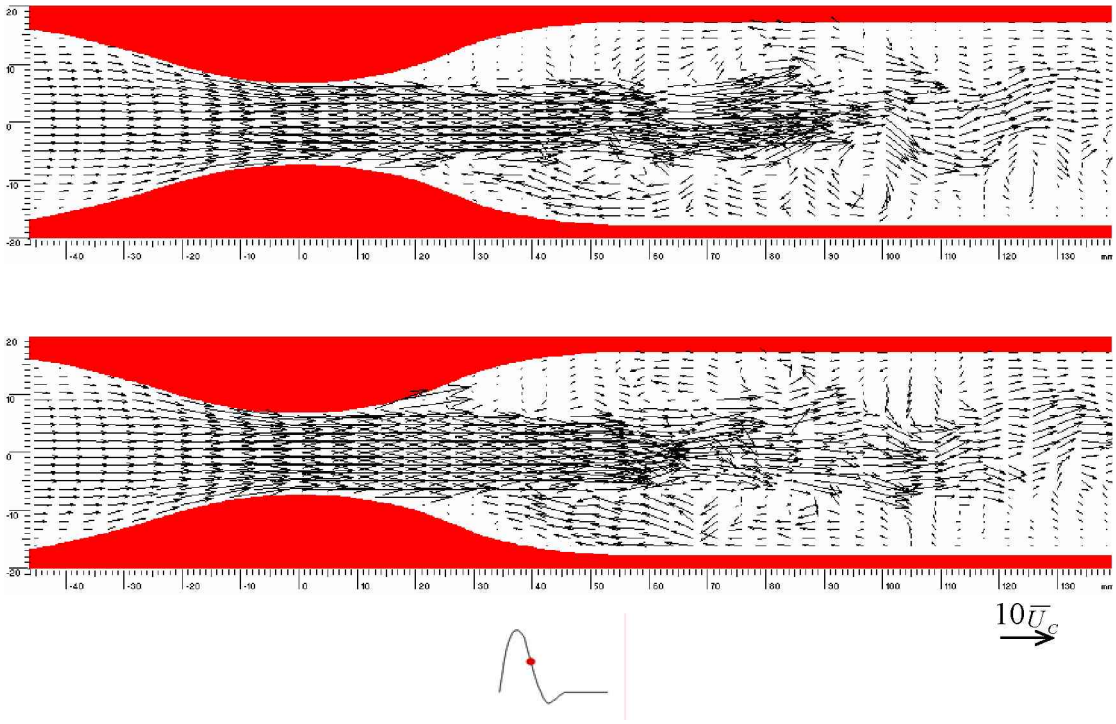

Fig.43: Comparison between the individual vector maps used to calculate the mean vector maps shown in Fig.42c and Fig.43c. Position in waveform as shown. a) 51% occlusive severity, b) 84% occlusive severity.

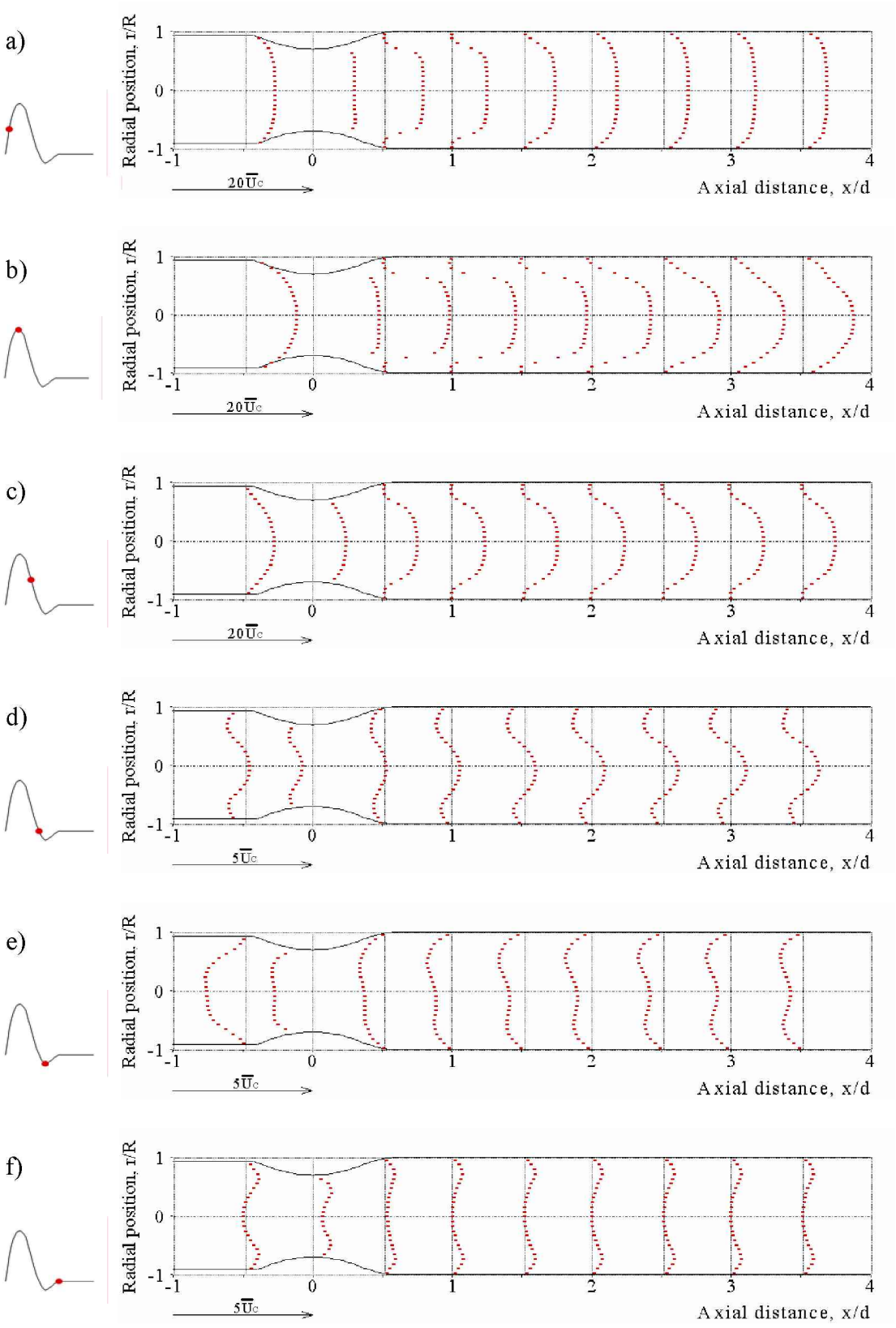

Fig.44: Velocity profiles, derived from PIV data (51% occlusive severity), biphasic flow.

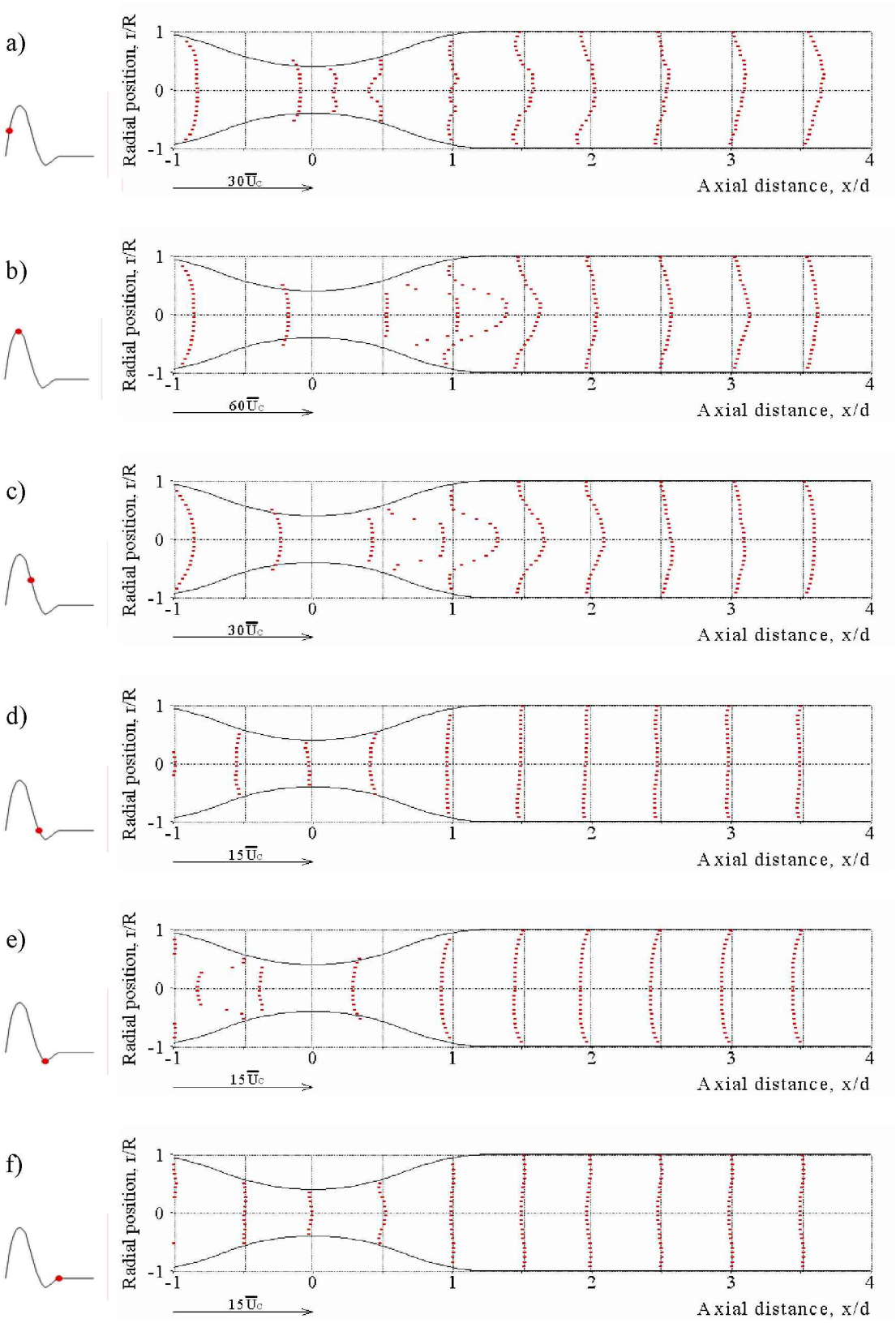

Fig.45: Velocity profiles, derived from PIV data (84% occlusive severity), biphasic flow.

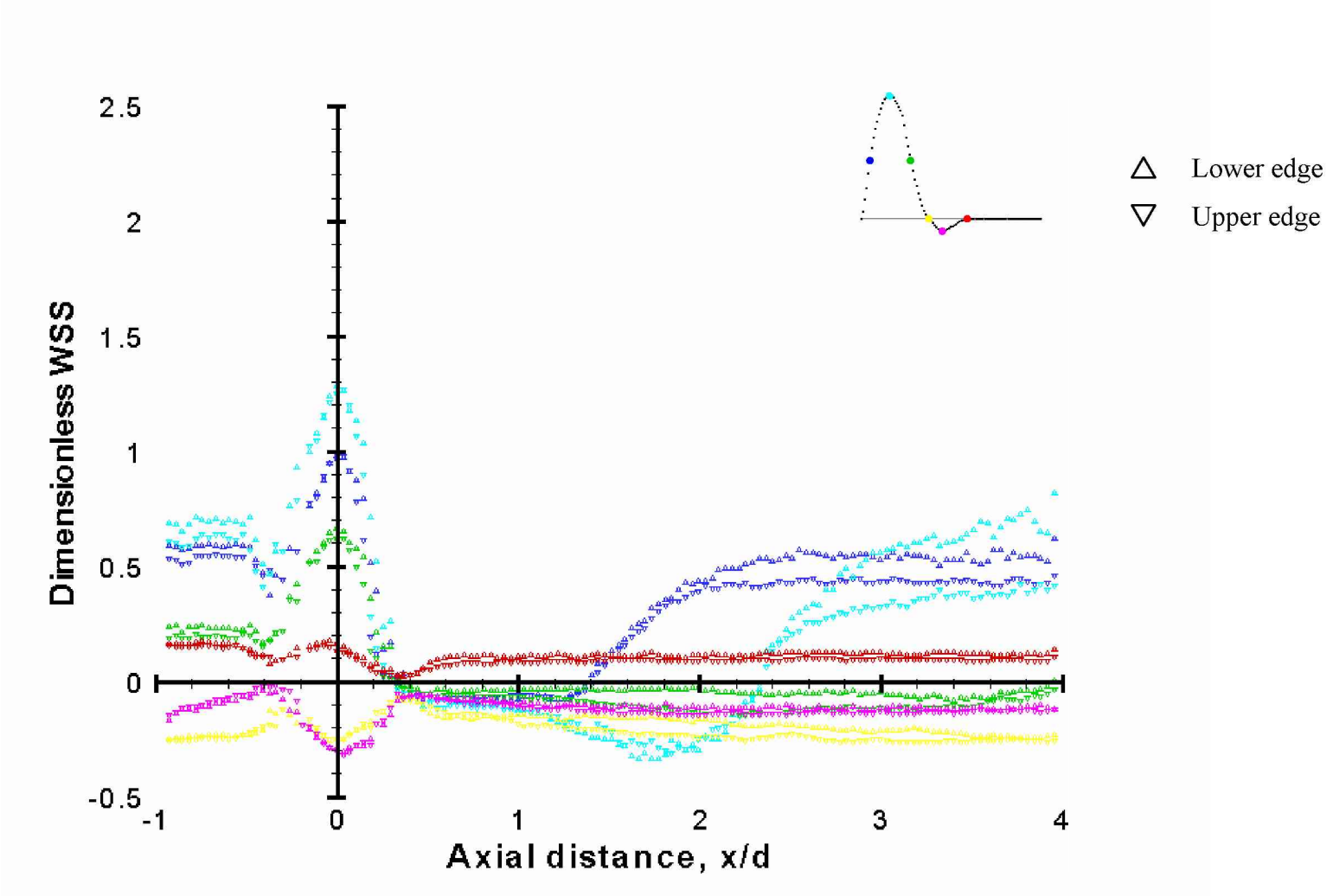

Fig.46: Wall shear stress distribution, derived from PIV data (51% occlusive severity), for biphasic flow.

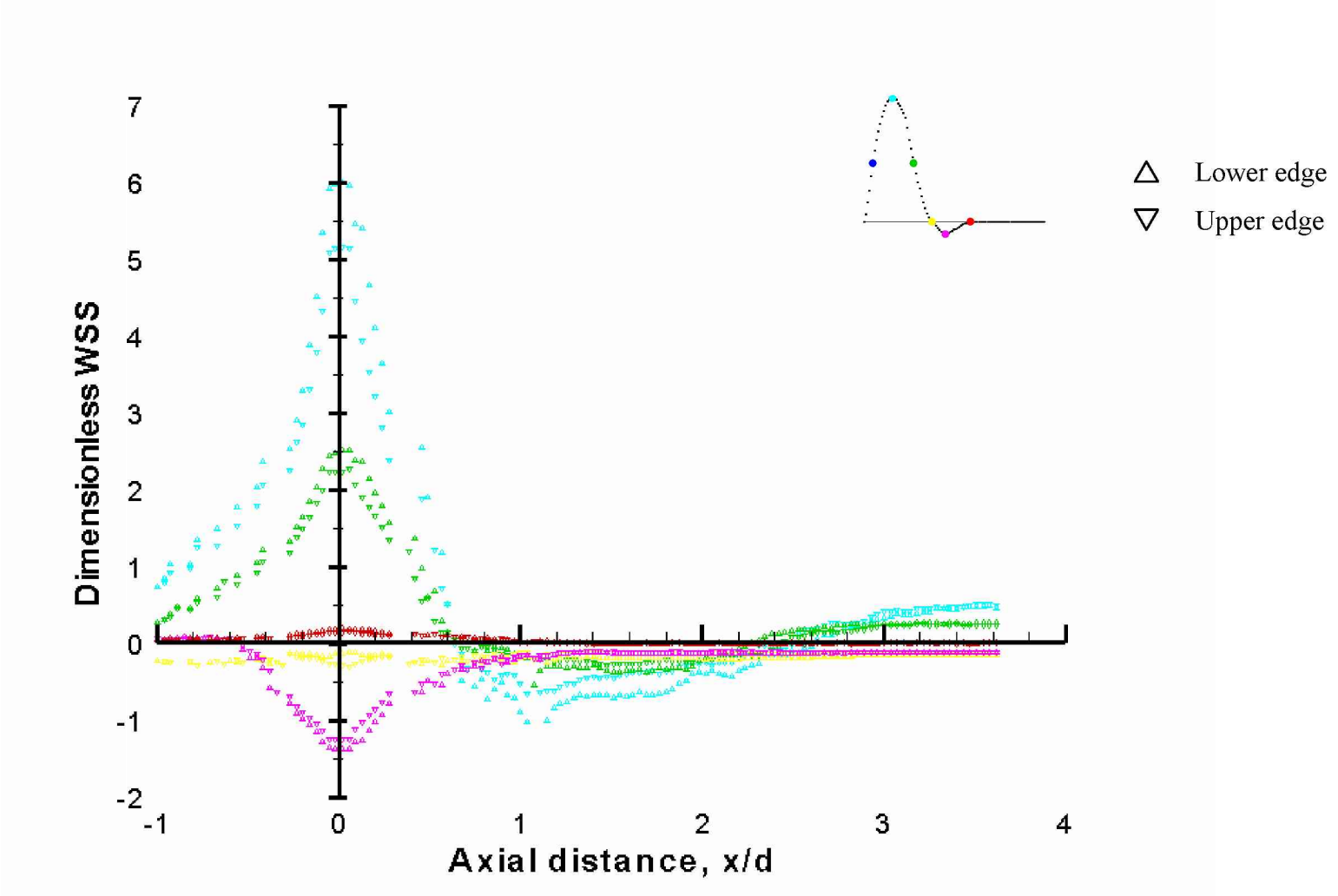

Fig.47: Wall shear stress distribution, derived from PIV data (84% occlusive severity), for biphasic flow.

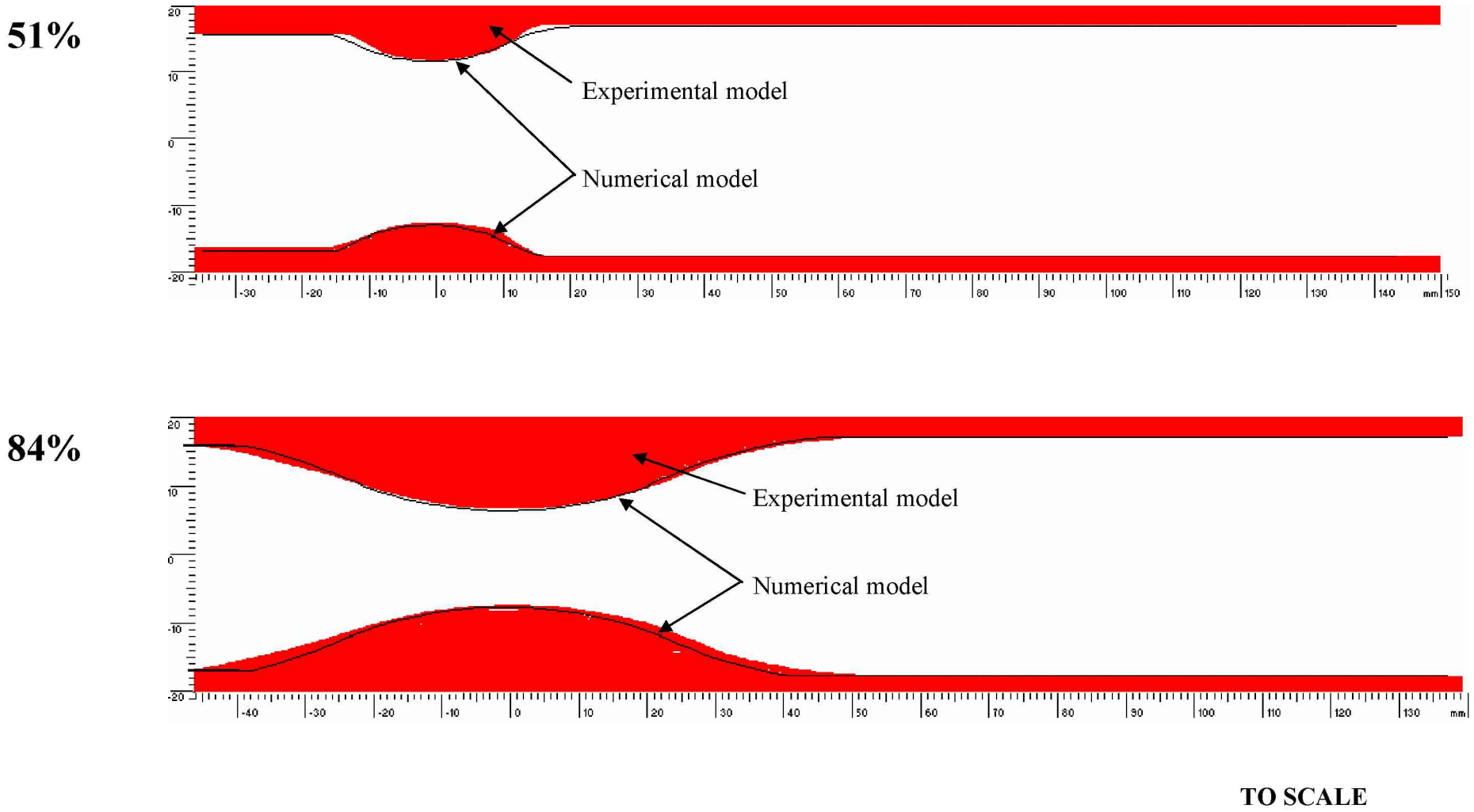

Fig.48: Comparison between experimental and mesh geometries.

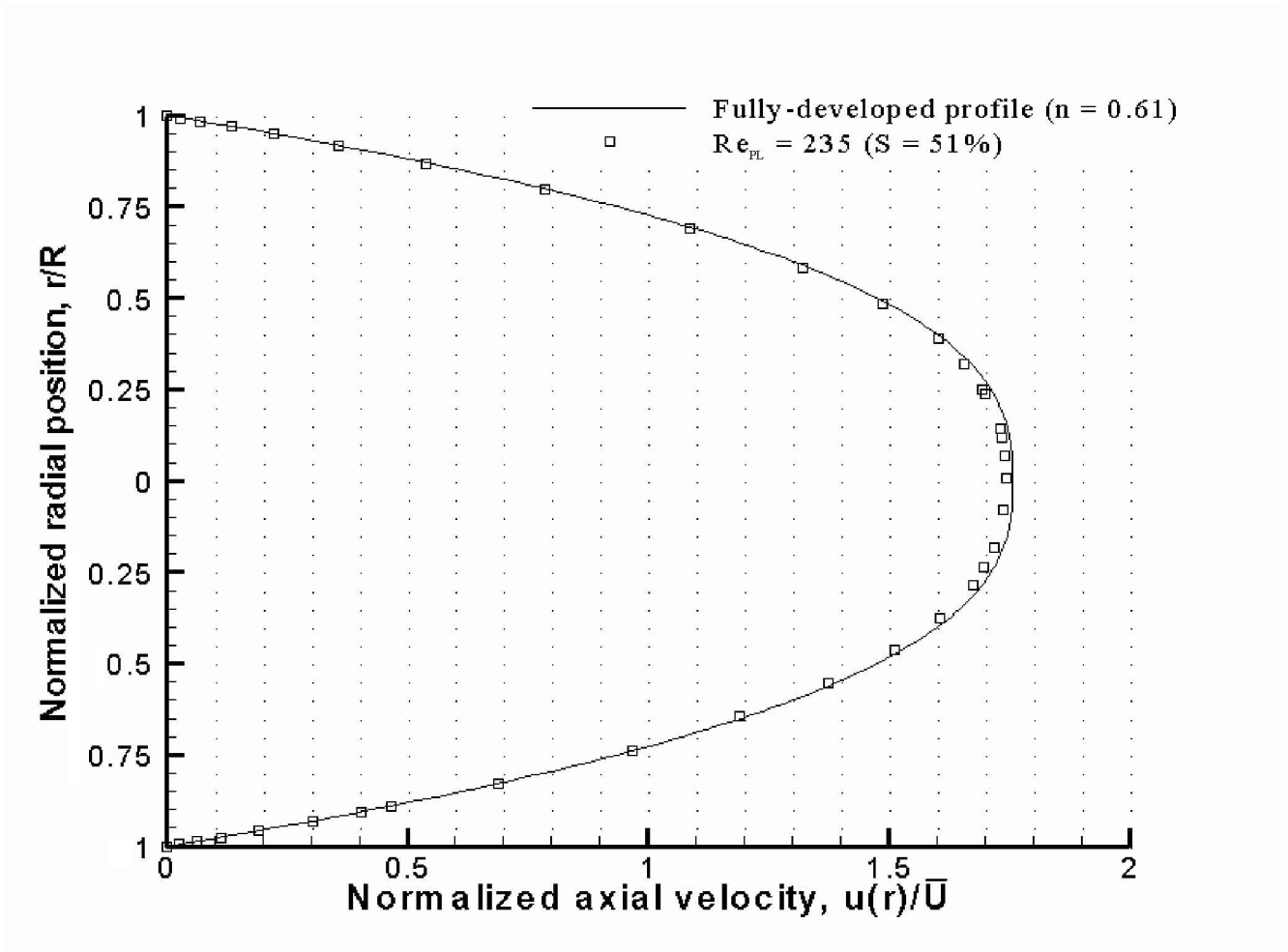

Fig.49: Comparison of theoretical fully-developed velocity profile (n = 0.61) with numerical data, obtained proximal to the occlusion (*in vitro*-scale).

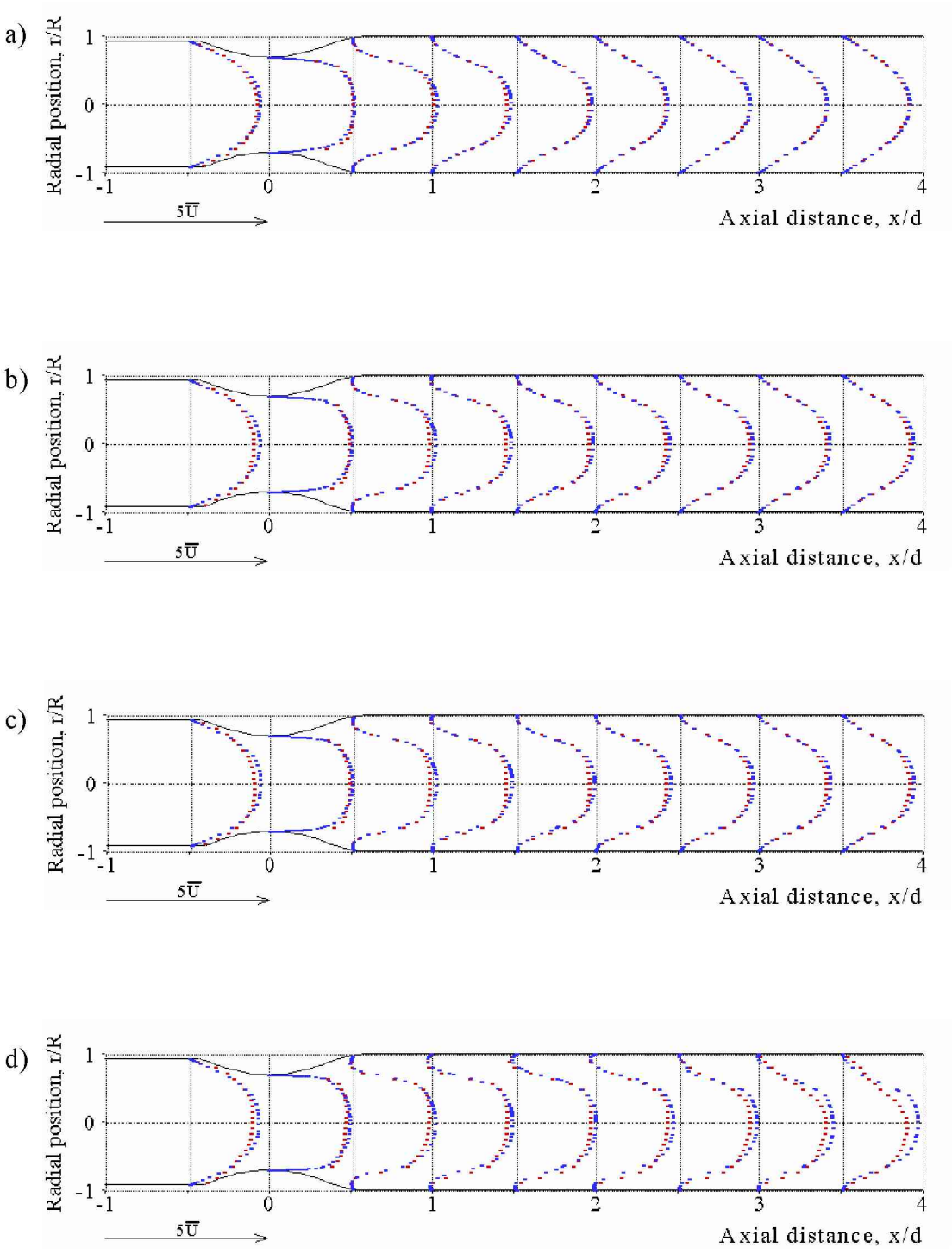

Fig.50: Velocity profiles (51% occlusive severity) for a) Re_{PL} = 74, b) Re_{PL} = 180, c) Re_{PL} = 235 and d) Re_{PL} = 617. Comparison between PIV and CFD data.

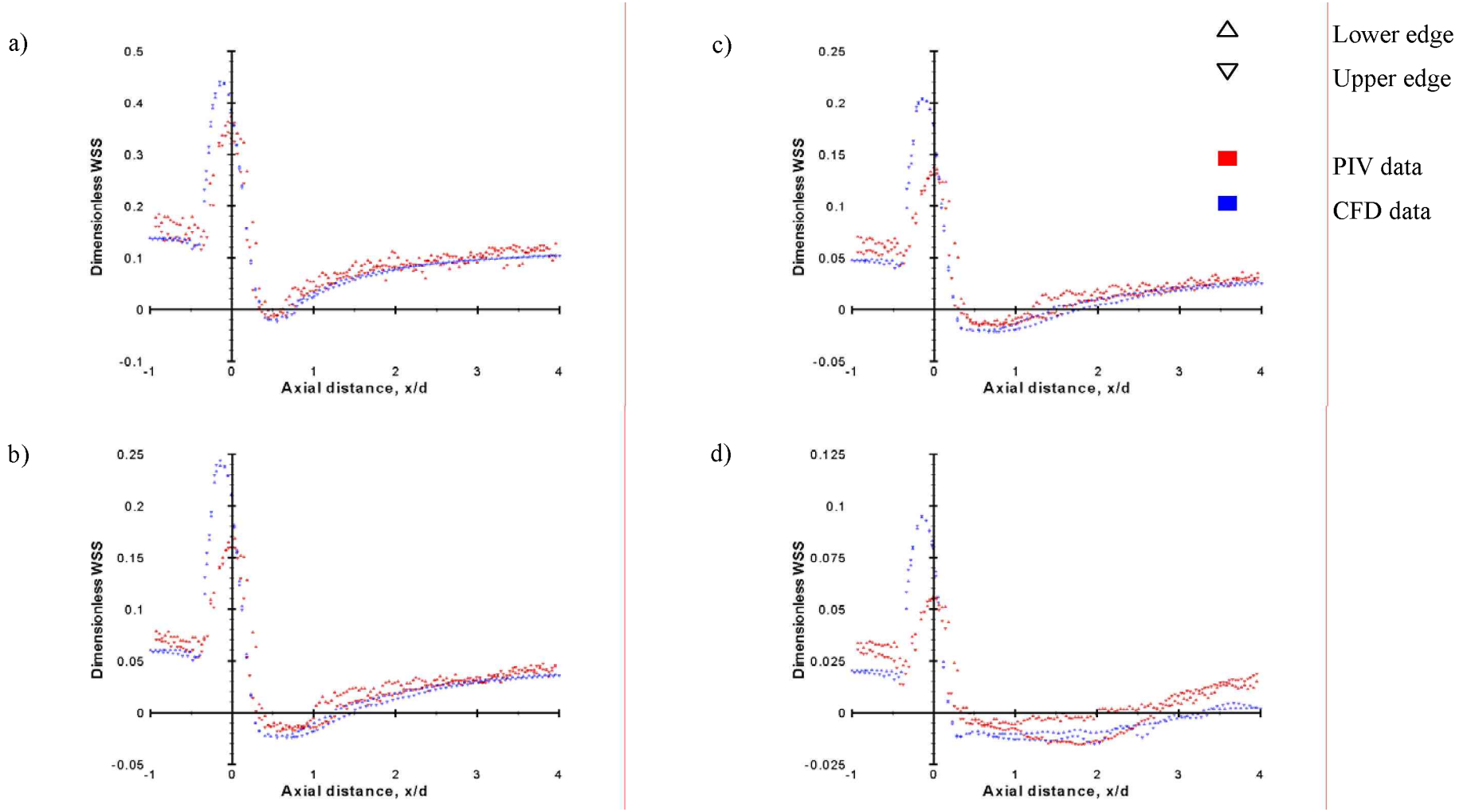

Fig.51: Wall shear stress distributions (51% occlusive severity) for a) Re_{PL} = 74, b) Re_{PL} = 180, c) Re_{PL} = 235 and d) Re_{PL} = 617. Comparison between PIV and CFD data.

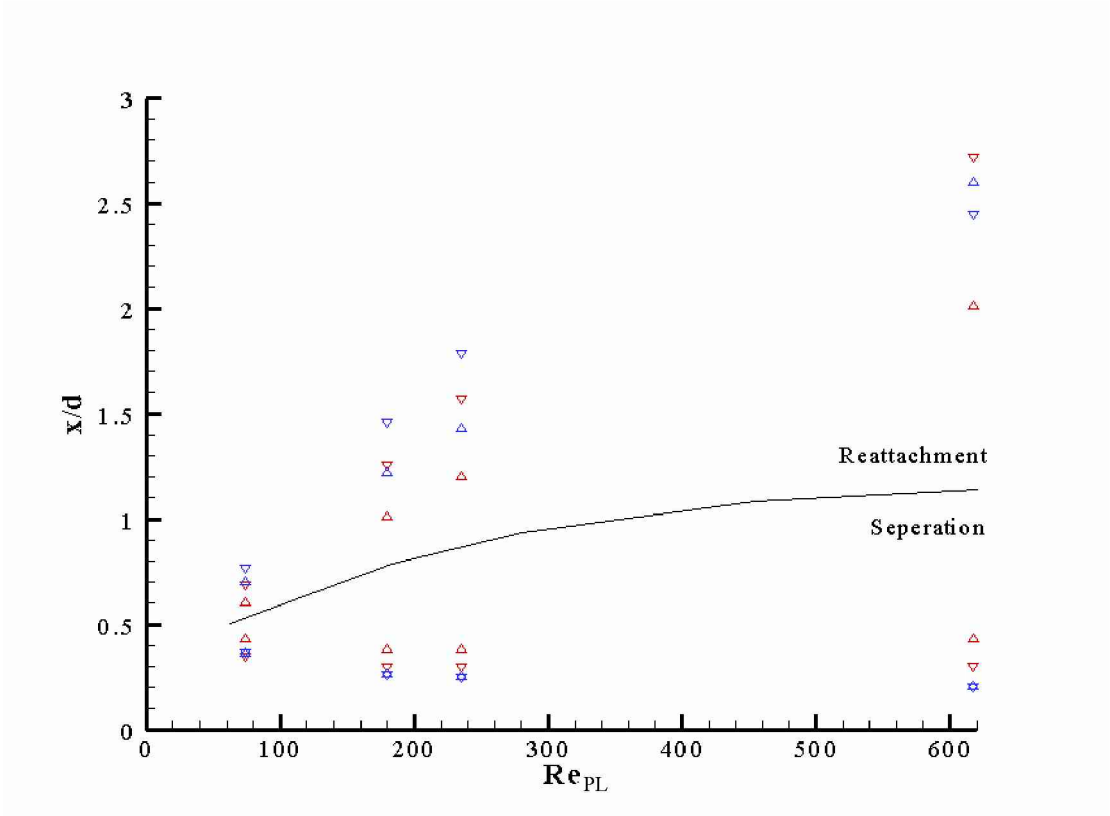

Fig.52: Variation of separation and reattachment points with Reynolds number under steady flow conditions (51% occlusive severity). Comparison between PIV and CFD data.

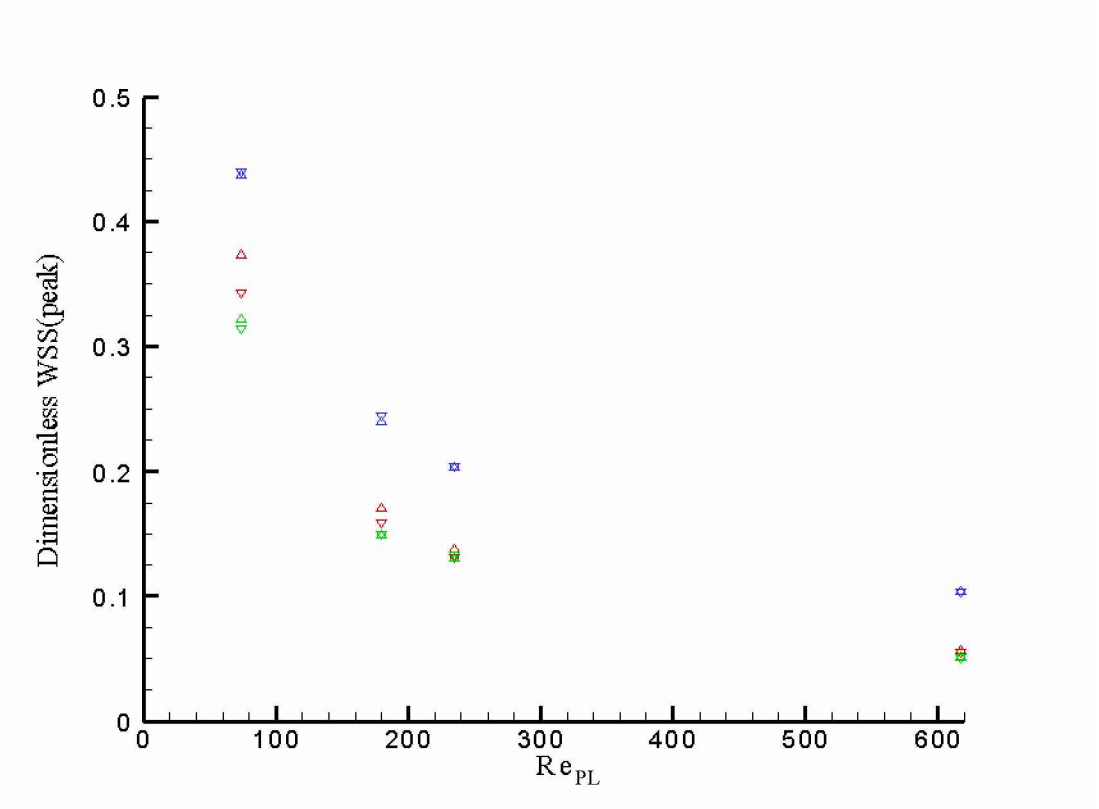

△ Lower edge

▽ Upper edge

■ PIV

■ CFD (using the vector closest to the wall)

■ CFD (using the same vector location that was used in PIV estimation)

Fig.53: Variation of dimensionless peak wall shear stress at the throat of the occlusion with Reynolds number, under steady flow conditions (51% occlusive severity). Comparison between PIV and CFD data.

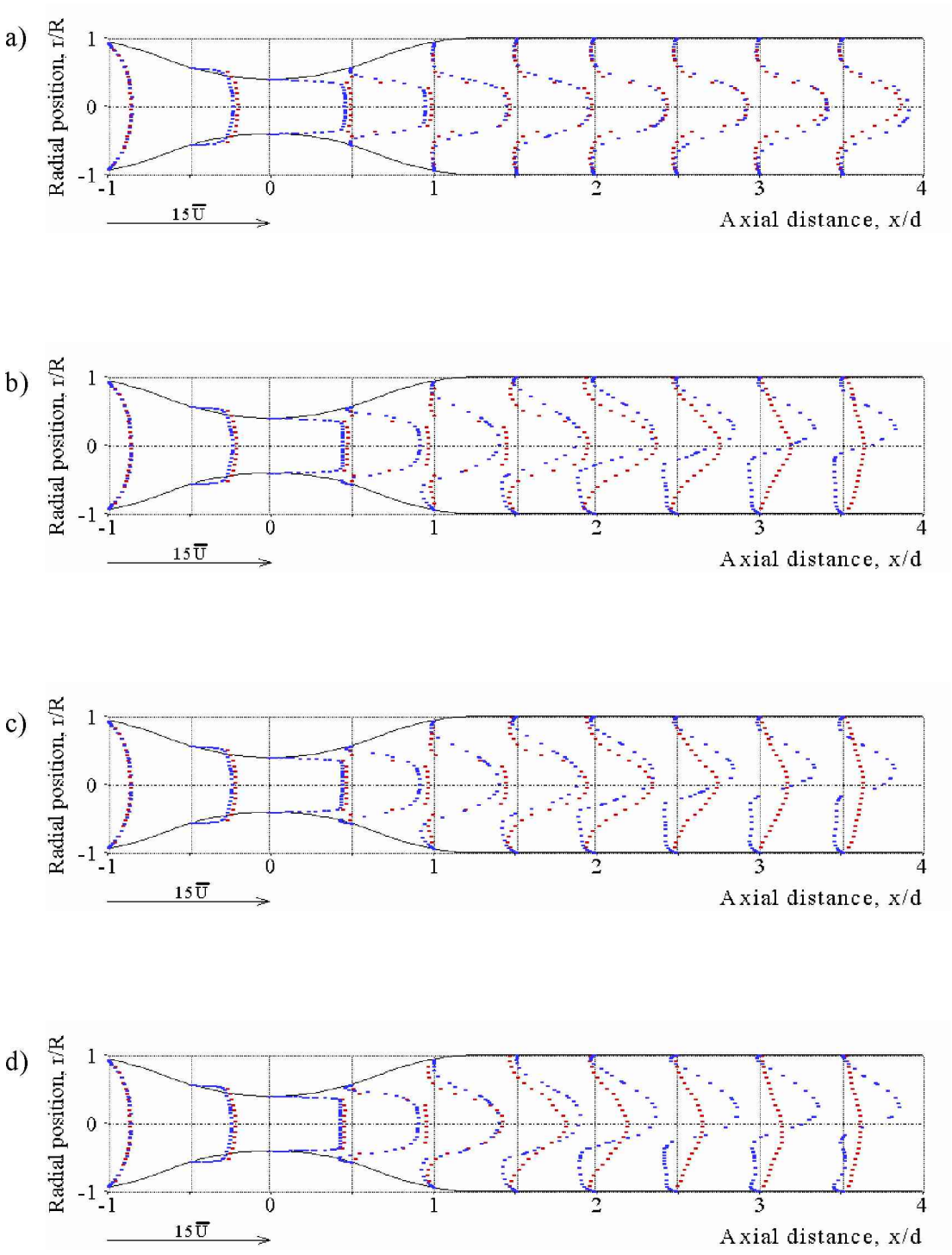

Fig.54: Velocity profiles (84% occlusive severity) for a) Re_{PL} = 74, b) Re_{PL} = 180, c) Re_{PL} = 235 and d) Re_{PL} = 617. Comparison between PIV and CFD data.

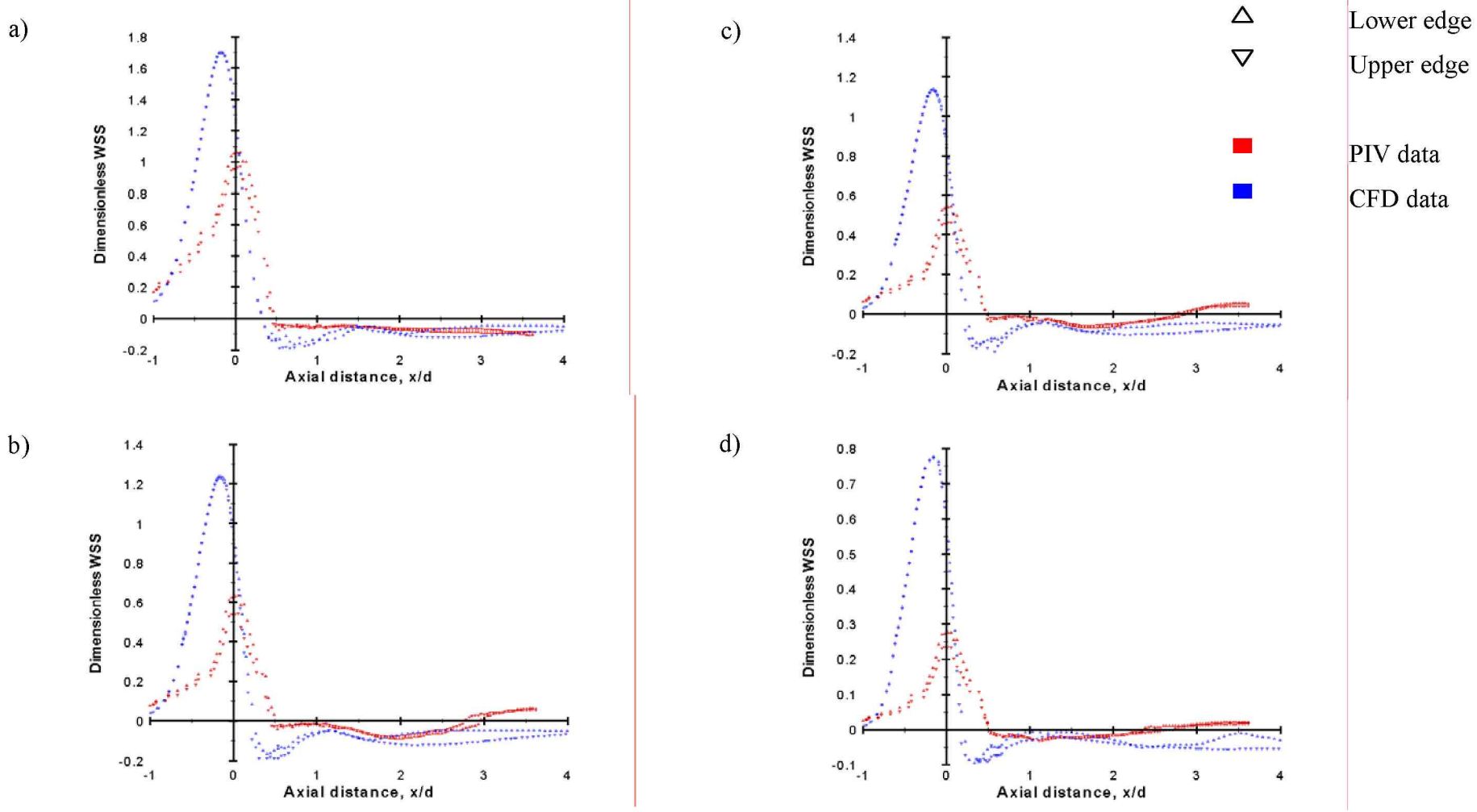

Fig.55: Wall shear stress distributions (84% occlusive severity) for a) Re_{PL} = 74, b) Re_{PL} = 180, c) Re_{PL} = 235 and d) Re_{PL} = 617. Comparison between PIV and CFD data.

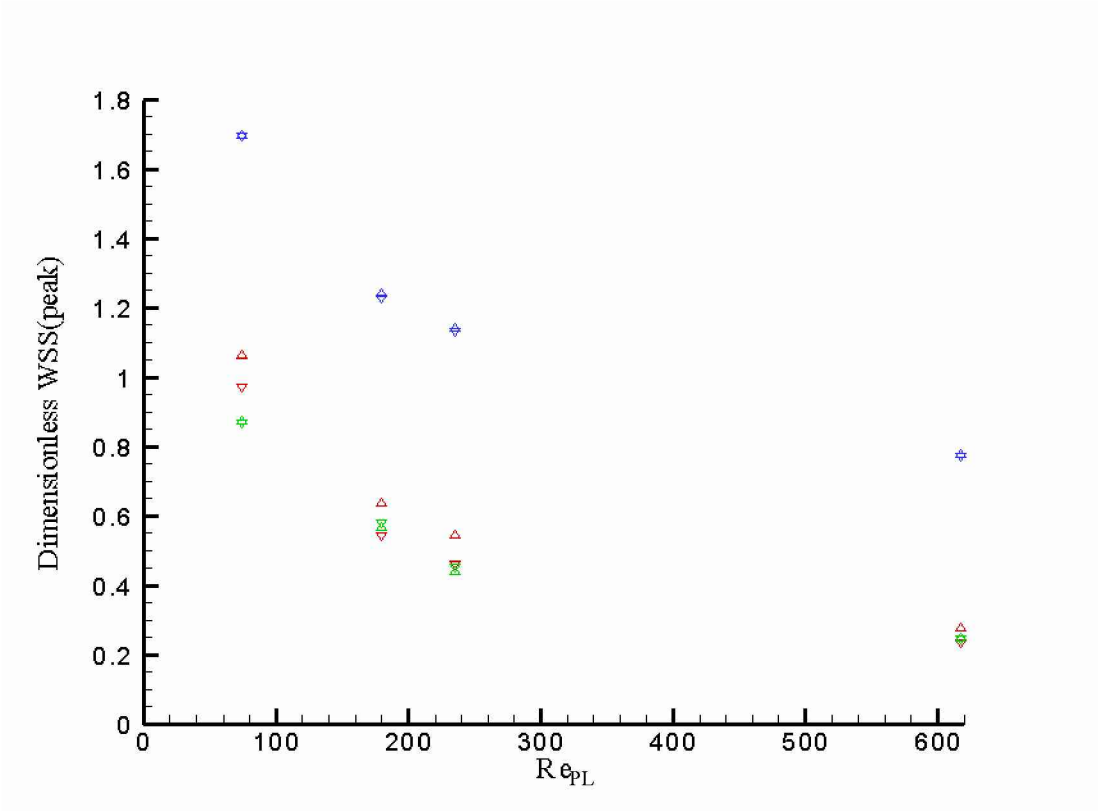

Fig.56: Variation of dimensionless peak wall shear stress at the throat of the occlusion with Reynolds number under steady flow conditions (84% occlusive severity). Comparison between PIV and CFD data.

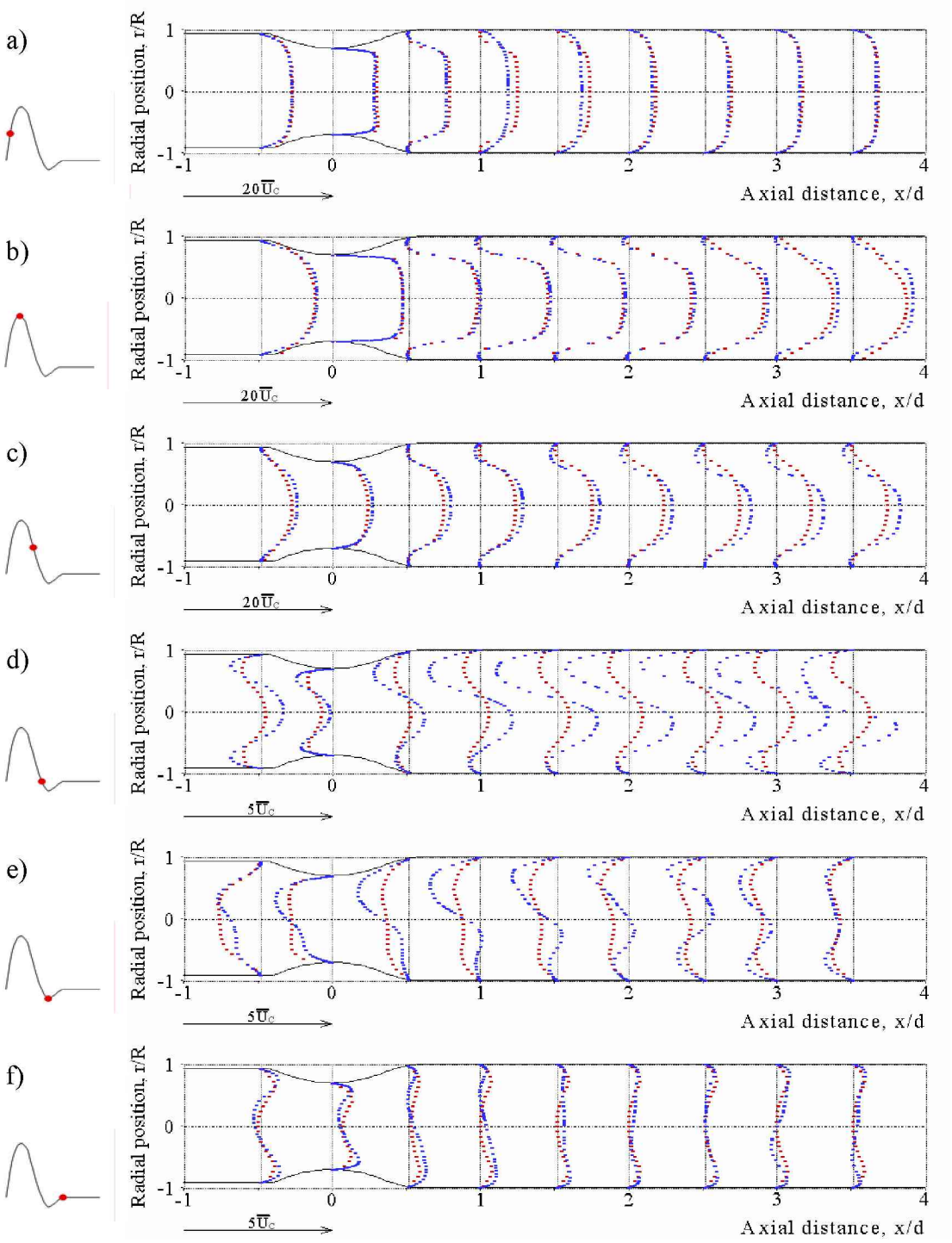

Fig.57: Velocity profiles (51% occlusive severity) for biphasic flow. Comparison between PIV and CFD data.

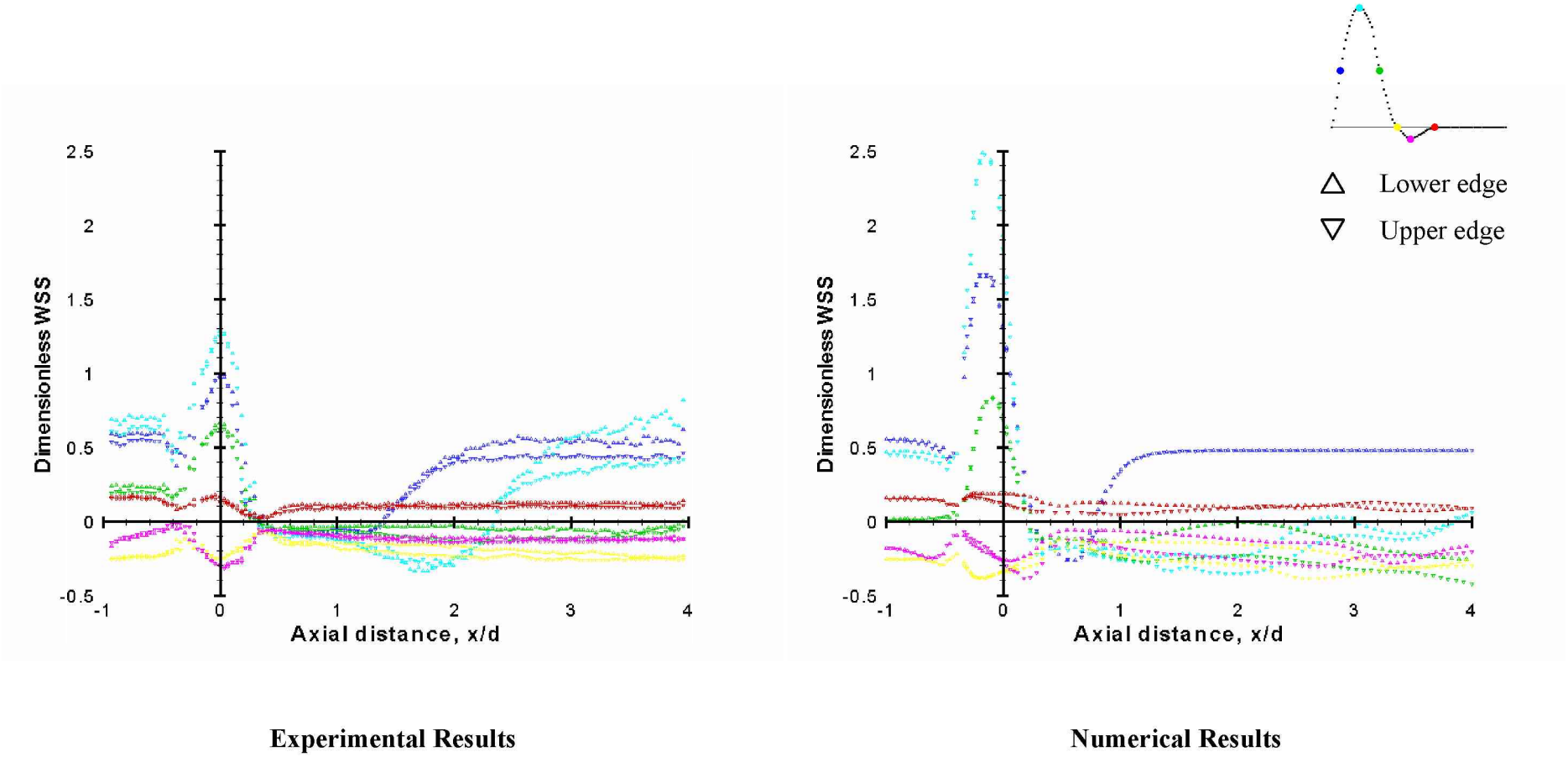

Fig.58: Wall shear stress distributions (51% occlusive severity) for biphasic flow. Comparison between PIV and CFD data.

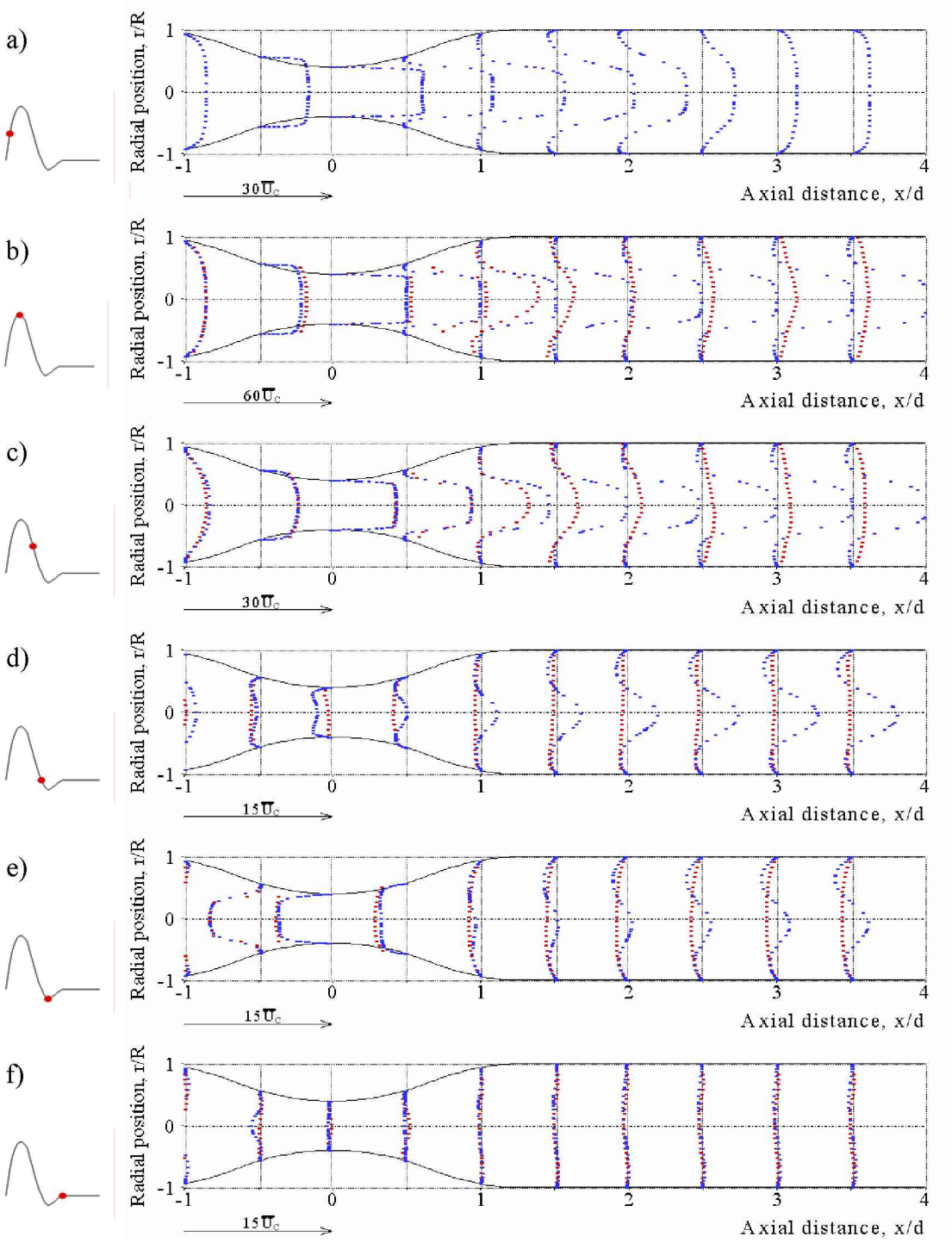

Fig.59: Velocity profiles (84% occlusive severity) for biphasic flow. Comparison between PIV and CFD data.

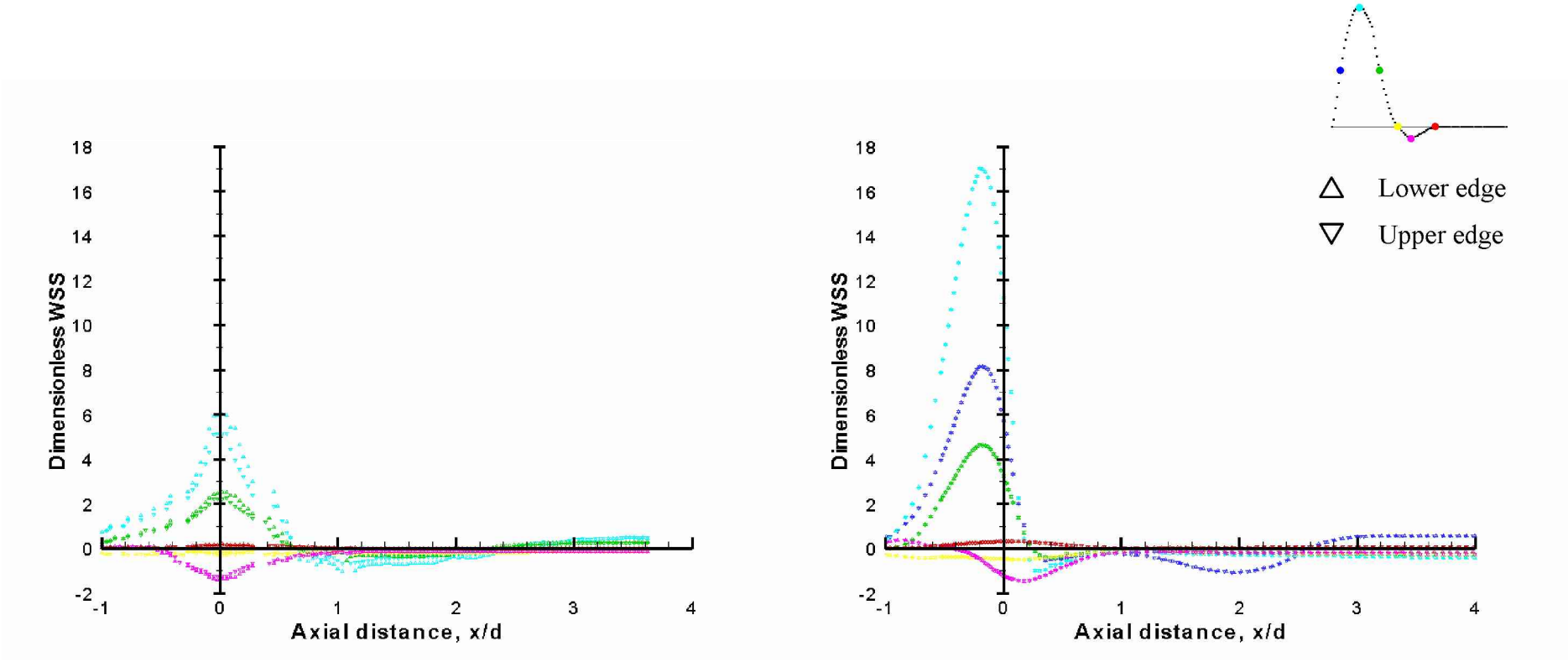

Fig.60: Wall shear stress distributions (84% occlusive severity) for biphasic flow. Comparison between PIV and CFD data.

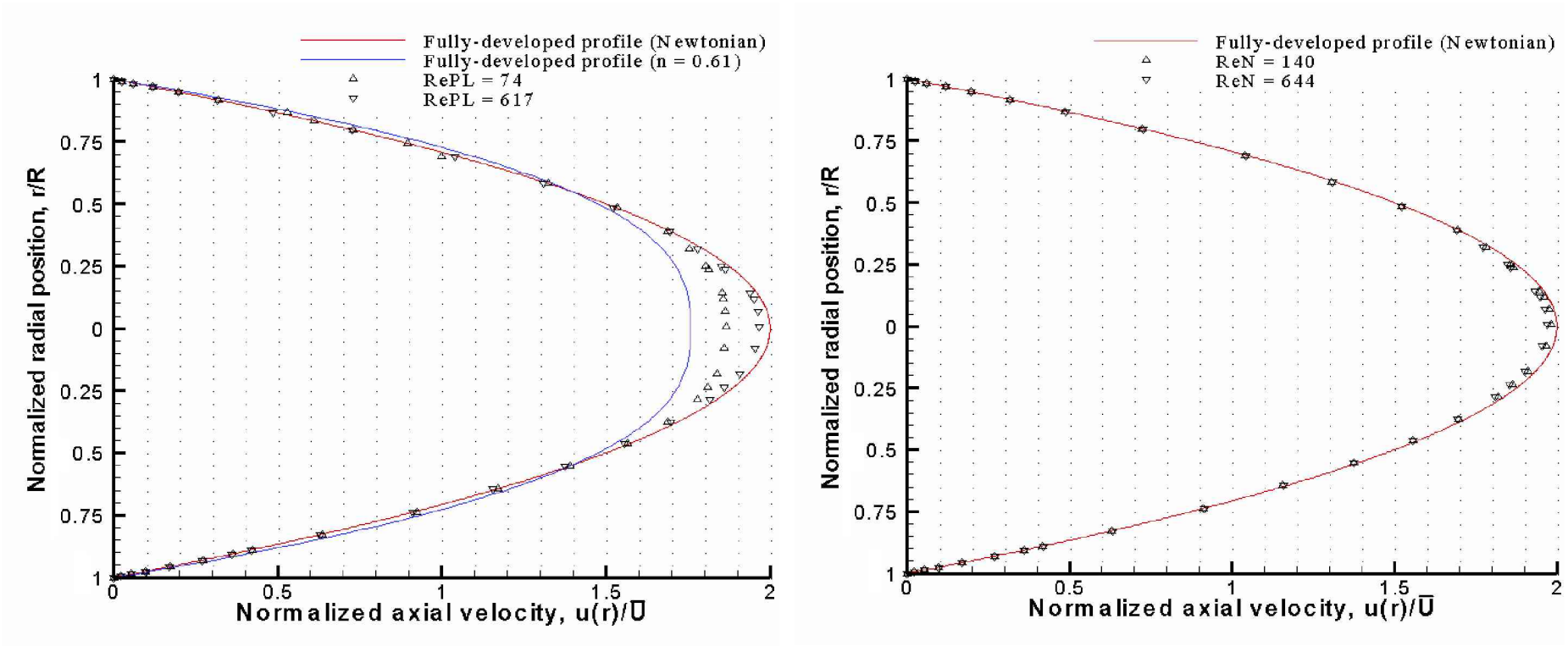

a) Modified Power-Law fluid model

b) Newtonian fluid model

Fig.61: Comparison of theoretical fully-developed velocity profiles with numerical data, obtained proximal to the occlusion (*in vivo*-scale) in the 51% occlusive severity domain.

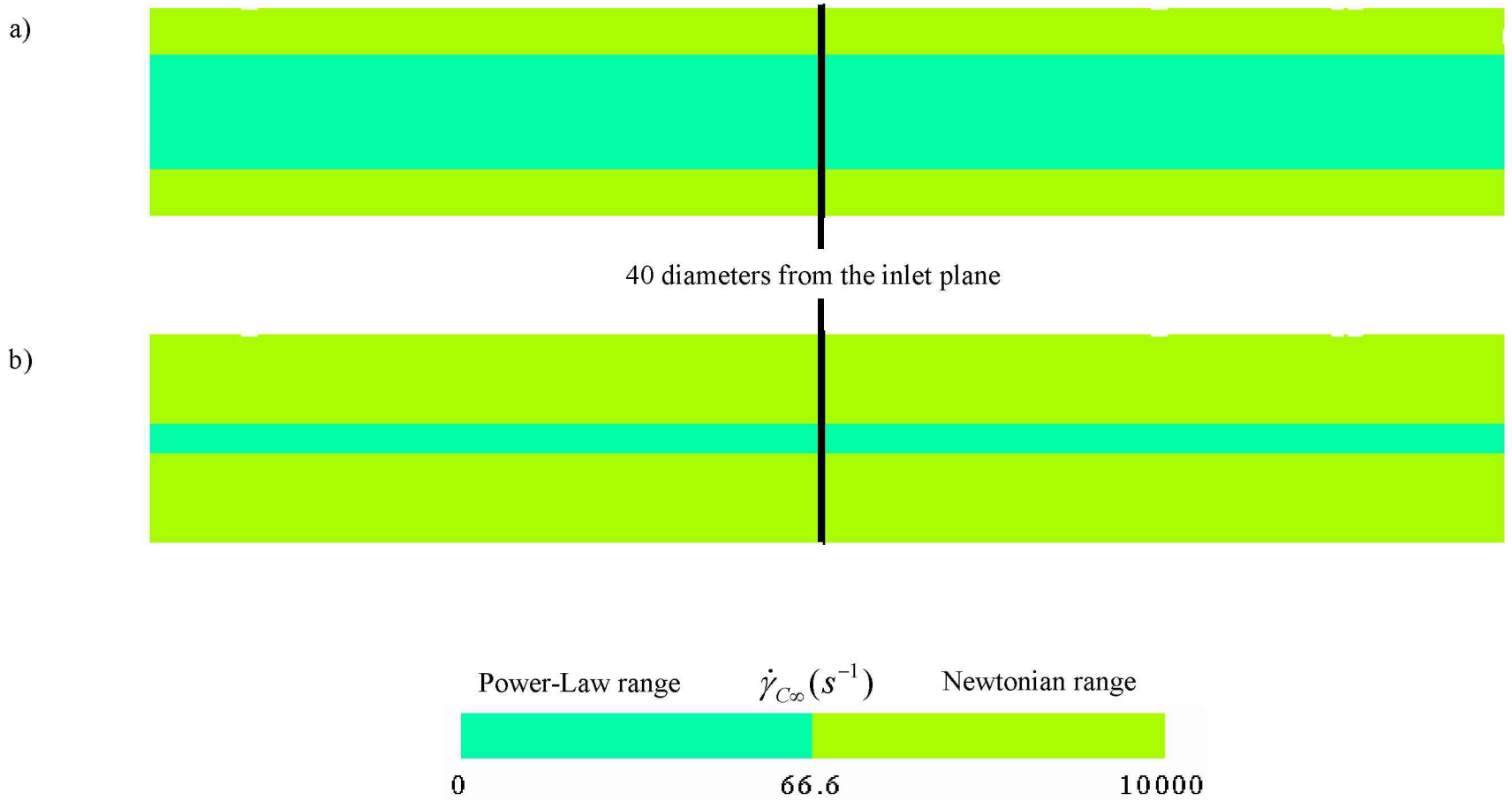

Fig.62: Contour maps of shear rate magnitude. a) Re_{PL} = 74, b) Re_{PL} = 617.

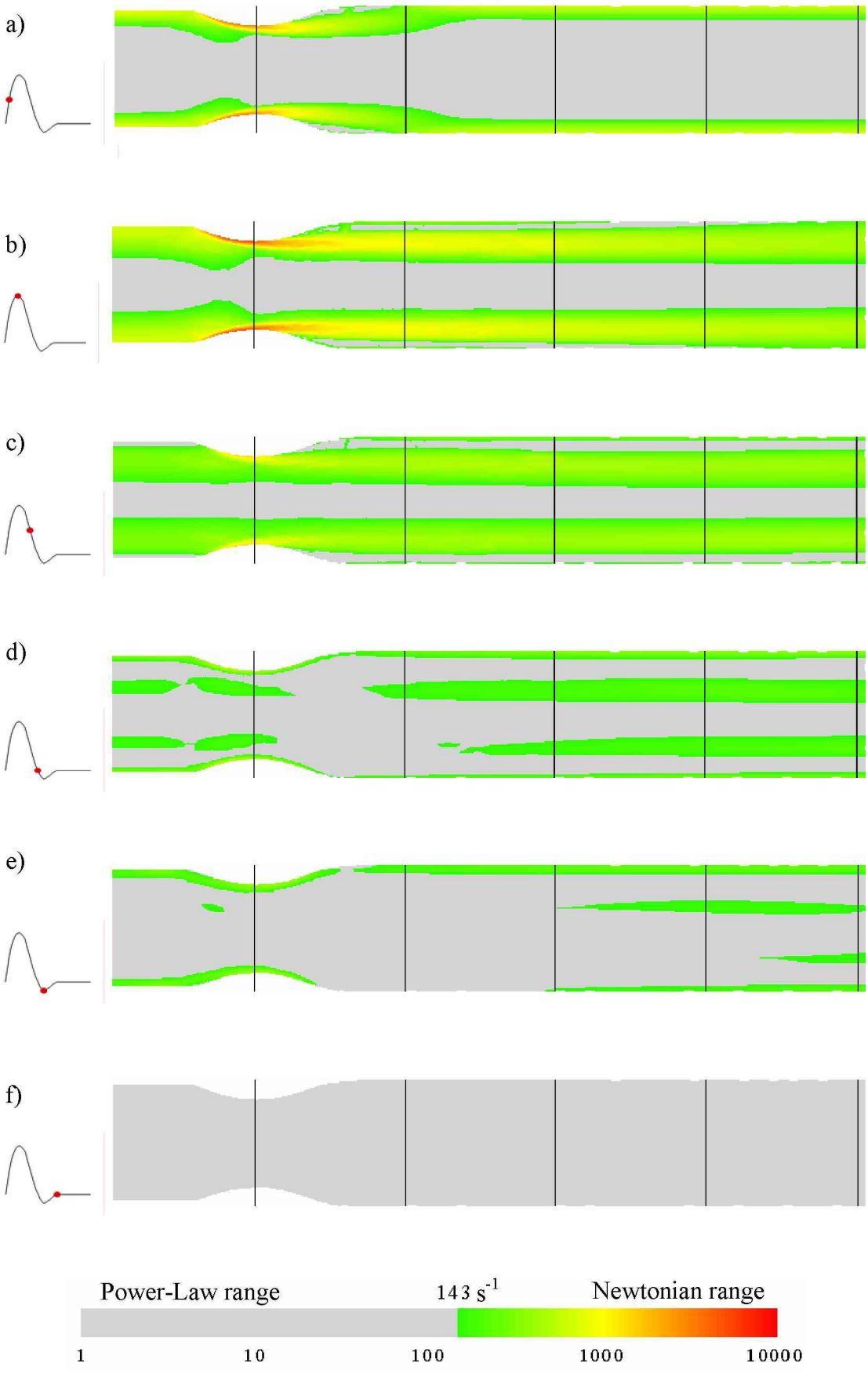

Fig.63: Contour maps of shear rate magnitude (51% occlusive severity) for biphasic flow. Intervals shown every diameter.

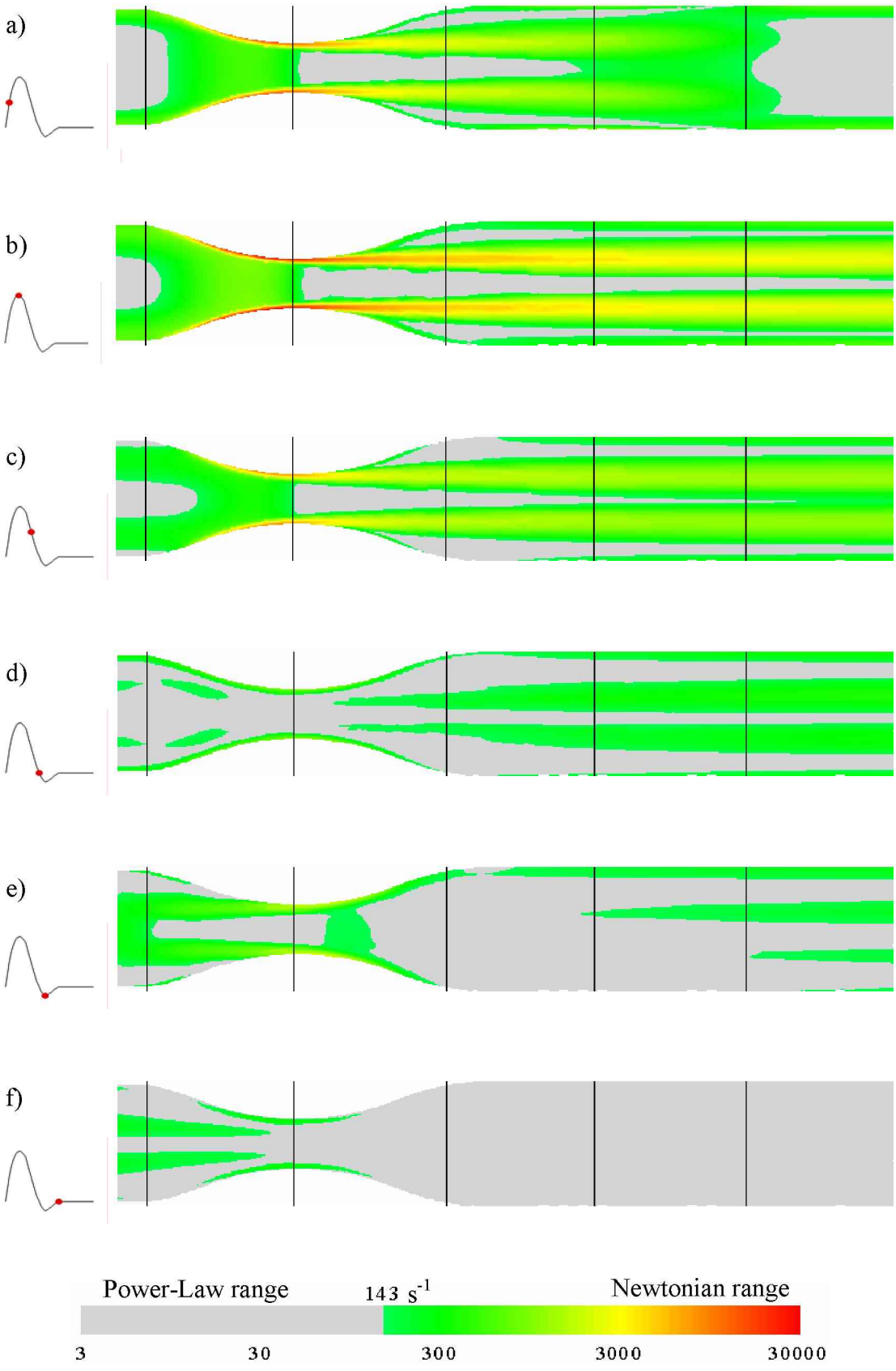

Fig.64: Contour maps of shear rate magnitude (84% occlusive severity) for biphasic flow. Intervals shown every diameter.

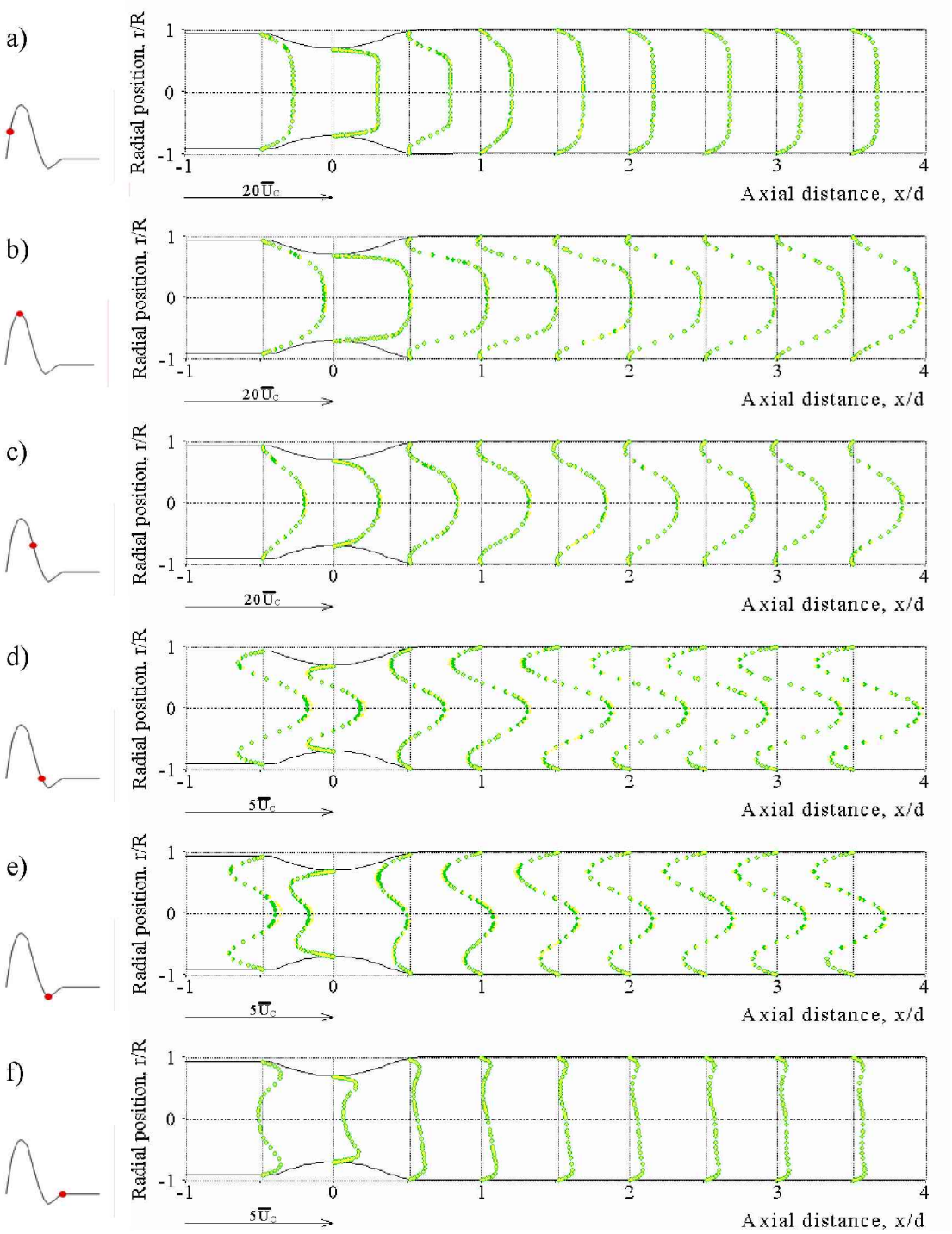

Fig.65: Velocity profiles for 51% stenosis severity, Biphasic flow conditions.

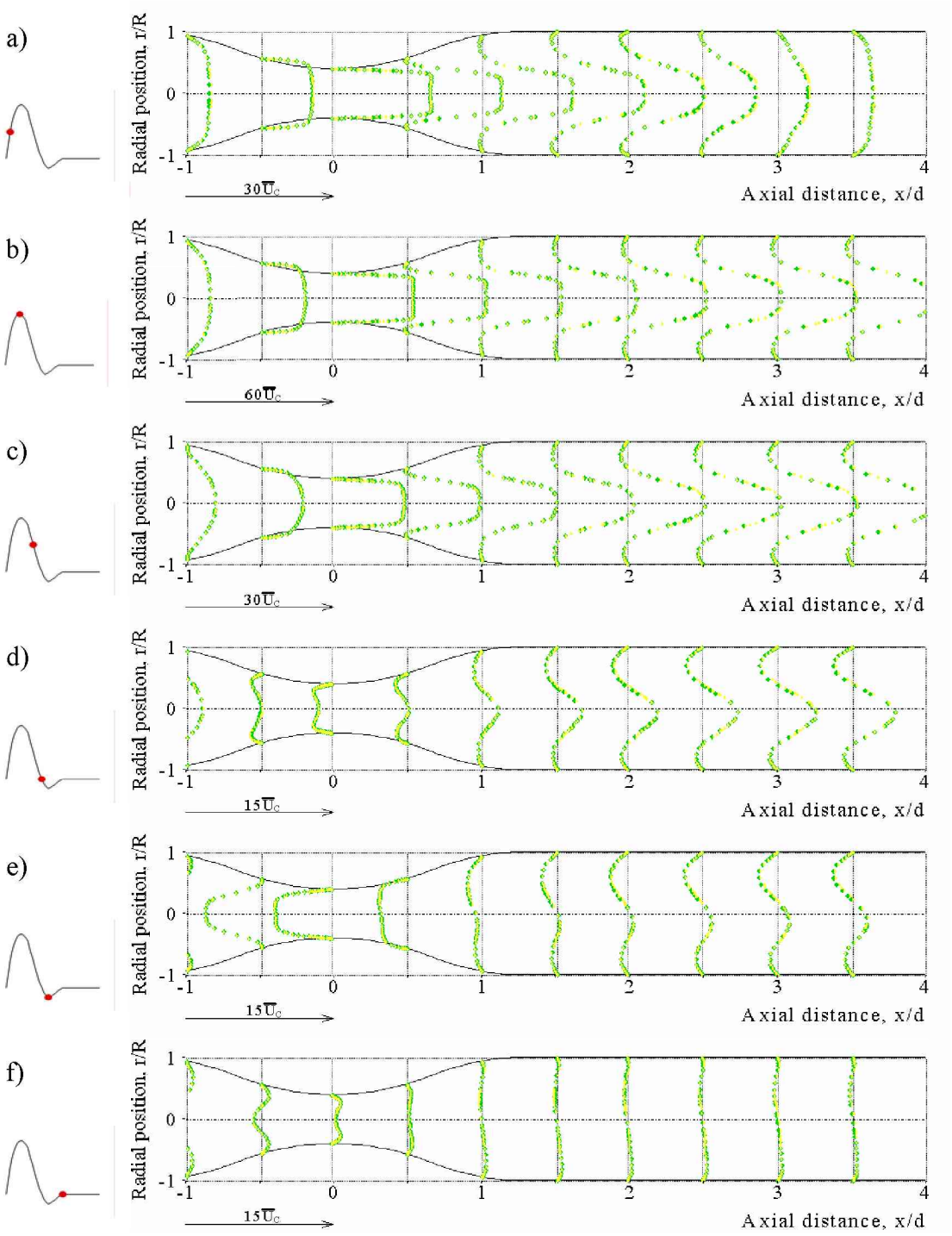

Fig.66: Velocity profiles for 84% stenosis severity, Biphasic flow conditions.

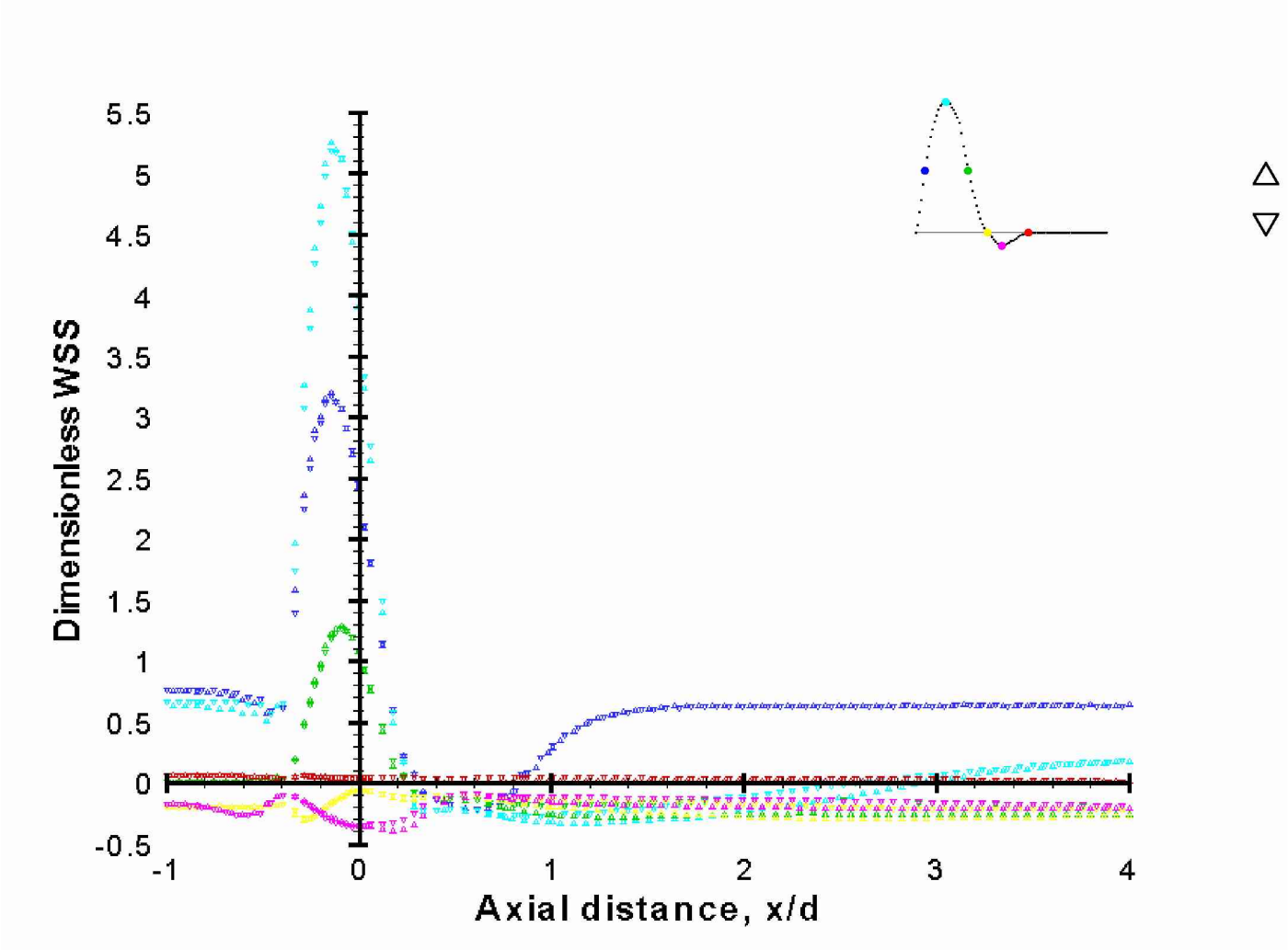

Fig.67: Wall shear stress distribution over the biphasic waveform cycle, (51% occlusive severity). CFD data using blood analogue.

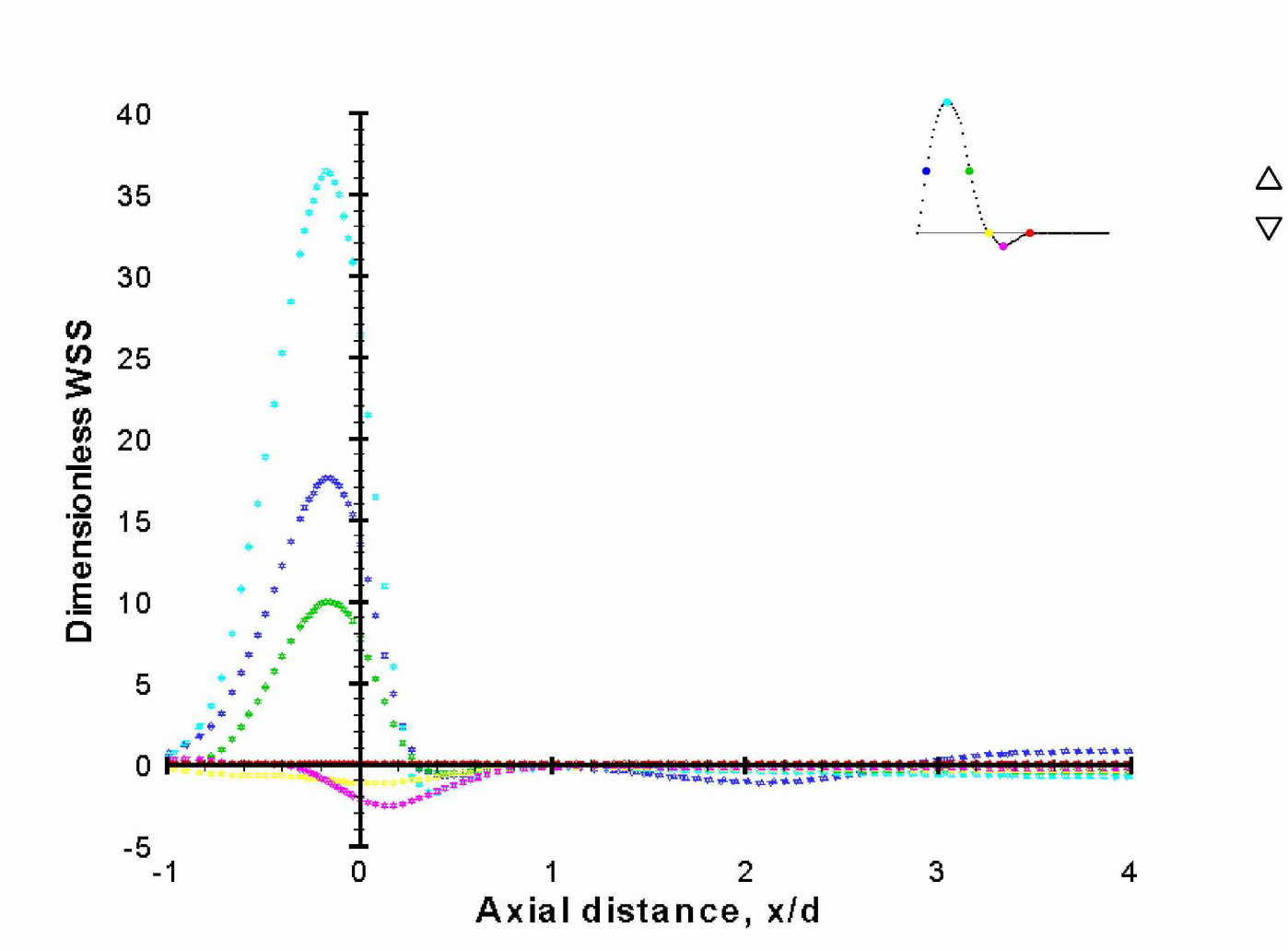

Fig.68: Wall shear stress distribution over the biphasic waveform cycle, (84% occlusive severity). CFD data using blood analogue.

Appendix A – Dimensional Analysis for a Power-Law Fluid under Pulsatile Conditions

The shear viscosity of blood, η is described by the Power-Law relationship:

$$\eta = \kappa \dot{\gamma}^{(n-1)}$$

At the extremities of the shear range however, viscosity is limited such that:

$$\dot{\gamma} < \dot{\gamma}_{C0} \rightarrow \eta = \eta_0$$

$$\dot{\gamma} > \dot{\gamma}_{C\infty} \rightarrow \eta = \eta_\infty$$

This is shown graphically as follows:

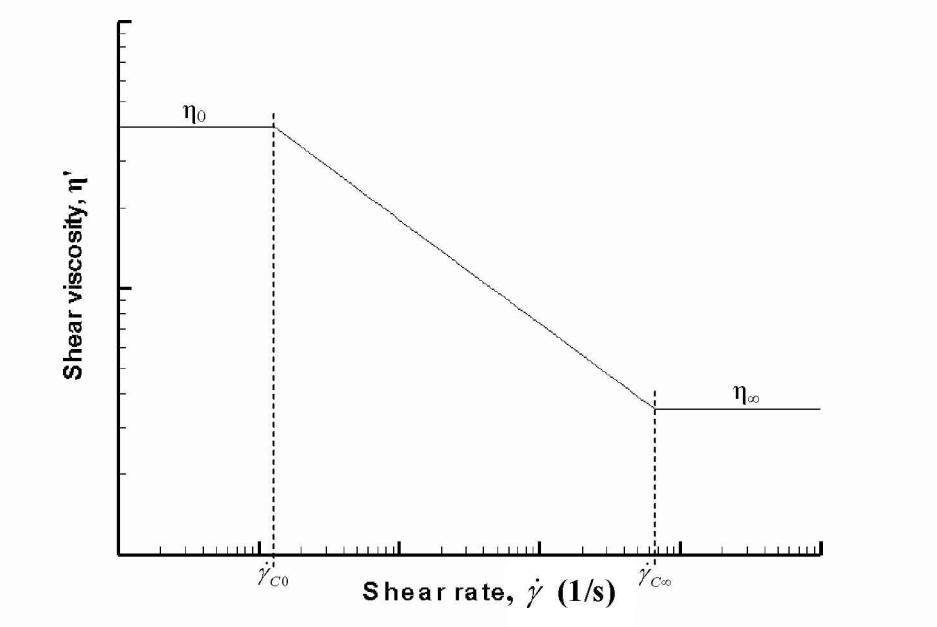

The properties of a fluid, and the way it behaves, are governed by the following parameters:

Density, ρ	kg/m^3	$\left[\frac{M}{L^3}\right]$
Power-Law index, n		[–]
Power-Law consistency, κ	Pa.s^n	$\left[\frac{M}{LT^{(2-n)}}\right]$
High shear rate viscosity, η_∞	Pa.s	$\left[\frac{M}{LT}\right]$
Low shear rate viscosity, η_0	Pa.s	$\left[\frac{M}{LT}\right]$

The parameters which affect the flow of such a fluid are related to the geometry employed and the pulsatile nature of the waveform:

Diameter, d	m	$[L]$
Cycle-averaged mean velocity, $\overline{U}_C$	m/s	$\left[\frac{L}{T}\right]$
Peak to peak amplitude of waveform, $\hat{u}$	m/s	$\left[\frac{L}{T}\right]$
Angular frequency of waveform, ω	rad/s	$\left[\frac{1}{T}\right]$

Wall shear stress, τ_w is defined as a function of:

$$\begin{array}{ccccccccccccc} \tau_w & = & f & (& \kappa & , & n & , & \rho & , & \eta_0 & , & \eta_\infty \\ \frac{M}{LT^2} & & & & \frac{M}{LT^{(2-n)}} & & [-] & & \frac{M}{L^3} & & \frac{M}{LT} & & \frac{M}{LT} \end{array}$$

$$\begin{array}{ccccccccccc} , & d & , & \overline{U}_c & , & \hat{u} & , & \omega &) \\ & L & & \frac{L}{T} & & \frac{L}{T} & & \frac{1}{T} & \end{array}$$

Eliminating mass:

$$\begin{array}{ccccccccccccc} \frac{\tau_w}{\rho} & = & f & (& \frac{\kappa}{\rho} & , & n & , & \frac{\eta_0}{\rho} & , & \frac{\eta_\infty}{\rho} \\ \frac{L^2}{T^2} & & & & \frac{L^2}{T^{(2-n)}} & & [-] & & \frac{L^2}{T} & & \frac{L^2}{T} \end{array}$$

$$\begin{array}{ccccccccc} , & d & , & \overline{U}_c & , & \hat{u} & , & \omega &) \\ & L & & \frac{L}{T} & & \frac{L}{T} & & \frac{1}{T} & \end{array}$$

Eliminating time:

$$\begin{array}{ccccccccccccc} \frac{\tau_w}{\rho \overline{U}_c^{\,2}} & = & f'' & (& \frac{\kappa}{\rho \overline{U}_c^{\,(2-n)}} & , & n & , & \frac{\eta_0}{\rho \overline{U}_c} & , & \frac{\eta_\infty}{\rho \overline{U}_c} \\ [-] & & & & L^n & & [-] & & L & & L \end{array}$$

$$\begin{array}{ccccccc} , & d & , & \frac{\hat{u}}{\overline{U}_c} & , & \frac{\omega}{\overline{U}_c} &) \\ & L & & [-] & & \frac{1}{L} & \end{array}$$

Eliminating length

$$\begin{array}{ccccccccccccc} \frac{\tau_w}{\rho \overline{U}_c^{\,2}} & = & f''' & (& \frac{\kappa}{\rho d^n \overline{U}_c^{\,(2-n)}} & , & \frac{\eta_0}{\rho d \overline{U}_c} & , & \frac{\eta_\infty}{\rho d \overline{U}_c} & , & n \\ [-] & & & & [-] & & [-] & & [-] & & [-] \end{array}$$

$$\begin{array}{ccccc} , & \frac{\hat{u}}{\overline{U}_c} & , & \frac{\omega d}{\overline{U}_c} &) \\ & [-] & & [-] & \end{array}$$

Therefore, the above dimensional analysis dictates that:

Dimensionless wall shear stress: $$\mathrm{T} = \frac{\tau_w}{\frac{1}{2}\rho \overline{U}_c^{\,2}}$$

is some function of:

Reynolds number, $$\mathrm{Re}_{PL} = \frac{\rho d^n \overline{U}_c^{\,(2-n)}}{\kappa}\ ,\ \mathrm{Re}_0 = \frac{\rho d \overline{U}_c}{\eta_0}\ ,\ \mathrm{Re}_\infty = \frac{\rho d \overline{U}_c}{\eta_\infty}$$

Power-Law index, n

Pulsatility index, $$P.I. = \frac{\hat{u}}{\overline{U}_c} = \frac{u_{\max} - u_{\min}}{\overline{U}_c}$$

Strouhal number, $$St = \frac{\omega d}{\overline{U}_c}$$

$$\mathrm{T} = f\left(\mathrm{Re}_{PL}\ ,\ \mathrm{Re}_0\ ,\ \mathrm{Re}_\infty\ ,\ n\ ,\ P.I.\ ,\ St\right)$$

(NB: In order to relate the non-dimensional WSS to a recognisable physical quantity, division by the factor $\frac{1}{2}$ means that WSS is made non-dimensional by dividing it by the dynamic pressure. This does not affect dynamic similarity since the actor $\frac{1}{2}$ is dimensionless.

Appendix B – Equations Governing Fluid Flow

The Navier-Stokes equations describe the motion of fluids. They are derived from principles of conservation relating to mass and momentum.

The conservation of mass equation (often referred to as the Continuity Equation) is based upon the assumption that mass cannot be created or destroyed; the mass of a closed system remains constant.

- Continuity Equation…

$$\frac{\partial \rho}{\partial t} + \frac{\partial (\rho u)}{\partial x} + \frac{\partial (\rho v)}{\partial y} + \frac{\partial (\rho w)}{\partial z} = 0$$

The conservation of momentum equations are derived through a consideration of Newton's second law; that a change in the momentum of a fluid particle (its acceleration) is the result of changes in the forces acting on the particle.

- Conservation of x-momentum…

$$\frac{\partial u}{\partial t} = -\left[u\frac{\partial u}{\partial x} + v\frac{\partial u}{\partial y} + w\frac{\partial u}{\partial z} \right] + \frac{1}{\rho}\left[-\frac{\partial p}{\partial x} + \frac{\partial \tau_{xx}}{\partial x} + \frac{\partial \tau_{yx}}{\partial y} + \frac{\partial \tau_{zx}}{\partial z} \right]$$

- Conservation of y-momentum…

$$\frac{\partial v}{\partial t} = -\left[u\frac{\partial v}{\partial x} + v\frac{\partial v}{\partial y} + w\frac{\partial v}{\partial z} \right] + \frac{1}{\rho}\left[-\frac{\partial p}{\partial y} + \frac{\partial \tau_{xy}}{\partial x} + \frac{\partial \tau_{yy}}{\partial y} + \frac{\partial \tau_{zy}}{\partial z} \right]$$

- Conservation of z-momentum…

$$\frac{\partial w}{\partial t} = -\left[u\frac{\partial w}{\partial x} + v\frac{\partial w}{\partial y} + w\frac{\partial w}{\partial z} \right] + \frac{1}{\rho}\left[-\frac{\partial p}{\partial z} + \frac{\partial \tau_{xz}}{\partial x} + \frac{\partial \tau_{yz}}{\partial y} + \frac{\partial \tau_{zz}}{\partial z} \right]$$

p	Pressure	N/m^2
t	Time	s
u	Component of velocity in x-direction	m/s
v	Component of velocity in y-direction	m/s
w	Component of velocity in z-direction	m/s
ρ	Fluid density	kg/m^3
τ_{xx}	Shear stress acting in the x-direction on faces normal to the x-direction	N/m^2
τ_{xy}	Shear stress acting in the y-direction on faces normal to the x-direction	N/m^2
τ_{xz}	Shear stress acting in the z-direction on faces normal to the x-direction	N/m^2
τ_{yx}	Shear stress acting in the x-direction on faces normal to the y-direction	N/m^2
τ_{yy}	Shear stress acting in the y-direction on faces normal to the y-direction	N/m^2
τ_{yz}	Shear stress acting in the z-direction on faces normal to the y-direction	N/m^2
τ_{zx}	Shear stress acting in the x-direction on faces normal to the z-direction	N/m^2
τ_{zy}	Shear stress acting in the y-direction on faces normal to the z-direction	N/m^2
τ_{zz}	Shear stress acting in the z-direction on faces normal to the z-direction	N/m^2

Appendix C – Integration of Velocity Profiles (Proof of Continuity)

In fully-developed laminar pipe flow, the axial velocity is defined using the following:

$$u(r) = \overline{U}\left(\frac{3n+1}{n+1}\right)\left\{1-\left(\frac{r}{R}\right)^{\left(\frac{n+1}{n}\right)}\right\} \qquad \text{Equation C1}$$

For a Newtonian fluid (n = 1), the above equation reduces to the simpler form:

$$u(r) = 2\overline{U}\left\{1-\left(\frac{r}{R}\right)^{2}\right\} \qquad \text{Equation C2}$$

Likewise, the fully-developed profile of a Power-Law fluid (where n = 0.61) reduces to the approximate form:

$$u(r) = 1.7578\,\overline{U}\left\{1-\left(\frac{r}{R}\right)^{2.6393}\right\} \qquad \text{Equation C3}$$

The profiles generated using Equations C2&C3 assume the following shape.

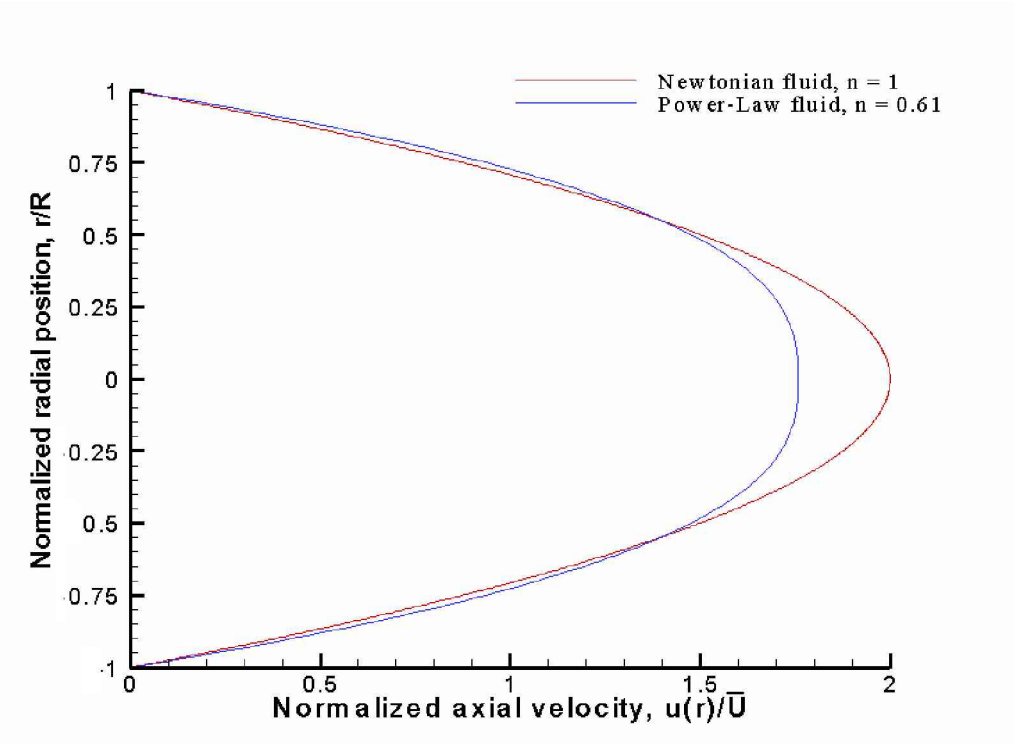

A comparison of the areas bound by the above profiles may appear to suggest that continuity is not maintained (the area bounded by red is larger than that bounded by blue). However, it is important to remember that the volumetric flow rate is defined as the volume bounded by the three-dimensional velocity profile, not the area bounded by the two-dimensional profile. Integration of axial velocity, u(r) across the three-dimensional radial plane allows the calculation of the bounded volume (and hence volumetric flow rate), from which the maintenance of continuity can be confirmed. Since the above velocity profiles are defined by algebraic equations (C2 and C3), their integration can be done easily using mathematical techniques.

The volumetric flow rate q, of fluid moving with local axial velocity u(r), through a pipe of radius r, is calculated by integrating the flow across the radial plane. This is written mathematically in the following form.

$$q = \int_0^R 2\pi r\, u(r)\, dr \qquad \text{Equation C4}$$

For the Newtonian fluid, substitute Equation C2 into C4 and perform the subsequent integration…

$$q = \int_0^R 2\pi r \left(2\overline{U} \left\{ 1 - \left(\frac{r}{R} \right)^2 \right\} \right) dr$$

$$= 4\pi \overline{U} \int_0^R \left(r - \frac{r^3}{R^2} \right) dr$$

$$= 4\pi \overline{U} \left[\frac{r^2}{2} - \frac{r^4}{4R^2} \right]_0^R$$

$$= 4\pi \overline{U} \left(\left(\frac{R^2}{2} - \frac{R^4}{4R^2} \right) - 0 \right)$$

This integration reduces to the characteristic equation relating bulk flow velocity ($\overline{U}$), cross-sectional area of the pipe (πR^2) and volumetric flow rate (q).

$$q = \overline{U}\, \pi R^2$$

Likewise, substituting Equation C3 into C4 and performing the subsequent integration for the Power-Law fluid…

$$q = \int_0^R 2\pi r \left(1.7578\overline{U} \left\{ 1 - \left(\frac{r}{R} \right)^{2.6393} \right\} \right) dr$$

$$q = 3.5155\pi\overline{U} \int_0^R \left(r - \frac{r^{3.6393}}{R^{2.6393}} \right) dr$$

$$= 3.5155\pi\overline{U} \left[\frac{r^2}{2} - \frac{r^{4.6393}}{4.6393R^{2.6393}} \right]_0^R$$

$$= 3.5155\pi\overline{U} \left(\left(\frac{R^2}{2} - \frac{R^{4.6393}}{4.6393R^{2.6393}} \right) - 0 \right)$$

$$= 3.5155\pi\overline{U} \left(\frac{R^2}{2} - \frac{R^2}{4.6393} \right)$$

Again, this integration is reduced to the characteristic equation obtained previously for the Newtonian fluid:

$$q = \overline{U}\pi R^2$$

The above discussion indicates that the velocity profiles, defined by Equations C2&C3, represent fully-developed laminar conditions in which the volumetric flow rates are equal, hence satisfying the requirements of continuity.